4 Thermal regime of the lithosphere from heat flow data

This chapter discusses the thermal regime of the lithosphere constrained by surface heat flow measurements. Other methods used to assess thermal structure of the lithosphere, such as xenolith geotherms and conversions of seismic velocities and seismic attenuation to mantle temperatures are discussed in Chapter 5. The goal of such a subdivision of constraints on crustal and upper mantle temperatures is to separate thermal models related to the global heat flow balance of the Earth from thermal models coming from, largely, non-potential field data.

The number of broad overviews of geothermal studies is limited (e.g. Sclater *et al*., 1980; Stein, 1995). Pollack *et al*. (1993) provide an overview of global patterns of surface heat flow based on their compilation of a significant portion of borehole measurements available at that time. Overviews of the thermal regime of the lithosphere are given by Stein and Stein (1992) for the oceans and by Artemieva and Mooney (2001) and Artemieva (2006) for the continents. Beardsmore and Cull (2001) review practical applications of heat flow measurements, largely in relation to geothermal exploration. Jaupart and Mareschal (2004) discuss data on heat production and its contribution to surface heat flow, and a new monograph addressing various aspects of geothermal research is being published (Jaupart and Mareschal, 2010).

4.1 Field observations and laboratory data

4.1.1 Heat flow measurements

The thermal regime of the Earth provides critical information on its evolution through geological history by putting energy constraints on the processes of planetary accretion and differentiation. Although the energy that the Earth receives from the Sun is about two orders of magnitude greater than the global heat loss from the planet's interior, most of the solar energy is reradiated and the temperature in the Earth is controlled by internal heat: at present about 80% of heat flow from the planet's deep interior comes from radiogenic heat production, while the remaining 20% is the result of secular cooling of the Earth which includes latent heat from solidification of the core (Malamud and Turcotte, 1999).

Knowledge of the present thermal state of the Earth is crucial for models of crustal and mantle evolution, mantle dynamics and processes in the deep interior, which are reflected in geophysical observations such as seismic elastic and anelastic models, electromagnetic and gravity models, and geoid observations. Physical properties of crustal and mantle rocks determined by remote geophysical sensing are temperature dependent, and interpretations of

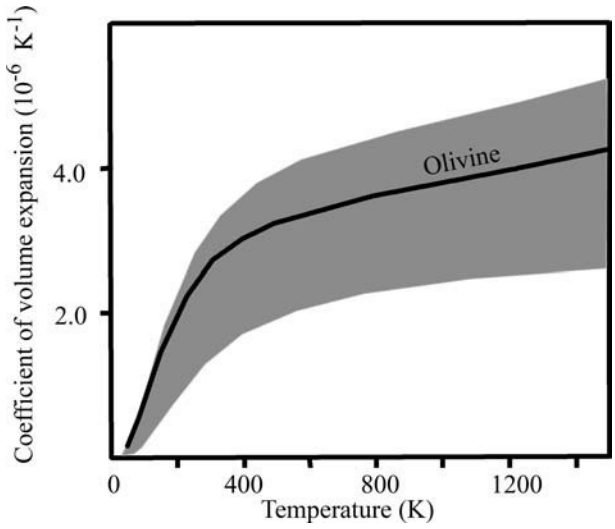

Fig. 4.1 Range of thermal expansion coefficients for common mantle minerals (source: Duffy and Anderson, 1989).

geophysical data sets are impossible without information on the thermal regime of the crust and the mantle. For example, numerous laboratory measurements indicate that seismic velocities and seismic attenuation are strongly temperature dependent (in particular at sub-solidus temperatures), implying that the temperature signal is an important part of any seismic model (Chapter 3). Mantle viscosity, which defines the vigor of mantle convection, depends exponentially on temperature. Similarly, electrical conductivity of mantle and crustal rocks also shows exponential dependence on temperature (Chapter 6), and the temperature effect on density through thermal expansion manifests itself in gravity and geoid anomalies (Fig. 4.1).

Mechanisms of heat transfer and dimensionless numbers

Three mechanisms transfer heat to the surface of the Earth: conduction, convection, and advection (the role of the fourth heat transfer mechanism, radiation, is minor). Most heat loss through the Earth's surface is by conduction, and thus it is the *conductive heat flow* that is measured in geophysics and commonly quoted as terrestrial heat flow. However, locally near-surface convective or advective heat flow components can be significant, such as forced (tectonically driven) convection in volcanic regions and at mid-ocean ridges and free convection caused by water circulation through the oceanic crust. In the deep interior, convection in the mantle and in the liquid outer core plays an important role in the thermal regime of the planet on geological times. Advection of heat driven by free or forced convection plays an important role in near-surface heat transfer in regions with high hydraulic crustal permeability, such as sedimentary basins.

The Péclet number Pe is a dimensionless number that relates the rate of advection due to material flow to the rate of thermal diffusion:

$$\mathrm{Pe} = [\text{advection rate}]/[\text{thermal diffusion rate}] = VL/\chi \tag{4.1}$$

where V is the velocity of material flow, L is a characteristic length scale of the process and χ is thermal diffusivity. Advective heat transfer dominates when $\mathrm{Pe} \gg 1$, whereas conduction dominates when $\mathrm{Pe} \ll 1$. For $\chi = 10^{-6}$ m^2/s and $V = 1$ cm/year (typical for magma uplift beneath spreading ridges), $\mathrm{Pe} \sim 3 \times 10^{-4}\ L$ (in m). This means that the thickness of the conductive layer beneath a spreading ridge is less than 3 km (i.e. less than thickness of the oceanic crust), and the thermal regime beneath spreading ridges is controlled by advection. This has important implications for interpretation of heat flow measurements in the oceans.

The Nusselt number Nu is the dimensionless ratio of convective to conductive heat transfer:

$$\mathrm{Nu} = [\text{convective heat}]/[\text{conductive heat}] = hL/\lambda \tag{4.2}$$

where h is the convective transfer coefficient (proportional to heat flow change and inversely proportional to the heat transfer surface area, temperature difference between the layers, and time), L is a characteristic length scale of the process and λ is thermal conductivity. When the Nusselt number is close to unity the flow is laminar; at $\mathrm{Nu} \sim 100$–1000 the convection pattern becomes turbulent.

The Prandtl number Pr is the dimensionless ratio of kinematic viscosity v ($v = \mu/\rho$) to thermal diffusivity χ:

$$\mathrm{Pr} = [\text{viscous diffusion rate}]/[\text{thermal diffusion rate}] = v/\chi = C_\mathrm{p}\mu/\lambda \tag{4.3}$$

where C_p is specific heat, ρ is density, and μ is dynamic viscosity. The Prandtl number does not depend on a length scale, but depends only on material properties. For the mantle, $\mathrm{Pr} \sim 10^{25}$. In heat transfer, the Prandtl number controls the relative thickness of the thermal boundary layer. For example, when Pr is large, the heat diffuses very slowly and the thermal boundary layer is thick.

The Rayleigh number Ra is a dimensionless number associated with buoyancy-driven flow (i.e. free convection). When the Rayleigh number is below the critical value, heat transfer is primarily by conduction; when Ra exceeds the critical value, heat transfer is primarily by convection. For the Earth's mantle, the Rayleigh number indicates the vigor of convection and (in the case of internal heating) is:

$$\mathrm{Ra} = \frac{gp^2\alpha AD^5}{v\chi^\lambda} \tag{4.4}$$

where g is gravity acceleration, ρ is density, α is the thermal expansion coefficient, χ is thermal diffusivity, λ is thermal conductivity, v is kinematic viscosity, A is the rate of radiogenic heat production, and D is the thickness of the convective layer.

Accuracy of heat flow measurements

Data on surface heat flow together with geological and tectonic information are interpreted in terms of the thermal structure of the deep interior. Heat conduction in a medium is described by Fourier's law:

$$Q_i = \lambda_{ij} \frac{\partial T}{\partial z_j} \tag{4.5}$$

where Q_i is heat flow (the vector of specific energy flow rate), λ_{ij} is the thermal conductivity tensor, and the last term is the vector of temperature gradient. This equation provides the basis for near-surface heat flow measurements: the temperature gradient along vertical profiles in near-surface boreholes is the primarily directly measurable parameter, which, for known thermal conductivity of near-surface rocks, is converted into surface heat flow values.

The typical accuracy of thermal conductivity measurements on borehole core samples is 7–10% (largely because laboratory measurements are not done at *in situ* conditions, while *in situ* variations in porosity and fluid saturation of shallow crustal rocks have a significant effect on thermal conductivity; commonly laboratory measurements on low-porosity crystalline rocks provide conductivity values lower than at *in situ* conditions). The accuracy of modern measurements of temperature gradient is 5% or less; however it is important that measurements are made when the temperature distribution in a borehole (disturbed by drilling) equilibrates to steady state. Unfortunately, the latter requirement is not always met, in particular when industrial boreholes are used for geothermal research. The resulting uncertainty in surface heat flow measurements (even assuming temperature equilibrium was reached in a borehole) can amount to *c*. 15% as indicated by a comparison of heat flow data from nearby sites (Jaupart *et al*., 1982). The major source of noise (in addition to measurement accuracy) is shallow water circulation.

Since in most cases only the vertical component of the temperature gradient is measured, the strong anisotropy of thermal conductivity of most sedimentary and metamorphic rocks may cause lateral flow of heat. Thus, in most cases data on near-surface heat flow require corrections for factors, such as sedimentation (e.g. von Herzen and Uyeda, 1963), surface topography variations, presence of rocks with anomalous thermal conductivity (such as salt domes) (for details see Beardsmore and Cull, 2001). Other factors, such as groundwater circulation, especially in shallow boreholes, are difficult to account for. While the effects of sedimentation are important only in a limited number of locations where sedimentation rates exceed 10^{-3}–10^{-4} m/year and a thick sedimentary cover is present, fluctuations of near-surface temperatures associated with paleoclimate changes may lead to variations of deep temperatures and temperature gradients in the shallow crust and thus have an important effect on heat flow measurements in most continental locations. In particular, the most pronounced climatic variations in the northern parts of Europe and North America are associated with glaciations.

Paleoclimatic corrections

Fluctuations of near-surface temperatures, such as caused by glaciation, can lead to variations in deep temperatures and temperature gradients in the shallow crust (Fig. 4.2). Variations in temperature gradient $\Delta\gamma$ can be found from solution of the (1D) thermal conduction boundary problem:

$$\frac{\partial T}{\partial t} = \chi \frac{\partial^2 T}{\partial z^2} \tag{4.6}$$

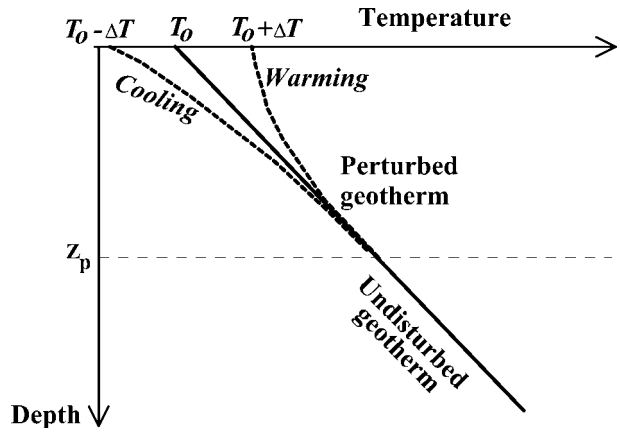

Fig. 4.2 Relation of borehole temperatures to climate changes.

$$T(0,t) = \begin{cases} 0, & t < \tau_1 \\ \Delta T, & \tau_1 < t < \tau_2 \end{cases}$$

$$T|_{Z\to\infty} \to T_0 + \gamma z$$

where γ is the equilibrium temperature gradient, ΔT is the difference in surface temperature during and after glaciation, τ_1 and τ_2 are the times elapsed from the end and from the beginning of glaciation, respectively. Solution of the boundary problem provides the value of the unperturbed temperature gradient in the crust (Beck, 1977):

$$\Delta\gamma = \Delta T\left\{\frac{1}{\sqrt{\pi\chi\tau_1}}\exp\left[-\left(\frac{z}{2\sqrt{\chi\tau_1}}\right)^2\right] - \frac{1}{\sqrt{\pi\chi\tau_2}}\exp\left[-\left(\frac{z}{2\sqrt{\chi\tau_2}}\right)^2\right]\right\} \qquad (4.7)$$

When τ_2 is unknown, paleoclimatic disturbances of the temperature gradient can be found from the first term of this equation. The value of $\Delta\gamma$ decreases with depth and with increasing τ_1 (Fig. 4.3). Typically, at depths $z > 1.5$ km the effect of glaciation on the surface heat flow is less than 2 mW/m^2 and is often neglected. However, in certain locations where near-surface temperature changes during a recent glaciation were significant, present-day temperatures can be perturbed even in deep boreholes. In particular, in some parts of the Baltic Shield perturbation of the present surface heat flow can be as large as 15–20 mW/m^2 (Balling, 1995).

4.1.2 Thermal conductivity

For a known thermal conductivity of near-surface rocks, the temperature gradient measured in heat flow studies is converted into surface heat flow values (Eq. 4.5). Although radiative heat transfer may play some role at high temperatures (higher than 600 °C, and in particular at temperatures above 1200 °C due to the strong temperature dependence of the radiative conductivity of polycrystalline rocks, e.g. Hofmeister, 1999), its role in the thermal regime

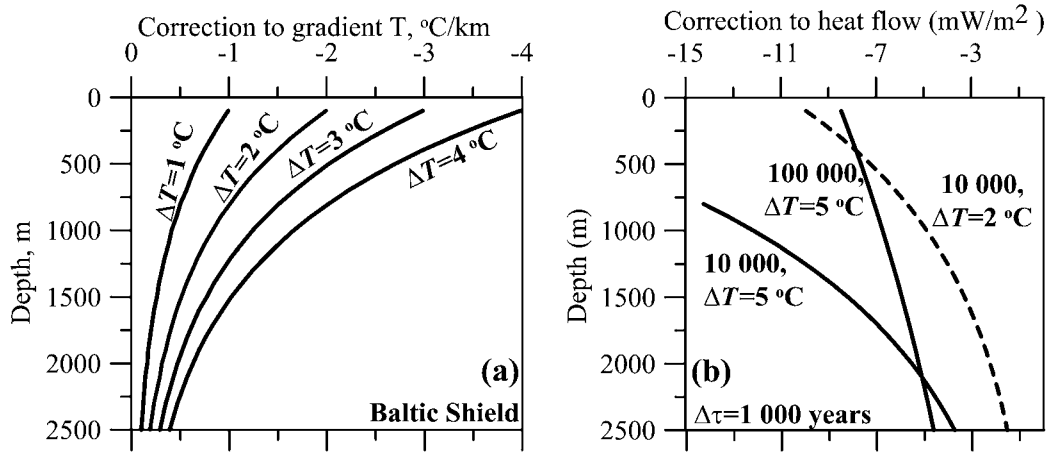

Fig. 4.3 Corrections to temperature gradient (a) and surface heat flow (b) due to recent glaciations. (a) Paleoclimate corrections for the Baltic Shield for different values of near-surface temperature changes with lower ΔT values for higher latitudes. (b) An example illustrating the effects of the age of glaciation (numbers on the curves) and variations in near-surface temperature ΔT on surface heat flow, assuming that glaciation lasted for 1000 years and the thermal conductivity of shallow crust is 3.0 W/m/K.

of the Earth remains unknown, and it is usually quantified by introducing effective (conductive plus radiative) thermal conductivity. High-temperature measurements of thermal conductivity always include a radiative component.

Laboratory measurements of thermal conductivity of sedimentary and crystalline rocks together with seismic models of crustal structure provide the basis for models of depth and lateral variations of thermal conductivity (Horai, 1971). An overview of the subject can be found in Clauser and Huenges (1995). Laboratory measurements of thermal conductivity of rocks form the basis for several extended collections. Although these compilations are commonly dominated by rocks from certain tectonic provinces, some general conclusions are summarized in the following.

Mineral composition

Mineral composition is the major factor controlling the thermal conductivity of crustal and mantle rocks (Fig. 4.4).

- For any given rock type, thermal conductivity may vary by as much as a factor of two to three.
- Thermal conductivity in plutonic and metamorphic rocks depends significantly on feldspar and quartz content, respectively, while porosity variations have a strong effect in sedimentary and volcanic rocks.
- Thermal conductivity of the lithospheric mantle is controlled by the relative amount of olivine and clinopyroxene with ~30% difference in their conductivities (Schatz and Simmons, 1972). However, since changes in olivine and clinopyroxene content between

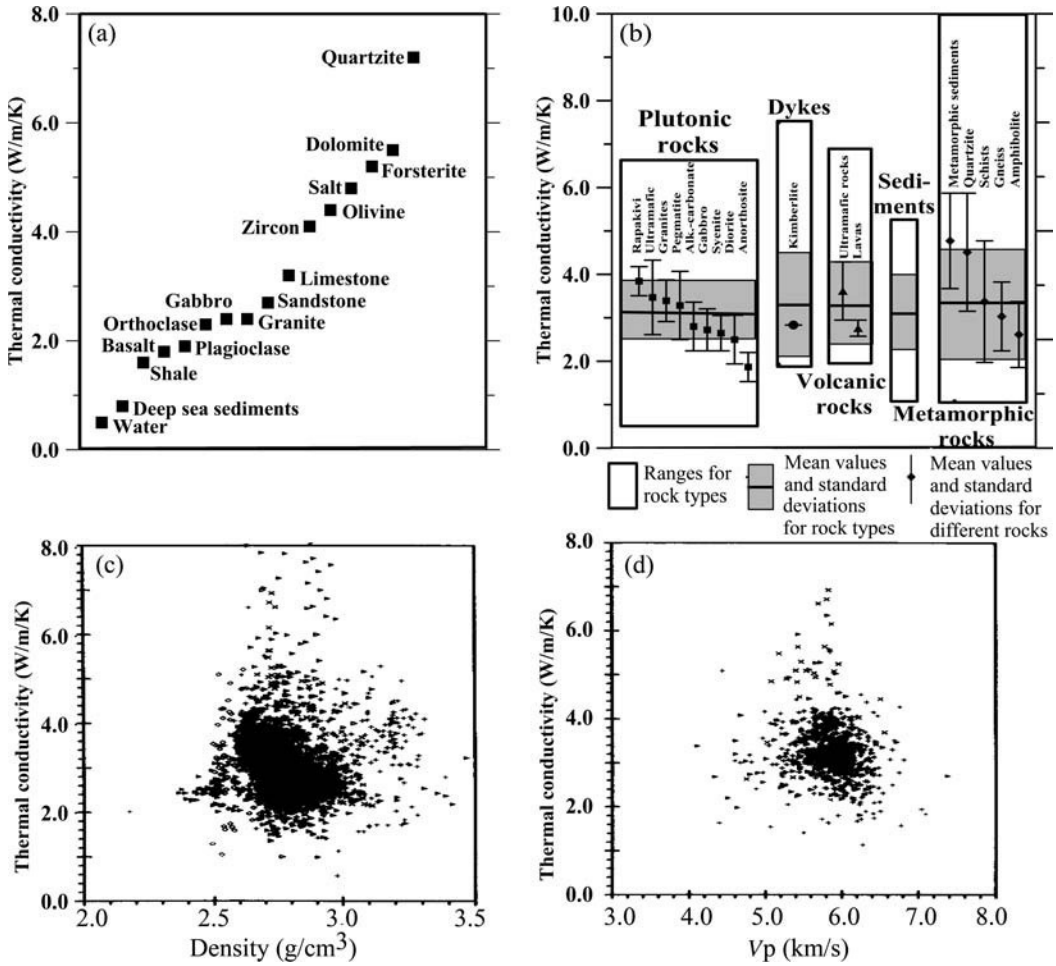

Fig. 4.4 Thermal conductivity of common minerals and rocks, (a) – global observations; (b–d) data from the Baltic Shield (source: Kukkonen and Peltoniemi, 1998).

Archean and post-Archean provinces are complimentary to each other, the net effect of compositional variations on the bulk mantle conductivity is ~0.1 W/m/K, and no significant variations in thermal conductivity of the lithospheric mantle of different ages are expected (Levy *et al.*, 2010).

- There is no straight-forward correlation between thermal conductivity and seismic velocities or between thermal conductivity and density (Fig. 4.4).

Porosity and fluid saturation

Thermal conductivity depends significantly on porosity: according to some studies, a 5% porosity increase can produce a 25% drop in thermal conductivity (Jessop, 1990). However,

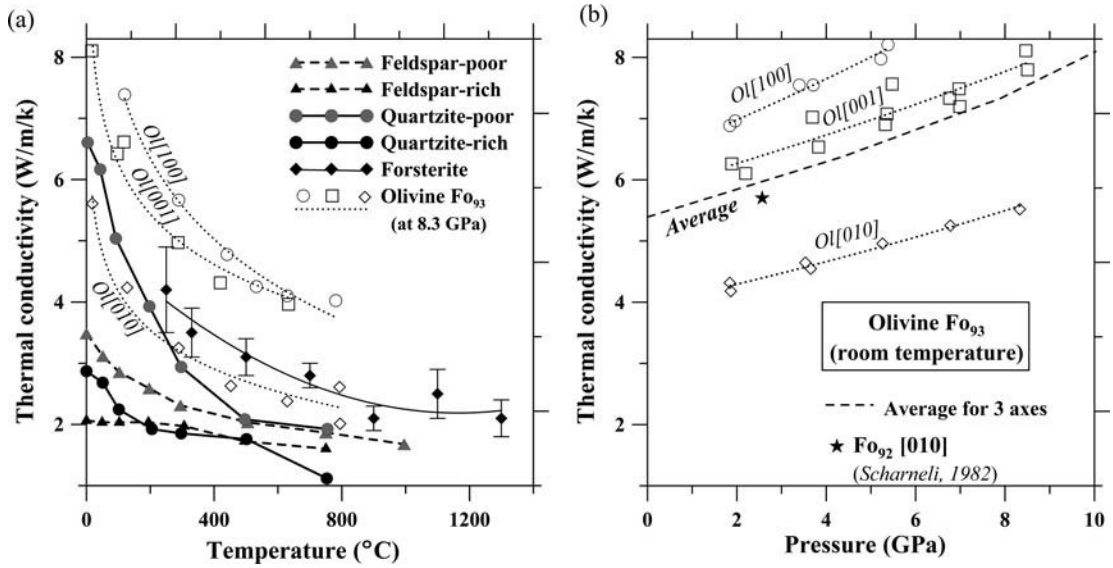

Fig. 4.5 (a) Temperature dependence of the thermal conductivity of plutonic rocks (dashed lines), metamorphic rocks (thick solid lines), and mantle forsterite (diamonds with uncertainties and thin solid line) (data of Clauser and Huenges, 1995; Schatz and Simmons, 1972). Plutonic rocks include feldspar-rich (syenite, anorthosite, hypersthenite) and feldspar-poor (granite, alkali granite, diorite, quartz diorite, monzonite, tonalite, gabbro, hornblende gabbro, peridotite, lherzolite, bronzitite, dunite, olivinite, granodiorite). Metamorphic rocks include quartzites and quartz-poor rocks (marble, serpentinite, eclogite, albitite, slate, amphibolite). The thermal conductivity in olivine (a and b) is highly anisotropic and is shown along three crystallographic axes (dotted lines with open symbols that refer to different measurements) (data of Osako *et al.*, 2004).

the effect depends critically on the shape of the pore space (Horai, 1971; Rocha and Acrivos, 1973) and on the composition of the saturating fluid (Artemieva and Chesnokov, 1991).

Effect of temperature

Thermal conductivity of most rocks decreases with temperature.

- In metamorphic and plutonic rocks, the temperature-induced conductivity decrease depends significantly on the content of the dominant mineral phase (quartz and feldspar, respectively); the temperature effect is stronger for feldspar-poor and quartz-rich rocks (Fig. 4.5). A number of approaches based on laboratory data have been proposed to extrapolate thermal conductivity to high temperatures. The following temperature-dependent function is used for rock types representative of the lithosphere (limestones, metamorphic, felsic, and mafic igneous rocks) (for details on individual rock types see overview by Zoth and Haenel, 1988):

$$\lambda[\mathrm{W/m/K}] = 0.86 + 662/(350 + T[^{\circ}\mathrm{C}]). \tag{4.8}$$

- Another relationship between thermal conductivity λ and temperature T often used for the upper crust is:

$$\lambda[\mathrm{W/m/K}] = \lambda_o/(1 + cT[^oC]), \tag{4.9}$$

  where λ_o is the thermal conductivity at $T = 0$ °C and at near-surface pressure conditions and c is a material constant (in the range 0–0.003 °C^{-1}) empirically determined from experimental studies on different rock samples (e.g. $c = 0.001$ for the upper, "granitic", crust) (Cermak and Rybach, 1982).
- At temperatures typical for the lower crust (200–600 °C), the thermal conductivity of basalts is almost constant (≈2.0 W/m/K) and does not depend on temperature.
- The temperature dependence of the thermal conductivity of peridotite is not well known and commonly a constant value of 4.0 W/m K is assumed for the upper mantle (Schatz and Simmons, 1972). Recently Xu *et al.* (2004) have proposed the following expression for olivine:

$$\lambda[\mathrm{W/m/K}] = \lambda_o(298/\mathrm{T[K]})^n \tag{4.10}$$

  where $\lambda_o = 4.08$ W/m/K and $n = 0.406$.

  For mantle olivine, another expression based on experimental studies of the temperature dependence of thermal conductivity along three crystallographic axes is (Osako *et al.*, 2004):

$$\lambda[\mathrm{W/m/K}] = \lambda_o + cT[\mathrm{K}] \tag{4.11}$$

  where $\lambda_o = 1.91$, 0.84, and 2.08 W/m/K along the [100], [010], and [001] axes, respectively, with the corresponding values of constant $c = 2088$, 1377, and 1731 W/m (Fig. 4.5).
- In contrast with lattice (or phonon) conductivity, the "radiative thermal conductivity" follows a T^3-law and becomes significant at $T > 1000$–1200 °C (Clauser, 1988). For this reason, thermal conductivity typically decreases with temperature until around 1000–1200 °C, when the radiative component balances this decrease. Analytical expressions for the temperature dependence of radiative and phonon thermal conductivity in the mantle based on a review of experimental and theoretical estimates are proposed by Hofmeister (1999).

Effect of pressure

Conductivity increases slightly with pressure and typically linear relations are applied for its pressure dependence (e.g. Horai and Susaki, 1989; Seipold, 1992). In granites and metamorphic rocks, thermal conductivity increases by *c*. 10% at pressures 0–500 MPa, with the stronger increase over the first 50 MPa due to porosity decrease. The pressure dependence of thermal conductivity in mantle olivine has been parameterized as (Osako *et al.*, 2004):

$$\lambda[\mathrm{W/m/K}] = \lambda_o \exp(b\ P[\mathrm{GPa}]), \tag{4.12}$$

where $\lambda_o = 6.61$, 3.98, and 5.91 W/m/K along the [100], [010], and [001] axes, respectively, with the corresponding values of constant $b = 0.038$, 0.042, and 0.034 [GPa]$^{-1}$ (Fig. 4.5).

The first-order effect of both temperature and pressure on thermal conductivity can be approximated as (Ketcham, 1996):

$$\lambda[\mathrm{W/m/K}] = 0.86 + 662/(350 + T[^oC]) + 0.041\ P\ [\mathrm{Kb}]. \tag{4.13}$$

Anisotropy

Most volcanic and plutonic rocks are, to first order, isotropic, while the thermal conductivity of many sedimentary and metamorphic rocks is strongly anisotropic. For example, in sheet silicates thermal conductivity in the directions parallel and perpendicular to the main cleavage plane may vary by a factor of 6–8.

In olivine, the anisotropy of thermal conductivity and thermal diffusivity is observed for all ranges of upper mantle temperatures and pressures (Fig. 4.5). The corresponding expressions for the temperature and pressure dependence of thermal conductivity along three crystallographic axes are given by Eq. 4.11–4.12 (Osako *et al*., 2004).

4.1.3 Thermal expansion, thermal diffusivity, and specific heat

Other thermal parameters that are widely used in thermal studies include the thermal expansion coefficient α, thermal diffusivity χ, and specific heat capacity at constant pressure C_p. The latter parameter is not very well constrained and is typically considered to be $C_p = 1000$–1200 J/kg/K in most rocks (Oxburgh, 1980). Later experimental studies indicate that specific heat is temperature dependent and can be parameterized as (Berman and Aranovich, 1996):

$$C_p(T)[\mathrm{J/kg/K}] = a_1 + a_2/T^{1/2} + a_3/T^3, \tag{4.14}$$

where temperature T is in K and coefficients $a_1 = 233.18$, $a_2 = -1801.6$, $a_3 = -29.794 \times 10^7$ for forsterite and $a_1 = 252$, $a_2 = -2013.7$, $a_3 = -6.219 \times 10^7$ for fayalite.

The thermal expansion coefficient α is typically assumed to be in the range $(3.0$–$3.2) \times 10^{-5}$ K^{-1}. However, an experimental study indicates that in the temperature range 325 °C to the melting point the thermal expansion of forsterite increases smoothly from 2.8 to 4.5 K^{-1} (Fig. 4.1) and can be approximated by a linear dependence on temperature as (Bouhifd *et al*., 1996):

$$\alpha(\mathrm{T}) = \alpha_o + cT[\mathrm{K}], \tag{4.15}$$

where $\alpha_o = 2.832 \times 10^{-5}$ K^{-1} and $c = 3.79 \times 10^{-8}$ K^{-2}.

Thermal diffusivity can be expressed through other parameters as

$$\chi = \lambda/\rho C_p, \tag{4.16}$$

where λ is the thermal conductivity and ρ is the density. In crustal rocks, thermal conductivity λ can range within broad limits leading to large variations in thermal diffusivity values. For example, in the lower crust with typical values of $\rho = 2900$ kg/m^3, $C_p = 1000$ J/kg/K and $\lambda = 2.0$ W/m/K, $\chi = (0.6$–$0.7) \times 10^{-6}$ m^2/s, which is 50–70% of its upper mantle value. For the upper mantle rocks, $\lambda = 4.0$ W/m/K (Schatz and Simmons, 1972), $\rho = 3350$ kg/m^3, and eq. (4.16) yields a thermal diffusivity value $\chi \sim (1.0$–$1.2) \times 10^{-6}$ m^2/s.

Experimental studies of thermal diffusivity in mantle olivine indicate that its strongly anisotropic temperature dependence can be approximated by a linear dependence, similar to eq. (4.11), with the coefficients of $\chi_o = -0.06$, -0.13, and -0.03 ($\times 10^{-6}$ m^2/s) along the

Table 4.1 Half-lives of ^{232}Th, ^{238}U, ^{40}K, and ^{235}U isotopes

Parent isotope	Present-day relative concentration*	Daughter isotope	Half-life, by mass
^{238}U	0.9927	^{206}Pb	4.47 Ga
^{235}U	0.0072	^{207}Pb	0.704 Ga
^{232}Th	4.0	^{208}Pb	14.01 Ga
^{40}K	1.6256	^{40}Ca (~89.5%)	1.25 Ga
^{40}K	1.6256	^{40}Ar (~10.5%)	11.93 Ga

(after Dickin, 1995; Van Schmus, 1995).
* Relative concentration normalized by the abundance of total U for K:U:Th ≈ 12700:1:4.

[100], [010] and [001] axes, respectively, with the corresponding values of constant $c = 938$, 626, and 832 ($\times 10^{-6}$ m^2/s/K). The pressure dependence of thermal diffusivity has the form of eq. (4.12) with coefficients $\lambda_o = 2.50$, 1.53, and 2.16 ($\times 10^{-6}$ m^2/s) along the [100], [010], and [001] axes, respectively, with the corresponding values of $b = 0.033$, 0.040, and 0.035 [GPa]$^{-1}$ (Osako *et al.*, 2004).

4.1.4 Heat production

Major heat-producing isotopes

Radioactive decay of long-lived isotopes (^{232}Th, ^{238}U, ^{40}K, and ^{235}U, listed in order of decreasing importance for the present-day thermal balance of the Earth) provides internal thermal energy and largely defines the temperatures in the planetary interior. Present-day relative concentrations and half-lives of ^{232}Th, ^{238}U, ^{40}K, and ^{235}U isotopes are listed in Table 4.1. Potassium is one of the so-called large-ion lithophile elements (LIL); it is an important component of several rock-forming minerals (e.g. orthoclase, biotite, leucite) and concentrates in evolved crustal rocks such as granites and shales. Uranium and thorium are also LIL elements, but in contrast to potassium they are found only as trace minerals in common rocks and their abundances can vary over several orders of magnitude. Because U, Th, and K are all LIL elements, they display a similar presence in the Earth when bulk concentrations are considered. The K/U ratio is (1.0–1.3) $\times 10^4$ for the bulk Earth, primitive mantle, and continental crust and the Th/U ratio is 3.7–4.0 (Van Schmus, 1995), and relative abundances of radioactive isotopes in the Earth are near:

$$\mathrm{K} : \mathrm{U} : \mathrm{Th} \approx 10,000 : 1 : 3.7. \tag{4.17}$$

Data, although not well constrained, on radiogenic heat production in the bulk Earth, primitive mantle, and the crust, together with data on abundances of Th, U, and K isotopes allow for modeling of the thermal history of the Earth (Fig. 4.6). For a thick (~ 250 km) continental lithosphere, the time-scale of thermal diffusion:

$$\tau \sim L^2/\chi \tag{4.18}$$

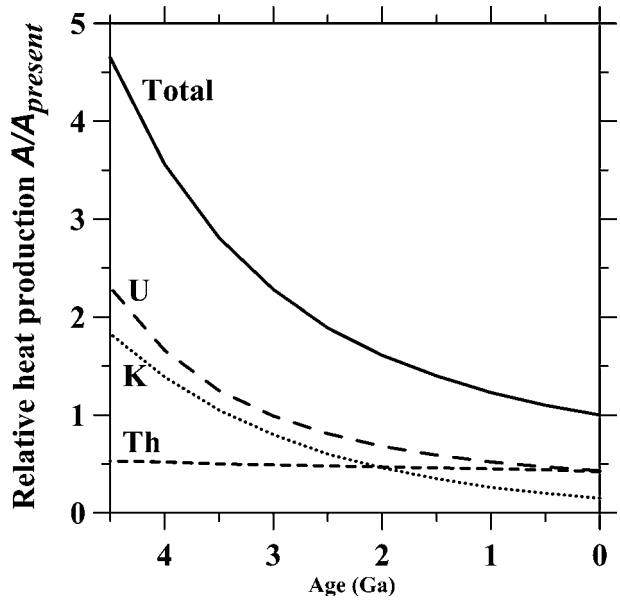

Fig. 4.6 Heat production in the Earth relative to the present total (source: van Schmus, 1995). Assumed present abundances are: K = 200 ppm, Th = 74 ppb, U = 20 ppb (eq. 4.17).

(where L is lithosphere thickness and χ is thermal diffusivity, typically 1 mm^2/s) is comparable to the half-lives of radioactive isotopes and thus the steady-state regime is not achieved (Michaut and Jaupart, 2004). In particular, long half-lives of radioactive isotopes imply that, even at constant thermal boundary conditions at the lithospheric base, it undergoes secular cooling due to radioactive heat loss. This heat loss is estimated to be ~50–150 °C/Ga. In a Proterozoic (~1.5 Ga old) region, secular cooling contributes ~3 mW/m^2 to the surface heat flow; although this value is smaller than the accuracy of heat flow measurements, it is comparable to the radiogenic contribution of the lithospheric mantle to the total surface heat flow.

The bulk amount and the depth distribution of radiogenic elements in the crust and in the mantle are still largely unknown. However, information on radioactive heat production in the crust is critical for thermal modeling, since the contribution of crustal heat production to surface heat flow can vary from <20% to >80% (Fig. 4.7). Several complementary approaches are used to address these questions, since no single technique for estimating the crustal radiogenic heat production $A(z)$ has proved to be consistently accurate. Up to the present, in most thermal studies the distribution of crustal heat production is an assumption rather than a constraint.

Laboratory measurements

Near-surface samples

Laboratory measurements of heat production in near-surface rocks form the basis for models of the heat production in sedimentary cover and the upper crust. In the laboratory, radiogenic

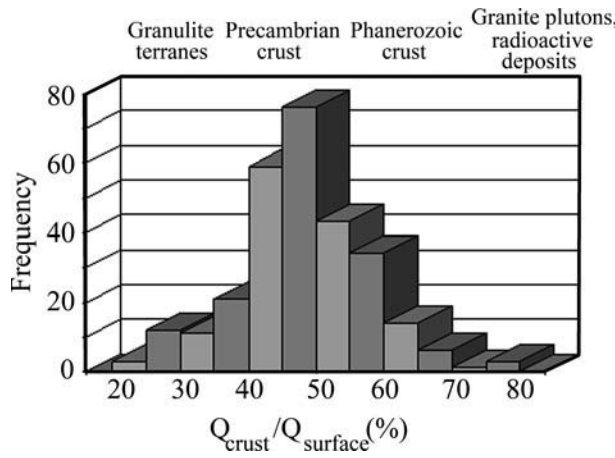

Fig. 4.7 Contribution of radiogenic heat flow generated in the continental crust to surface heat flow (after Artemieva and Mooney, 2001).

heat production is usually determined by measuring the radioactive isotope abundances in ~1 kg samples through their natural decay. The bulk heat production H (in W/kg) of a rock sample is the sum of the contributions from ^{232}Th, ^{238}U, ^{40}K, and ^{235}U isotopes, and the heat production per unit volume A is calculated from H and the rock density ρ as: $A = \rho H$. For mantle heat production the expression has the form (Ashwal *et al*., 1987):

$$A = \rho(0.097\mathrm{U} + 0.026\mathrm{Th} + 0.036\mathrm{K}), \tag{4.19}$$

where the concentrations of isotopes of U and Th are in ppm (parts per million), the concentration of K is in wt. %, density ρ is in g/cm^3, and A is in μW/m^3. The concentrations of Th and K in the Earth are well constrained and the average ratios Th/U and K/U between isotope concentrations are known (eq. 4.17). Since most crustal rocks contain less than 20% of potassium, the intrinsic radiogenic heat production of Earth materials is largely defined by the amount of uranium and thorium present (Jaupart and Mareschal, 2004).

Systematic regional sampling of near-crustal rocks either on a regular grid or by calculating a weighted average of values for various lithologies present in a geological province provides unbiased distributions of heat production over large areas. Such detailed studies have been performed in various continental locations (Western Australia, Canada, Baltic Shield, and China) and indicate the presence of a significant scatter of heat production at all scales: the values may be quite variable laterally and vertically within a single pluton and within a geological province as well as in rocks of the same bulk composition from different locations (Fig. 4.8). For example, heat production in gneisses from the Yilgarn craton (Western Australia, Fig. 3.82) varies from near-zero values to >6 μW/m^3 with an average value of 2.6 ± 1.9 μW/m^3, while in gneisses from the Gawler craton (Central Australia) the average value is 3.7 ± 3.6 μW/m^3; variations of heat production in all near-surface rocks of the Yilgarn craton and the Baltic Shield span from near-zero values to >12 μW/m^3. The Archean granulites from the Jequie-Bahia terrane (Brazil) is another example: in contrast to

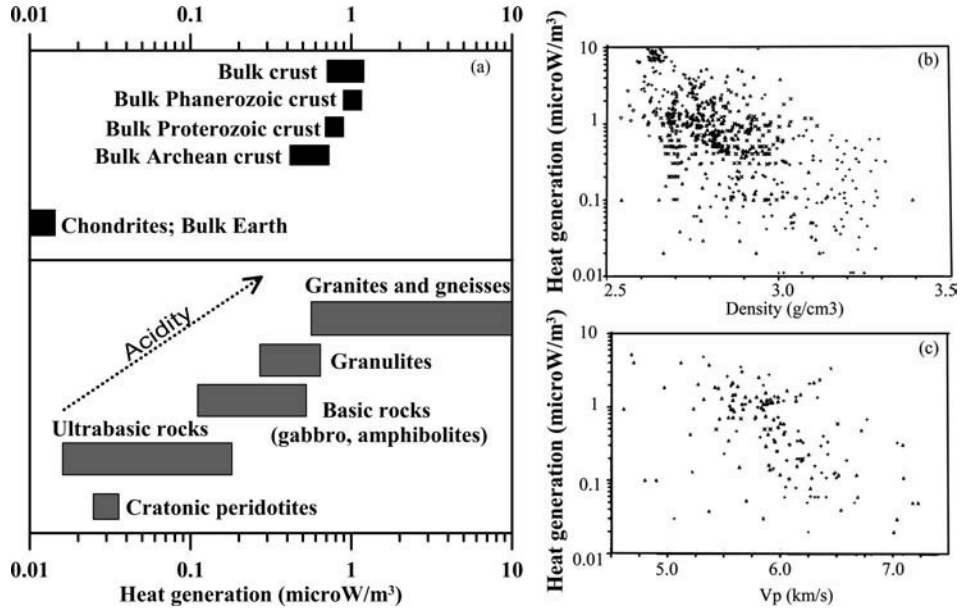

Fig. 4.8 Heat production in rocks. (a) General trends in heat production variations in common minerals, rocks, and in the crust. Sources: Nicolaysen *et al*., 1981; Weaver and Tarney, 1984; Taylor and McLennan, 1985; Fountain, 1986; Shaw *et al*., 1986; Ashwal *et al*., 1987; Fountain *et al*., 1987; Pinet and Jaupart, 1987; Rudnick and Presper, 1990; Ketcham, 1996; McLennan and Taylor, 1996; Gao *et al*., 1998; Rudnick *et al*., 1998; Rudnick and Nyblade, 1999; Beardsmore and Cull, 2001. (b–c) Heat production versus rock density and Vp velocity for the Baltic Shield (source: Kukkonen and Peltoniemi, 1998).

global observations ($A < 1$ μW/m^3), these granulites have high values of heat production, up to >10 μW/m^3 with an average value >2.5 μW/m^3 (Iyer *et al*., 1984).

To complicate matters, shallow rocks may not be representative of deeper rocks from the same massif: for example, near-surface water circulation leads to uranium depletion in granites and may thus lead to an erroneous estimate of uranium concentration in the upper crust (Jaupart and Mareschal, 2004). Another factor modifying the concentration of heat-producing elements in near-surface rocks is leaching of radioactive elements by weathering. As a result, the error in heat production estimates in near-surface samples is *c*. 20% (Jaupart *et al*., 1982), although analytical errors do not exceed 5% (with the largest errors for low-radioactivity samples).

Correlation between seismic velocity and heat production

Experimental measurements on near-surface rocks indicate that heat production may not be predicted reliably from seismic velocity (e.g., Fountain, 1986; Kern and Siegesmund, 1989) (Fig. 4.8), in contrast to earlier laboratory measurements on a small data set from a few European locations. Data from the KTB and the Kola Superdeep boreholes also do not confirm that seismic velocities and heat production are correlated. These results are of little

Table 4.2 Exposed cross-sections of the continental crust

Structure	Exposed crust (km)	Total crustal thickness (km)	Reference
Vredefort structure, South Africa	20	36	Nicolaysen *et al*., 1981
Lewisian fragment, Scotland	20	40	Weaver and Tarney, 1984
Wawa–Kapuskasing transect, Canada	25	43	Ashwal *et al*., 1987
Pikwitonei structure, Canada	30	40	Fountain *et al*., 1987
Southern Norway	?	28	Pinet and Jaupart, 1987

surprise: the isotopes of Th, U and K are incompatible elements, i.e. they are not readily incorporated into mineral lattices. Radioactive isotopes tend to concentrate in silicic igneous rocks and at grain boundaries, and thus

(i) their abundances do not closely follow major element abundances and
(ii) heat production is not directly related to bulk rock chemistry.

Although a very general trend in the increase of heat production from ultrabasic to basic and acid rocks can be recognized (Fig. 4.8), a large scatter in heat production values is documented for rocks of the same lithology.

Exposed cross-sections of the deep crust

While laboratory measurements on rocks from ophiolite complexes provide data on heat production in the deep parts of the oceanic crust, several continental locations provide a unique opportunity to measure directly heat production in middle crustal rocks and to determine directly an average vertical profile of heat production in the crust (Fountain and Salisbury, 1981; Nicolaysen *et al*., 1981; Weaver and Tarney, 1984; Ketcham, 1996; Ashwal *et al*., 1987; Fountain *et al*., 1987; Pinet and Jaupart, 1987). The upper 15–30 km of the crust, which is equivalent to 50% to 75% of the total crustal thickness, is available for direct studies in the exposed (overturned) sections of several Precambrian regions: the Vredefort structure (South Africa), the Wawa–Kapuskasing transect and the Pikwitonei structure (both in the Superior Province, Canada), the Lewisian terrane (Scotland), the Sveconorwegian–Svecofennian province (southern Norway), and metamorphic core complexes from Arizona (USA) (Table 4.2). This means that in all exposed sections, the lower parts of the crust (as much as 15–21 km as in the Vredefort, Wawa–Kapuskasing, and Pikwitonei sections) are unavailable for direct study. As a result, the heat production of the lower crust is poorly constrained. Additionally, it is not known how representative the exposed cross-sections of the crust in general are.

Laboratory measurements on rocks sampled from exposed crustal cross-sections indicate that in the middle crustal rocks heat production typically ranges from 0.2 to 0.4 $\mu W/m^3$. However, significantly higher heat production values, 0.4 to 0.5 $\mu W/m^3$, have been determined for Precambrian granulite terranes of the Canadian Shield along the 100 km long Wawa–Kapuskasing transect which has been interpreted as a cross-section through the upper 25 km of the crust (Fig. 4.9). These granulites were interpreted as mid-crustal rocks

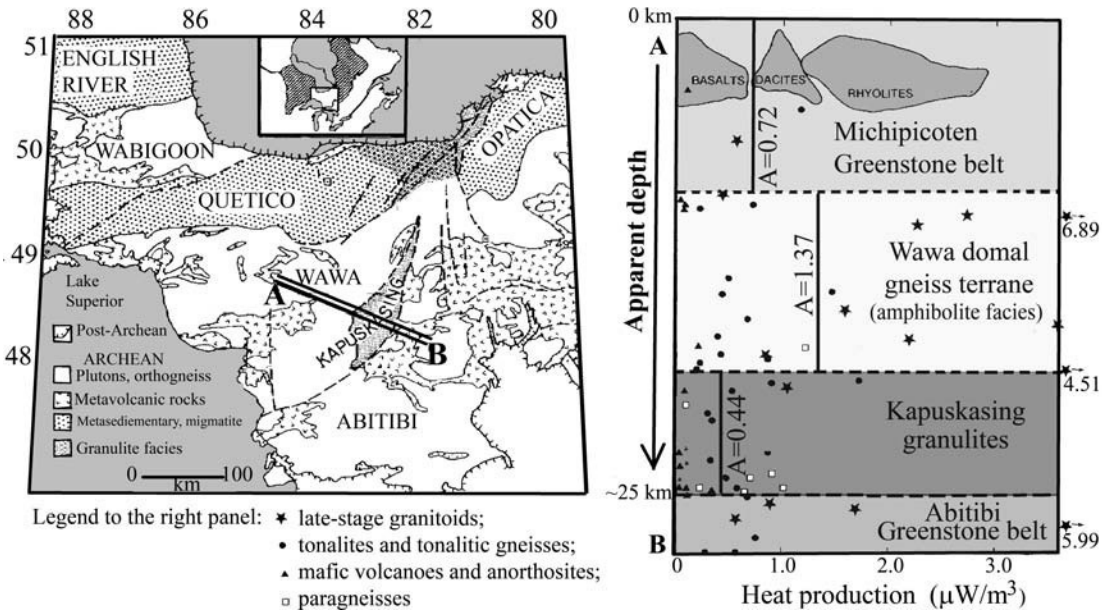

Fig. 4.9 Heat production in the Archean crustal cross-section (redrawn from Ashwal *et al*., 1987). Left panel: generalized geological map of the Superior Province, Canadian Shield, showing the location of the transect A–B. Right panel: heat production in individual rock samples (symbols) and average heat production (vertical lines) in different terranes along the transect A–B. The boundaries between the terranes are shown by dashed lines. The transect A–B is interpreted as an oblique cross-section of the upper ~25 km of the Archean crust, which was uplifted along a major thrust fault.

located at apparent depths of ~18–25 km. Some authors speculate that these high heat production values may continue into the lower crust, below 25–30 km depth (Ashwal *et al*., 1987; Rudnick and Presper, 1990).

In the Sveconorwegian–Svecofennian province of the Baltic Shield (southern Norway) two outcrops of granulite facies rocks are interpreted to be parts of the same lower crustal horizon; they are overlain by amphibolite facies terranes interpreted as representative of metamorphic conditions at middle crustal levels. The average heat production is 1.6 $\mu W/m^3$ in the Norwegian amphibolites and 0.4 $\mu W/m^3$ in granulites. Heat production in mafic granulites varies globally from 0.06 to 0.4 $\mu W/m^3$, which provides a range of possible variations in the lowermost crust (e.g., Pinet and Jaupart, 1987; Rudnick and Fountain, 1995), and values of 0.1 $\mu W/m^3$ or 0.4 $\mu W/m^3$ are commonly used in thermal modeling (Table 4.3). It is worth noting that for a typical 13-to-16-km-thick continental lower crust (Rudnick and Fountain, 1995), a 0.3μ W/m^3 difference in assumed values of lower crustal heat production results in a 4–5 mW/m^2 difference in estimates of mantle heat flow and in a 20–70 km difference in estimates of lithospheric thermal thickness (Artemieva and Mooney, 2001). Moreover, thermal models with high values of heat production (0.4–0.5 $\mu W/m^3$) throughout the entire lower crust would predict zero (or even negative) mantle heat flow in

Table 4.3 Typical thermal properties of the continental lithosphere

Layer	Heat production, $\mu W/m^3$	Thermal conductivity, W/m/K
Sediments	0.7–1.3	0.5–4.0
Upper crust	0.4–7.0	2.5–3.0
Middle crust	0.2–0.5	2.0–2.5
Lower crust*	0.1–0.4	2.0
Lithospheric mantle*	0–0.01	4.0

* Inferred values

continental regions with low surface heat flow (such as parts of the Siberian craton, the Baltic Shield, and the Canadian Shield), implying that lower values of heat production (as low as 0.1 $\mu W/m^3$) may be characteristic of the lower crust, at least in some tectonic settings.

Bulk heat production of the crust

Chemical constraints

In spite of the small volume of continental crust on the planetary scale (it constitutes only ~0.53% of the mass of silicate Earth (mantle left after core formation but prior to continental crust extraction)), it contains 20% to 70% of incompatible elements, which include heat-producing radioactive isotopes of Th, U, and K (Rudnick *et al*., 1998 and references therein). This fact defines the important role the continental crust plays in any chemical mass-balance models and in thermal modeling. Calculations of global crustal/mantle chemical budgets are based on redistribution of heat-producing elements in the Bulk Silicate Earth between the continental crust and mantle reservoirs. In spite of a large set of assumptions (e.g. on the composition of the Bulk Silicate Earth and mantle reservoirs, and on the structure of mantle convection), they provide a narrow range of estimates of bulk heat production in the continental crust, 0.74–0.86 $\mu W/m^3$ (O'Nions *et al*., 1979; Allègre *et al*., 1988). For a typical crustal thickness of ~40 km on the continents, these values yield ~30–35 mW/m^2 of crustal contribution to surface heat flow. This implies that in the Precambrian terranes where surface heat flow is, on average, 41–49 mW/m^2 (Nyblade and Pollack, 1993), mantle heat flow should be 6–19 mW/m^2. However, in the cratonic terranes with very low surface heat flow (<30 mW/m^2 as reported for some terranes of the Superior, Siberian, and West African cratons (Sass and Behrendt, 1980; Duchkov *et al*., 1987; Levy *et al*., 2010)) these estimates of bulk crustal heat production are, clearly, too high.

Petrologic studies provide independent constraints on average concentrations of radioactive isotopes in crust and mantle. These estimates are based on studies of mantle and crustal xenoliths, chemical composition of granulite facies terranes, and models of crustal growth complemented by heat flow constraints (e.g., Weaver and Tarney, 1984; Taylor and McLennan, 1985; Shaw *et al*., 1986; Rudnick and Fountain, 1995; McLennan and Taylor, 1996; Gao *et al*., 1998; Rudnick *et al*., 1998; Rudnick and Nyblade, 1999). However, because of the large variability in heat production at all scales, extrapolations from rock samples to the

Table 4.4 Average bulk heat production of the continental crust*

	Heat production ($\mu W/m^3$)	Reference
Bulk continental crust	0.58–0.70	Taylor and McLennan, 1985; McLennan and Taylor, 1996
	0.74–0.86	O'Nions *et al*., 1979; Allègre *et al*., 1988
	0.92–0.93	Weaver and Tarney, 1984; Rudnick and Fountain, 1995
	1.00	Gao *et al*., 1998
	1.12	Christensen and Mooney, 1995
	1.25	Wedepohl, 1995
	1.31	Shaw *et al*., 1986
Archean crust	0.35–0.55**	Artemieva and Mooney, 2001
	0.4–0.5	Rudnick *et al*., 1998
	0.48	Taylor and McLennan, 1985
	0.50	Rudnick and Fountain, 1995
	0.61	Weaver and Tarney, 1984
	0.64	McLennan and Taylor, 1996
	0.93 (North China)	Gao *et al*., 1998
Proterozoic crust	0.7–0.9**	Artemieva and Mooney, 2001

* Inferred values
** Typical values, the ranges estimated for different cratons are given in Table 4.5.

whole crust are subject to many uncertainties. As a result, published estimates of bulk heat production in the crust vary by a factor of two. Typically, estimates range from 0.48 to 0.61 $\mu W/m^3$ in the Archean crust (with some regional values as low as 0.35 $\mu W/m^3$ and as high as 0.93 $\mu W/m^3$) to 0.58–0.93 $\mu W/m^3$ in the Proterozoic crust, and to 0.96–1.38 $\mu W/m^3$ in the Phanerozoic crust (Table 4.4). Furthermore, a poorly known value for heat production in the lower crust (rarely exposed for direct studies below 25–30 km depth) results in significant uncertainty in petrologic models of bulk crustal heat production. Apparently systematic variations in bulk crustal heat production with age reflect the chemical heterogeneity of the continental crust: the composition of the Archean crust is dominated by Na-granitoids, while younger crust is dominated by K-rich granitoids (Martin, 1993).

Morgan (1985) has argued that the global trend of a decrease in surface heat flow with age from Phanerozoic to Archean can be explained by a decrease in crustal radioactivity. Although both petrologic data and thermal constraints indicate that, in general, bulk crustal heat production is lowest in the Archean crust and largest in the Phanerozoic crust (Sclater *et al*., 1980; Vitorello and Pollack, 1980; Morgan, 1985; Taylor and McLennan, 1985; Rudnick *et al*., 1998; Artemieva and Mooney, 2001; Jaupart and Mareschal, 2004), this trend only holds globally. Because of large regional variability, a particular geological province should not necessarily fit global values for its age group. Furthermore, a contrast in crustal heat production between Precambrian terranes of different ages is not necessarily required by heat flow data from South Africa (Ballard *et al*., 1987; Artemieva and Mooney, 2001) (Table 4.5).

Table 4.5 Average bulk heat production (in $\mu W/m^3$) in the Precambrian crust*

Archean and Paleoproterozoic crust	A	Meso-Neoproterozoic crust	A
South Africa	0.49–0.78	South Africa	0.61–0.77
Yilgarn	0.39–0.52	Northern Australia	0.78–1.40
Pilbara	0.56	Southern Australia	1.03–1.55
Sino-Korean Craton	0.57–1.00	Yangtze Craton	0.58–1.24
Dharwar Craton	0.36–0.50	Gondwana basins (Indian Shield)	0.86–1.18
Baltic Shield (Kola-Karelia) and Ukrainian Shield	0.36–0.49	Atlantic Shield (South America)	0.62–0.83
Superior Province	0.29–0.47	Grenville	0.39–0.95
Siberian craton (Anabar Shield and Yenisey Ridge)	0.17–0.38		
Siberian Platform	0.37–0.49		
Aldan Shield	0.61		

* Inferred values
(Source: Artemieva and Mooney, 2001)

Estimates from surface heat flow

Surface heat flow observations provide additional constraints on bulk crustal heat production (e.g. Artemieva and Mooney, 2001; Table 4.5). The simplest requirement is that mantle heat flow should not exceed the lowest measured surface heat flow in a region. Another constraint comes from the fact that surface heat flow measurements are effectively 1D (in the vertical direction) and ignore the horizontal component of heat conduction. The wavelength of surface heat flow variations provides important information on the depth distribution of heat-producing elements: the contribution of deep layers of high heat production to surface heat flow is wiped out by lateral heat conduction caused by lateral heat production variations in the crust, so that only the near-surface heat-producing bodies affect surface heat flow variations (Jaupart, 1983). This observation effectively allows for separation of surface heat flow anomalies produced by lateral and vertical variations in crustal heat production from anomalies of subcrustal (mantle) origin: the latter will produce detectable surface heat flow perturbations with wavelength of several hundred kilometers (Fig. 4.10). The effect of lateral variations in heat production on surface heat flow is discussed in more detail later.

A combination of (i) heat flow observations with (ii) lower crustal and mantle xenolith data, (iii) models of crustal structure and evolution, and (iv) laboratory data on heat production in rocks has been used to estimate the composition of the continental crust and its bulk heat production (Taylor and McLennan, 1985; McLennan and Taylor, 1996; Rudnick *et al*., 1998; Rudnick and Nyblade, 1999). These and other similar studies indicate that in Precambrian terranes crustal contribution to surface heat flow is between 20 and 44 mW/m^2 and typically makes >50% of observed surface heat flow. However, at present any tight constraints on the relative contributions of the crust and mantle to surface heat flow are not possible. For example, a comparison of conductive geotherms based on model concentrations of K, Th, and U isotopes in the Archean continental crust with xenolith geotherms

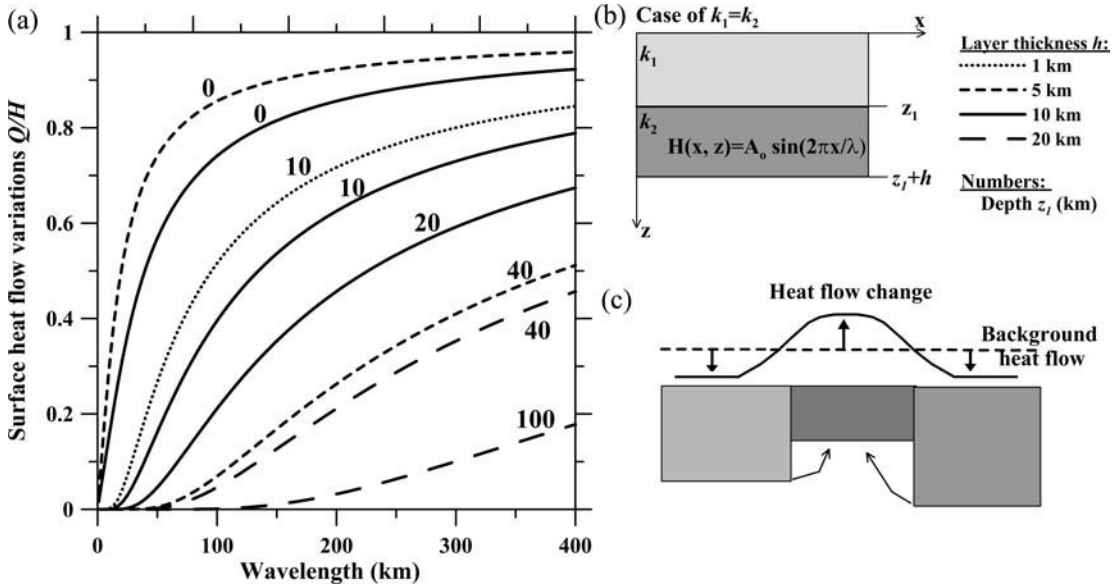

Fig. 4.10 (a) Amplitude of surface heat flow variations Q (expressed as a fraction of the Q value in the absence of horizontal heat conduction) produced by a horizontal layer with laterally sinusoidal (with wavelength λ) and vertically uniform distribution of heat production over thickness h (schematically shown in insert b). The layer is located at depth z_1 (the values of z_1 are indicated by numbers on the curves) and generates additional heat flow H. Surface heat flow is poorly sensitive to radioactivity contrasts located at large depth, and short wavelength radioactivity variations are not reflected in the surface heat flow. A heat flow anomaly (of any origin) in the mantle will produce a surface heat flow anomaly of wavelength of several hundred kilometers. (c) Horizontal heat transfer smoothes lateral variations in radioactivity: heat flow in the thin block is enhanced by contributions from the deep parts of the neighboring blocks where, in turn, heat flow becomes reduced. (After Jaupart, 1983.)

(see Chapter 5) indicates that either the crust should have very low heat production or that xenolith geotherms reflect frozen-in mineral equilibria and correspond to a transient thermal regime associated with magmatism (Rudnick *et al*., 1998). In the latter case, crustal heat production can be relatively high.

Heat production in the mantle

Little is known about heat production in the lithospheric mantle. The only direct information is based either on studies of mantle xenoliths or massif peridotites (fragments of lithospheric mantle in Phanerozoic fold belts). There is a large variation in heat-producing elements in peridotites from different settings (Table 4.6). Mean values of heat production calculated for massif peridotites from Phanerozoic fold belts and for lithospheric peridotites carried in alkali basalts in Proterozoic continental regions are 0.018 $\mu W/m^3$ and 0.033 $\mu W/m^3$, respectively. In cratonic settings, mean values of heat production range from 0.028 $\mu W/m^3$ in non-

Table 4.6 Heat production in mantle peridotites (in $\mu W/m^3$)

Settings	Mean	Median
Off-craton, massif peridotites	0.018	0.006
Off-craton, spinel peridotites	0.033	0.013
On-craton, all	0.093	0.044
On-craton, kimberlite-hosted	0.104	0.050
On-craton, non-kimberlite-hosted	0.028	0.019

(Source: Rudnick *et al*., 1998)

kimberlite hosted peridotites to 0.104 $\mu W/m^3$ in peridotites contaminated by kimberlite magmas, i.e. *mantle metasomatism increases the content of heat-producing elements* (Rudnick *et al*., 1998). In contrast, peridotites from the Phanerozoic Oman ophiolite have extremely low heat production (0.002 $\mu W/m^3$) that is comparable to heat production in the N-MORB mantle source (Jochum *et al*., 1983).

High heat production values in the lithospheric mantle may be difficult to reconcile with xenolith geotherms from the Archean cratons and surface heat flow, since for Kaapvaal data the best agreement is achieved for mantle heat production values between 0 to 0.03 $\mu W/m^3$ (Rudnick and Nyblade, 1999). This would imply that the concentration of heat-producing elements in cratonic peridotites may be non-representative of the Archean lithospheric mantle (Rudnick *et al*., 1998). A possible explanation for radioactive enrichment of continental lithosphere is that radioactive elements can accumulate there during metasomatic processes (Petitjean *et al*., 2006). However, for the Kaapvaal craton geotherms calculated for mantle peridotite values as high as 0.07–0.08 $\mu W/m^3$ still fall within the 95% confidence limits for the P–T xenolith data (Rudnick and Nyblade, 1999).

Geochemical studies indicate that the amount of apatite, which is widespread in Phanerozoic lithospheric mantle, may be greatly underestimated (O'Reilly and Griffin, 2000). However, apatite has high concentrations of U and Th (60 ppm and 200 ppm, respectively), and its abundance may have a dramatic effect on the heat budget of the mantle and lithospheric temperatures. Estimates show that in the case where the apatite content in the lithospheric mantle is ~0.5%, heat production of the lithospheric mantle due to apatite alone would be ~0.2 $\mu W/m^3$, and apatite abundance in a 70 km-thick Phanerozoic lithospheric mantle would contribute *c*. 12 mW/m^2 to mantle heat flow.

A commonly assumed value of 0.01 $\mu W/m^3$ for heat production of the lithospheric mantle (Table 4.3) can be justified by a simple analysis of the heat balance of the Earth (Petitjean *et al*., 2006). If heat production in the primitive mantle is 5 pW/kg (Jochum *et al*., 1983; McDonough and Sun, 1995) and bulk heat production in the crust is known (e.g. the values reported by Rudnick and Fountain, 1995), then the radiogenic heat generated in the present-day mantle is 3.15 pW/kg and, assuming a mantle density of 3300 kg/m^3, its heat production is 0.01 $\mu W/m^3$ (see p. 232).

Vertical and lateral variations in heat-producing elements

Correlation between heat flow and heat production

Early analyses of heat flow and heat production measurements in plutonic rocks demonstrated that these two parameters are related linearly (Birch *et al*., 1968; Roy *et al*., 1968) (Fig. 4.11a). This empirical observation led to the concept of a "heat flow province", i.e. a region in which surface heat flow Q is related to surface radioactivity A_o as:

$$Q = Q_r + D\,A_o \tag{4.20}$$

where Q_r is termed the "reduced heat flow" and the slope parameter D with units of length is termed the "characteristic depth". The physical meaning of the constants Q_r and D permits several interpretations. Constant Q_r is commonly interpreted as the heat flow below the uppermost crustal layer of thickness D (typically $D \sim 10$ km), where most of the heat-producing elements are concentrated (i.e. granitic upper crust).

Two observations are important in relation to equation (4.20):

(1) The heat flow province concept is a thermal, but not a petrological concept, and thus a single tectonic structure may comprise several "heat flow provinces".
(2) In general, the correlation between heat flow and near-surface heat production weakens when data from both plutonic and metamorphic sites are included, and the smallest scatter of data around the best-fit line is observed when all data are from plutonic sites.

Statistical correlation between heat flow and near-surface heat production has been observed in most of the continental regions (see Artemieva and Mooney, 2001 for an overview). It has been argued, however, that in some regions relationship (4.20) does not hold, in particular when data from sites of diverse tectonic origin are forced into a single "heat flow province". The Paleoproterozoic Trans-Hudson Orogen (the central Canadian Shield) is an example. The orogen is formed by several distinct belts with different origins and lithologies: the Flin Flon Belt is made up of arc volcanic and plutonic rocks; the Lynn Lake Belt is formed by island arc volcanic rocks; the Thompson Nickel Belt contains metasedimentary rocks; other domains are made up of Archean gneisses. While a correlation between surface heat flow and surface radioactivity hardly exists for the entire orogen, the two parameters are correlated statistically within the individual orogen-forming belts, each of which apparently makes an individual "heat flow province" (Fig. 4.11b).

Since equation (4.20) is effectively 1D and it ignores lateral heat transfer, the scatter around the linear fit is, in part, caused by 2D and 3D heat flow effects which smooth lateral variations in heat production. The effect of horizontal variations in heat production in the crust on surface heat flow and thus on the $Q - A_o$ relationship (4.20) has been examined for harmonic (Jaupart, 1983) and random (Vasseur and Singh, 1986) lateral distributions of heat sources in the crust with a constant or exponential vertical distribution. The analytical expressions for a cylindrical pluton and for a 2-layer structure with variable thermal conductivities in the layers and for different cases of uniform and exponential depth distribution of heat production (with laterally uniform or sinusoidal distribution within the layers) can be found in Jaupart (1983). The results of these studies indicate the following:

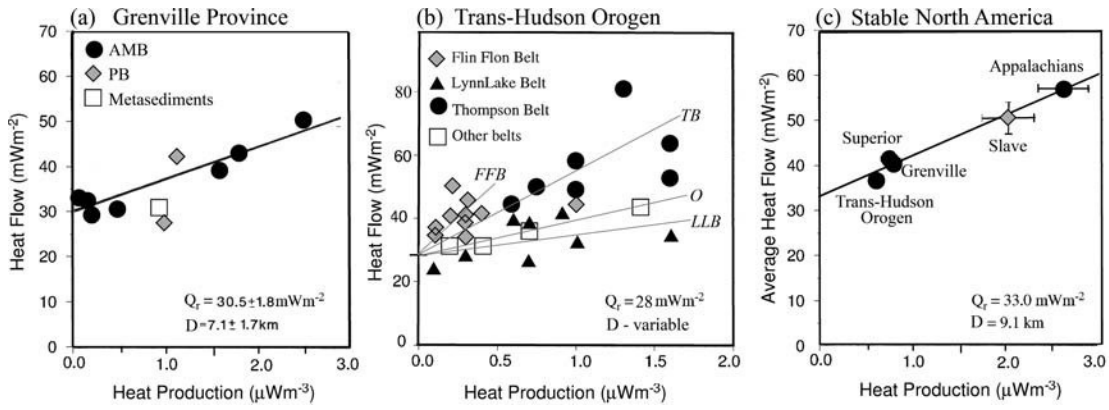

Fig. 4.11 Plots of heat flow as a function of radiogenic heat production in different tectonic provinces of stable North America (after Pinet *et al*., 1991; Mareschal *et al*., 1999; Perry *et al*., 2006). (a) Data from the crystalline terranes of the Allochtonous Monocyclic Belt (AMB) and the Parauchtonous Belt (PB) of the Grenville province (the eastern Canadian Shield). Most of the measurements were made on low and intermediate grade metamorphic rocks (charnockites, granites, gneisses) and anorthosites. The parameters Q_r and D are for the best-fit linear relation through these data (Eq. 4.20). (b) Data from the Paleoproterozoic Trans-Hudson Orogen (the central Canadian Shield). The orogen is formed by several distinct belts with different origins and different lithologies. The correlation between heat flow and heat production is marginal for the entire orogen due to fundamental geological and geochemical contrasts between the component belts. However, data for the individual belts will fit linear relations with the same values of Q_r for all belts but with different D. (c) Average values for the Superior provinces and the Slave craton (for the latter the amount of data remains limited) of the Canadian Shield, and data for the Trans-Hudson Orogen (excluding the Thompson Belt), the Grenville Province, and the Appalachians.

- Lateral heat flow smoothes variations in heat production so that only shallow anomalies are well reflected in surface heat flow (Fig. 4.10).
- The slope D (depth-scale), due to the averaging effects of lateral heat transfer, is an average of various thicknesses of radioactive layer in the region of study (Fig. 4.11b).
- The wavelength of lateral variations in radioactivity is important: heat flow smoothing by lateral heat transfer in the crust is efficient over lateral distances of ~350 km (Jaupart, 1983). For example, for $D = 10$ km (a typical estimate of the D-layer thickness in many continental regions) all heat production anomalies of wavelength less than ~100 km will be reduced to less than 80% of their amplitude in surface heat flow (Fig. 4.10).
- In almost all cases, lateral heat flow results in an apparently lower D-value as obtained from the heat flow–heat production plot than the actual thickness of the radioactive layer. The amplitude of this reduction depends on the radial distance over which the (randomly distributed) heat production is correlated. If the thickness of the radioactive D-layer is much smaller than the scale of horizontal fluctuations in radioactivity, vertical heat flow prevails and the effect of lateral heat production heterogeneity on Q and on linear correlation (4.20) is insignificant. However, if the scale of horizontal fluctuations in radioactivity is small compared to D, the contribution of lateral heat flow to surface heat flow variations becomes important (Vasseur and Singh, 1986).

- The fact that the apparent depth-scale D is more sensitive to horizontal variations in radioactivity than to the actual thickness of the D-layer questions the meaning of a single linear heat flow–heat production correlation. To resolve this contradiction, Jaupart (1983) proposed that relationship (4.20) should have the form:

$$Q = Q_r + D_U A_U + D_{Th} A_{Th} + D_K A_K, \tag{4.21}$$

  where A_U, A_{Th}, A_K are heat production and D_U, D_{Th}, D_K are the corresponding depth-scales for uranium, thorium, and potassium, respectively, and in the simplest interpretation, it is D_{Th} that characterizes the depth scale of radioactive enrichment.
- Since horizontal heat flow caused by lateral variations in radioactivity effectively averages radiogenic heat production in the crust (over lateral distances of ~350 km), Q_r corresponds to a large-scale average of surface heat flow from which radioactivity contrasts in the shallow crust are subtracted and thus, it allows for calculation of lithospheric geotherms (Jaupart, 1983).

Depth variations of heat production

Theoretical constraints

A compilation of published D-values together with a global analysis of heat flow and heat production data for the regions, where linear relationship (4.20) is statistically valid, demonstrate significant regional variations of D with values ranging from 4 to 16 km. These variations do not seem to correlate with any physical or geological phenomena, which prevents straightforward interpretation of D in physical, petrologic, and tectonic terms. In particular, there is no global correlation between the D parameter and the age of crustal provinces, although within the same continent the D value commonly increases from the Archean to the Proterozoic terranes (Artemieva and Mooney, 2001).

Equation (4.20) implies that (in the case of 1D heat conduction) the vertical distribution of heat-producing elements within a heat flow province can be described by a single function. Several functions have been proposed for this purpose, the most common are linear (or step-like) and exponential (Fig. 4.12ab). The exponential function, which assumes that crustal radioactivity decreases exponentially with depth as $A(z) = A_o \exp(-z/D)$ has received special attention (Lachenbruch, 1970) since it is the only function that takes into account differential erosion at the surface. In the case of an exponential function, Q_r approximately corresponds to the base of the crust. The assumption of an exponential decrease of A with depth has however been challenged by numerous studies. Another way to meet the erosion argument is to question the assumption that the D-value remains constant through geological history (Jaupart, 1983).

A broad correlation between heat production and rock acidity (Fig. 4.8) together with lithological stratification of the crust (where acidity decreases with depth while mafic assemblages increase with depth) suggests that there should be a general trend of heat production decrease with depth. This conclusion is, in general, supported by regional studies on exposed cross-sections of the continental crust (e.g. Swanberg *et al.*, 1974; Nicolaysen *et al.*, 1981; Weaver and Tarney, 1984; Ashwal *et al.*, 1987; Pinet and Jaupart, 1987; Ketcham, 1996); but, only a few reported vertical cross-sections show a simple pattern of

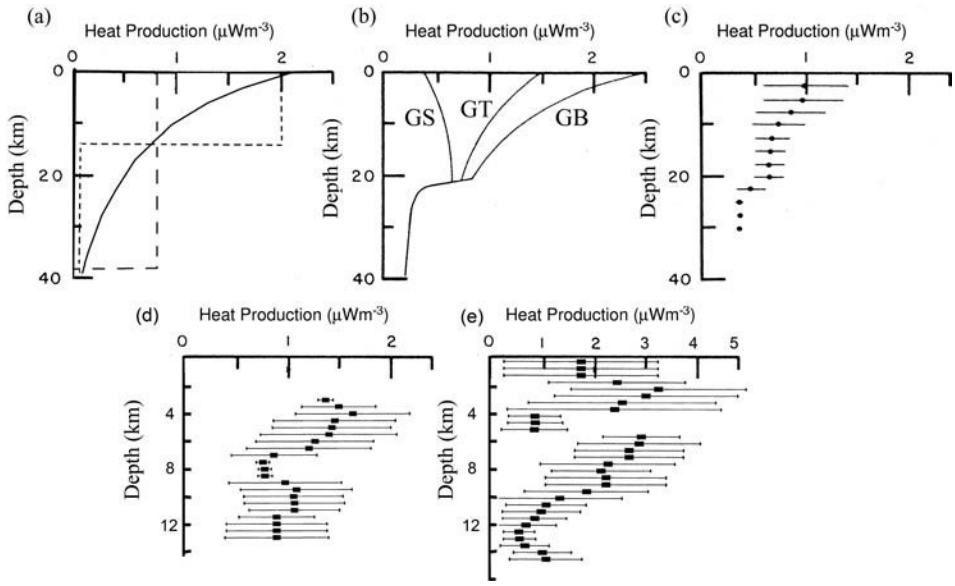

Fig. 4.12 Depth distribution of heat production in continental crust (a–c from Fountain *et al*., 1987; d–e from Ketcham, 1996). (a) Theoretical models of exponential, linear, and constant heat production distribution. The bulk (integral) heat production of the crust is approximately the same for all three models shown. (b) Theoretical models of Allis (1979) for greenstone terrane (GS), gneiss terrane (GT), and granitoid batholith (GB). (c) Weighted average of heat production in the crust along the cross-section of exposed crust in the Pikwitonei structure (the Superior Province, Canada). (d–e) Depth distribution and standard deviations in two Arizona metamorphic core complexes obtained by a moving average. Note different depth scales in (d–e) and different horizontal scale in (e).

heat production that resembles a linear or an exponential function (Fig. 4.12c–e). In most cases, no systematic trend is observed for the vertical distribution of heat production.

Data from the Kola Superdeep Borehole

The most striking evidence for non-systematic variation of heat production with depth is provided by data from deep drillholes, such as the SG-3 in the Kola peninsula (Russia) and the KTB in Germany. Unfortunately, the number of publications in international journals describing the unique data from the Kola borehole is limited. Several monographs published in Russian summarize major scientific results (e.g. Kola Superdeep, 1984; 1998).

Scientific drilling in the Kola peninsula started in 1970 and a depth of 7263 m was reached in April 1975. This marked the end of the first stage of drilling, after which no further drilling took place until October 1976, when the second drilling stage, based on different technology and equipment, started. At the second stage, several drillholes were drilled below a 7 km depth mark and in 1984 a depth of 12 000 m was reached (Fig. 4.13). The temporary termination of drilling for 1.5 year in 1975–1976 is important from a scientific point of view: thermal equilibrium in the borehole was re-established during this time and, as a result, high quality thermal measurements were made in 1976 down to ~7 km depth. Thermal parameters measured during the next decade down to ~9 km depth and deeper are less reliable since they were measured under transient thermal conditions.

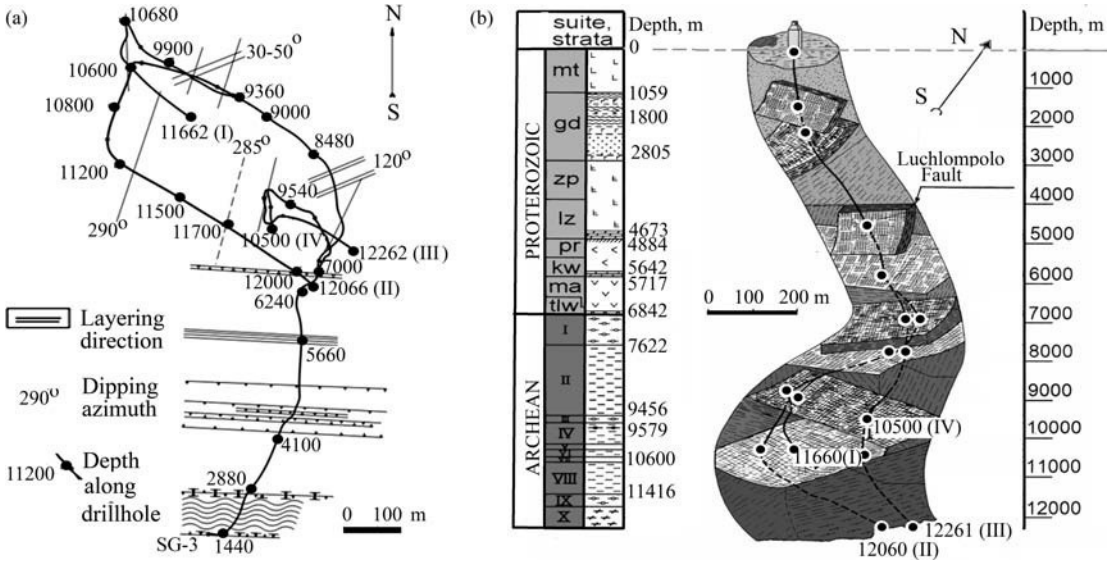

Fig. 4.13 Kola Superdeep Borehole SG-3 (after Gorbatsevich and Smirnov, 1998). Structural and anisotropic properties of the upper-middle crust estimated from the deviation of the drillholes from the vertical (left and right panels) shown together with (a) horizontal projections of four drillholes (marked I to IV) of SG-3, (b) lithological and structural cross-section along the borehole. A simplified list of rock lithology along the boreholes includes: metapelitic tuff of ultrabasic composition and metadiabases at 0–1 km depth; metaphyllites, metatuffs, metadiabases, metasandstones at 1–2.8 km depth; schistozed metadiabases, amphibolitized metagabbro-diabases at 2.8–4.7 km depth; dolomites, sandstone, and dolomitized sandstone at 4.7–4.9 km depth; schists at 4.9–5.6 km depth; quartzitic sandstones, carbonate-micas, and quartz-micas schists at 5.6–5.7 km depth; amphibolites and schists at 5.7–6.8 km depth; pegmatites, gneisses, biotite-amphibole-plagioclase paraschists at 6.8–7.6 km depth; gneiss-schist, amphibolites, migmatites down to a 10 km depth (data source: Atlas of physical rock properties from the cross-section of Kola Superdeep Borehole; Moscow, 1982, Ministry of Geology, USSR. Unpublished Report).

The upper 6842 m of the superdeep borehole SG-3 cut Paleoproterozoic plutonic rocks of the Karelian basement; the Archean granites and metamorphic rocks extend from 6842 m to 12 262 m (Fig. 4.14). The age of the Archean basement is 2.93–2.76 Ga (the U–Pb method), with the oldest rocks being ~3.15–2.89 Ga old (the Sm–Nd method). The major Luchlompolo fault crosses the borehole at a depth of ~4.8 km.

Heat production in the Proterozoic formations varies from ~0.4 $\mu W/m^3$ in plutonic rocks to ~1.3 $\mu W/m^3$ (with maximum values of ~2.5 $\mu W/m^3$) in metasediments (Fig. 4.14). The peak in heat production at *c*. 4.8 km depth correlates with the major fracture zone, and high heat production is explained by fluid migration and redistribution of radioactive elements. Heat production in the Archean gneisses is between 0.8 and 1.2–1.7 $\mu W/m^3$. On the whole, no decrease in heat production is observed down to ~12 km depth. Laboratory measurements on core samples from the Kola drillhole indicate that heat production is controlled primarily by U and Th content; the content of Th increases through the entire sampled depth, both in the Proterozoic and in the Archean rocks (Kola Superdeep, 1984; 1998).

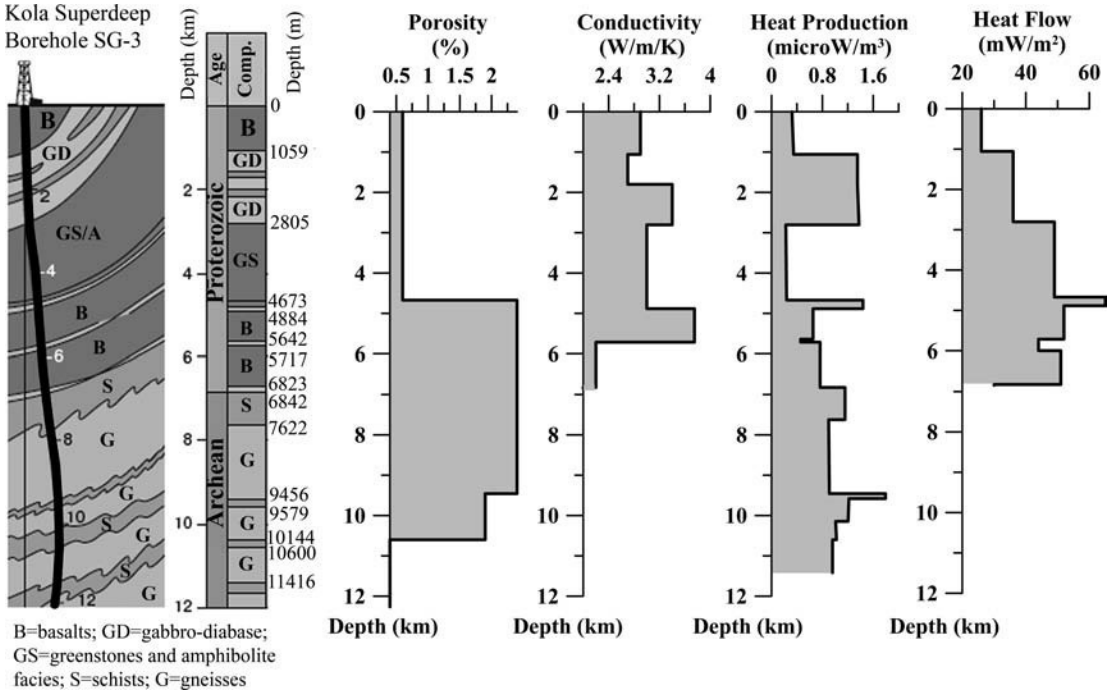

Fig. 4.14 Schematic cross-section of the Kola Superdeep Borehole SG-3 (Kola Peninsula, Baltic Shield, Russia) and depth distribution of several parameters (porosity, thermal conductivity, and heat production averaged for each lithological unit, and heat flow). Note that most variations in all parameters correlate with changes in rock lithology. Peaks in heat production and heat flow at *c.* 4.8 km and 9.5 km depths correlate with major fracture zones. Measurements of thermal parameters are highly reliable down to ~7 km depth (the borehole was sealed for 1.5 years prior to measurements to re-establish thermal equilibrium); thermal measurements down to ~9 km depth were made at transient thermal conditions (not shown). Thermal gradient is *c.* 16 °C/km at 2.8–4.3 km, 16.5–20 °C/km at 4.3–5.0 km, 22 °C/km at 5.0–6.6 km, 25 °C/km down to 6.8 km, 15 °C/km at 6.8–7.0 km, and 23 °C/km at 7.0–7.2 km depth. Near-surface heat flow (in the upper 1.0 km) is 26 ± 2 mW/m^2 and increases to 36 ± 4 mW/m^2 at 1.0–2.8 km depth. Heat flow at depths of 2.8–4.3 km (49 ± 1 mW/m^2), where rock composition is relatively homogeneous and porosity is low, is considered to be representative of a deep thermal regime. A localized narrow zone of anomalously high heat flow (65 ± 7 mW/m^2) at depth 4.3–4.9 km is probably caused by fluid circulation in the Luchlompolo fault zone. Data sources: http://superdeep.pechenga.ru/; Kola Superdeep, 1984; 1998.

One of the big surprises from the Kola borehole is data on surface heat flow. As mentioned earlier, high quality measurements of thermal gradient are available down to ~7 km depth. The average value of the thermal gradient increases with depth from 10 °C/km at near-surface to ~18 °C/km in the lower levels of the borehole (~7 km). Changes in thermal gradient approximately correlate with boundaries between different formations (suites) (Fig. 4.14). The temperature at 12 km depth is 212 °C, in contrast to the expected 120 °C. High crustal temperatures are likely to be caused by high radioactivity in the Archean

basement. Based on borehole data, the temperature at 42 km depth (Moho?) is expected to be as high as 580 °C.

Thermal conductivity along the entire depth of the borehole varies from 2.5 to 3.6 W/m/K with typical values ~2.8–2.9 W/m/K. Data on thermal conductivity and thermal gradient allow for calculation of heat flow, which surprisingly is highly variable along the borehole depth and, in contrast to expectations, increases in the upper 5 km of the cross-section. Heat flow in the upper 1.0 km is 26 ± 2 mW/m^2 and reaches 49 ± 1 mW/m^2 at depths of 2.8–4.3 km. It is heat flow at this depth interval, where the rock composition is relatively homogeneous and porosity is low, that is considered by some authors to be representative of a deep thermal regime of the region. Low values of near-surface heat flow are attributed to the effects of water circulation, recent glaciation, and denudation. A localized narrow zone of anomalously high heat flow (65 ± 7 mW/m^2) at depth 4.3–4.9 km is probably caused by fluid circulation in the Luchlompolo fault zone. There is a sharp decrease in heat flow below the fault, to 48–56 mW/m^2 with a further decrease below 6.8 km depth (since measurements below this depth were made at transient thermal conditions, they should be treated with caution).

To conclude, the patterns of depth distribution of porosity, thermal gradient, heat production, heat flow (and many other parameters) measured in the upper 12 km of the crust of the Baltic Shield are in strong contrast with expectations based on theoretical models. Geothermal studies from several other deep drillholes worldwide show similar complicated patterns of depth distribution of thermal parameters and heat flow. It is still debated which heat flow values should be considered as "surface heat flow" in each of the cases.

Reduced heat flow

In relation (4.20), Q_r is the difference between the surface heat flow and the product DA_o, which is the heat generated within the upper crustal layer enriched in heat-producing elements. Thus the value of Q_r gives a rough approximation of the non-radiogenic component of heat flow. Sometimes Q_r is equated with heat flow at the Moho (mantle heat flow). However, this is only correct for some specific assumptions on depth variations of heat production (Fig. 4.12a). In most cases, the term Q_r does not incorporate heat generated by radioactive isotopes in the middle and lower crusts. The latter can amount to 10–15 mW/m^2.

In spite of these limitations, Sclater *et al*. (1980) suggested that

Q_r must have a general geophysical significance for old continental crust.

A global analysis of the heat flow–heat production relationship does indeed show a clear trend with an increase in Q_r value with age from Archean through Proterozoic to Paleozoic regions (Fig. 4.15). The mean values range from ~20 mW/m^2 in the Archean regions of West Africa and Eurasia to ~30 mW/m^2 in the Archean regions of South Africa, Canada, South America, and Australia, and to ~30–35 mW/m^2 in the Proterozoic regions with a scatter in Q_r values of ~20 mW/m^2 between different cratons of a similar age (Artemieva and Mooney, 2001). A decrease Q_r with age is likely to imply a decrease in mantle heat flow beneath the ancient continental regions. However, one should not forget that

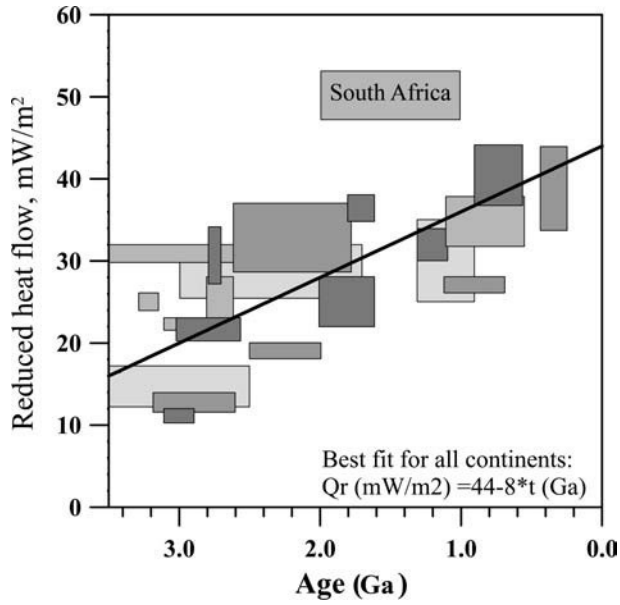

Fig. 4.15 Reduced heat flow versus age (after Artemieva and Mooney, 2001). Boxes correspond to individual continental terranes; the horizontal size shows age ranges, the vertical size reflects variations in estimated values of the reduced heat flow obtained by different authors. South Africa remains apart from the general trend.

estimates of Q_r are biased by both the limitations associated with Eq. 4.20 (in particular, a quasi-1D assumption) and the accuracy of heat flow and heat production measurements.

Values of Q_r for the Archean cratons are close to the estimates of mantle heat flow in the best-studied Archean cratons of Canada and South Africa (see Table 4.11). Based on the analysis of surface heat flow and crustal structure, heat flow through the Moho is estimated to be ~10–15 mW/m^2 in the Canadian shield and ~17 mW/m^2 in the Kaapvaal craton (Jaupart and Mareschal, 1999). Xenolith geotherms for the Kalahari craton (South Africa) are fit best by thermal models which imply ~18–19 mW/m^2 for heat flow across the Moho (Rudnick and Nyblade, 1999). A comparison of Q_r with mantle heat flow in these cratons indicates that only about 10–15 mW/m^2 should be generated in the crustal radiogenic layer (see Section 4.4.2 for details). If this layer is 10 km thick, its mean heat production should amount to 1.0–1.5 μW/m^3.

A decrease in Q_r with age correlates with a similar trend for surface heat flow on the continents, and worldwide on the continents the difference between surface and reduced heat flow appears to be almost independent of crustal age, ~17 mW/m^2 for best-fit linear approximations, with slightly lower values for the Archean cratons and slightly higher values for the Phanerozoic regions (Artemieva and Mooney, 2001). Although this observation apparently argues in favor of a nearly uniform contribution by crustal radioactivity DA_o into variations in surface heat flow, one should not forget that this global generalization does not necessarily hold in individual geological provinces.

4.2 Heat flow data

This section provides an overview of heat flow observations worldwide. Because of the principal differences in the thermal structure of the oceanic and the continental lithosphere, they will be discussed in detail in Sections 4.3 and 4.4, respectively.

4.2.1 Global compilations of surface heat flow

Measurements of temperature gradient in near-surface boreholes together with data on thermal conductivity of near-surface rocks allow calculation of surface heat flow (Eq. 4.5). The uncertainty (accuracy) of high quality surface heat flow measurements is ~15% and is associated with:

(1) the accuracy of analytic measurements of thermal conductivity (7–10%) and temperature gradient (<5%);
(2) natural factors, some of which cannot be reliably assessed (groundwater circulation, denudation history, changes in paleoclimate); the effect of natural factors on the quality of heat flow data is minimized by eliminating measurements from shallow (<100–300 m) boreholes;
(3) the conditions for borehole measurements (in particular, if steady-state thermal regime was re-established in the borehole after drilling);
(4) the assumption on quasi-vertical heat flow (Eq. 4.5); this assumption fails in the case of lateral heat transfer due to high contrasts in thermal properties of the crust; in such cases borehole measurements may significantly underestimate (overestimate) the actual heat flow from the deep interior;
(5) the assumption on conductive origin of surface heat flow (Eq. 4.5); this assumption fails in regions where the convective (and advective) heat flow component is expected to be significant and thus borehole measurements can be non-representative of the deep thermal regime. Such regions include (a) tectonically active regions (in particular, continental regions of magmatism and mid-ocean ridges), and (b) ocean floor where water circulation through the oceanic crust may lead to an underestimate of heat flow (see Section 4.3).

Heat flow measurements were initiated in the UK at the end of the nineteenth century (Everett, 1883). However, the first modern measurements of terrestrial heat flow began only in the late 1930s on the continents (Benfield, 1939; Bullard, 1939; Krige, 1939) and the 1950s in the oceans (Revelle and Maxwell, 1952). The first compilation of available heat flow measurements into a database is almost half a century old (Lee and Uyeda, 1965) and it included about 1000 measurements, most of them off-shore. Progress in thermal studies has resulted in routine measurements of heat flow and a fast accumulation of new data, which by 1976 included ~1700 on-shore and ~3700 off-shore measurements (Jessop *et al.*, 1976). This compilation formed the basis for the first global analysis of heat flow data and global heat loss which was performed in two classical studies of Chapman and Pollack (1975) and Sclater *et al.* (1980). The major results of these studies remain undisputed, although the number of heat flow measurements has increased dramatically over the past decades.

The heat flow compilation by Jessop *et al*. (1976) made the basis of the most recently published global heat flow database which includes a total of 24 774 heat flow measurements (Pollack *et al*., 1993). The database includes all available measurements but with a large diversity in data quality and reliability. Low quality heat flow measurements include primarily industrial measurements in shallow boreholes affected by groundwater circulation, in boreholes where a steady-state thermal regime was not achieved at the time of measurement, and measurements using non-conventional techniques (in particular, in South America). The database can be downloaded at: http://www.heatflow.und.edu; interpolated values of heat flow based solely on high-quality measurements can be downloaded at: www.lithosphere.info (Fig. 4.16). Up to date, the compilation

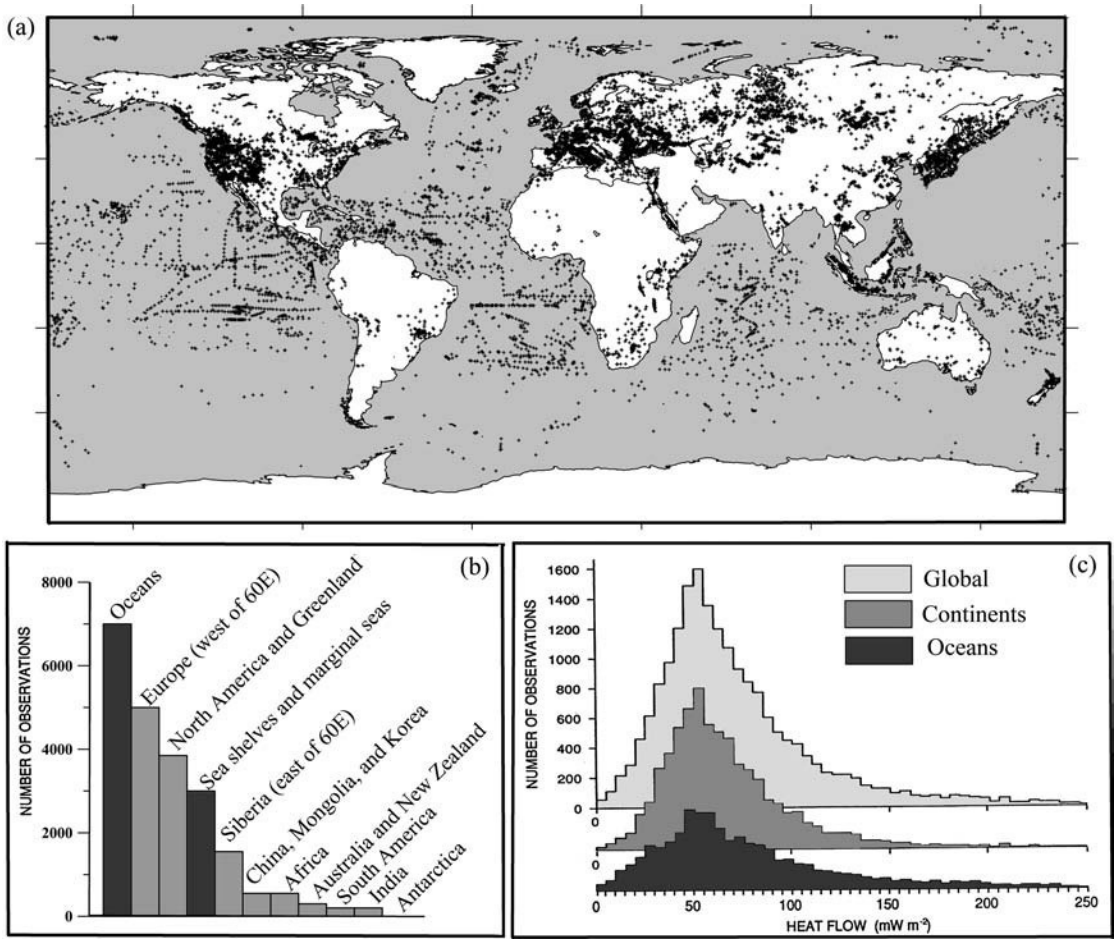

Fig. 4.16 Global statistics of heat flow measurements. (a) Heat flow data coverage. (b) Histogram illustrating geographical data coverage (based on an updated compilation of Pollack *et al*., 1993). (c) Statistics of measured heat flow values (redrawn from Pollack *et al*., 1993). Since 1993, the number of borehole measurements has substantially increased for North America, India, China, South America, and the oceans. However, new data do not affect the global statistics.

of Pollack and co-authors remains the most complete published database of surface heat flow. Newer versions updated for continuing borehole measurements are becoming available at the websites of the IHFC (the International Heat Flow Commission) and NOAA (National Oceanic and Atmospheric Administration).

4.2.2 Global trends in surface heat flow

Fig. 4.16a,b displays global coverage by heat flow measurements. Although at present the number of heat flow measurements is twice the size it was in 1993 (in particular, a significant number of new data became available in Canada, India, Norway and in the oceans), the general pattern of data coverage has not changed significantly: heat flow measurements are still available for only about 50% of the globe. Most measurement campaigns have focused either on easily accessible areas or on tectonically important regions. No, or very few, measurements have been taken in large areas of South America, Arctic North America, Africa, Arabia, Greenland, and Antarctica. In the oceans, most of the measurements have been made in the tropical and middle latitudes, with very few data in high latitudes. Even the oceans with a sufficient number of measurements suffer from patchy data coverage. In spite of the existence of "white spots", uneven coverage, and geographical biases, which result in significant spatial limitations for thermal models, several robust features can be clearly recognized in the available data. They allow statistical interpretation of data and meaningful conclusions on the thermal regime of the Earth's interior.

- Continental and oceanic distributions of heat flow appear very similar (Fig. 4.16c). However, this similarity is misleading because of a strong hydrothermal effect on measurements in the oceans (see discussion in Section 4.3.3).
- The mean heat flux on continents is lower than in the oceans (Figs. 4.16c; 4.17), 65 mW/m^2 and 101 mW/m^2, respectively, with a global mean of 87 mW/m^2.
- Surface heat flow is highly variable (Fig. 4.18); strong lateral variability is observed even at small distances. The reported values range from near-zero to several hundred mW/m^2, with the most common values 0–125 mW/m^2 and a range of vertical temperature gradient of 10–80 °C/km.
- In general, higher heat flow is observed in young structures both on continents and in the oceans (Fig. 4.19). In oceans the highest values typically correlate with mid-ocean ridges.

4.3 Thermal regime of oceanic lithosphere

4.3.1 Age dependence of seafloor topography and heat flow

According to plate tectonics, oceanic lithosphere is created at mid-ocean ridges by passive upwelling of hot mantle material (magma). Magma cools to form oceanic lithosphere which behaves like a plate and, as more magma is intruded at the spreading center, it moves away from the ridge. The combined effect of ocean spreading and lithosphere consumption at subduction zones results, in general, in a decrease in ocean area with age (Fig. 4.20) (Sclater

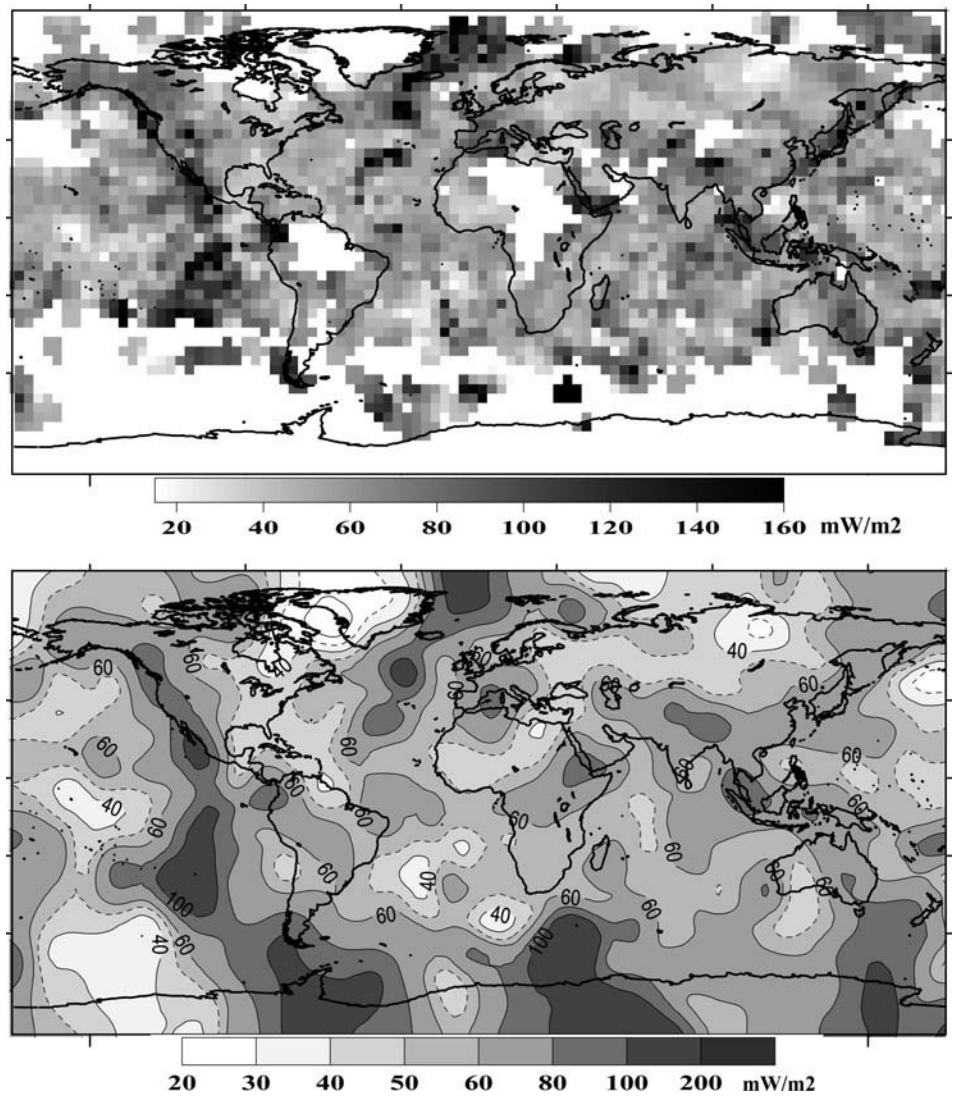

Fig. 4.17 Global surface heat flow (based on an updated compilation of Pollack *et al*., 1993). Top: averaged on a 5 deg x 5 deg grid; bottom: global interpolation with a low-pass filter. Solid lines – heat flow contours with a 20 mW/m^2 step; dashed lines – contours of 30 and 50 mW/m^2. Small-scale anomalies are smeared both laterally and in amplitude.

et al., 1980). Most of the young oceanic lithosphere is generated in the fast spreading South Pacific Ocean (the spreading rate along the East Pacific Rise is up to 130 mm/yr). Oceans with slow spreading rates, such as the Atlantic and Indian Oceans, where the spreading rate is *c*. 4 times slower than in the South Pacific, have area–age distributions similar to the North Pacific Ocean, which has only the western branch.

The general age dependence of ocean floor topography and oceanic heat flow has been recognized since the 1960s (e.g. von Herzen and Uyeda, 1963; Langseth *et al*., 1966; Sclater

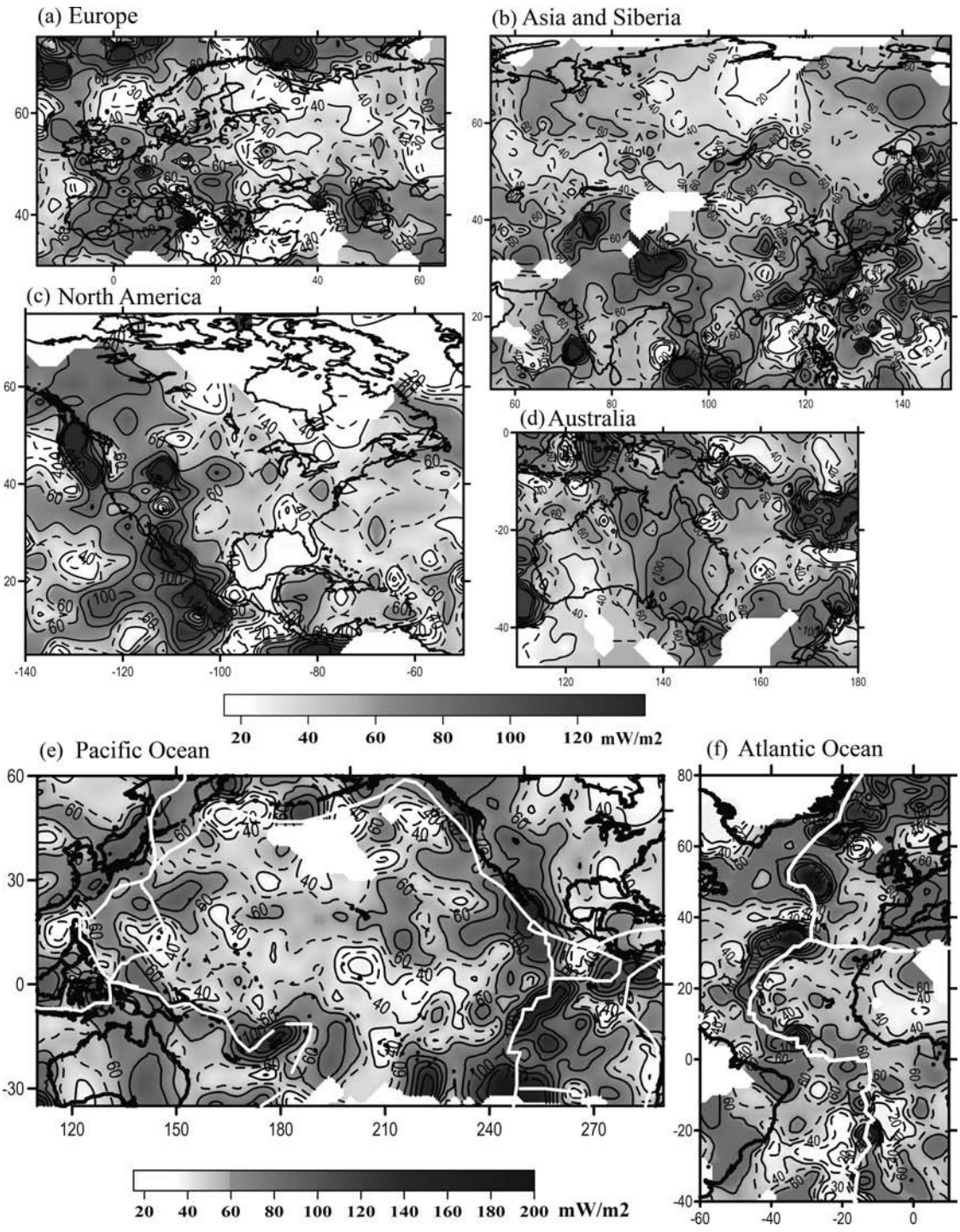

Fig. 4.18 Surface heat flow in regions with a high density of measurements, interpolated on a 5 deg x 5 deg grid: (a) Europe; (b) Asia and Siberia; (c) North America; (d) Australia and New Zealand; (e) Pacific Ocean; (f) Atlantic Ocean. White – areas with no heat flow data; white lines in (e–f) – plate boundaries.

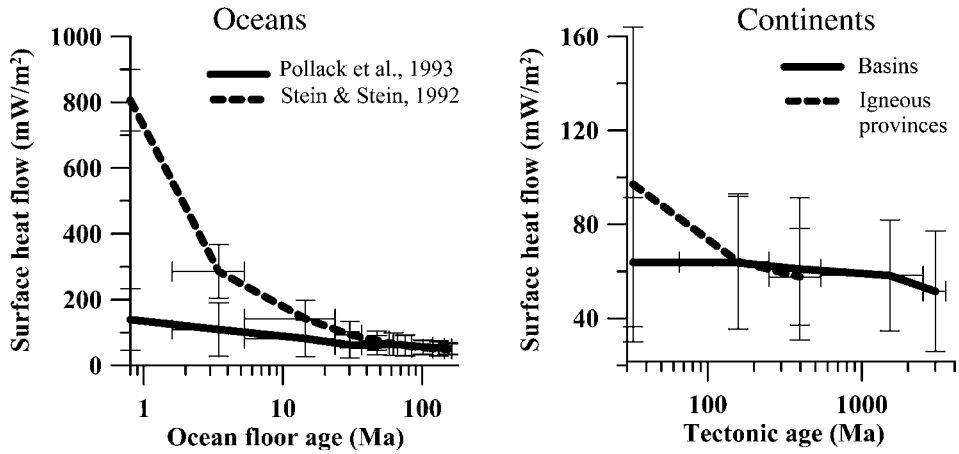

Fig. 4.19 Mean heat flow values for continental and oceanic regions versus age (Source: Pollack *et al*., 1993; Stein and Stein, 1992). Bars – standard deviations. The large discrepancy in two sets of estimates for young (<20–30 Ma) oceans is caused by the strong effect of sea water circulation through the oceanic crust that is not covered by deep-sea low-permeability sediments (see discussion in Section 4.5). Conventional heat flow measurements only determine the conductive component of heat flow and thus significantly underestimate the heat loss in young oceans. On the continents, a significant difference exists between stable and young (Meso-Cenozoic) tectonic regions.

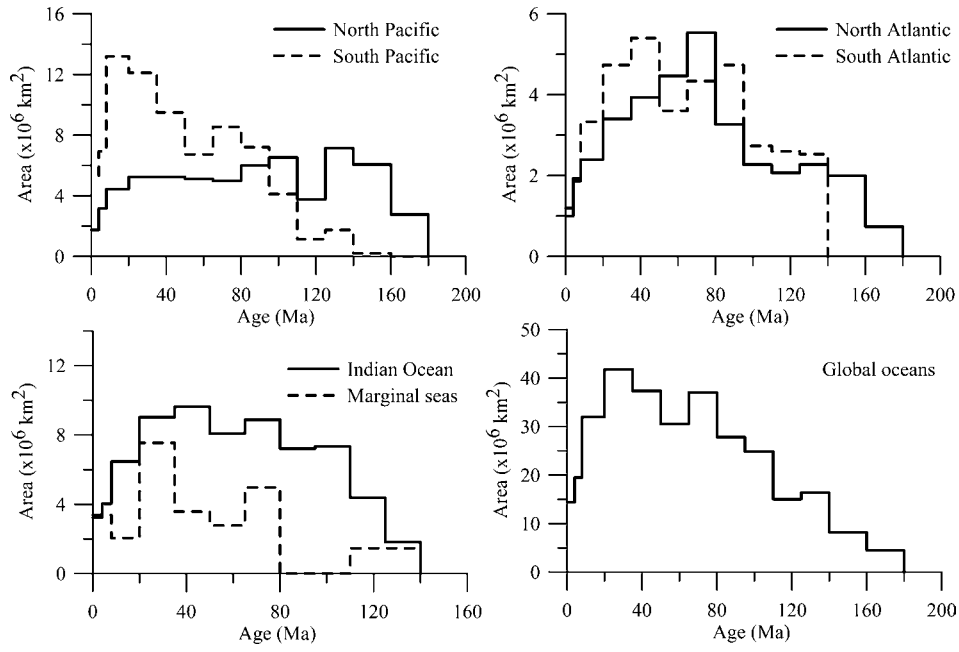

Fig. 4.20 Ocean floor area as a function of ocean age (after Sclater *et al*., 1980). Note different vertical scales.

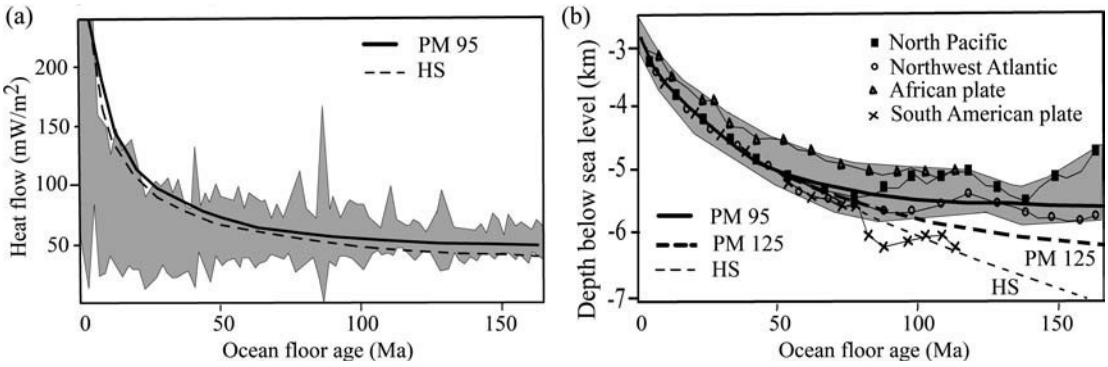

Fig. 4.21 Heat flow (a) and depth below sea level (b) in the oceans as a function of ocean age (after Stein and Stein, 1992). Gray shading – upper and lower bounds of observations. Thick solid and dashed lines in (a,b) – theoretical predictions for plate models (PM) with 125-km- and 95-km-thick plates (Parsons and Sclater, 1977; Stein and Stein, 1992). Thin dashed line labeled HS – theoretical predictions based on instantaneous boundary layer cooling of an infinite half-space for the same parameters as the plate models. Symbols and thin lines in (b): depth data averaged for 5 Ma bins for four oceans. Significant differences between plates hamper any global reference model for ocean bathymetry.

and Francheteau, 1970). The highest heat flow and the shallowest topography are observed at mid-ocean ridges; heat flow decreases from more than 200 mW/m^2 in the youngest oceanic lithosphere near mid-ocean ridges to 50–60 mW/m^2 in the old (>70 Ma) ocean floor, while ocean depth, in general, increases from ~2.5–3 km in young oceans to ~5–6 km in old oceans (Fig. 4.21; compare with Fig. 3.121). Age variations in seafloor bathymetry and heat flow can be approximated by the square root of ocean age: $1/\sqrt{\text{age}}$ for depth variations and $\sqrt{\text{age}}$ for heat flow variations (Davis and Lister, 1974). There is, however, a large scatter in topography, especially for the old oceanic lithosphere, where most of the seamounts, swells, and oceanic plateaus are located. Because of hydrothermal circulation, for heat flow the square root of age law only holds approximately for crust older than ~2–6 Ma, covered by a thick layer of impermeable sediments (Fig. 4.22); old oceans (>80 Ma), however, also may deviate from a simple square root of age relationship.

4.3.2 Normal oceans

Cooling, contraction, and sedimentation of oceanic lithosphere explain qualitatively heat flow decrease and ocean depth increase with ocean floor age. Cooling of lithospheric plates is described by the heat conduction equation (e.g. Turcotte and Schubert, 1982). The boundary condition at the base of the plate can be specified either by heat flux (with variable plate thickness) or by temperature (with fixed plate thickness). Shear heating associated with plate motion (Schubert *et al*., 1976) or a uniform distribution of radioactive elements in the upper 300 km of the mantle (Forsyth, 1977) have been proposed as maintaining constant heat flux at the lithospheric base. In contrast, small-scale convection in the upper mantle has been proposed as a mechanism for maintaining constant temperature at the lithospheric base (McKenzie, 1967; Richter, 1973). The choice of boundary condition implies different

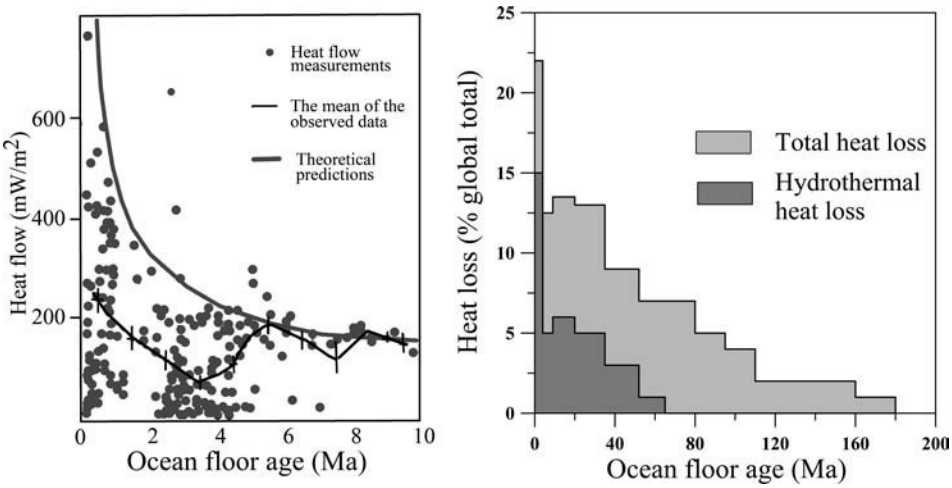

Fig. 4.22 Heat flow near ocean spreading centers. Left: Heat flow at the Galapagos spreading center (Source: Anderson and Hobart, 1976; modified after Sclater *et al.*, 1980). Right: Estimated heat loss through oceanic provinces (Source: Sclater *et al.*, 1980).

assumptions about the nature of the thermal boundary layer and results in two different types of models of thermal evolution of the oceanic lithosphere: cooling half-space and plate model. In oceanic thermal models, radiogenic heat production is commonly ignored because radiogenic elements (which are present in the mantle in very low concentrations, see Section 4.1.4) are further removed from the mantle during melt generation.

Cooling half-space model

Model predictions and empirical relationships

Conductive cooling of a half-space (an oceanic plate as it moves away from the mid-ocean ridge axis where it has been created) explains the observed $1/\sqrt{\text{age}}$ variations in seafloor depth and $\sqrt{\text{age}}$ heat flow variations for the young oceans (Davis and Lister, 1974; Turcotte and Schubert, 1982; Carlson and Johnson, 1994). Temperature variation $T(\text{age}, z)$ with depth z and ocean floor age is given by:

$$T(\text{age}, z) = T_{\text{m}}\ \text{erf}(z\sqrt{4\chi\ \text{age}}) \tag{4.22}$$

where T_{m} is the initial temperature of the half-space (mantle temperature), χ is the thermal diffusivity of the mantle,

$$\text{erf}(x) = \frac{2}{\sqrt{\pi}} \int_0^x \text{e}^{-y^2}\,\text{d}y \tag{4.23}$$

is the error function, and the thermal boundary layer thickens with time t as:

$$\delta \sim \pi\sqrt{\chi t}. \tag{4.24}$$

In the real Earth, the geotherm approaches mantle adiabat T_m asymptotically. The constant on the right-hand side of eq. (4.24) depends on the choice of temperature T which is assumed to be close enough to T_m to be considered as the basal temperature of the thermal boundary layer. The thickness of oceanic lithosphere L (i.e. the thickness of the thermal boundary layer over the cooling half-space in the case of no radioactive sources) is (Schubert *et al.*, 2001, eq. 4.22):

$$L[\text{km}] = 2\ \text{erfc}^{-1}(\Delta T)\sqrt{\chi t}\ \sim\ c_2\sqrt{\text{age}} \tag{4.25}$$

where $\text{erfc}(\Delta T) = 1 - \text{erf}(\Delta T)$ is the complementary error function of (ΔT) and age is in Ma. For a thermal diffusivity value $\chi = 10^{-6}$ m^2/s ~ 31.5 km^2/Ma, and assuming that the base of TBL is defined by a 10% temperature anomaly with respect to T_m ($\Delta T = 0.1$), the constant $c_2 \sim 12.6$ km/Ma$^{1/2}$. For 5% and 20% temperature anomalies at the base of TBL, constant c_2 has similar values, 12 km/Ma$^{1/2}$ and 14.5 km/Ma$^{1/2}$, correspondingly.

For the oldest oceanic lithosphere of ~180 Ma which is present in the western Pacific Ocean (Fig. 2.22), formal solution of eq. (4.25) gives a lithospheric thickness of 150–175 km. These values are about twice the traditional geophysical estimates for old oceans (Fig 3.121). However, a recent tomographic model apparently indicates that a +2% *V*s anomaly beneath the western Pacific persists down to ~120 km depth, and a +1% *V*s anomaly down to 150–170 km (Fig. 3.99d).

Aging oceanic lithosphere, which thickens as $\sqrt{\text{age}}$, becomes heavier and its surface subsides. The depth to the unsedimented basement D (assuming that the cooling thermal boundary layer subsides by the Airy isostatic compensation) is:

$$D(\text{age}) = D_r + c_1\sqrt{\text{age}}, \tag{4.26a}$$

$$\text{where } c_1 = \alpha T_m\sqrt{4\chi/\pi}\ \rho_m/(\rho_m - \rho_w), \tag{4.26b}$$

D_r is the depth to the ridge crest, ρ_m and ρ_w are mantle and seawater densities, respectively, and α is the volume thermal expansion coefficient for mantle. A simple empirical relationship based on bathymetry and age data from the North Pacific and North Atlantic Oceans younger than ~80 Ma yields:

$$D[\text{km}] = 2.5 + 0.35\ \sqrt{\text{age}}, \tag{4.26c}$$

where age is in Ma. In fact, the subsidence rate c_1 is commonly estimated to be between 336 and 344 m/Ma$^{1/2}$, but a commonly used value is 350 m/Ma$^{1/2}$. There are, however, large regional variations in parameters. For example, a number of systematic studies along the East Pacific Rise show variations in ridge depth from 2000 to 3200 m, and variation in the associated subsidence rate between 50 and 450 m/Ma$^{1/2}$.

Given that conductive heat flow across the boundary layer is $Q \sim \lambda\Delta T/\delta$ (where λ is thermal conductivity and ΔT is the temperature drop across the thickening boundary layer, compare with eq. 4.5), seafloor heat flow decreases with lithospheric age as $1/\sqrt{\text{age}}$. Assuming that the temperature at the basement surface is 0 °C, the surface heat flow Q (age) is:

$$Q(\text{age}) = \lambda\ T_m/\sqrt{\pi\chi\ \text{age}}. \tag{4.27a}$$

An empirical relationship for heat flow observations from oceans younger than ~80 Ma yields:

$$Q = 473/\sqrt{\text{age.}} \tag{4.27b}$$

Thus, variations in heat flow and bathymetry with ocean age jointly reflect changes in oceanic geotherms with age. The basal temperature estimated from the fit with observations is $T_m \sim 1335–1370$ °C.

Mantle potential temperature

The basal temperature T_m, which is an important parameter which defines variations of heat flow and bathymetry with ocean age in the cooling half-space model (eqs. 4.22, 4.25–4.27), is the potential temperature of the mantle (i.e. the temperature of the mantle if it were decompressed adiabatically to the surface). Starting from the early 1970s, the potential temperature of the oceanic mantle has been studied experimentally from the geothermometry of oceanic tholeiites from different spreading centers. These provide the lower bound temperatures necessary to generate olivine tholeiites as a primary melt from the mantle source rock, and these estimates are not sensitive to the composition of the pyrolite model (Table 6.2). The range of all temperature values determined for rocks from the Pacific and Atlantic Oceans varies from ~1200 °C to ~1450 °C (e.g. Fig. 6.4) with median values around 1290–1350 °C. For a standard set of thermodynamic parameters (Section 4.1), it yields the adiabatic temperature gradient

$$(\mathrm{d}T/\mathrm{d}Z)_s = T\alpha g/C_p \sim 0.5 - 0.6\,^{\circ}\mathrm{C/km}, \tag{4.28}$$

where T is the absolute temperature, g is the gravitational acceleration, α is the coefficient of thermal expansion ($\alpha \sim 3 \times 10^{-5}$ 1/K), and C_p is the heat capacity at constant pressure ($C_p \sim$ 1000–1200 J/kg/K). With increasing pressure, the value of α decreases; however this effect is compensated by an increase in temperature with depth, so that the adiabatic temperature gradient is approximately constant in the upper mantle. The above conclusions are based on an assumption that the mantle potential temperature beneath oceanic spreading centers is the same as elsewhere.

In agreement with these conclusions, McKenzie and Bickle (1988) argue that if "normal" oceanic crust of uniform thickness 7.1 ± 0.8 km (which is an average thickness of oceanic crust unaffected by plumes or fracture zones, White *et al*., 1992) is formed by decompressional melting, mantle potential temperature should be $T_m \sim 1315 \pm 13$ °C.

Cooling half-space model and ocean floor flattening

The cooling half-space (boundary layer) model successfully explains the observed heat flow and bathymetry for ocean floor younger than ~70–80 Ma. However, it fails to predict the flattening of the ocean floor topography, observed (apparently, see below) for oceans older than ~80 Ma (Fig. 4.21). Moreover, the flattening of the seafloor starts at different ages in different oceans (Marty and Cazenave, 1989) and is often asymmetric with respect to ridge

axes (e.g. Morgan and Smith, 1992). Several mechanisms have been proposed to explain ocean floor flattening:

- heat flow perturbations at the lithospheric base (e.g. due to asthenospheric flow, small-scale convective instabilities, or hotspots) that provide additional heat from the mantle, balance heat loss through the lithosphere, and prevent it from fast cooling (Crough, 1975; Oldenburg, 1975; Heest and Crough, 1981);
- pressure forces in the asthenosphere underneath the oceanic thermal boundary layer (TBL) (Phipps Morgan and Smith, 1992);
- a pre-existing chemical boundary layer (CBL, formed by melt extraction and, as a result, dehydrated and chemically buoyant) which might control the thickness of the TBL by affecting secondary convection at its base (i.e. the CBL might effectively work as a conductive lid not involved in mantle convection) (Lee *et al.*, 2005).

It should be noted that theoretical and observational studies over the last decade cast serious doubt over whether ocean floor flattening takes place in reality:

- in the 3D Earth, "ocean floor flattening" can be an artifact of theoretical predictions, since the $\sqrt{\text{age}}$ predictions are based on 2D thermal boundary-layer theory (Bercovici *et al.*, 2000);
- two recent case studies (Korenaga and Korenaga, 2008; Adam and Vidal, 2010) suggest that "ocean floor flattening" is an artifact of field observations (see below).

Plate model

Traditional approaches

To account for departure of heat flow and bathymetry from the $\sqrt{\text{age}}$ law in old ocean basins, the "plate model" in which the base of the TBL is considered as an isothermal boundary has been proposed (McKenzie, 1967; Richter, 1973). In this model, the plate (oceanic lithosphere) is generated at a constant temperature beneath a mid-ocean ridge spreading with constant velocity. The "base of the plate" has no physical meaning, but the plate is assumed to have constant thickness to approximate constant heat flow, as observed in old oceans. Constant temperature at the base of the plate (oceanic lithosphere) as suggested by small variations in thickness of the oceanic crust (see discussion below) is maintained by small-scale convection in the upper mantle caused by instabilities growing at the base of the cooling lithosphere that become effective only below old ocean and regulate the plate thickness. The plate consists of two parts: a rigid mechanical upper layer on top of a viscous thermal boundary layer (Parsons and McKenzie, 1978). Cooling results in thickening of both of the layers, the thermal boundary layer becomes unstable at an ocean age of ~60 Ma, and small-scale convection creates the observed thermal and bathymetry patterns (Fig. 4.23). The model has a singularity in heat flow at the mid-ocean ridge, which can be removed by changing the boundary conditions.

In the case of constant thermal conductivity, the temperature distribution within the plate has an analytical solution, and when the spreading rate is >10 mm/yr the geotherm only depends on the age of the plate (McKenzie, 1967) and can be approximated as:

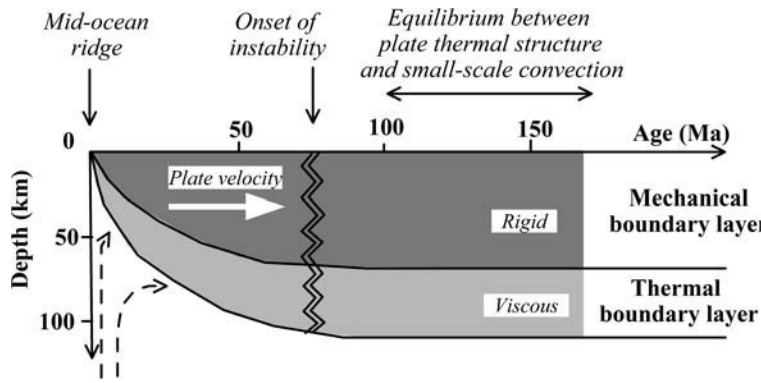

Fig. 4.23 Simplified diagram showing the subdivision of oceanic plate into rigid mechanical boundary layer and viscous thermal boundary layer (modified after Parsons and McKenzie, 1978). Dashed lines – mantle flow.

$$T(\text{age}, z) = T_{\text{m}}(z/L + \Sigma\ 2/n\pi \sin(n\pi z/L) \exp(-\chi(n\pi/L)^2 \text{age})) \qquad (4.29)$$

where L is the plate thickness, z is the depth below the plate surface, and T_{m} is the basal temperature. Similarly, bathymetry variations with depth can be calculated for isostatically compensated plate and constant thermal expansion coefficient as:

$$D(\text{age}) = D_{\text{r}} + L/2\ \alpha T_{\text{m}}\rho_{\text{m}}/(\rho_{\text{m}} - \rho_{\text{w}})(1 - 8/\pi^2 \Sigma j^{-2} \exp(-\chi(j\pi/L)^2 \text{age})) \qquad (4.30)$$

where $j = 1,3,5$. The plate model does not explicitly provide the $\sqrt{\text{age}}$ dependence for heat flow and ocean floor topography:

$$Q(\text{age}) = \lambda T_{\text{m}}/L(1 + 2\Sigma \exp(-\chi(n\pi/L)^2\ \text{age})), \qquad (4.31)$$

here the first term provides the asymptotic heat flow for old seafloor. The use of a Green's function approach allows us to express the asymptotic solution for young oceans away from the ridge crest in a form with explicit $\sqrt{\text{age}}$ dependence (Parsons and Sclater, 1977). The predictions of the cooling half-space model and the plate model are similar for young oceans, but differ for oceans older than 70–100 Ma (Fig. 4.21). In contrast to the cooling half-space model, the plate model predicts a near-constant ocean floor depth in the old oceans, as well as the age of the departure of bathymetry and heat flow from the $\sqrt{\text{age}}$ law.

A detailed analysis of the parameter space of the plate model shows that it is not possible to obtain all of the lithospheric parameters from data. Assuming that lithosphere density, thermal conductivity, and heat capacity are known, data on heat flow and bathymetry allow for calculation of plate thickness, temperature at its base, and thermal expansion coefficient α (Fig. 4.24; Table 4.7). A plate model with 125 ± 10 km-thick lithosphere, a basal temperature of 1350 ± 275 °C, and $\alpha = (3.2 \pm 1.1) \times 10^{-5}$ °C^{-1} explains the observed age variations in ocean floor topography and heat flow in the North Pacific better than a cooling half-space model (Parsons and Sclater, 1977). For old oceans this model, however, still overestimates the topography and gives wrong predictions for heat flow. Stein and Stein (1992) further modified the plate model to yield a better fit to observations and suggested that a plate with 95 ± 10 km-thick lithosphere, a basal temperature of 1450 ± 100 °C, and $\alpha = 3.1 \times 10^{-5}$ °C^{-1} provides

Table 4.7 Parameters specifying the plate model

Constant	Estimate
$c_1 = 2\rho\alpha T\sqrt{\chi/\pi}\ /\ (\rho\text{-}\rho_w)$	$350 \pm 65\ (\text{Ma})^{1/2}$
$c_2 = L^2/9\chi$	64–80 Ma
$c_3 = \rho L\alpha T/2(\rho\text{-}\rho_w)$	3900 ± 350 m
$c_4 = \rho\ C_p\ T\sqrt{\chi/\pi}$	–
$c_5 = 0.22\ L^2/\chi$	–
$c_6 = \lambda T/L$	33.5 ± 4.2 mW/m^2

(after Parsons and Sclater, 1977). Parameters: T – temperature at the lithosphere (plate) base; L – plate thickness; α – coefficient of thermal expansion of the lithosphere; ρ and ρ_w – density of lithosphere (at $T = 0$ °C) and water; $\chi = \lambda/\rho c_p$ – thermal diffusivity of the lithosphere, λ – thermal conductivity, c_p – specific heat at constant pressure. Commonly assumed values are: $\rho = 3300$ kg/m^3; $\rho_w = 1000$ kg/m^3, $c_p = 1.17$ kJ/kg/K, $\lambda = 3.14$ W/m/K.

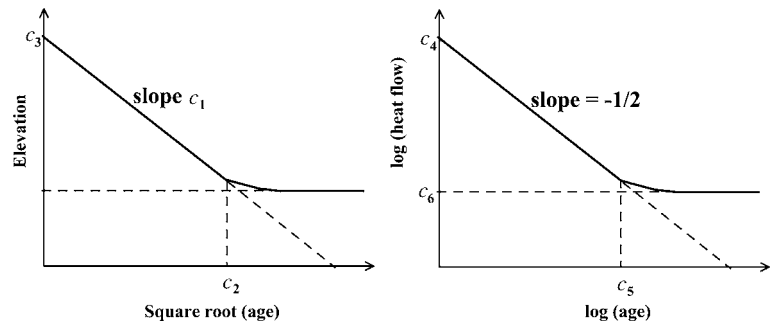

Fig. 4.24 Parameter space for the plate model (after Parsons and Sclater, 1977). See Table 4.7 for definitions of the constants c_1–c_6.

better fit to the observed topography and heat flow for ocean ages >70–100 Ma. Their model predicts that for oceans younger than 20 My, heat flow Q and bathymetry D can be expressed as:

$$Q_{oc} = 510/\sqrt{\text{age}}, \quad D = 2.6 + 0.365\ \sqrt{\text{age}} \tag{4.32}$$

where the age of the ocean floor is in Ma, heat flow Q_{oc} is in mW/m^2, and bathymetry is in km.

Oceanic geotherms

The plate model is commonly used to calculate the average thermal structure of the oceanic lithosphere as a function of ocean age (Fig. 4.25). It also allows for speculation on melting conditions in the oceanic mantle (Fig. 4.26). In particular, the plate model of Stein and Stein

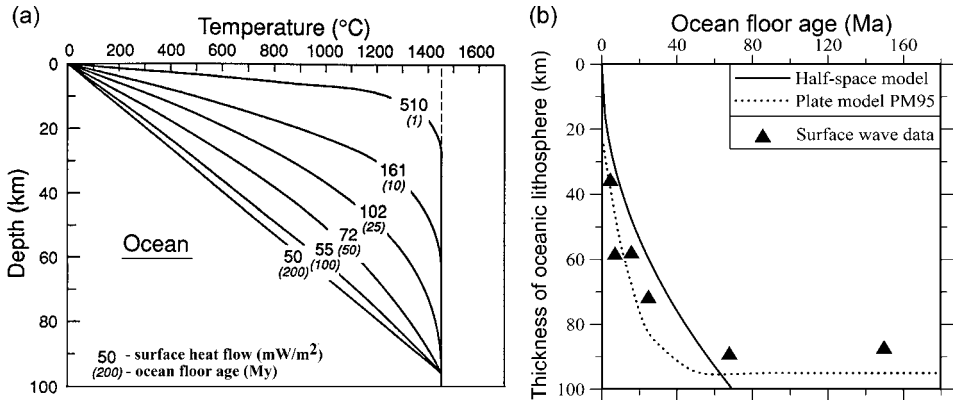

Fig. 4.25 Thermal structure of normal oceans. (a) Family of conductive geotherms for oceanic lithosphere calculated for plate model PM95 with plate thickness 95 km and temperature at the plate base 1450 °C (from Pollack *et al*., 1993). When the temperature dependence of thermal conductivity is taken into account, temperatures in the oceanic mantle become lower than shown in (a). (b) Thickness of oceanic lithosphere predicted by a cooling half-space model and plate model PM95. Symbols – surface wave estimates of lithosphere thickness (see Fig. 3.121). For young oceans (<80 Ma), seismic data agree with both models. For old oceans, old seismic data do not support the half-space model, while recent data indicate that lithosphere beneath old parts of the Pacific Ocean can extend down to ~120–150 km (Fig. 3.99d).

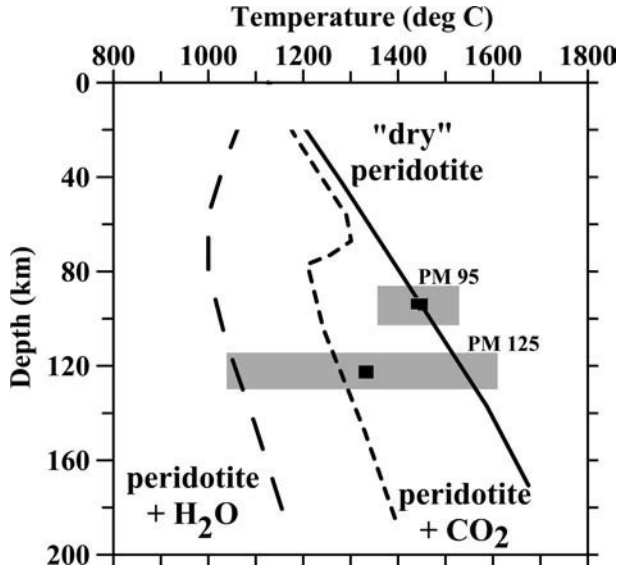

Fig. 4.26 Best estimates (black boxes) and range of uncertainties (gray boxes) for the temperature and thickness of oceanic plate for two plate models (based on plate models of Parsons and Sclater, 1977; Stein and Stein, 1992) compared with peridotite solidi: solid line – melting of a natural dry peridotite (Takahashi, 1986; Hirschmann, 2000); dashed lines – melting of peridotite saturated with H_2O and CO_2 (compilation by Wyllie, 1995).

(1992) with a 95 km-thick oceanic plate suggests dry peridotite melting in oceanic mantle. This result may be inconsistent with data on electrical conductivity which favor the wet composition of suboceanic mantle (Hirth *et al*., 2001).

McKenzie *et al*. (2005) analyzed the effect of temperature-varying thermal conductivity $\lambda(T)$ and thermal expansion $\alpha(T)$ on oceanic mantle geotherms in the plate model. In the case of constant λ, any changes in model parameters produce changes in both the depth–age curve and in the heat flow–age curve. In the case of temperature-dependent conductivity $\lambda(T)$, different heat flow–age curves can correspond to the same depth–age curve, since the analytical solution uses a Fourier expansion of temperature variations in which only the odd terms contribute to the depth variations, but both odd and even terms contribute to the heat flow variations. When temperature dependence of thermal conductivity is taken into account, the predicted temperatures in the oceanic mantle become lower than Fig. 4.25 predicts (e.g. McKenzie *et al*., 2005). A decrease in λ with a temperature increase reduces the temperature in the center of the plate compared to the analytical solution. Since temperature decrease causes decrease in α, the resultant effect is a greater amount of ocean floor subsidence. The latter, however, is counteracted by a significant reduction in plate thickness.

Alternative approaches

Alternatively, the thermal regime of normal oceanic lithosphere can be calculated if the thermal expansion coefficient is known (for example, from laboratory measurements on peridotite samples). An additional constraint on melting temperature (and thus on the potential temperature of the mantle) can be applied by requiring that the oceanic crust be produced by decompression melting of passively ascending mantle material at a mid-ocean ridge. In such a formulation, plate thickness remains the only free parameter in the system (McKenzie *et al*., 2005).

In a general case, the thickness of "normal" oceanic crust z (in km) generated by decompressional melting can be parameterized as:

$$z = [T_{\mathrm{m}} - 1242]/10.32, \tag{4.33}$$

where T_{m} is the mantle potential temperature (in °C), and for a potential temperature increase of 12.5 °C crustal thickness increases by 1 km (McKenzie *et al*., 2005). The plate model of Parsons and Sclater (1977) is more consistent with estimates of mantle potential temperature, since the potential temperature of 1450 °C (plate model of Stein and Stein, 1992) would generate by decompressional melting a 16 km-thick crust. This further implies that temperature variations in the oceanic mantle are very small since the standard deviation of 0.8 km in the average thickness of oceanic crust (7.1 ± 0.8 km) corresponds to a temperature variation of only ~10 °C. The latter explains the success of the plate model, which is based on an assumption of constant temperature at the base of the plate.

Testing half-space and plate models by observation

Carson and Johnson (1994) compared the predictions of the half-space and plate models with mean depth and depth to basement reported from the Deep Sea Drilling Project (DSDP) and Ocean Drilling Program (ODP). They concluded that:

- the cooling half-space $\sqrt{\text{age}}$ models can meaningfully fit the drilling and mean depth data for oceans younger than 73–81 Ma; for young (<~80 Ma) seafloor, cooling half-space models require a basal temperature of 1300–1370 °C; the minimum plate thickness compatible with best fitting cooling half-space models for young seafloor is ~120 km;
- plate models can also meaningfully fit the drilling and mean depth data for ocean ages <81 Ma; the best fitting plate models for young (<~80 Ma) seafloor require systematically higher temperatures of 1450–1470 °C and systematically thinner plates, 102–118 km, than derived from corresponding fits to the half-space model for young seafloor;
- no cooling plate model can explain variations in bathymetry with age over the entire range of ocean ages, 0–165 Ma; the misfit dramatically fails for ocean ages >81 Ma; the plate model of Stein and Stein (1992) minimizes the overall misfit at the expense of producing large misfits (above the limit of acceptable systematic misfit) over the entire range of ocean ages;
- failure of the plate model to explain the drilling data may indicate that the plate model is too simple to account for the full range of depth variations with age, and that the cooling history of old ocean floor cannot be approximated by extension of the cooling history of young ocean floor; depth versus age variations in old oceans can be explained by thermal perturbations superimposed on a "normal" half-space cooling trend.

Small-scale convection and geoid

Ocean floor flattening with age could not be explained by cooling half-space models and led to the development of plate models. However, plate models do not include any assumptions on physical mechanisms of flattening of old ocean floor. Proposed mechanisms for flattening included small-scale convection (McKenzie, 1967; Richter, 1973) and formation of oceanic plateaus and islands, since older oceans are more likely to have experienced anomalous evolution (e.g. Smith and Sandwell, 1997). For example, it was argued that all of the Pacific Ocean floor older than 80 Ma lies within 800 km of hotspots or hotspot tracks (Schroeder, 1984).

An alternative model of thermal evolution of old oceanic lithosphere has been proposed by Doin and Fleitout (1996). In contrast to the plate model, which assumes that the base of the oceanic lithosphere is at constant temperature, these authors assumed constant basal heating of oceanic lithosphere by small-scale mantle convection. The model agrees well with the plate model predictions for oceans younger than 80 Ma, provides a good fit for the bathymetry and heat flow for old-age oceans, but, in comparison with the plate model, predicts several hundreds of meters of subsidence in oceans older than 100 Ma and requires a thermal expansion coefficient much larger than assumed in plate models.

Another approach to modeling thermal evolution of oceanic lithosphere is based on the analysis of geoid data (e.g. Cazenave *et al.*, 1983; Cazenave, 1994). Since cooling of the oceanic plate with age as it moves away from the spreading center leads to a change in its density, in theory one would expect geoid variations with ocean floor age. In practice, however, almost no correlation is observed between the two parameters, because the geoid signal is dominated by (i) long-wavelength components associated with density anomalies in the deep mantle and (ii) short-wavelength signals related to fracture zones and flexural

anomalies in the shallow lithosphere. Later attempts (e.g. DeLaughter *et al*., 1999) demonstrated that the application of spatial bandpass filtering allows for extraction of some age-dependent signal from the geoid. However, since isostatic geoid signals predicted from cooling half-space and plate models differ only in wavelength (for old ocean floor, the plate model predicts a zero slope of the geoid due to constant plate thickness, while the cooling half-space model does not), the filtered geoid data do not allow discrimination between the two models for ocean floor evolution (Hager, 1983). Seismic data also cannot reliably discriminate between the two models (Fig. 4.25b): while old interpretations of surface-wave data indicated a 90 km-thick lithosphere beneath old oceans, recent interpretations from the Pacific Ocean suggest that it may extend down to ~120–150 km, which would agree with the predictions of the cooling half-space model (eq. 4.25).

Ocean floor flattening: fact or artifact?

Two recent studies (Korenaga and Korenaga, 2008; Adam and Vidal, 2010), however, question the very seafloor flattening for old oceans and, as a result, question the necessity of using the plate model for the evolution of oceanic lithosphere. In fact, it has already been noted by Parsons and Sclater (1977) that there is no clear physical mechanism that determines the plate thickness, and the thickness of the slab is prescribed arbitrarily to fit the data on heat flow and bathymetry.

Korenaga and Korenaga (2008) argue that the analysis of bathymetry variations with age used in two popular plate models (Parsons and Sclater, 1977; Stein and Stein, 1992) was based on the entire data set, without excluding regions with "anomalous oceanic crust", such as hotspots and plateaus. As a result, for old oceans it is biased by data from anomalous regions because, due to isostasy, regions with anomalously thick crust produce topographic highs. Significant variations in the area of anomalous regions in different oceans may be the reason for significant differences in bathymetry versus ocean age variations between the oceans (Fig. 4.21).

Korenaga and Korenaga (2008) excluded data with a random signal, such as caused by crustal thickness variations, and limited their analysis of bathymetry–age data to the "normal seafloor", i.e. to regions unperturbed by hotspots and plateaus. They found that in this case the subsidence rate of ocean floor (the constant C_1 in Fig. 4.24; Table 4.7, eq. 4.26a) is 10% less, ~320 m/Ma$^{1/2}$. This, lower than conventional, value of the subsidence rate can be explained by the cooling half-space model, but with a reduced thermal expansivity of the mantle. The results of an earlier study (Nagihara *et al*., 1996) also indicate that data on heat flow and isostatically corrected depth measurements follow the curve expected from the cooling half-space model (although with some offset in age).

Another recent study by Adam and Vidal (2010) suggests that ocean floor flattening is an artifact caused by confusing "*flow lines*" with "*age trajectories*". Age trajectories follow an age gradient and are usually used in analysis of the age dependence of bathymetry and heat flow. In contrast, flow lines represent a mantle convection pattern underneath the ocean floor and thus characterize thermal boundary cooling. Since the cooling half-space model assumes a constant plate velocity, these are flow lines that should be used for comparison with theoretical predictions of the cooling half-space model, but not age trajectories. Flow lines may differ

strongly from age trajectories as an example from the Pacific Ocean illustrates. The difference is caused by the change in mantle convection pattern and in plate velocity that took place in the Pacific at ~47–50 Ma. Along the flow lines, no flattening is observed at old ocean floor ages in the Pacific Ocean, even far away from the ridge, while there is an apparent flattening along age trajectories. Along the flow lines, the bathymetry D shows a linear relation to the square root of the distance from the ridge $\sqrt{x}$ (compare with eq. 4.26):

$$D(x) = D_r + c_2\sqrt{x}, \tag{4.34}$$

where D_r is the ridge depth, and c_2 is the subsidence rate estimated to be in the range 0.5–3.5 m/m$^{1/2}$. In the Pacific Ocean, this relation is satisfied all along the plate, from the ridge to the subduction zone. If plate velocity is known, the distance from the ridge can be converted to the ocean floor age which, assuming a constant velocity of 9 cm/year for the Pacific plate, yields the subsidence rate between 200 and 900 m/Ma$^{1/2}$. Thus, Adam and Vidal (2010) conclude that there is no ocean floor flattening for old Pacific, and there is no need, in general, to invoke plate models to explain bathymetry in old oceans.

4.3.3 "Anomalous" oceans

Subduction zones, marginal basins, and accretionary prisms

A complicated thermal structure of subduction zones arises from their complex tectonic configuration. Horizontally, subduction zones can be roughly subdivided into forearc, arc, and back-arc (Fig. 4.27). Vertically they include the subducting slab and the overlying mantle wedge; the latter includes the convective asthenosphere and the conductive lithospheric mantle (oceanic or continental) of the overriding plate. The mantle wedge (both its lithospheric and asthenospheric parts) can variably be infiltrated by fluids and melts. The thermal structure of subduction zones is highly variable (Peacock, 1990; Kelemen *et al*., 2003; Fukao *et al*., 2004; Pozgay *et al*., 2009) and depends on several parameters (Peacock, 2003) such as:

- the thermal structure of the subducting plate that depends on its age;
- the thermal structure (thickness) of the overriding plate;
- the angle of subduction;
- the convergence rate;
- the flow in the mantle wedge which depends on its rheology and coupling between the asthenosphere and the subducting plate;
- shear heating at the upper surface of the slab;
- processes of dehydration and metamorphism that affect mantle solidus;
- advective heating by raising melts;
- deformation and erosion.

Systematic studies of heat flow variations across subduction zones have been performed in the western Pacific. Between the trench axis and the volcanic arc, where oceanic lithosphere is returned to the mantle and cold lithospheric plate subducts downward, heat flow is very low, sometimes close to zero, and lithospheric temperatures in the subducting slab are

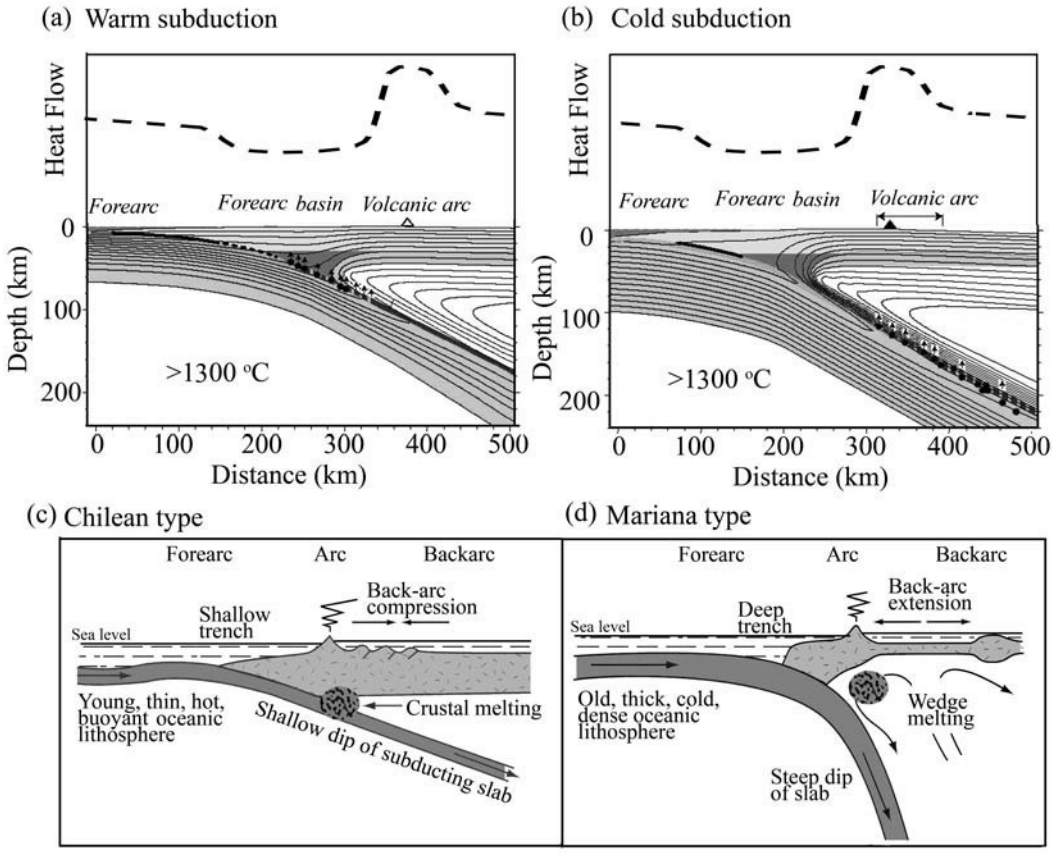

Fig. 4.27 Thermal structure of subduction zones based on theoretical constraints. (a, b) Schematic diagram of heat flow and temperature variations across warm and cold subduction zones. Oceanic plates are shown by gray shading. (c, d) Two end-member models of subduction zones based on the age of subducting slabs (modified after Uyeda and Kanamori, 1979). Thermal structures of the Chilean-type and Mariana-type subduction zones are significantly different.

depressed in comparison with adjacent oceanic mantle (Fig. 4.27). The thermal structure of the slab is asymmetric due to frictional heating at its upper surface. Melting of the mantle wedge above the subducting slab and associated volcanism result in high heat flow over the volcanic arcs behind the subduction zones due to upward advection of heat by magmas. These regions are also characterized by a large scatter in heat flow values.

Petrologic studies of mantle xenoliths from subduction zones worldwide (continent–ocean collision zones at the Kamchatka–Kurils arc, the Japan arc, and the Cascades (western USA); ocean–ocean collision zones at the Lesser Antilles (the Caribbean), the South Sandwich arc in the South Atlantic, the Izu–Bonin–Mariana arc, the Taiwan–Luzon volcanic arc, and the New Ireland island arc (in the Pacific Ocean) have revealed significant variations in their equilibration temperatures (Neumann and Simon, 2009). Most ultra-refractory harzburgites in oceanic forearcs have typically low equilibration temperatures,

in the range 950–1050 °C; however the formation of magmas of such a composition requires high degrees of partial melting. Higher equilibration temperatures (>1100 °C) are determined for xenoliths from the continental arc of SW Japan, the Mariana back-arc rift, and the South Sandwich fracture zone; in addition to higher equilibration temperatures, these xenoliths also have fertile compositions.

Data on surface heat flow, seismic velocity, and xenolith thermobarometry (Fig. 4.28; for further details see Chapter 5) were used to examine the thermal structure of continental back arcs associated with subduction zones in the circum-Pacific and Southern Europe (Currie and Hyndman, 2006). These results suggest the presence of a thin (~60 km) lithosphere with uniformly high temperatures in the shallow mantle within the back arcs that extends over lateral distances of 250 km to >900 km and spreads over the back-arc widths. These authors conclude that

> a broad hot back arc may be a fundamental characteristic of a subduction zone that places important constraints on back-arc mantle dynamics. In particular, the thermal structure predicted for slab-driven corner flow is inconsistent with the observed uniformly high back-arc temperatures.

The preferred model of Currie and Hyndman (2006) includes a vigorous thermal convection in the back-arc upper mantle that brings the heat upward from the deeper mantle; it is facilitated by low viscosities due to fluids hydration from the subducting plate (Arcay *et al*., 2006). The predicted time-scale for thermal equilibration of the lithosphere in a continental back arc is ~300 Ma after subduction termination.

Similarly to oceanic subduction zones, zones of continental subduction are associated with volcanism and high heat flow over the volcanic arcs behind subduction zones due to upward heat advection by magmas. Some subduction zones (e.g. the northern part of the Andes and the Cascades in northwestern USA) have low heat flow; in these regions either no active arc volcanism is present or volcanism has migrated back from the trench.

Under a favorable stress regime, lithosphere extension associated with subduction zones can lead to the creation of new oceanic lithosphere in zones of back-arc spreading. Sclater *et al*. (1980) have analyzed data from marginal basins where both reliable heat flow data and age estimates were available. These included the Tyrrhenian Sea, the Balearic Basin (both in the Mediterranean), the Parece Vela and the West Philippine back-arc basins (both in the western Pacific), the Coral Sea, and the Bering Sea. This analysis demonstrated that for these basins the mean heat flow is similar to the major ocean basins of similar age and follows the theoretical $\sqrt{\text{age}}$ predictions. This implies that extensional processes similar to ocean spreading are responsible for the formation of back-arc basins. However, the depth of ocean floor in marginal basins is ~1 km deeper than expected for their age, perhaps because the small size of these basins may affect the efficiency of small-scale convection and basal heating (Louden, 1980; Watanabe *et al*., 1977; Park *et al*., 1990).

Heat flow measurements in accretionary prisms remain limited. The reported values are highly variable, both within a single prism and between different prisms, and probably reflect hydrothermal circulation in a highly porous water-saturated sedimentary layer (Davis *et al*., 1990; Foucher *et al*., 1990; Yamano *et al*., 1992). Some studies, however, suggest that heat flow in accretionary prisms can be lower than average (Watanabe *et al*., 1977).

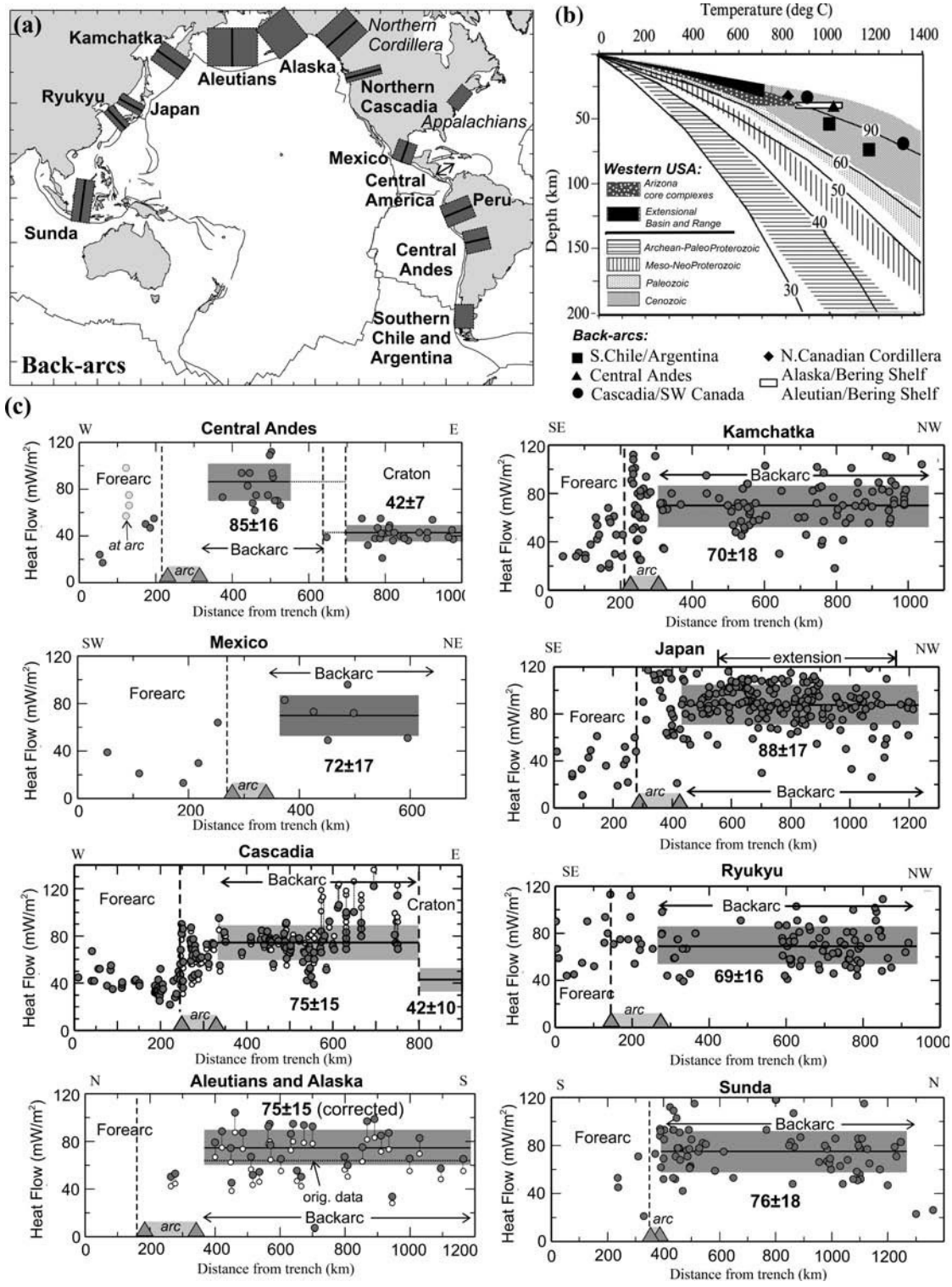

Fig. 4.28 Thermal regime of continental back-arcs. (a) Location map; (b) lithosphere temperatures in back-arcs (different symbols) based on mantle xenoliths P-T arrays plotted on top of typical continental geotherms (see Fig. 4.33 for details); the range of lithospheric temperatures in Cenozoic western USA is shown for comparison (data of Lachenbruch and Sass, 1977; Ketcham, 1996); (c) surface heat flow across different subduction zones (sources: (a) and (c) modified after Currie and Hyndman, 2006).

Ocean plateaus and hot spots

Several mechanisms have been proposed to explain the "anomalous" bathymetry in oceans (i.e. its departure from the $\sqrt{\text{age}}$ law):

(1) extra heating of the lithosphere by mantle plumes, shear heating, or vigorous secondary convection (Parsons and McKenzie, 1978; Schubert *et al*., 1976; Davies, 1988);
(2) dynamic support from pressure-driven asthenospheric flow (Phipps Morgan and Smith, 1992);
(3) isostatic uplift of regions with anomalously thick crust which produces topographic highs.

Heat flow in oceanic regions with anomalous (non-square-root of age) bathymetry has been best studied in the Pacific: in the South Pacific Superswell (located between approximately 5°–30° S and 120°–150° W), the Darwin Rise (25° N–5° S, 160° E–160° W), and the Hawaiian hotspot swell. The presence of mantle upwellings with higher than normal mantle temperatures has been proposed for these regions to explain their shallow bathymetry. In particular, the thickness of the elastic lithosphere beneath the South Pacific Superswell has been estimated to be ~10 km thinner than beneath other hotspots and beneath "normal" regions of the Pacific Ocean (Calmant *et al*., 1990).

However, the South Pacific Superswell and the Darwin Rise have normal heat flow that does not differ from other regions of the Pacific with similar lithosphere ages (Fig. 4.18) (Stein and Abbott, 1991). Similarly, heat flow measurements indicate that neither Hawaii, nor several other hotspots (Bermuda, Cape Verde, Crozet) have high heat flow (Courtney and Recq, 1986; Courtney and White, 1986; Detrick *et al*., 1986; von Herzen *et al*., 1989). Heat flow in these oceanic regions hardly differs from the values measured in ocean basins of similar ages and thus suggests that anomalous bathymetry is caused by dynamic support from the mantle, rather than by a thermal anomaly. This conclusion is supported by seismic tomography data that does not display low-velocity anomalies in the upper mantle beneath the Hawaiian Swell and the south-central Pacific (Fig. 3.99).

4.4 Thermal regime of continental lithosphere

4.4.1 Heat flow on the continents

Global observations

Data coverage of heat flow measurements on the continents still remains very uneven (Fig. 4.16). Along with densely sampled regions in Europe, North America, Asia, South Africa, and Australia, some large areas have very sparse data coverage (e.g. Arctic North America and north-central South America), while in other areas (e.g., north and central Africa, Antarctica and most of Greenland) heat flow measurements are still absent.

A large scatter of heat flow values is observed in tectonic provinces of all ages. In Precambrian regions, formed by accretion of Archean and Proterozoic terranes of different

tectonic origin, it largely reflects complex, chemically heterogeneous crustal structure, particularly with respect to the distribution of heat-producing isotopes. In Phanerozoic regions, the diversity in surface heat flow reflects both crustal heterogeneity and variations in the thermal regime of the sublithospheric mantle.

The lowest heat flow values on the continents (20–30 mW/m^2) are reported for some of the Precambrian shields (e.g. the Archean Kola-Karelian province of the Baltic Shield, the Siberian craton, the northern parts of the Superior province in Canada, and the West African craton) (e.g. Sass and Behrendt, 1980; Duchkov *et al*., 1987; Kukkonen and Joeleht, 1996; Levy *et al*., 2010). The lower boundary on surface heat flow in these regions is set by mantle heat flow if almost no radiogenic heat is generated in the crust. Assuming that average crustal heat production is as low as in mafic granulites, 0.1–0.4 W/m^3 (Tables 4.3, 4.4) (e.g., Pinet and Jaupart, 1987; Rudnick and Fountain, 1995) and the crustal thickness is 40 km, it yields ~4–16 mW/m^2 for heat flow at the Moho in regions with surface heat flow of 20 mW/m^2.

Very low values of surface heat flow have been reported from some non-cratonic settings as well, e.g. in the 1500 km-long Magnitogorsk block in the Southern Urals where surface heat flow is ~25 mW/m^2 as compared to 40–50 mW/m^2 in the East European Platform. Possible explanations of such low heat flow anomalies include paleoclimatic variations (Fig. 4.3), unusually low crustal heat production, lateral groundwater heat transfer, or anomalously low mantle heat flow (e.g. associated with the Paleozoic subduction zones as proposed for the central part of the southern Urals) (Kukkonen *et al*., 1997).

The highest heat flow on the continents (with average regional values of 120–130 mW/m^2) is observed in regions with advective heat transfer by ascending magmas, such as in Cenozoic zones of extension, lithosphere thinning, and volcanism. The upper limit on surface heat flow is apparently set by the start of crustal melting, since at this level of heat flow near-solidus temperatures are reached at the crustal base.

High heat flow associated with shear heating is expected at continental transform faults (e.g. Leloup *et al*., 1999). However, heat flow measurements around the San Andreas fault in western North America do not display systematic variations in values as a function of distance from the fault (Lachenbruch and Sass, 1980) and recent studies suggest that heat flow near the San Andreas fault is dominated by conduction. The discrepancy between theoretical predictions and observations can be attributed to a complex interlink between fluid pressure, effective normal stress, melting, frictional stability, and other processes that control frictional heat generated during fault slip (see d'Alessio *et al*., 2006 for details).

Age dependence of continental heat flow

In spite of limitations in data coverage and a large scatter in heat flow values, age dependence of continental heat flow had already been proposed in the 1960s (Lee and Uyeda, 1965). Further studies have supported this empirical relationship (Polyak and Smirnov, 1968; Vitorello and Pollack, 1980; Morgan, 1984) and shown that globally it holds, roughly, for both the crustal ages and the tectono-thermal ages of continental terranes (Fig. 4.29). Surface heat flow increases from 41 ± 11 mW/m^2 in the Archean terranes through 46 ± 15 mW/m^2 and 49 ± 16 mW/m^2 in the Mesoproterozoic and Neoproterozoic terranes, respectively, to >60 mW/m^2 in Phanerozoic regions (Pollack *et al*., 1993b; Nyblade and Pollack,

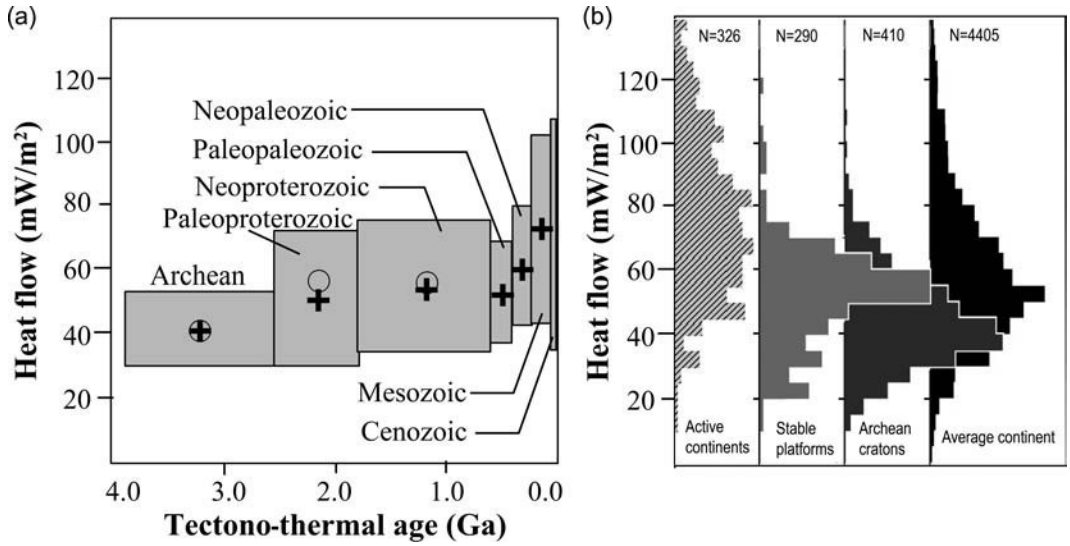

Fig. 4.29 (a) Observed continental heat flow versus tectono-thermal age (age of the last major tectonic or magmatic event at the measurement sites) averaged for seven age groups (gray boxes). Vertical dimension of boxes indicate ± one standard deviation of heat flow data from the mean (marked by crosses); horizontal dimension shows age range (Source: Morgan and Sass, 1984). A decade later update of heat flow database by all available borehole measurements at that time (Pollack *et al.*, 1993) did not change results based on the earlier data set (circles). (b) Normalized histograms for continental heat flow measurements for three types of tectonic provinces based on the 3SMAC regionalization (Nataf and Richard, 1996). N – number of heat flow measurements (source: Röhm *et al.*, 2000).

1993). This trend can roughly be approximated as $Q_o = 65–9*t$, where Q_o is the surface heat flow in mW/m^2 and t is the crustal age in Ga.

By analogy with the oceans, a simple model of a cooling thermal boundary layer has been proposed to explain the global age dependence of continental heat flow (Crough and Thompson, 1976). However, the model does not fit observations for the Precambrian terranes older than *c*. 1.5 Ga, for which it predicts nearly constant heat flow values.

At present, the age dependence of continental heat flow is commonly attributed to:

- the relaxation time of the lithosphere after a major tectono-thermal event,
- a systematic variation in crustal heat production with age,
- a systematic variation in lithospheric thickness and mantle heat flow with age,
- a combination of the above three factors.

Heat flow across the cratonic margins

As a result of the strong lateral heterogeneity of surface heat flow, the difference in heat flow values between tectonic provinces of dissimilar ages can significantly deviate from global averages. For example, in South Africa the contrast in surface heat flow between the Archean Kaapvaal craton and the surrounding Neoproterozoic mobile belts is significantly higher than suggested by global values, ~25 mW/m^2 versus ~8 mW/m^2 (Ballard and

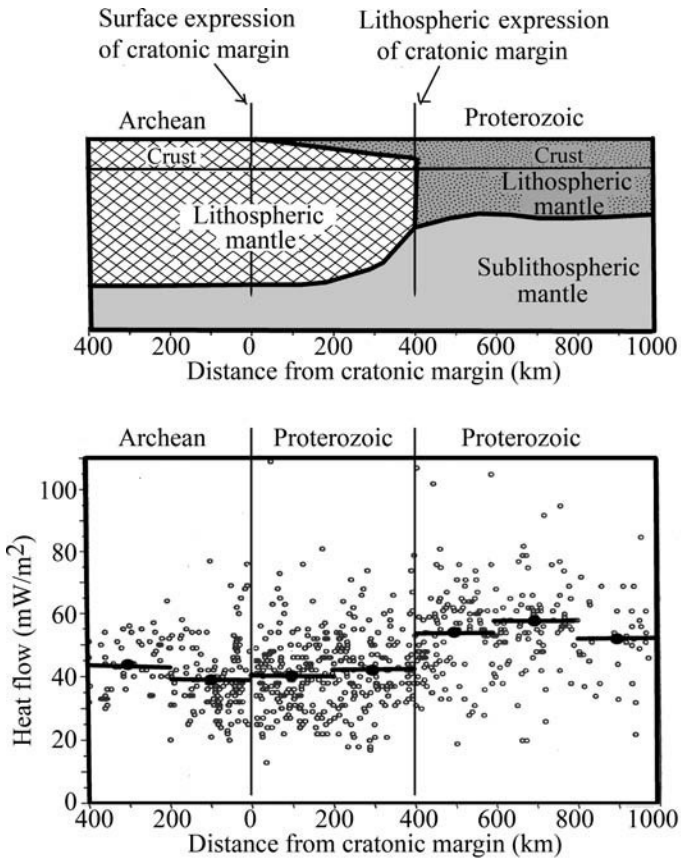

Fig. 4.30 Heat flow versus distance from the margins of Archean cratons for heat flow measurements from Precambrian terranes worldwid (lower part). Horizontal bars – averages over 200 km intervals (Sources: Nyblade and Pollack, 1993; Nyblade, 1999). The upper part displays a sketch of the corresponding lithospheric structure. Note that surface expression of cratonic margin as evidenced by geological and tectonic data may not coincide with the deep lithospheric boundary between Archean and younger terranes (see also Fig. 3.67).

Pollack, 1987). Similarly, a step-like change in surface heat flow by 20–30 mW/m^2 is observed across the Trans-European Suture Zone at the western margin of the East European craton and at the western edge of the North American craton (Fig. 4.18).

Nyblade and Pollack (1993) have analyzed worldwide data from the Precambrian terranes and argued that, although the transition from the Archean to Proterozoic terranes is marked globally by a pronounced increase in surface heat flow, the change in heat flow pattern does not necessarily correspond to the surface expression of the cratonic margin (Fig. 4.30). A regional pattern of decreased heat flow in Proterozoic terranes located within a 200–400 km-wide zone along the margins of the Archean cratons has been recognized at some Archean–Proterozoic boundaries: at the western margin of the Kalahari craton in South Africa (Ballard *et al*., 1987), at the eastern margin of the Superior province in North America, and at the south-western margin of the Baltic Shield in Europe (Nyblade and Pollack, 1993).

Contrary to this, Jaupart and Mareschal (1999) do not observe any clear geographic trend at the eastern margin of the Canadian Shield, where in some regions (e.g. in the Abitibi province) heat flow increases from the craton margin to its center, and surface heat flow in the late Proterozoic Grenville province is the same as in the Archean terranes of the Superior province and in the early Proterozoic Trans-Hudson orogen (see Fig. 3.66 for a location map). Based on the Canadian heat flow observations, these authors argue that the regional heat flow pattern at the cratonic margins in South Africa solely reflects higher radioactivity of crustal rocks in the Proterozoic terranes. In contrast, Nyblade and Pollack (1993) propose that overthrusting of the Proterozoic crust onto the Archean lithosphere can explain low heat flow outside the margins of the Archean cratons (Fig. 4.30). This hypothesis is supported by seismic data of the LITHOPROBE transects across the Canadian Shield, which indicate that the boundaries between the terranes of different ages are not vertical, and that the age of the crust and the underlying mantle can be significantly different within a 100–200 km-wide zone along these boundaries. In particular, the middle Proterozoic crust of the Grenville province overthrusts the Archean mantle of the Superior province (Fig. 3.67), leading to a uniform surface and mantle heat flow across the lithospheric terranes of *apparently* different ages at the Superior–Grenville boundary. Additionally, atypically low heat flow observed in the Grenville province can be attributed to the time delay of thermal front propagation associated with the passage of the Grenville province over the Great Meteor and Monteregian hotspots at 180 Ma and 100 Ma, respectively (Morgan, 1983; Nyblade, 1999). For a lithospheric thickness of ~150–200 km, the time required for a thermal perturbation to reach the surface (eq. 4.18) and become seen in surface heat flow is comparable with the age of the hotspots. This observation is supported by seismic tomography models (which provide "snapshots" of the mantle in contrast to the "inertial" heat flow image) that do not reveal the presence of a deep lithospheric keel beneath the Grenville province (e.g. van der Lee and Nolet, 1997a), in contrast with conclusions reached by Jaupart and Mareschal (1999).

4.4.2 Continental geotherms

Time-scale of thermal equilibration

Surface heat flow variations in continental regions can be interpreted in terms of the thermal structure of the continental lithosphere (Artemieva and Mooney, 2001). In stable continents, the thermal structure of the lithosphere can be approximated by the steady-state solution of the thermal conductivity equation. Note, however, that due to secular cooling of the Earth combined with radioactive decay of heat-producing elements, any steady-state thermal constraint is an approximation for the real Earth (Michaut and Jaupart, 2007) (see Section 4.1.4 for details).

The steady-state solution of the thermal conductivity equation is applicable to regions that have not experienced a major tectonic event for several hundred million years (Fig. 4.31). The exact time depends on the characteristic time of thermal equilibration which defines the time delay for a thermal front associated with a thermal perturbation at depth z to reach the surface and to become reflected in the surface heat flow (eq. 4.18). Figure 4.31 shows the estimated time-scale for the thermal diffusivity value widely used in the literature, $\chi = 10^{-6}$ $m^2/s \sim 31.5\ km^2/Ma$. This implies that the steady-state approximation is valid for significant

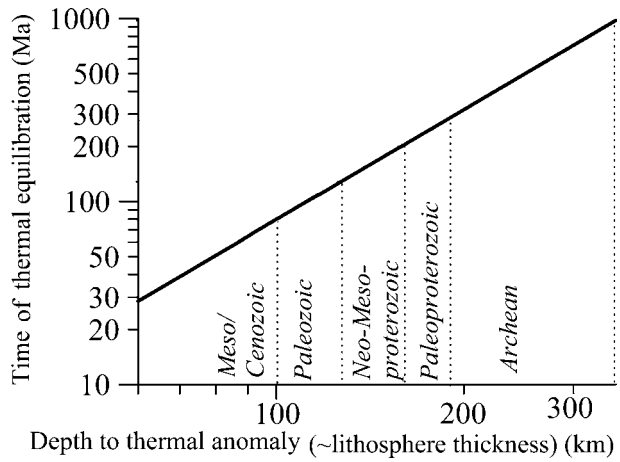

Fig. 4.31 Time-scale of thermal equilibration in the upper mantle (note logarithmic scales of the axes). The plot shows the minimum time required for a thermal perturbation in the upper mantle (at the base of the lithosphere) to be conductively transferred to the surface to become reflected in surface heat flow. Conductive heat flow measured in Cenozoic regions does not reflect the present thermal regime of the mantle beneath these regions.

parts of the continents which include old platforms (commonly with shelves) and many regions of Paleozoic tectono-magmatic activity where thermal equilibrium is expected to be re-established. In younger regions (<250 Ma), surface heat flow measured in boreholes may reflect the past thermal regime, but not the present thermal state of the mantle since, due to a slow rate of conductive heat transfer, thermal perturbation in the mantle has not yet reached the surface and is not yet reflected in surface heat flow. The lithosphere of these tectonically young regions is characterized by a transient thermal regime and the steady-state thermal approximation is invalid there.

The transient response of the lithosphere to a mantle thermal anomaly can be further illustrated by the passage of a hotspot underneath a continental lithosphere. The upper limit for a temperature anomaly associated with a plume is ~ 300 °C, compared to the ambient mantle temperature (e.g. McKenzie *et al*., 1974; Gurnis, 1988; Schilling, 1991; also Fig. 4.39). An abrupt temperature increase, by 300 °C, at the lithospheric base causes a perturbation of its thermal regime and an increase in surface heat flow (Fig. 4.32). However, in a thick cratonic lithosphere this effect cannot be quickly detected. For example, if the cratonic lithosphere of the Grenville province passed over the Great Meteor and Monteregian hotspots at 180 Ma and 100 Ma, respectively (Morgan, 1983), the corresponding present-day surface heat flow increase could only be 5–8 mW/m^2, i.e. close to the uncertainty limit associated with heat flow measurements (Nyblade, 1999).

Conductive geotherms for stable continents

The temperature distribution in stable (i.e. in thermal equilibrium) continental lithosphere can be calculated from the thermal conductivity equation,

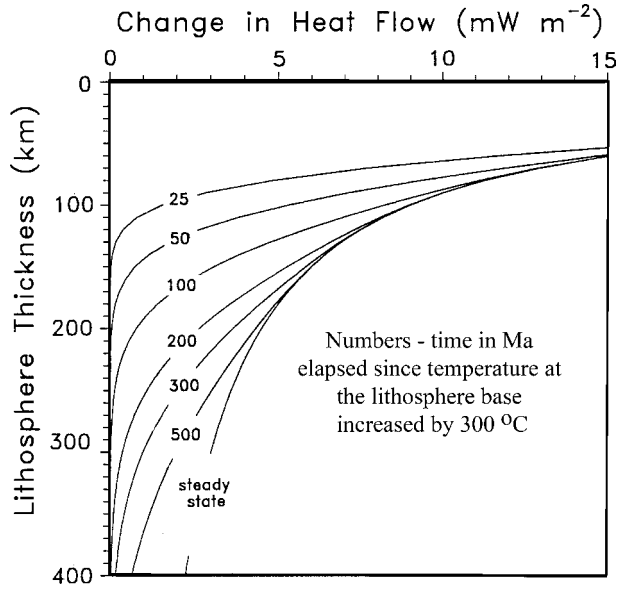

Fig. 4.32 Changes in surface heat flow associated with a step-like 300 °C temperature increase at the lithospheric base. Vertical axis – lithosphere thickness prior to thermal perturbation; numbers on the curves – elapsed time (in Ma) (after Nyblade, 1999).

$$\text{div}\ (\lambda(x,y,z)\ \text{grad}T) + A(x,y,z) = \rho c(x,y,z)\partial T/\partial t \tag{4.35a}$$

which in the steady-state case takes the form:

$$\text{div}\ (\lambda(x,y,z)\ \text{grad}T) + A(x,y,z) = 0, \tag{4.35b}$$

where T is temperature, $\lambda(x,y,z)$ is the thermal conductivity, and $A(x,y,z)$ is the radiogenic heat production. Boundary conditions at the top and the bottom include: (i) fixed temperature at the surface and (ii) either fixed *temperature* or fixed *heat flow* at the base. Additional boundary conditions (such as the symmetry of the temperature field) are set at the vertical boundaries.

The fact that the boundary conditions at the base of the lithospheric plate are unknown creates a fundamental problem for solution of the boundary problem (further discussed in the next subsection): the problem is ill-posed unless these conditions are assessed from independent data. The situation is similar to that of the oceanic thermal models, where the boundary condition at the base of the lithospheric plate on constant heat flow or constant temperature leads to two classes of models, the cooling half-space and the plate model, respectively.

An independent constraint on *temperature* at the lithospheric base can be derived, for example, from data on mantle melting temperature (solidus), while surface heat flow data $Q_o(x,y,0)$ provide a constraint on *heat flow* variations in the mantle. When the boundary condition at the base is known, the solution of Eq. (4.35b) is defined by lateral and vertical distributions of thermal parameters (radioactive heat production and thermal conductivity) within the lithosphere.

In many cases, the 1D approach to calculation of continental geotherms (temperature–depth profiles) is used since small-scale lateral variations of thermal conductivity and radiogenic heat production, in particular in the crust, are poorly known. In the 1D case, the temperature $T(z)$ at a depth z can be extrapolated from the surface temperature T_o and surface heat flow Q_o as:

$$T(z) = T_o + zQ_o/\lambda(z) - z^2A(z)/2\lambda(z). \quad (4.36)$$

A family of conductive geotherms was first calculated by Pollack and Chapman (1977). Because of the simplicity of model assumptions, this family of conductive geotherms, commonly referred to as "reference geotherms", is widely used in literature for comparisons with other temperature estimates (Fig. 4.33). Table 4.8 summarizes the assumptions on which these geotherms are based. In short, the major assumptions are:

- a steady-state thermal regime regardless of the surface heat flow value;
- the concept of heat flow provinces (Section 4.1.4);
- generation of 40% of surface heat flow in the upper 8 km-thick crustal layer ("*D*-layer"), with the remaining 60% coming from below (and resulting from mid–lower crustal radioactivity, mantle radioactivity, and heat flow from the mantle);
- a globally uniform crustal thickness of 40 km;
- constant thermal conductivity of 2.5 W/m/K throughout the entire crust.

Data on surface heat flow variations together with data on the crustal structure and geological and tectonic information (interpreted in terms of lateral and vertical variations of thermal properties of crustal and mantle rocks) allow for calculation of *regional* continental geotherms. The surface heat flow database of Pollack *et al*. (1993) updated for newer borehole measurements formed the basis for a worldwide thermal model of the continental lithosphere (Artemieva and Mooney, 2001). It was constrained only by the most reliable heat flow values, based on quality criteria discussed by Pollack *et al*. (1993). In particular, heat flow data from shallow boreholes potentially affected by ground-water circulation and data obtained by non-conventional methods were excluded from the analysis. Additionally, the original heat flow data were analyzed, as far as possible, for potential regional perturbations and included paleoclimatic corrections to surface heat flow data due to climatic changes, such as Pleistocene glaciations (which in the northernmost areas can be as large as 15–20 mW/m^2, Fig. 4.3). The calculations were carried out for about 300 blocks with an area of $1° \times 1°$ to $5° \times 5°$ in size, where individual heat flow measurements in closely spaced boreholes were averaged for lithospheric blocks with similar crustal structure, ages, and tectonic setting.

In spite of significant differences between model assumptions (see Table 4.8 for details), conductive geotherms calculated globally from regional crustal and heat flow data in stable continental regions (Artemieva and Mooney, 2001) agree well with the family of reference continental geotherms of Pollack and Chapman (1977). Lithospheric temperatures fall between the reference geotherms for 30 and 40 mW/m^2 in the Archean–Paleoproterozoic terranes, and are close to the reference geotherms for 50 and 60 mW/m^2 in the Meso-Neoproterozoic and Paleozoic terranes (Fig. 4.33). The analysis also suggests that in the Precambrian terranes only ~30% of surface heat flow is generated in the upper crustal layer

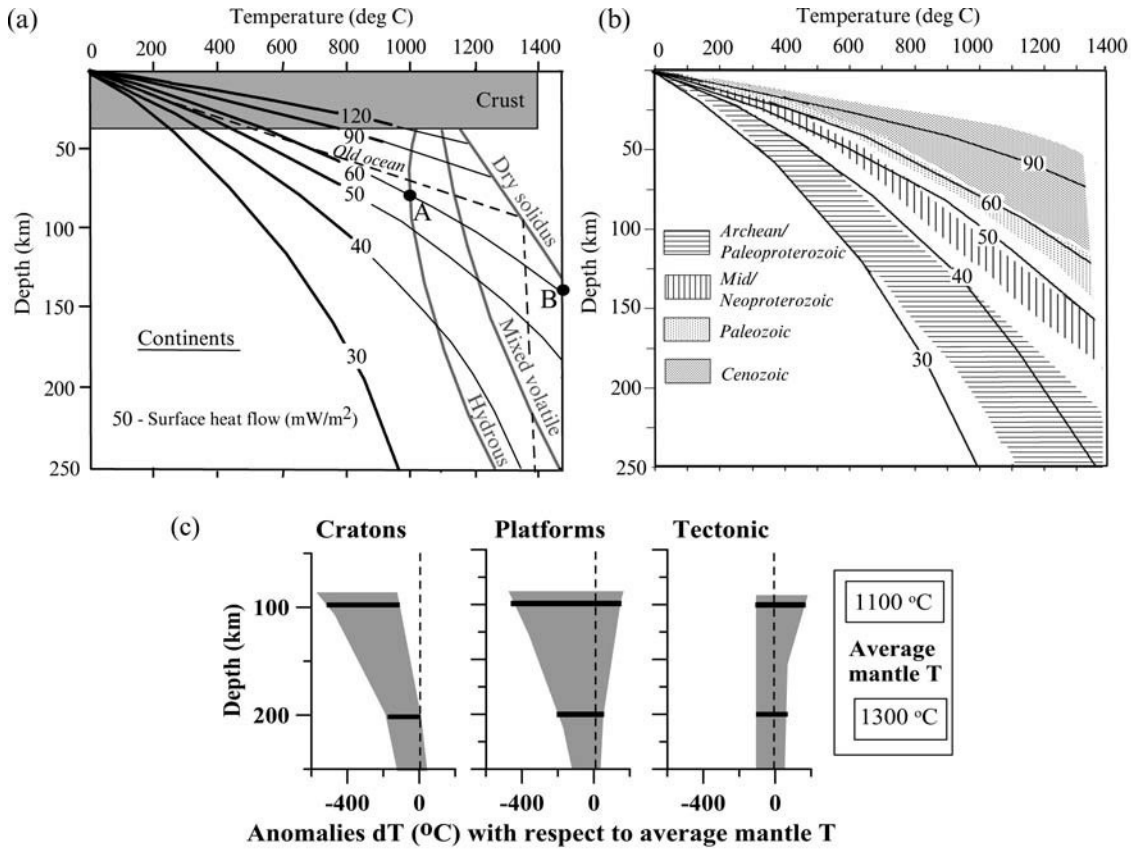

Fig. 4.33 Continental conductive geotherms. (a) A family of conductive geotherms versus surface heat flow (Source: Pollack and Chapman, 1977; Pollack *et al*., 1993). This set of geotherms is commonly referred to in the literature as "reference geotherms". Thin lines at higher temperatures indicate that non-conductive heat transfer can be important in the lower parts of the lithosphere. For comparison, dashed line shows a typical old ocean geotherm which corresponds to surface heat flow of ~50 mW/m^2. For the same surface heat flow, at any given depth continental temperatures are lower than oceanic due to radioactive heat generated in the continental crust. Gray lines – peridotite solidi for different volatile compositions. Note that, depending on the mantle composition, the thickness of thermal lithosphere defined by the intersection of a geotherm with mantle solidus, can be significantly different. For a 60 mW/m^2 reference geotherm, lithosphere thickness is ~80 km in the case of hydrous peridotite (A) and ~140 km in the case of dry peridotite (B). (b) Typical geotherms for continental regions of different ages constrained by heat flow data for stable continents and by xenolith data for active regions (see Table 4.8 for details, after Artemieva and Mooney, 2001). Thin lines with numbers – reference geotherms (Pollack and Chapman, 1977) as in (a) for different surface heat flow values. (c) Typical ranges of temperature differences between cratons, platforms, and tectonically active regions as compared to the average mantle (for average mantle temperatures of 1100 °C at a 100 km depth and 1300 °C at 200 km depth).

Table 4.8 Thermal parameters used in steady-state continental thermal models

	Pollack and Chapman, 1977	Rudnick *et al*., 1998	Artemieva and Mooney, 2001
Crustal thickness	40 km	41 km	Variable, based on regional seismic data*
Heat production in sediments	Ignored	Ignored	0.7–1.3 μW/m^3 (based on regional lab data)
Heat production in the upper crust	40% of Q_o is generated in the upper D-layer (D = 8 km); this yields mean heat production in the D-layer: $A_D = 0.4\ Q_o/D$	14 km thick with 60% of A_{cr} (yields mean value of 0.7–1.2 μW/m^3)	0.4–6.7 μW/m^3 (based on regional lab data), 0.4–0.5 μW/m^3 at $z > 12$ km
Heat production in the middle-lower crust	0.25 μW/m^3	Middle: 13 km thick with 34% of A_{cr} (mean 0.4–0.75 μW/m^3) Lower: 14 km thick with 6% of A_{cr} (mean 0.07–0.12 μW/m^3)	Middle: 0.2–0.4 μW/m^3, Lower: 0.1 μW/m^3
Bulk crustal heat production, A_{cr}	Not assumed *a priori*, $0.01Q_o$+0.2 μW/m^3 (yields 0.5–1.4 μW/m^3 for Q_o in the range 30–120 mW/m^2)	0.4–0.7 μW/m^3; preferred values: 0.4–0.5 μW/m^3 for Q_o = 40 mW/m^2 and 0.7 μW/m^3 for Q_o=50 mW/m^2	Not assumed *a priori*, 0.3–1.0 μW/m^3
Mantle heat production	0.01 μW/m^3 at $z < 120$ km, 0.0084 μW/m^3 at $z > 120$ km	0.02–0.10 μW/m^3; preferred value 0.03 μW/m^3	0.01 μW/m^3 if $Vp < 8.3$ km/s, 0.004 μW/m^3 if $Vp > 8.3$ km/s
Thermal conductivity in the upper crust	2.5 W/m/K at $T < 500$ °C with $k(T)$** at $T > 500$ °C	2.6–2.7 W/m/K	Sediments: 0.5–4.0 W/m/K, Upper: $k(T)$** in the range 2.5–3.0 W/m/K
Thermal conductivity in the lower crust	$k(T)$** at $T > 500$ °C	2.6–2.7 W/m/K	Middle: 2.0–2.5 W/m/K, Lower: 2.0 W/m/K
Thermal conductivity in the mantle	–	$k(T)$**	4.0 W/m/K
Treatment of high-heat flow regions	Assumed to be steady state	Not considered	Excluded from steady-state modeling; $T(z)$ based on xenolith data and transient models

* Subdivision of the crust into the upper, middle, and lower layers is based on Vp seismic velocities with the tops of the layers defined by 5.6 km/s, 6.4 km/s, and 6.8 km/s, respectively.
** Based on Schatz and Simmons (1972).
A_{cr} – bulk crustal heat production.

enriched by radiogenic elements, and the contribution of this layer increases in the younger crust to ~40% as assumed by Pollack and Chapman (1977).

Typical continental geotherms constrained by heat flow data for stable continents and by xenolith data for active regions indicate that the temperature difference between cratons, platforms, and tectonically active regions as compared to the average mantle is, correspondingly, -310 ± 200 °C, -160 ± 260 °C, and $+30 \pm 130$ °C at 100 km depth and *c.* -90 ± 70 °C, -80 ± 100 °C, and -30 ± 70 °C at 200 km depth (for average mantle temperatures of 1100 °C at a 100 km depth and 1300 °C at a 200 km depth; the uncertainties indicate standard deviations of the calculated geotherms rather than the true uncertainties of the modeling) (Fig. 4.33c). These values are in a general agreement with mantle temperatures calculated from joint interpretation of gravity and tomography models (Deschamps *et al.*, 2002).

Uncertainties in conductive geotherms

Because of the large uncertainty in the lateral and vertical distribution of thermal parameters in the lithosphere, a large set of conductive geotherms can be produced for any surface heat flow value. This makes it difficult to assess the accuracy of estimates of continental temperatures and lithospheric thermal thickness. Sensitivity analyses indicate that for a typical range of possible variations of heat production and thermal conductivity, continental temperatures are constrained with an accuracy of ~50–100 °C at a 50 km depth and ~100–150 °C at a 100–150 km depth (see Table 4.9 for details).

One of the possibilities for testing the accuracy of continental geotherms constrained by surface heat flow is to compare them with independent data, such as xenolith P–T arrays (see Chapter 5 for details and a discussion of the uncertainties associated with xenolith geotherms). For example, Rudnick *et al.* (1998) used mantle xenolith data from the Archean cratons of South Africa, Tanzania, and Siberia together with typical values of surface heat

Table 4.9 Sensitivity analysis for steady-state conductive continental geotherms

Change of model parameter	Temperature at $z = 50$ km	Temperature at $z = 100$ km	Lithospheric thickness	Mantle heat flow
Average crustal heat production 20% higher	9–13% (50–70 °C) lower	11–16% (100–130 °C) lower	15–30% (25–80 km) greater	8–10% (4–5 mW/m^2) lower
Average crustal conductivity 10% higher	8% (30–60 °C) lower	5% (30–60 °C) lower	3–6% (5–10 km) greater	No effect
Mantle conductivity 17% lower	2–3% (10–15 °C) higher	8% (50–80 °C) higher	3–8% (10–15 km) lower	No effect
Surface heat flow 5% higher	7–8% (30–50 °C) higher	8–9% (50–90 °C) higher	10% (10–25 km) lower	2–3% (2–3 mW/m^2) higher

(from Artemieva and Mooney, 2001; the model parameters are specified in Table 4.8)

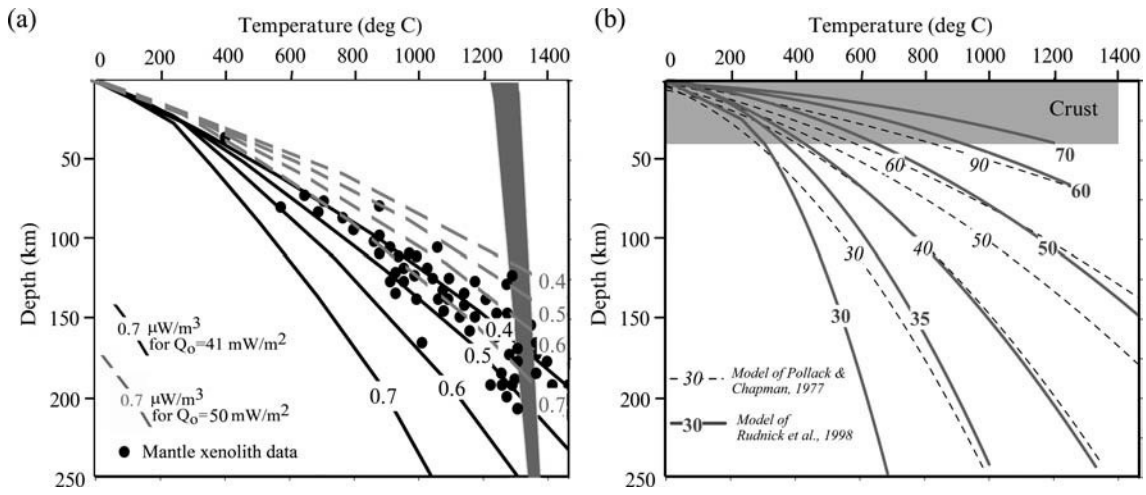

Fig. 4.34 Continental conductive geotherms calibrated by xenolith data from the Archean cratons (see Table 4.8 for model details, source: Rudnick *et al*., 1998). (a) Geotherms corresponding to surface heat flow of 41 mW/m^2 (black lines) and 50 mW/m^2 (gray dashed lines) for a variety of bulk crustal compositions (with bulk crustal heat production of 0.4–0.7 μW/m^3, numbers on the curves) for mantle heat production of 0.03μW/m^3. Gray shading – mantle adiabat. (b) The same as in (a) but calculated for various values of surface heat flow (numbers on the curves) assuming bulk crustal heat production of 0.5 μW/m^3 (solid lines). Dashed lines – reference geotherms of Pollack and Chapman (1977). Note that two families of conductive geotherms agree only for a heat flow ~40 mW/m^2 (typical for Archean regions) that was used for calibration of crustal heat production in (a).

flow in the Archean regions to calibrate bulk crustal heat production and heat production in the lithospheric mantle. The determined values of thermal parameters were used to constrain the cratonic geotherms (Fig. 4.34). These geotherms match closely with conductive geotherms for regions with low surface heat flow (<50 mW/m^2) typical for the cratonic regions. Realistic geotherms (chosen to fit xenolith P–T arrays) require low, but non-zero heat production in the lithospheric mantle and low bulk crustal heat production which corresponds to the heat production of average granulites (Fig. 4.8). The heat production values preferred by Rudnick *et al*. (1998) are 0.4–0.5 μW/m^3 for the Archean crust and 0.03 μW/m^3 for the Archean lithospheric mantle:

- For higher values of bulk crustal heat production, geotherms do not intersect the mantle adiabat.
- Similarly, in the case that all surface heat flow results from crustal radioactivity sources, the temperature below the Moho is constant and never intersects the mantle adiabat.
- The shape of the actual distribution of heat production in the crust has a minor effect on the Moho temperature and no effect on mantle temperatures.
- In the case of no radiogenic sources in the crust, the calculated geotherms become similar to geotherms for old oceans.
- If, however, xenolith P–T arrays reflect the transient thermal regime in the cratonic lithosphere associated with magmatism, bulk heat production in the Archean crust can

be higher than the preferred values and the lithospheric thickness can be greater than predicted from the preferred heat production values.

An extension of the model of Rudnick *et al*. (1998) beyond the Archean crust, to continental regions with higher heat flow (>50 mW/m^2), displays a large discrepancy compared with the conductive geotherms of Pollack and Chapman (1977), and thus implies that bulk heat production in the post-Archean crust and the lithospheric mantle can be significantly higher than the values preferred by Rudnick and co-authors (Fig. 4.34). The discrepancy stems from the fact that, in the approach of Pollack and Chapman (1977), bulk crustal heat production A_{cr} is inexplicitly scaled by surface heat flow values Q_o as $A_{cr} = 0.01\,Q_o + 0.2$ μW/m^3. For the range of considered surface heat flow values (30–120 mW/m^2) this yields A_{cr} ranging from 0.5 to 1.4 μW/m^3, while the preferred values of Rudnick and co-authors are fixed at 0.4–0.5 μW/m^3. From the other side, the formal solution of the steady-state thermal conductivity problem for regions with high heat flow as calculated by Pollack and Chapman (1977) may be misleading since these regions are likely to have a transient thermal regime of the lithosphere.

Mantle heat flow and mechanisms of surface heat flow variations in stable continents

The thermal conductivity boundary problem (Eq. 4.36) can be solved with conditions at the bottom boundary either for a constant heat flux (e.g. Jaupart and Mareschal, 1999), or for a constant temperature (e.g. Pollack and Chapman, 1977; Artemieva and Mooney, 2001). For the oceans, there are no obvious physical mechanisms to keep a constant heat flux at the plate bottom, while small variations in oceanic crustal thickness suggest that temperature variations at the base of the lithospheric plate are small (~15 °C) (McKenzie *et al*., 2005). The situation is more complicated for the continental lithosphere. Assuming that the average potential temperature beneath the oceans and the continents is kept constant by large-scale mantle circulation, one should expect that a constant temperature at the lithospheric base (equal or close to the mantle potential temperature) rather than a constant heat flux from the mantle is the more likely situation beneath the continents. Because there are two options for the boundary conditions at the lithospheric base, lateral variations in surface heat flow of stable continents can be attributed to two end-member models with heat flow variations resulting primarily from:

- differences in crustal heat production (the case of a constant heat flux at the base) (e.g. Morgan, 1984; Jaupart and Mareschal, 1999), or
- lithospheric thickness (and thus mantle heat flow) variations (e.g. Ballard and Pollack, 1987; Nyblade and Pollack, 1993a).

Most of the practical approaches to calculation of lithospheric geotherms account for both of these effects (e.g. Artemieva and Mooney, 2001). Although the effect of thermal conductivity variations within the lithosphere on continental geotherms has gained some attention recently, its contribution to surface heat flow variations is insignificant (Levy *et al*., 2010; see discussion in Section 4.1.2).

Precambrian regions with a steady-state thermal regime provide natural test sites for examining the relative contributions of crustal heat production and mantle heat flow in surface heat flow variations. In particular, worldwide analyses of surface heat flow variations across the Archean–Proterozoic boundaries indicate some heat flow increase from older to younger crust (e.g. Figs. 4.29, 4.30), while some geochemical evidence suggests that bulk crustal heat production in the Archean crust can be lower than in the Proterozoic crust (Table 4.4 and Section 4.1.3). A number of possibilities have been proposed to explain this possible age dependence of bulk crustal heat production:

(1) greater erosion of the Archean crust;
(2) selective survival of the Archean crust only with low crustal heat production;
(3) enrichment of the Proterozoic upper crust by radioactive isotopes during orogenic events;
(4) secular changes in crust-forming processes.

Although lower heat flow together with (possibly) lower bulk crustal heat production in the Archean terranes suggests that crustal heat production plays an important role in surface heat flow variations, other lines of evidence suggest a complex interplay between crustal heat production and mantle heat flow contributions to surface heat flow. Regional studies indicate that either one or the other mechanism can dominate on a regional scale. For example, thermal models in which surface heat flow variations are explained entirely by variations in crustal radioactivity cannot satisfy xenolith geotherms for South Africa, and variations in lithospheric thickness should be the principal factor controlling the surface heat flow pattern in the region (Nyblade and Pollack, 1993a,c). Ballard and Pollack (1987) have proposed that a thick lithosphere of the Archean Kalahari craton diverts mantle heat sideways to the surrounding Proterozoic mobile belts and further complicates the pattern of regional surface heat flow variations. This hypothesis is supported by recent mantle convection models that have focused on the insulating effect of continents. They demonstrate the similarity between trends in surface and mantle heat flow variations, interpreted as evidence that variations in crustal radioactivity are not the major factor controlling surface heat flow variations (Cooper *et al*., 2006).

In contrast, detailed analysis of the crustal structure and heat flow data in the Canadian Shield and in the South African craton (Jaupart and Mareschal, 1999) was used to argue that most surface heat flow variations in these provinces can be attributed to heterogeneous crustal heat production. This and similar studies suggest that mantle heat flow in the Canadian Shield apparently has a uniform value through Precambrian terranes of different ages (~12 mW/m^2), with no evidence for a diversion of mantle heat from the Archean terranes to younger adjacent regions (Lenardic *et al*., 2000) (Tables 4.10, 4.11). Indeed, the Canadian Shield is composed of a large number of small (sometimes less than 50–100 km across) distinct crustal terranes, which amalgamated at 2.72–2.69 Ga. Strong crustal heterogeneity leads to significant lateral large-amplitude surface heat flow variations with short wavelength (commonly less than 100 km), suggesting their crustal origin (Fig. 4.35).

However, with new, very low, heat flow data being accumulated in the northern parts of the Superior province (not shown in Table 4.10), the emerging picture is becoming more complicated. Very low values of surface heat flow (<30 mW/m^2) reported for large areas of the Siberian craton, some parts of the Baltic Shield, and the

Table 4.10 Heat flow in the main Precambrian–Paleozoic provinces of North America

Tectonic province	Tectono-thermal age (Ga)	Average heat flow (mW/m^2)
Superior province	2.7	42 ± 10
Trans-Hudson Orogen	1.9	42 ± 11
Grenville province	1.0	41 ± 11
Appalachians	0.4	57 ± 13

(source: Jaupart and Mareschal, 1999)

Table 4.11 Mantle heat flow in Precambrian and Paleozoic regions

Region	Moho heat flow (mW/m^2)*	Source**
Archean–Mesoproterozoic cratons	**10–30**	AM01
Canadian Shield (Superior province and	10–15	JM99
Trans-Hudson Orogen)	12–13	J98
	12–18	L10
	13–18 (Kapuskasing)	A87
	15–18	AM01
	18–25	RN99
Siberian craton (all)	10–22	AM01
Daldyn–Alakit terrane	10–15	AM01
- ″ -	10	MK05
Anabar Shield (Siberia)	~20	AM01
West African craton	10–15	AM01
Lewisian (Scotland)	11–16	WT84
Slave craton	12.4	MK05
Baltic Shield	12–15	AM01
Russian Platform	13–22	AM01
Kaapvaal craton	5–12 (Vredefort)	N91
	17	JM99
	17–25, best fit 18	RN99
	19–20	AM01
Western Australia	18–23	AM01
Central Australia	25–30	AM01
India	17–30	AM01
Sveco-Norwegian (Baltic Shield)	20–21	PJ87
South American craton	25–30	AM01
Northern China	25–30	AM01
Neoproterozoic–Paleozoic	**25–50**	AM01

* Heat flow at the base of the lithosphere is the same as at the Moho for heat production in the lithospheric mantle $A = 0\ \mu W/m^3$ and ~1–3 mW/m^2 less than at the Moho for $A = 0.01\ \mu W/m^3$.

** References: A87 = Ashwal *et al*., 1987; AM01 = Artemieva and Mooney, 1999; 2001; J98 = Jaupart *et al*., 1998; JM99 = Jaupart and Mareschal, 1999; L10 = Levy *et al*., 2010; MK05 = McKenzie *et al*., 2005; N81 = Nicolaysen *et al*., 1981; PJ87 = Pinet and Jaupart, 1987; RN99 = Rudnick and Nyblade, 1999; WT84 = Weaver and Tarney, 1984.

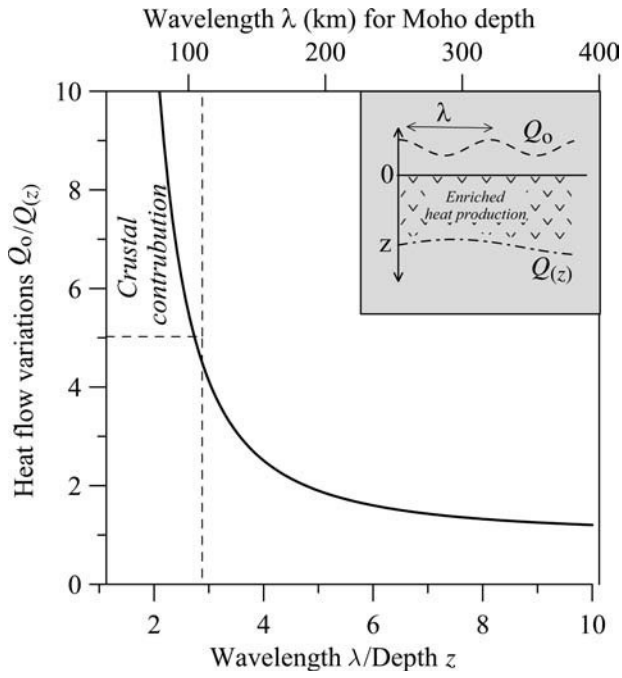

Fig. 4.35 The ratio between the magnitude of heat flow anomalies at the surface and at depth as a function of the wavelength of surface heat flow variations and depth to the anomaly (assumed to be produced by laterally sinusoidal distribution of heat production). To distinguish between surface heat flow anomalies of shallow and deep origin, as a rule of thumb, Jaupart and Mareschal (1999) suggest use of the wavelength of surface heat flow variations $\lambda > 2.8z$, which produces surface heat flow anomalies of magnitude 5 times higher than at depth z. In such an interpretation, surface heat flow anomalies with $\lambda<110$ km are generated within the crust (for crustal thickness 40 km), while heat flow anomalies at the base of the cratonic lithosphere (at ~215 km depth) produce surface heat flow variations with $\lambda > 600$ km.

northern parts of the Canadian Shield require low mantle heat flow and, as a consequence, large lithospheric thickness in these regions (Fig. 4.36, Table 4.11) (Artemieva and Mooney, 2001; Levy *et al*., 2010). In particular, a 6 mW/m^2 change in mantle heat flow in cold cratonic regions can be associated with variations in lithospheric thickness of ~100 km (Levy *et al*., 2010) (Fig. 4.37). A simple estimate shows that heat flow at the Moho, Q_M, cannot be less than 10–12 mW/m^2 even in regions with a very low surface heat flow. For purely conductive heat transfer in the lithospheric mantle,

$$Q_M = \lambda[T_{TBL} - T_M]/[z_{TBL} - z_M] \quad (4.37)$$

where λ is the thermal conductivity of the lithospheric mantle, T and z are temperature and depth, respectively, and the indexes TBL and M refer to the base of the lithosphere and the Moho. Assuming a crustal thickness of 40 km, the lithospheric mantle extending

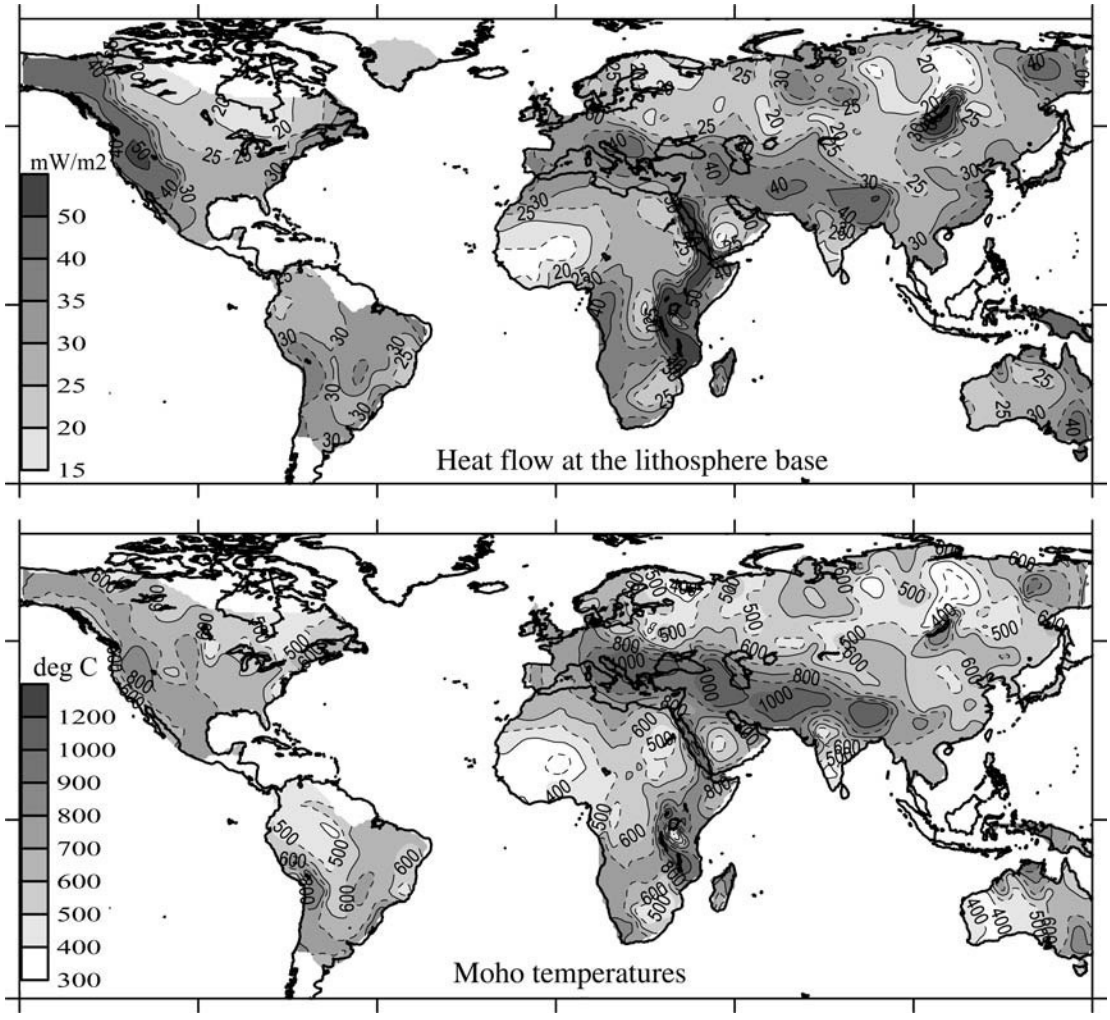

Fig. 4.36 Thermal regime of continental lithosphere constrained by heat flow data (Source: Artemieva and Mooney, 1999; 2001). The maps are constrained by a 15 deg × 15 deg interpolation; data coverage is shown in Fig. 4.16. (a) Mantle heat flow at the base of the lithosphere; (b) temperatures at the Moho (or at 40 km depth in regions where crustal thickness is poorly known).

down to the transition zone (410 km depth), mantle potential temperature of 1350 °C at the base of the lithosphere, and Moho temperature along a 30 mW/m^2 conductive reference geotherm, yields $Q_M \sim 11.5$ mW/m^2 for $\lambda = 4$ W/m/K and $Q_M \sim 10$ mW/m^2 for $\lambda = 3.5$ W/m/K.

Numerical models of mantle convection with floating continents (Lenardic and Moresi, 2001) resolve an apparent contradiction between two competing models of lithospheric thermal structure (controlled primarily by crustal heat production or by mantle heat flow variations) and demonstrate that they are the end-member solutions for layered and whole-

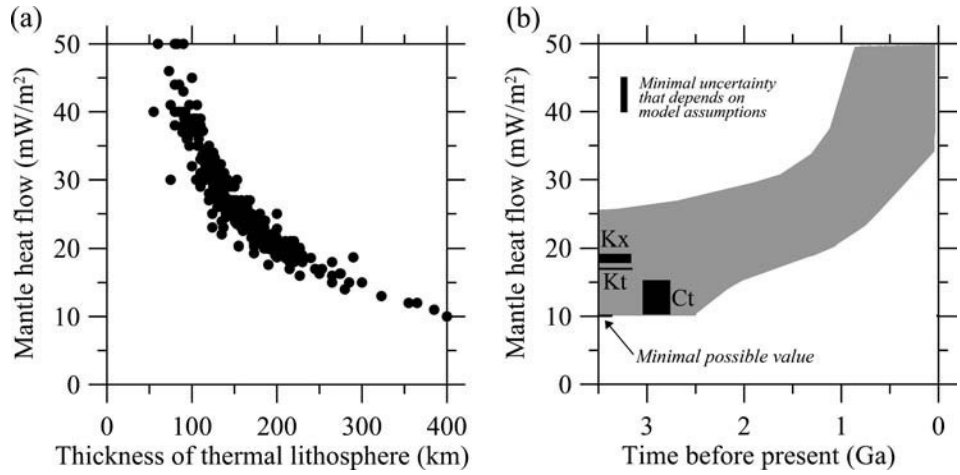

Fig. 4.37 Typical variations of mantle heat flow with lithospheric thickness (a) and with tectono-thermal age (b). Dots in (a) and gray shading in (b) correspond to the values calculated in global steady-state modeling of surface heat flow data (Source: Artemieva and Mooney, 1999; 2001). Other estimates of mantle heat flow: Kaapvaal craton (Kt) and Canadian Shield (Ct) thermal model (Jaupart and Mareschal (1999); Kaapvaal xenolith data (Rudnick and Nyblade, 1999). There is a significant uncertainty associated with the assumed values of thermal parameters. In particular, Jaupart and Mareschal (1999) assume four times higher heat production in the lower crust, which results in systematically lower values of mantle heat flow (on average, by 4–5 mW/m^2).

mantle convection models: the thermal resistance of the convecting mantle depends on the thickness of the upper thermal boundary layer and the system has a compensation mechanism for the former by adjusting the thickness of the latter. In the case of layered convection (i.e. thin convecting layer), the effect of lithospheric thickness on mantle heat flow is strong and large surface heat flow variations can be explained by small variations in relative lithospheric thickness (i.e. in the ratio of TBL to system depth). On the contrary, in case of whole mantle convection the dependence of mantle heat flow on lithospheric thickness is becoming weak.

Thermal evolution of the mantle and the "Archean paradox"

Heat generated by radioactive isotopes decreases exponentially with time, so that its present value is *c*. 4.5 times less than at 4.5 Ga and *c*. 2.5 times less than at 3.0 Ga (Fig. 4.38a). This means that the average mantle heat flow and mantle temperatures should have been significantly higher in the Archean than at present (e.g. Wasserburg *et al*., 1964). In contrast, the lack of massive crustal melting in the Archean and Archean geotherms constrained by mineral assemblages in Archean high-grade terranes suggest that the Archean mantle temperatures were not significantly different from the present ones (Bickle, 1978; Burke and Kidd, 1978; England and Bickle, 1984).

The contradiction between certain lines of evidence that suggest that the Archean average mantle heat flux was significantly higher than at present and the evidence that Archean

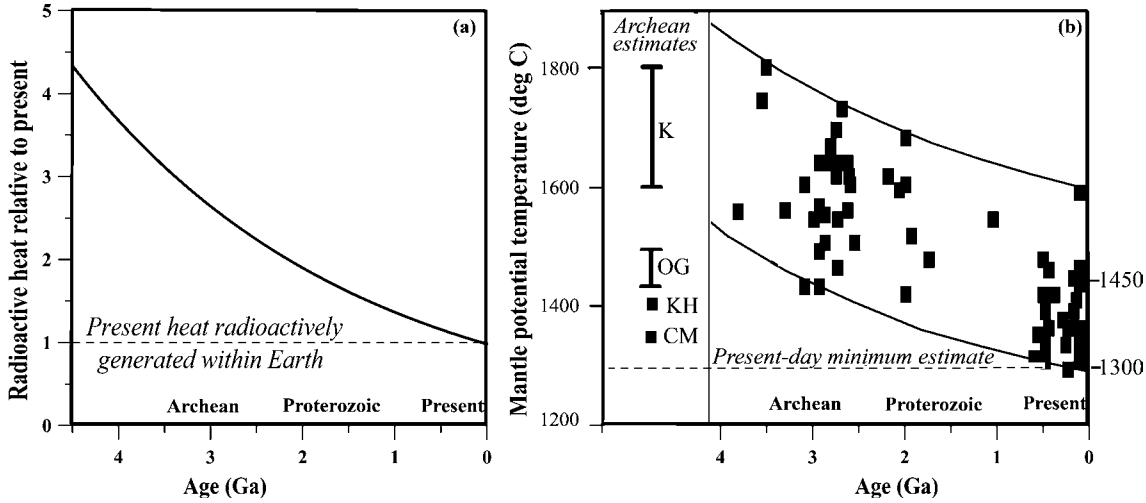

Fig. 4.38 Thermal history of the Earth. (a) Heat generated within Earth (normalized by its present-day value) by three major heat-producing isotopes: potassium, uranium, and thorium (based on estimates of van Schmus, 1995). (b) Potential temperatures of the upper mantle (hypothetical temperatures of mantle adiabatically brought up to the surface without melting) calculated for MORB-like ophiolite suites and greenstone belts (source: Abbott *et al.*, 1994). The upper and lower boundaries (exponential curves) approximate the shape of the radiogenic heat production curve (Wasserburg *et al.*, 1964). Potential temperature of the present-day mantle is commonly estimated to be between 1300 °C and 1450 °C. Left insert in (b): summary of mantle potential temperatures in the Archean, based on komatiite (K) (Nisbet and Fowler, 1983) and hydrous komatiites (KH) melting models (Grove and Parman, 2004), ophiolite suites and greenstone belts (OG) (Abbott *et al.*, 1994), and mantle convection models (MC) (Campbell and Griffiths, 1992).

continental geotherms were similar to modern ones produces the so-called "Archean paradox". This could easily be resolved if the ratio of oceanic to continental mantle heat flow was greater in the Archean due to greater heat loss through the oceans. The most obvious way to explain the paradox is to assume that heat loss due to the creation and subduction of oceanic lithosphere was greater in the Archean than at present (e.g. Burke and Kidd, 1978). This assumption can be fulfilled if plate velocities in the past were faster and ridge lengths were greater (e.g. Bickle, 1978). Assuming that (a) the Archean cratons were much smaller than present-day continents and (b) applying the present-day statistics of plate configuration (size distribution versus normalized area) to the past, Abbott and Menke (1990) concluded that the length of plate boundaries at 2.4 Ga was ~2.2 times greater than their present length (with >60 cratons). Note that both of these assumptions may be fundamentally wrong. Furthermore, mantle convection models that treat mantle convection as a thermal boundary layer phenomenon cannot explain the spatially disproportionate heat loss: spatial averaging over different, but with same lateral size, columns of convective cells will produce the same local heat loss out of a convective layer regardless of the location (i.e. oceanic versus continental settings) (Lenardic, 1998).

The presence of the continental crust affects mantle convection and helps to overcome the latter problem of spatially disproportionate heat loss by creating fundamentally different boundary conditions at the crust–mantle interface in continents and oceans (Lenardic, 1998). In oceans, the boundary condition at the crust–mantle interface is for a constant temperature, which is achieved by the involvement of oceanic crust in convective mantle overturns and by a large contrast in effective thermal conductivity of the oceanic crust and the mantle. If the crust–mantle boundary condition on Archean continents is for a near-constant heat flux (in particular, due to comparable thermal conductivities of the continental crust and the mantle), it produces spatially variable thermal conditions at the top of the convecting mantle (i.e. at the base of the TBL). As a result, Archean continental geotherms can become stabilized, despite higher convective vigor in the Archean, by forcing a greater proportion of the heat to be carried through the oceans.

On the other hand, following the "devil's advocate" arguments of Hamilton (2007), one should bear in mind that (also see Section 9.2.1):

- there is no geological proof for the existence of lithospherically distinct oceans and continents in the Archean; thus mantle convection models based on a different thermal regime for continents and oceans in the Archean may be fundamentally biased;
- the extremely mobile Archean continental crust "was incapable of behaving as the semi-rigid plates required, by definition, for plate tectonics"; thus thermal models that assume Archean plate tectonics may be misleading.

Recent mantle convection modeling based on back-tracking the thermal history of Earth from present-day conditions suggests that surface heat flux did not need to be significantly higher in the past than at present (Korenaga, 2006). Assuming that (a) plate tectonics have operated since the Paleoproterozoic and (b) secular evolution of mantle convection is affected by depleted cratonic lithosphere, the model predicts that in the Archean, when the mantle was hotter, plate tectonics was more sluggish, with slower plate velocities than commonly assumed. For the Urey ratio $\gamma = 0.15–0.3$ ($\gamma = H/Q$ and is the measure of the relative importance of internal heating H with respect to total convective heat flux Q, Christensen, 1985), the whole-mantle convection model predicts moderate secular cooling of the Earth with similar surface heat flow in the past and at present, but with the progressively increasing role of internal heating (due to radioactive heat generation) back in time (compare with Fig. 4.38a).

To add to the "paradox", petrologic and geophysical estimates of the Archean mantle temperatures differ significantly. In particular, mantle temperatures ~300–500 °C hotter than modern ambient asthenosphere are required for generation of Archean komatiites (Nisbet and Fowler, 1983). Some petrologic studies suggest, however, that these ultramafic lavas, that are almost entirely unique for the Archean and require eruption temperatures of at least as high as 1600 °C (and up to 1800 °C), were probably erupted by hotspots and are not representative of "normal" Archean mantle (e.g. Abbott *et al*., 1994; Fig. 4.39). Furthermore, recent petrologic studies that interpret Archean komatiites as products of hydrous shallow melting predict that the Archean mantle was only slightly hotter (~100 °C) than at present (Grove and Parman, 2004). Geochemical data from ophiolite suites and greenstone belts provide lower Archean temperatures than komatiite data and require that upper mantle potential temperature in the late Archean (2.8 Ga) should be only

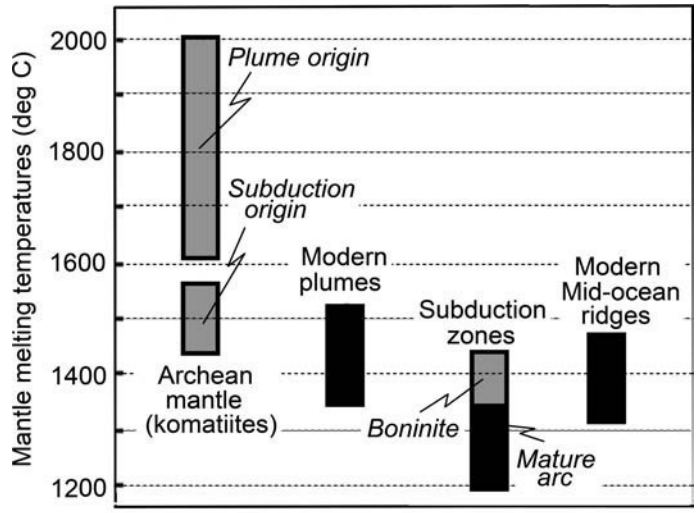

Fig. 4.39 Mantle melting temperatures for different modern and Archean tectonic settings (data sources: Tatsumi *et al*., 1983; Kinzler and Grove, 1992; Eggins, 1992; Baker *et al*., 1994; Wagner and Grove, 1998; Falloon and Danyushevsky, 2000; Grove and Parman, 2004).

~130–200°C hotter than at present (Abbott *et al*., 1994). More recent estimates based on mantle convection models indicate that the Archean mantle could, on average, be only less than 50 °C hotter than the present mantle (Campbell and Griffiths, 1992) (Fig. 4.38b).

Continental regions with transient thermal regime

Morgan (2001) argues that the transient thermal processes that operate in the continental lithosphere are, in general, similar to the processes that operate in the oceanic lithosphere. However, in contrast to the oceanic settings, the magnitude of these processes is less predictable due to thermal variations associated with the chemical heterogeneity of the continents.

Collisional orogens

Collisional orogens are characterized by a highly heterogeneous heat flow, with the highest values typically measured along the major fault zones. As for subduction zones, a steady-state approach is inapplicable to these tectonic structures. Thermo-kinematic models provide the best constraints on lithospheric temperatures in the orogens, such as the Alps (e.g., Royden *et al*. 1983; Davy and Gillet 1986; Bousquet *et al*., 1997). However, they require detailed information on dynamic processes in the mantle, which are usually not completely understood. As a result, thermo-kinematic models are poorly constrained and detailed knowledge on lithospheric temperatures is unavailable.

A 2D model of the lithosphere of the Alps which takes into account the processes of crustal shortening and formation of crustal and lithospheric roots during subduction is an example of

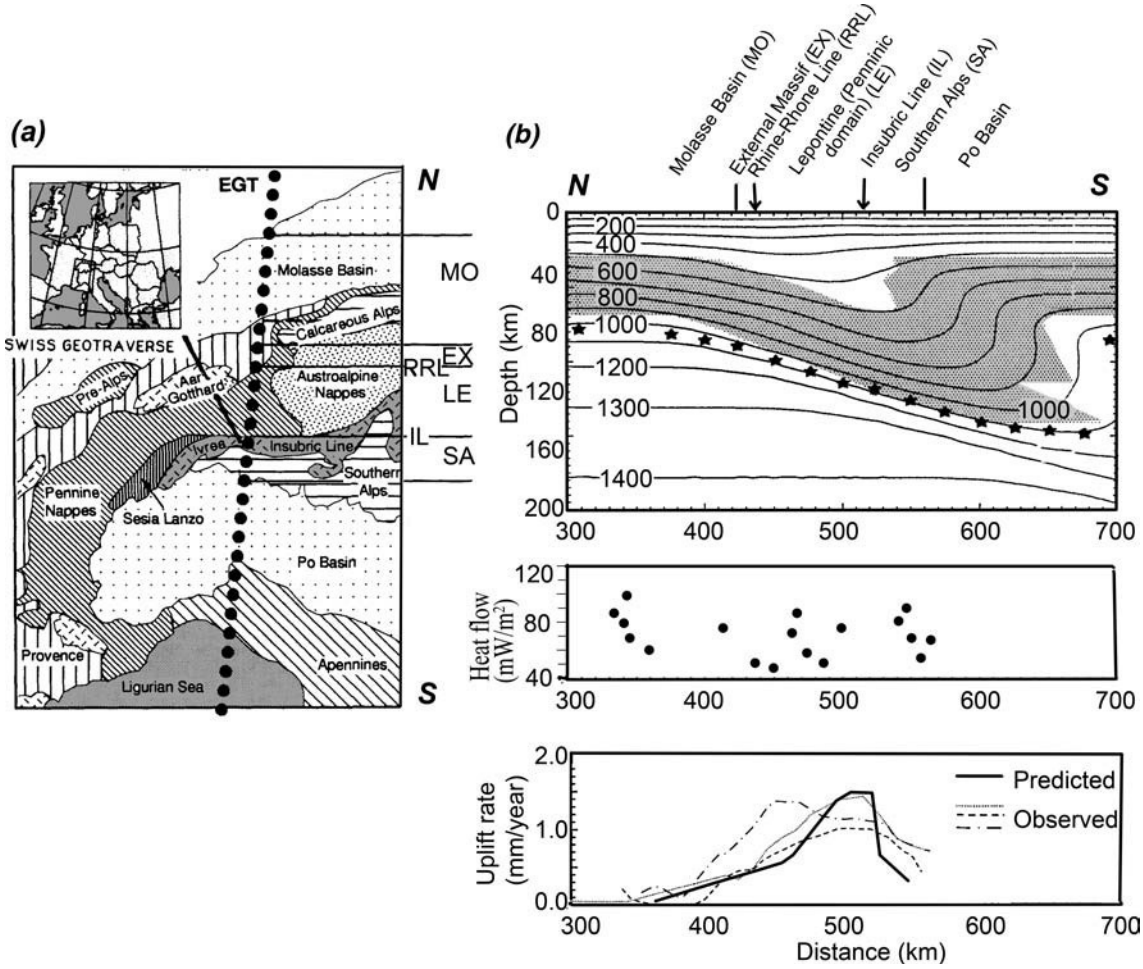

Fig. 4.40 Thermo-kinematic modeling for the Central and Western Alps. (a) Tectonic map showing the location of the European Geotraverse (EGT), (b) Top: cross-section along the EGT profile showing the predicted present-day lithospheric temperatures (asterisks – the lithosphere–asthenosphere boundary defined as the intersection of the geotherm with the mantle solidus; shaded area – the deformed lithospheric mantle derived from tectono-kinematic calculations); Middle: the present-day surface heat flow corrected for uplift and topography (the uncertainty is *c.* 20 mW/m^2), Bottom: the present-day uplift rates derived from geodetic observations (dashed lines) and the exhumation rates at the surface predicted by the kinematic model (from Okaya *et al.*, 1996).

an advanced thermo-mechanical model (Okaya *et al.*, 1996). This model predicts that, although the crustal thickness across the Alpine region changes from ~30 km to the north of the orogen to ~55–60 km beneath the Alps and to ~30–34 km in the south beneath the Po basin, the Moho is an almost isothermal boundary with a temperature of ~500–600 °C, while the lithospheric thermal thickness gradually increases southwards from ~80 km to the north of the orogen to ~120–150 km beneath the southern Alps–northern Apennines (Fig. 4.40).

Extended regions

The Basin and Range Province in western USA is a classical example of an extended continental region (Gans, 1987). The region is characterized by anomalously high surface heat flow relative to the global continental average of 65 mW/m^2 (Pollack *et al*., 1993): $92 \pm 9\ mW/m^2$ in the presently active Northern Basin and Range and $82 \pm 3\ mW/m^2$ in the presently quiescent Southern Basin and Range Province (Lachenbruch *et al*., 1994). Although average heat flow in the northern and southern parts of the Basin and Range is similar on the province-wide scale (Fig. 4.18), the two regions differ both in topographic elevations (~1.0 km in the south and ~1.8 km in the north with an abrupt transition between them) and in Cenozoic extension histories. The average total Cenozoic extension may be similar in both regions; but while crustal extension is still on-going in the Northern Basin and Range and has roughly doubled its area in the Cenozoic (the ratio of area size prior to and after the extension $\beta = 2$), the Southern Basin and Range Province has been relatively inactive during the past 10–15 Ma (Hamilton, 1987).

The observed province-wide heat flow anomaly can be explained by a broad range of simple extension models that predict the time-scale of the process of *c*. 10–50 Ma (e.g. McKenzie, 1978). Within the frame of extensional models, the high heat flow in the Northern Basin and Range has been successfully explained by the Cenozoic extension-related upward influx of material in the lithosphere which advectively transfers the heat, increases the surface heat flow, and affects the thermal structure of the lithosphere. The first stages of tectonic extension and magmatism, when surface heat flow rapidly increases by non-conductive processes, are followed by tectonic quiescence, when heat transfer becomes dominated by conduction. Heat conduction, which leads to a decrease in surface heat flow, is a slow process; its earlier stages are controlled by the thermal structure of the lithosphere at the end of tectonic activity, while the equilibrium thickness of the lithosphere controls its later stages.

Figure 4.41a, based on the extensional model of McKenzie (1978), illustrates evolution of the extensional geotherms. An instantaneous extension (i.e. faster than required to redistribute heat by diffusion) of a thermally equilibrated lithosphere by a factor of β causes lithosphere thinning by factor β and an increase in thermal gradient and surface heat flow by the same factor β. To the first order, high surface heat flow observed in the Basin and Range Province supports this model even quantitatively (Lachenbruch *et al*., 1994). For example, in the case where $\beta = 2$ (Fig. 4.41b), high heat flow is still close to its maximum value even after 15 Ma since termination of tectonism as observed in the Southern Basin and Range Province. However, a province-wide extension with $\beta = 2$ can also be achieved by an inhomogeneous extension with localized areas of high (e.g. $\beta = 10$) concentrated extension. Such areas will cool much faster and (neglecting lateral heat transfer) 15 Ma after the tectonism heat flow it will drop to <40% of its maximum value. Because of heat loss during the extension process, a uniform (as compared to instantaneous) lithosphere stretching at a constant rate requires slightly higher β to double the mantle heat flow (equations 15 and 16 in Lachenbruch and Sass, 1978).

Topographic elevation provides additional information for discriminating between various possible extensional models due to the buoyancy trade-off between extension and

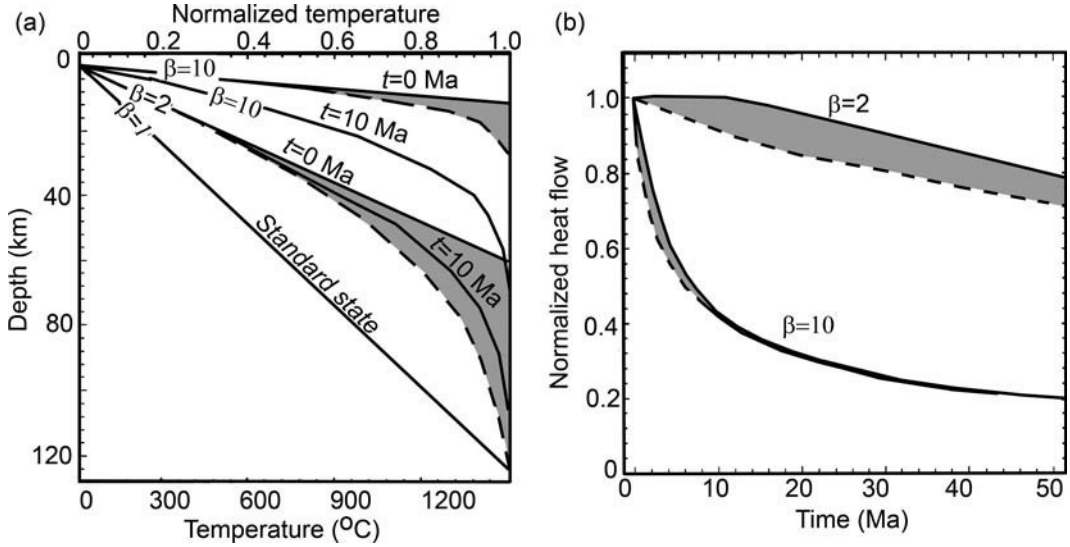

Fig. 4.41 Thermal model for extended regions (after Lachenbruch *et al.*, 1994). Radiogenic heat generation is neglected. (a) Lithospheric geotherms 0 Ma and 10 Ma after homogeneous stretching of a 125 km-thick lithosphere by a factor of $\beta = 2$ or $\beta = 10$ (solid lines). Dashed lines – steady-state geotherms for a uniform lithosphere extension that causes the same increase in heat flow as instantaneous stretching by factor $\beta = 2$ or $\beta = 10$. In the case where the lithospheric base is at constant temperature and extends uniformly at any rate so that heat flow increases twofold or tenfold, all geotherms fall within the gray areas. (b) Heat flow decay after lithosphere extension for the geotherms bounding gray regions in (a). Solid lines – heat flow for instantaneous stretching (β – stretching factor); dashed curves – for the steady-state case with a steady-state strain rate of 1 %/Ma (3×10^{-16} 1/s) and 25 %/Ma (10^{-14} 1/s) for $\beta = 2$ and $\beta = 10$, respectively.

magmatism (Lachenbruch and Morgan, 1990). This is, in particular, important in the Northern Basin and Range Province where high crustal extension ($\beta \sim 2$) is in apparent contradiction with high elevation and requires either the development of a compensating source of buoyancy during the extension or an extremely high elevation (~6 km above sea level) prior to the extension. Lithosphere delamination at the early stages of tectonism could produce topographic elevation despite stretching.

Metamorphic core complexes (MCCs), widely distributed in highly extended regions of western USA, provide additional information on the Cenozoic thermal evolution of the region (Fig. 4.42). The Arizona MCCs are interpreted to represent mid-crustal rocks that became exposed due to very fast (over a few million years) tectonic unroofing of 10–20 km of the upper crust. As discussed by Lachenbruch *et al*. (1994),

> such a massive removal of surface material should affect the surface heat flow in at least two ways: (1) it would expose warmer mid-crustal rocks, and for a time at least, cause a large local increase in heat flow, and (2) by removing the most radioactive (upper) part of the crust, it would cause a decrease in the steady state background heat flow, observable only after the initial warming decays.

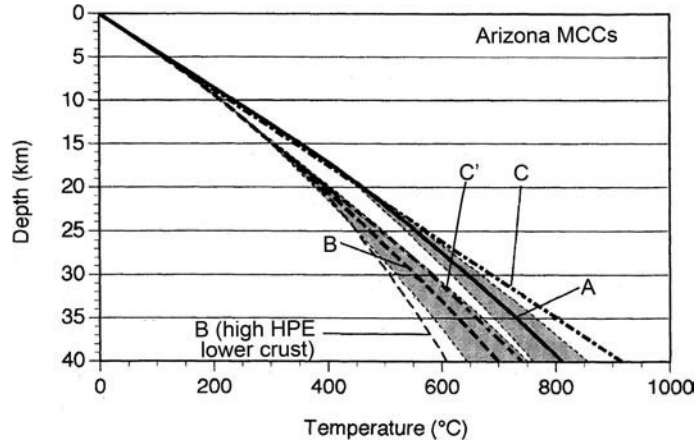

Fig. 4.42 Lithospheric geotherms A and B in Southern Basin and Range Province based on data from two metamorphic core complexes and assuming temperature- and pressure-dependent thermal conductivity and surface heat flow of 62 mW/m^2 (after Ketcham, 1996). In the case where mantle heat flow is 10 mW/m^2 lower, Moho temperatures will reduce by 235 °C. Shaded areas – estimated variability due to uncertainty in heat production (the corresponding distribution of heat production with depth for sets A and B is shown in Fig. 4.13(d–e), respectively). Geotherm C calculated for the lithosphere stretching model is shown for comparison (Lachenbruch and Sass, 1978). C′ – the same model as C but with constant thermal conductivity of 2.5 W/m/K.

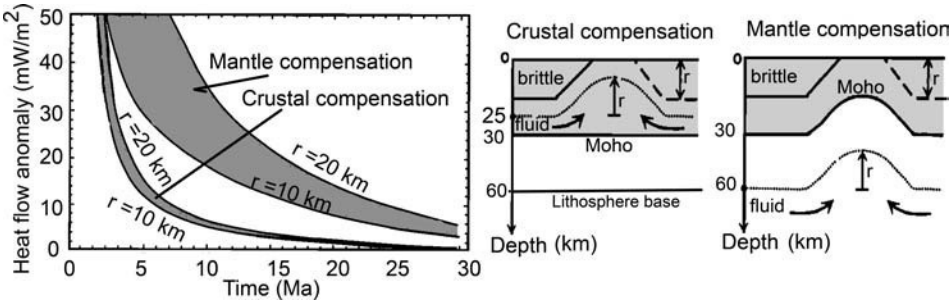

Fig. 4.43 Surface heat flow anomaly caused by an instantaneous unroofing with $r = 10$ km and $r = 20$ km in a 60 km-thick lithosphere at constant basal temperature (after Lachenbruch *et al.*, 1994). In the case of crustal compensation, the compensating return flow occurs at 25 km depth. In the case of mantle compensation in a warm lithosphere with temperature gradient of 23 K/km, the return flow occurs at 60 km depth. Radiogenic heat generation is neglected.

The evidence for the latter effect is provided by spatial correlation between the elongated low heat flow anomaly and the belt of MCCs in the Southern Basin and Range Province. A 1D thermal model of instantaneous unroofing (Block and Royden, 1990) implies that removal of the upper crustal material is compensated by a lateral material influx that occurs either in a ductile lower crust or at the base of the lithosphere (Fig. 4.43). The mechanism of crustal compensation is consistent with relatively uniform crustal thickness in the region, since (unroofed) regions with MCCs have the same crustal thickness as their surroundings.

Global patterns

Using the global heat flow data of Pollack *et al*. (1993) supplemented by newer heat flow measurements, Artemieva and Mooney (2001) calculated regional lithospheric temperatures in stable continents and found that for the typical values of heat flow observed in crustal terranes of different ages they are close to the reference conductive geotherms of Pollack and Chapman (1977) (Fig. 4.33). The thermal state of the continental lithosphere is illustrated by a set of maps (Figs. 4.36 and 4.44). For stable continents, tectonically quiescent at least since the mid-Paleozoic, these maps are derived from numerous geotherms constrained as the downward continuation of surface heat flow (eq. 4.36). The values of thermal parameters (thermal conductivity and heat production) in the sedimentary layer and in the upper crust are constrained by regional measurements on rock outcrops and borehole data, supplemented by regional detailed seismic data on the crustal structure. Seismic data are also used to determine the thicknesses of the middle and lower crustal layers, for which thermal parameters are fixed at constant due to large uncertainty in the actual values (Section 4.1, Table 4.8). Consistent model assumptions for stable continents permit meaningful comparisons of the thermal structure of the lithosphere. Since steady-state modeling is inapplicable to tectonically active regions, such as Cenozoic orogens and extended regions, in these regions temperatures at 50 km depth are assumed to be in the range 900–1100 °C, and the lithosphere thermal thickness is assumed to be 60–80 km, in accord with numerous petrologic and regional transient geothermal models (e.g., Lachenbruch and Sass, 1977; Polyakov *et al*., 1988; Mechie *et al*., 1994; Decker, 1995; Okaya *et al*., 1996; Le Pichon *et al*., 1997; Currie and Hyndman, 2006) (Fig. 4.39b).

The major results can be summarized as follows.

The base of the crust is not isothermal. Temperatures at the Moho vary widely from 300–500 °C in the Archean–Paleoproterozoic cratons to 500–800 °C in Meso- and Neoproterozoic regions, where the crustal thickness averages 40–45 km. In the Archean–Paleoproterozoic regions the highest temperatures at the Moho are expected to be either in the regions with anomalously thick crust, such as in central Finland, or in the regions that have been affected by Phanerozoic tectonic activity (e.g. the Sino-Korean craton). In young tectonically active regions, temperatures at the base of the crust can be as high as 800–900 °C. Moho temperatures can vary significantly over short lateral distances, reflecting not only variations in the thermal regime of the crust, but also variations in the crustal thickness and composition. For example, across the Trans-European Suture Zone, which is the major tectonic boundary in Europe between the Precambrian East European Craton and the Phanerozoic Europe, temperatures at the crustal base change from 450–550 °C within the craton (where the Moho is at a 40–45 km depth) to 600–700 °C at the base of the 30–32 km-thick Variscan crust.

The depth where lithospheric temperatures reach ~600 °C can be interpreted as the proxy for the base of the elastic lithosphere in continental regions where this depth exceeds the crustal thickness (Fig. 4.44b). Brittle–ductile transition in olivine corresponds to the critical isotherm of ~600–700 °C, and flexural rigidity of old (>200 Ma) continental lithosphere is dominated by olivine rheology of the mantle (Chapter 8). Analysis of the depth–temperature correlation of the intraplate continental seismicity indicates that most of it terminates at

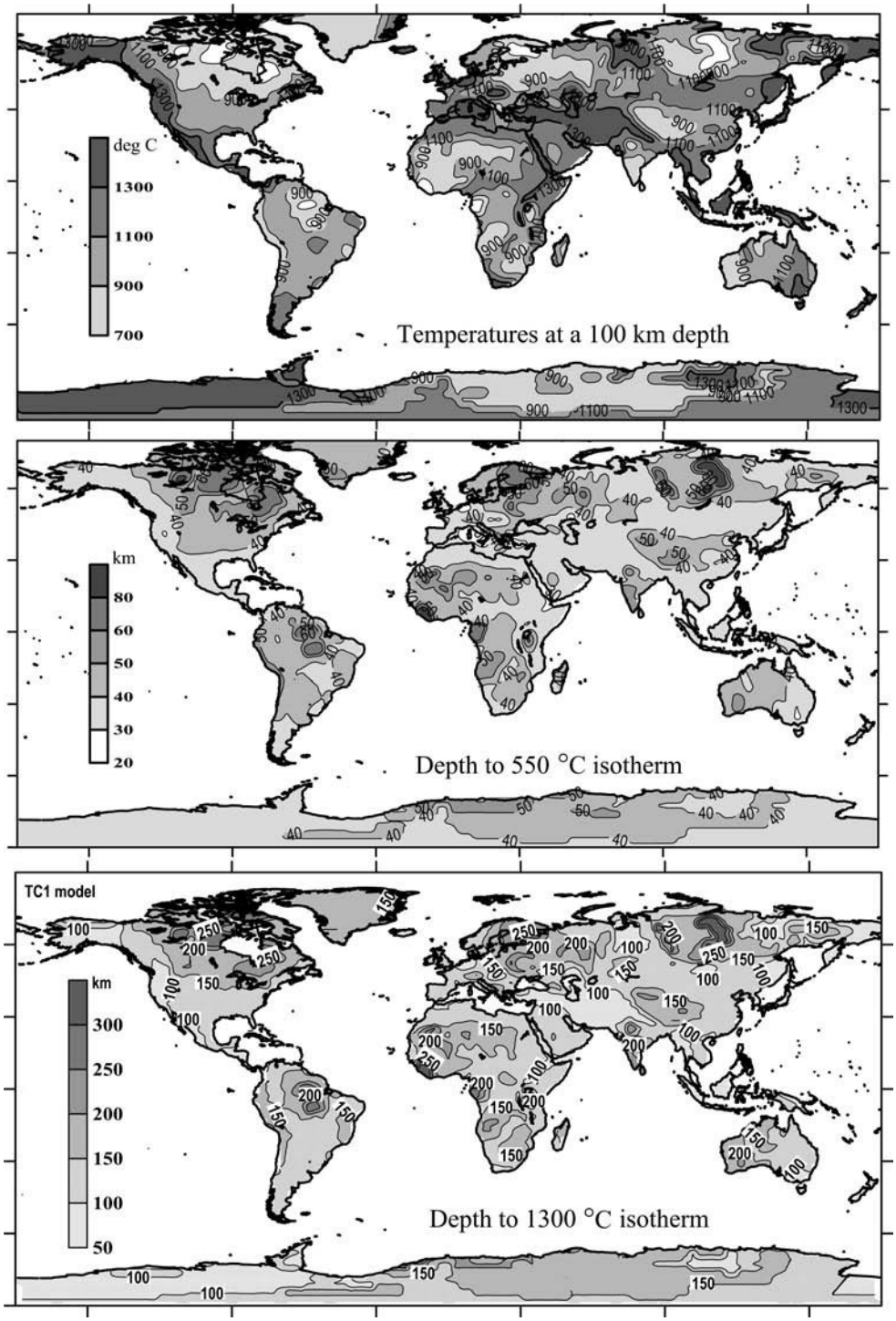
deg C
1300
1100
900
700
Temperatures at a 100 km depth
km
80
60
50
40
30
20
Depth to 550 °C isotherm
TC1 model
km
300
250
200
150
100
50
Depth to 1300 °C isotherm

Fig. 4.44 (cont.)

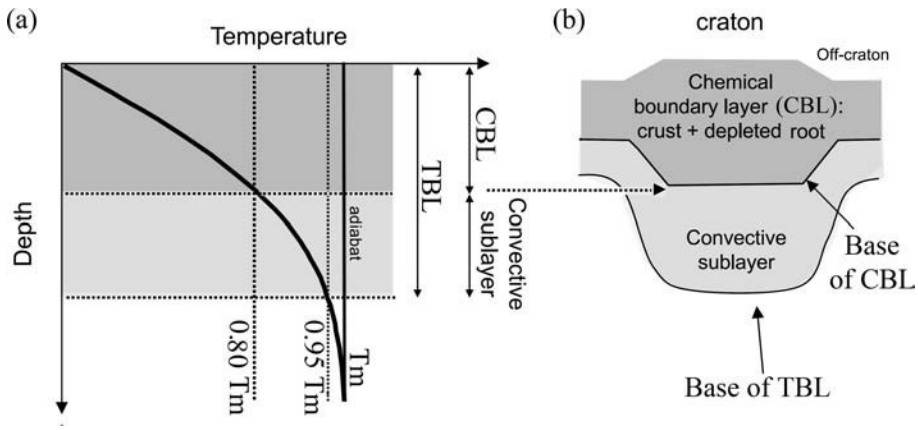

Fig. 4.45 Correlation between the thermal boundary layer (TBL), the chemical boundary layer (CBL), and the convective sublayer (CSL) (from Lee, 2006). The thickness of CSL is exaggerated. In this interpretation the base of the TBL is defined by the point at which the temperature becomes 0.95 of the ambient mantle temperature T_m.

lithospheric temperatures of 500–600 °C. The depth to 500–600 °C isotherm can also be considered as a proxy for the thickness of the magnetic layer (the maximal depth of crustal magnetization), since the Curie temperature for magnetite is close to 550 °C (Petersen and Bleil, 1982) (Section 5.4).

4.4.3 Thickness of thermal lithosphere

Thermal boundary layer

Heat flow from the deep interior is transferred upwards primarily by mantle convection. In the upper layers of the Earth the conduction mechanism of heat transfer starts to dominate; this upper part with mainly conductive heat transfer is termed the thermal lithosphere or TBL, the thermal boundary layer dominated by definition by conductive heat transfer. The transition from convection to conduction mechanisms is gradual and is responsible for the existence of the "convective boundary (sub)layer" in the upper mantle at the base of the TBL (Fig. 4.45a). Sometimes this convective boundary (sub)layer is considered as a part of the TBL (e.g. Cooper *et al.*, 2004; Lee *et al.*, 2005; McKenzie *et al.*, 2005).

Caption for figure 4.44 (cont.)
Thermal state of the continental lithosphere constrained by surface heat flow for stable regions, xenolith data for active regions, and statistical values for regions with no borehole data (Source: Artemieva, 2006). The step between the contours corresponds approximately to the uncertainty of the models. (a) Temperatures at 100 km depth shown with a 200 °C step in contours; (b) the depth to a 550 °C isotherm; the map is a proxy for the depth to the Curie isotherm, the depth to the brittle–ductile transition in olivine, and the thickness of the elastic lithosphere; (c) the depth to a 1300 °C isotherm shown with a 50 km step in contours; the map provides a proxy for the thickness of the thermal lithosphere. The interpolation used to construct these maps results not only in lateral smearing of short-wavelength anomalies, but also in a significant reduction in their amplitude.

Since large-scale seismic tomography samples the top of the convective mantle, lithospheric thickness estimated from seismic tomography models commonly extends deeper than the TBL, down to the base of the convective boundary (sub)layer. The thickness of the convective boundary (sub)layer, which is 40–50 km in the cratonic regions (Jaupart *et al*., 1998; Sleep, 2005), defines the amplitude of a systematic difference in lithospheric thickness estimates based on thermal and seismic tomography data, in particular in stable continental regions (Artemieva and Mooney, 2002).

In practice, the thickness of the TBL is commonly determined by the intersection of a lithospheric geotherm (actually, its linear downward continuation) with a mantle adiabat of T_m ~1350–1400 °C (which is mantle isentropic temperature at a depth of 100–150 km; the adiabatic gradient in the upper mantle is given by eq. 4.28). For surface heat flow <30 mW/m^2 the conductive geotherm asymptotically approaches the mantle adiabat at depths greater than ~300 km (Fig. 4.33) and the depth of their intersection (thickness of thermal lithosphere) cannot be reliably estimated. Since for typical upper mantle compositions the transition from high lithospheric viscosity to a lower asthenospheric viscosity (with effective values of ~10^{21} Pa s) starts at $T \sim 0.8T_m$, the thickness of the TBL (thermal lithosphere) is sometimes defined as the depth to a 1050–1100 °C isotherm (e.g. Pollack and Chapman, 1977).

The transition from high viscosity lithosphere to a lower viscosity asthenosphere is controlled not only by temperature, but also by mantle composition, in particular by volatile content. Because of the significant difference in mantle solidi, the thickness of the TBL can differ significantly for dry and wet peridotite melting (Fig. 4.33a). Furthermore, mantle melting leads to the formation of a chemical boundary layer that is depleted in meltable components and dehydrated, and thus may have a viscosity two orders of magnitude higher than the upper mantle viscosity (Hirth and Kohlstedt, 1996). Lee *et al*. (2005) argue that the CBL, formed by mantle melting and dehydration, does not participate in large-scale or secondary mantle convection and forms a conductive lid both in oceans and continents that controls the thickness of the TBL and plays a significant role in its preservation (Fig. 4.45).

Temperature distribution in the lithosphere, required to estimate the lithospheric thermal thickness, can be calculated from several techniques:

(1) cooling models for normal oceanic lithosphere, in which thickness of the oceanic TBL is approximated by eq. (4.25), $L \sim 11\ t^{1/2}$;
(2) steady-state thermal conductivity models for stable continental regions constrained by surface heat flow measurements;
(3) transient thermal models for active continents and anomalous oceans;
(4) petrologic constraints on lithospheric geotherms based on mantle xenolith data, metamorphic reactions;
(5) the depth to the Curie isotherm;
(6) conversion of seismic velocities, seismic attenuation, or electrical conductivity into temperatures constrained by laboratory measurements on physical properties of rocks at mantle P–T conditions;
(7) models of mantle convection that constrain mantle heat flow at the lithospheric base.

Some of these approaches are discussed in more detail in Chapter 5.

Global patterns for the continents

The age dependence of surface heat flow can, to first order, be recast as the relationship between lithospheric thermal thickness and age: statistically, regions with higher heat flow have thinner lithosphere. This transition is not, however, straightforward because of the non-uniform contribution of crustal heat production into the observed heat flow which results in significant scatter in age–thickness data (Fig. 4.46). Furthermore, since heat flow data coverage is very uneven and some of the regions are significantly oversampled in comparison to less studied regions, the best fit approximation for lithospheric thickness – the surface heat flow relationship may be misleading. For this reason, Fig. 4.47 shows only the upper and lower bounds as based on worldwide analysis of the thermal state of the continents (note that for regions with extremely low surface heat flow estimates of the TBL thickness are asymptotic). Although the exact depth extent of the cratonic lithosphere cannot be reliably assessed from thermal data (below ~300 km cold cratonic geotherms asymptotically approach the mantle adiabat so that the depth of their intersection cannot be determined), the depth to the 410 km mantle transition zone puts a natural limit on the base of the thermal lithosphere since the phase transition temperature at 410 km is expected to be close to the mantle potential temperature (Ito and Takahashi, 1989).

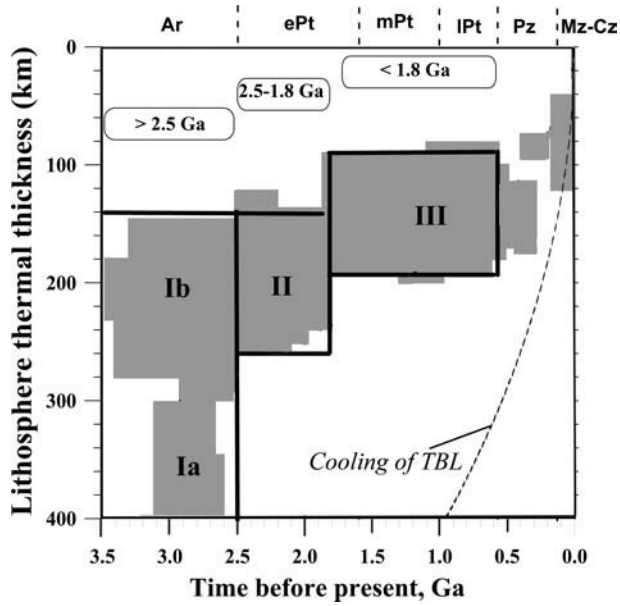

Fig. 4.46 Variations of lithospheric thermal thickness with tectono-thermal age. Gray shading shows lithospheric thickness estimates derived from surface heat flow (Source: Artemieva and Mooney, 2001). The Archean lithosphere has bimodal thickness distribution centered at ~350 and ~220 km. Key: Ar – Archean; ePt, mPt, lPt – early, middle, and late Proterozoic, respectively; Pz – Paleozoic; Mz-Cz – Meso-Cenozoic. Dotted line – theoretical curve based on cooling of thermal boundary layer (eq. 4.38).

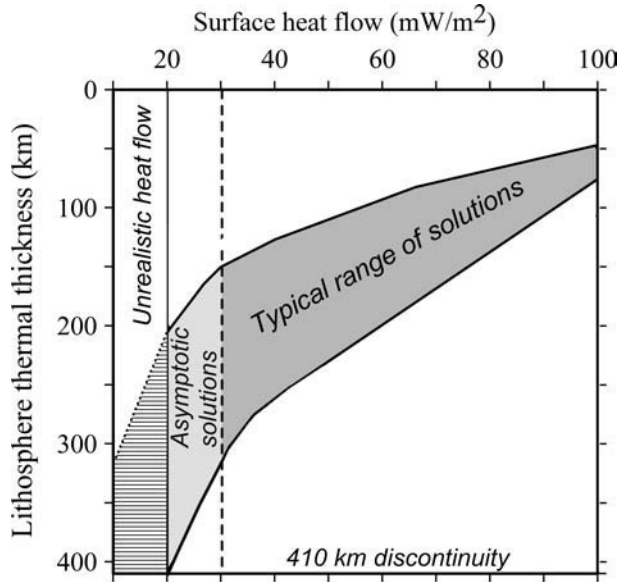

Fig. 4.47 Empirical relationship between surface heat flow and lithospheric thermal thickness. For each surface heat flow value, a large range of lithospheric thickness is possible, depending primarily on crustal heat production. For surface heat flow <30 mW/m^2 the conductive geotherm asymptotically approaches mantle adiabat and the depth of their intersection cannot be reliably estimated. The 410 km discontinuity limits the maximum possible thickness of thermal lithosphere.

The thickness of the continental lithosphere increases with tectono-thermal age (Fig. 4.46), but it does not follow the $\sqrt{\text{age}}$ pattern predicted by cooling of the thermal boundary layer (eq. 4.25). In contrast to the oceans where lithosphere thickness slowly increases with age in old oceans, old continents have deep-extending lithospheric roots (Fig. 4.46). A typical thickness of continental lithosphere is *c*. 200 ± 50 km in the Paleoproterozoic terranes, 140 ± 50 km in Meso-Neoproterozoic terranes, and 100–120 km in the Paleozoic regions (Artemieva and Mooney, 2001). The exceptions are the Archean cratons affected by Phanerozoic tectono-magmatic events (e.g. the Wyoming and the Sino-Korean cratons) where lithospheric thickness does not exceed 120–150 km. In tectonically active Cenozoic regions (except for the collisional orogens where subducting lithospheric slabs can reach a depth of ~200 km) the lithosphere thickness is typically 60–80 km.

Statistical analysis of thermal model constrained by surface heat flow

Lithosphere thickness–age correlation

A statistically significant correlation between the thermal state of the continental lithosphere and its age (Artemieva, 2006) is observed despite the large scatter of lithospheric thickness values (~100 km for any of the considered age intervals) (Tables 4.12, 4.13). This scatter is associated with uncertainties in the thermal model (*c*. 25% for the lithospheric thickness)

Table 4.12 Statistics of thermal structure of the continental upper mantle

	n	*T* at 50 km (°C)	*T* at 100 km (°C)	*T* at 150 km (°C)	Depth to 1300 °C (km)
Archean average	79	505 ± 121	770 ± 174	1010 ± 201	219 ± 73
Archean I (<3.0 Ga)	35	430 ± 98	653 ± 142	867 ± 189	269 ± 80
Archean II (>3.0 Ga)	33	527 ± 67	809 ± 76	1079 ± 89	197 ± 23
Archean III – reworked	11	691 ± 77	1046 ± 83	Above mantle adiabat	135 ± 15
Paleoproterozoic	56	592 ± 98	871 ± 126	1135 ± 137	182 ± 34
Mesoproterozoic	20	649 ± 91	979 ± 128	1261 ± 111	153 ± 25
Neoproterozoic	42	781 ± 116	1154 ± 146	Above mantle adiabat	121 ± 24
Paleozoic	62	731 ± 135	1102 ± 181	Above mantle adiabat	130 ± 30
Meso-Cenozoic	–	900 to 1200	Above mantle adiabat	Above mantle adiabat	60 to 90

(Source: Artemieva, 2006)

Table 4.13 Geologic and tectonic ages and lithospheric thermal thickness for major Precambrian provinces

Precambrian cratons	Basement age (Ga)*	Cratonization age (Ga)	Major tectonic events (Ga)	Thermal thickness (km) (uncertainty *c.* 25%)
Australian craton				
Pilbara craton	**3.5–3.0**	3.0	2.0–1.7, 1.3–1.0	170–230 km
Yilgarn craton	**3.7–3.4** gneiss and 3.0–2.6 granites (3.7)	2.7–2.6		170–230 km
Hamersley and Naberru basins	Archean ?		**2.8–2.3**	No data
Gawler carton	**2.7–2.6**	1.5	1.9–1.8, 1.6–1.5	170–190 km
North Australian craton	**2.1–1.9 (2.5)**	1.85	1.3–1.1	130–200 km
Central Australian mobile belt	**1.9–1.4**	1.2–1.1	1.8–1.6, 1.5–1.3, 1.1–1.0, 0.9–0.5	140–160 km
South American craton				
Amazonian craton (Guyana Shield)	**3.4 and 2.9–2.6** (3.5)	2.8–2.6	2.2–2.1, 1.85–1.55	No data
Mobile belts of Amazonian craton	**2.2–1.8**			No data
Central Brazil Shield	**3.0–2.8** (3.2)	2.8–2.6	2.1–1.9, 1.6–1.1, 0.7–0.5	No data
Mobile belts of Central Brazil Shield	Archean–Paleoproterozoic		**1.4**	No data
Atlantic Shield (Saõ Francisco craton)	3.2 (3.4)	2.8–2.6	2.1–1.9, 0.6	190–200 km

Table 4.13 (cont.)

Precambrian cratons	Basement age (Ga)*	Cratonization age (Ga)	Major tectonic events (Ga)	Thermal thickness (km) (uncertainty *c*. 25%)
Marginal belts of Atlantic Shield	**1.1**		0.7–0.5	110–160 km
Rio Apa craton	**1.6–1.0** (2.1)			No data
Indian craton				
Dharwar craton	**3.1–3.0**	2.6–2.5		180–200 km
Southern Granulite terrane	**3.3–3.0** (3.4)	2.6–2.5	2.1–2.0, 1.6–1.5, 0.9	180–230 km
Singhbhum craton	**3.4**	2.6–2.5	2.1	160–200 km
Aravalli craton	**3.4**	2.6–2.5	2.5–2.0, 1.8–1.5	160–200 km
Bhandara (Bastar) craton	**3.5–3.3**		2.2, 1.0	180–200 km
Cuddapah Basin	**2.0–1.5**		1.5–1.0	140–160 km
Narmada–Son Rift system			**0.6–0.5**	80–110 km
Siberian craton				
Aldan Shield & Stanovoy Ridge	**3.4–3.2**	3.1–2.9, 2.6–2.5	Partly at 2.0–1.8	140–190 km
Kolyma–Omolon and Okhotsk median massifs	**3.4**	?	1.6–0.5	No data
Anabar Shield	**2.9–2.7** (3.2)	2.6–2.5	1.9, partly at 0.9–0.5	190–350 km
Main Siberian craton	Mainly Archean (*c*. 75%), extensively reworked at **1.95–1.8 Ga** by epicratonic rifting	2.6–2.5	1.4–1.1, 0.8–0.5; Mz (Viluy basin)	150–350 km (120–140 km Viluy basin)
Pericratonic mobile belts	**3.2–2.5**		2.5, 1.9, 0.6	250–350 km
East-European craton				
Ukrainian Shield & Voronezh massif	**3.6–3.0**	3.2, 2.7–2.5	2.3–1.8, 1.4	170–230 km
Baltic Shield (Kola-Karelia & Lapland)	**2.9–2.7** (3.1)	2.7–2.6		200–300 km
SvecoFennian province	**2.0–1.8**			170–200 km
SvecoNorwegian province	1.75–1.5, extensively reworked at **1.1–0.9 Ga**		0.6–0.4	150–180 km
Transscandinavian Belt	1.8–1.6			110–140 km
East European platform	Archean (75%) and Paleoproterozoic (25%). Extensively reworked at **2.2–1.8 Ga** by widespread rifting	2.7–2.6	1.6–0.6	170–220 km
Volga–Urals anteclise	**~3.0**		1.6–0.6	200–220 km
Central Russia Rift System			**1.3–0.6**	170–200 km

Table 4.13 (cont.)

Precambrian cratons	Basement age (Ga)*	Cratonization age (Ga)	Major tectonic events (Ga)	Thermal thickness (km) (uncertainty *c*. 25%)
North American craton				
Wyoming craton	**3.96–3.4**, extensively reworked in Meso-Cenozoic	?	2.8–2.6, 1.9–1.8, 0.06	130–150 km
Slave craton	**3.96–3.1** gneiss and **3.1–2.6** granites	2.7–2.6	1.0–0.8	Few data points (ca. 200 km)
Wopmay Orogen (Bear province)	**1.9–1.8**			140–180 km
NE Churchill province (Hearne/Rae cratons)	**2.9–2.7** (3.5)	2.7–2.6		No data
W Churchill province (Taltson and Queen Maud blocks)	2.9–2.7, extensively reworked at **1.9–1.8 Ga**	2.7–2.6		No data
Trans-Hudson orogen	**2.0–1.8**			160–200 km
Superior craton (north-central part)	**>3.35 and 3.0–2.7**	2.7–2.6		175–240 km
Superior craton (southern part and Ungava craton)	**3.0–2.7 (3.4)**	2.7–2.6	**1.9–1.8**, 1.5–1.0	150–190 km
Nutak and Nain cratons (Labrador)	**3.9–3.4**		3.3–2.6	No data
Peripheral orogenic belts (Superior)			1.9–1.65, 1.3–1.0	No data
Penokean (Southern) province	**2.5–2.2** (3.5)		1.9–1.8	140–170 km
Yavapai (Central) province	**1.8–1.5**			140–170 km
Greenland & Lewisian	**3.82–3.7**	2.9–2.5		No data
Grenville province	**1.4–1.0**			140–200 km
Cathaysian craton				
Yangtze craton	Paleoproterozoic , extensively reworked in Meso-Cenozoic	1.85	1.05, 0.85–0.8	115–200 km
Orogenic belts at cratonic margins	**2.5–2.2, 1.86**			No data
Sino-Korean craton (Ordos, Ji-Lu nuclei)	**2.9–2.7** (3.57), extensively reworked in Meso-Cenozoic	2.6–2.5, 2.2–1.9	1.8–1.7, 1.5–1.4	115–200 km
Tarim craton	**Archean–Mesoproterozoic**	1.9, 1.0	1.5–1.4, 1.0, 0.85–0.6	No data
Median massifs (e.g. Junggar, Songliao)	**0.8–0.6**			140–180 km

Table 4.13 (cont.)

Precambrian cratons	Basement age (Ga)*	Cratonization age (Ga)	Major tectonic events (Ga)	Thermal thickness (km) (uncertainty *c*. 25%)
African craton				
Kaapvaal & Zimbabwe cratons	**3.5–3.2** (3.64)	3.2–3.0, 2.7–2.6	2.7–2.6	180–200 km
Peripheral orogenic belts, South Africa (e.g. Kheis, Magondi)	**2.0–1.8**			180–200 km
Mid-Proterozoic mobile belts, South and Central Africa (e.g. Namaqua-Natal, Irumides, Kibarian)	**1.3–1.0** (2.0)			120–140 km
Tanzanian craton	**3.0–2.6**		2.1–1.9	180–250 km
Central Africa (Angolian & Kasai cratons)	**3.5–3.4** and 3.0–2.6	2.7–2.55	2.1–1.75, 1.3, Pz–Mz	No data
Central Africa (Congo craton)	**Archean**, Extensively reworked in Phanerozoic		1.0	No data
West African craton (Archean shields)	**3.0–2.9** (3.5)	2.7–2.55	2.0, 0.8–0.6	240–350 km
West African craton (Taoudeni Basin and Man shield)	Archean–Paleoproterozoic, extensively reworked at **2.2–1.9 Ga**		1.0	240–350 km
Benin–Nigeria Shield	(3.5–3.0)		2.75, 0.6	150–200 km
Trans-Saharan Belt and Tuareg Shield	? (3.5), Extensively reworked at ~0.6 Ga	3.0, 2.1–1.95	1.1, 0.6	No data
Pan-African (Central African and Mozambique) mobile belts	**1.1–0.6**		0.65–0.55	90–140 km
Arabian–Nubian Shield	**0.95–0.68**			120–180 km
Antarctica				
Antarctic craton	Archean ? (3.8–3.93)	Unknown		No data

(Source: Artemieva, 2006)

* Basement age refers to the oldest known major crust-forming event (see references in Goodwin, 1996), it is not the age of the oldest known rocks (shown in brackets). In bold – ages used to constrain the continental thermal model TC1 (Artemieva, 2006).

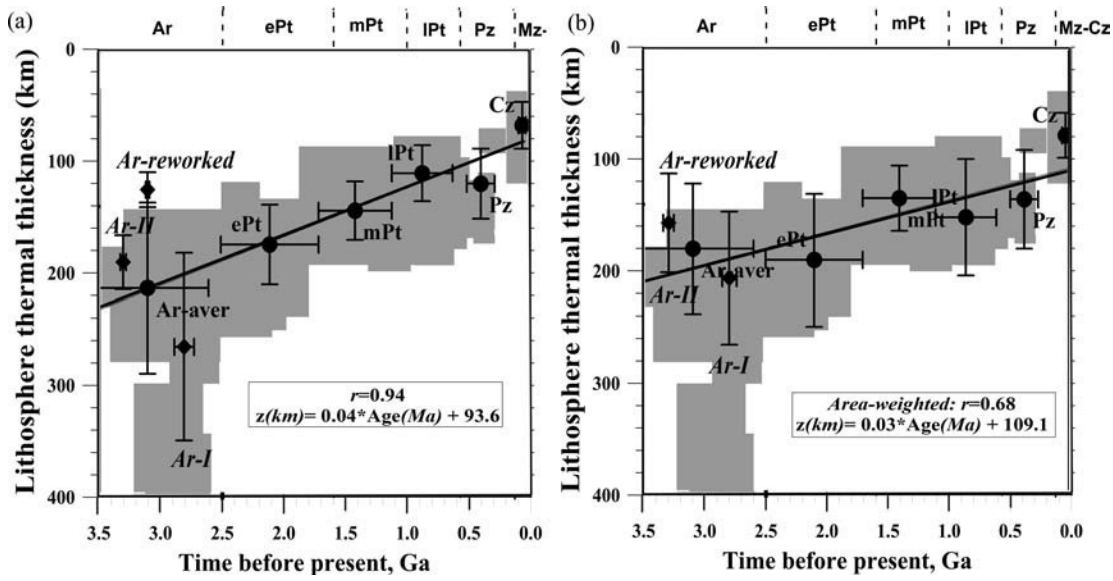

Fig. 4.48 Statistical analysis of variations of lithospheric thermal thickness with tectono-thermal age: (a) all continents; (b) area-weighted data for continents (Artemieva, 2006). Abbreviations are as in Fig. 4.46; Ar-I, Ar-II and Ar-average refer to young Archean (<3.0 Ga), old Archean (>3.0 Ga), and average values for all Archean terranes, respectively, excluding reworked Archean terranes.

and with a real scatter in lithospheric thickness values as a result of diverse tectonic evolution of terranes with similar ages.

If all lithospheric terranes are split into five groups by tectono-thermal age (the Archean (with all Archean terranes treated as one group), the early, middle, and late Proterozoic, and the Paleozoic, Table 4.12), the age–lithospheric thickness statistical correlation is surprisingly high ($r = 0.94$), and the average lithospheric thickness L can be approximated by a linear dependence as:

$$L[\text{km}] = 0.004^{*} t[\text{Ma}] + 93.6, \tag{4.38}$$

where t is the tectono-thermal age (Fig. 4.48a). This implies that, statistically, the minimal thickness of the continental lithosphere is ~90 km and it increases with age at a rate of ~4 km/100 My. This statistical relationship does not hold for some tectonic settings, such as modern zones of continent–continent or continent–ocean collision or Proterozoic terranes that are underthrust by Archean mantle. Furthermore, the statistics is significantly biased by the uneven distribution of borehole measurements over terranes of different ages: the correlation coefficient drops to, a still significant, value of $r = 0.68$ if the average values are area-weighted for terranes of different tectono-thermal age (Fig. 4.48b) and the lithospheric thickness roughly relates to tectono-thermal age as:

$$L[\text{km}] = 0.03^{*} t[\text{Ma}] + 109.1.$$

- Note that linear best-fits (eq. 4.38) do not have any physical meaning for the age-dependence of the thickness of the continental lithosphere, and are nothing more than mathematical approximations to the data.

Although the statistical analysis is based on tectono-thermal ages (the ages of the last major tectonic event) rather than the ages of the juvenile crust (i.e. the age of the major crust-forming event), such a distinction between geological and tectono-thermal age is speculative for many Precambrian terranes, where major crust-forming episodes were probably caused by large-scale thermal and tectonic events (e.g., superplumes or plate tectonic processes resembling those of the present). Moreover, some Archean–early Proterozoic terranes (e.g. the Wyoming, Sino-Korean, and Congo cratons) have undergone significant tectonic reworking in the Meso-Cenozoic. In the statistical analysis they are considered as a separate category of "reworked Archean cratons", since, having been formed under unique temperature and compositional conditions during the early evolution of the Earth, they are expected to have preserved, in part, the distinctive structure and composition of the lithosphere, different from that of Phanerozoic terranes (Artemieva, 2006).

To account for possible differences in the mechanisms of formation and later tectonic modification, the Archean terranes are subdivided into three groups: early Archean (older than 3.2–3.0 Ga), late Archean (3.0–2.5 Ga), and reworked Archean (with basement ages of 3.6–2.5 Ga). Surprisingly, unreworked Archean terranes display the opposite trend in variations of the lithospheric thickness with age: older Archean terranes (>3.0 Ga) have a lithospheric thickness of *c.* 200–220 km, while younger Archean terranes (<3.0 Ga) have lithospheric roots extending deeper than 250 km and perhaps as deep as 350 km (Fig. 4.49) (see next section for discussion).

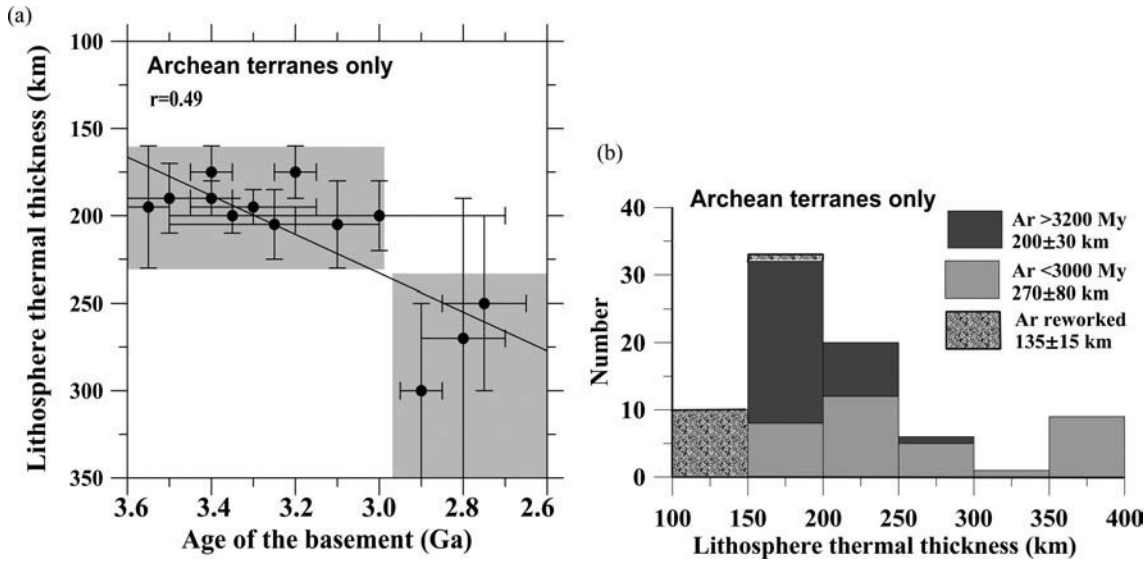

Fig. 4.49 (a) Variations of lithospheric thermal thickness with tectono-thermal age in Archean terranes (excluding reworked Archean cratons). (b) Statistics of lithospheric thermal thickness estimates for different Archean terranes. (Sources: Artemieva and Mooney, 2001; Artemieva, 2006.)

Global statistical thermal model

High statistical correlation between the ages and lithospheric geotherms, together with a $1° \times 1°$ database on lithospheric tectono-thermal ages (rather than the ages of the juvenile crust, Fig. 2.16), allows for constraining of the worldwide model TC1 of the thermal regime of the continents on a $1° \times 1°$ grid (Artemieva, 2006) (Fig. 4.44). The model is based on the following set of assumptions and simplifications.

(1) *Lithospheric geotherms*. Lithospheric temperatures in stable continental regions are constrained by high-quality surface heat flow data where available. In tectonically active continental regions (such as regions of Meso-Cenozoic extension, rifting, and volcanism) the thickness of the thermal lithosphere is assumed to be 60–100 km as indicated by xenolith geotherms. In modern zones of continent–continent or continent–ocean collision (e.g. the Andes, the Hellenic arc, the Alps) the lithospheric thickness is fixed at 220 km, in agreement with regional seismic tomography studies in continental collisional orogens which image the presence of subducted lithospheric slab in the upper mantle down to depths of 200–250 km. The Archean lithosphere of the Indian craton is assumed to underlain Tibet as suggested by recent seismic studies (e.g., Tilmann *et al*., 2003 and Fig. 3.95c).

(2) *Archean cratons*. Based on lithospheric geotherms constrained by surface heat flow and xenolith P–T arrays for the cratonic mantle (see Chapter 5), Archean cratons are subdivided into early Archean, late Archean, and reworked Archean. Lithospheric thickness is assumed to be ~220 km for the early Archean terranes of Central and Southern Africa, South America, Labrador, and Greenland, and 300 km for the late Archean Baltic Shield, Siberia craton, and the northern and northeastern parts of the Canadian Shield. The lithospheric thermal thickness in reworked Archean cratons is assumed to be 140 km.

(3) *Lithospheric ages*. A critical assumption of the model is that the age of the continental lithospheric mantle is the same as the age of the overlying crust (see Section 2.2). This assumption is based on Re–Os dating of mantle-derived cratonic xenoliths which suggests that the crust and the lithospheric mantle of the cratons have been spatially and temporally linked since their formation (Pearson, 1999). High-resolution seismic transects have demonstrated that this may not always be true, in particular along the cratonic margins. For example, Archean lithosphere underlies Proterozoic crust at the margins of the Fennoscandian and the Slave cratons and at the transition between the Superior and the Grenville provinces (BABEL Working Group, 1993; Clowes *et al*., 1998; Cook *et al*., 1999). However, nowhere are lateral extensions of Archean blocks underneath the younger crust seismically traced further than 100–200 km from the terrane boundary observed at the surface, and the uncertainty associated with assigning lithospheric mantle the same ages as the overlying crust has little effect on the resolution of the TC1 model. A larger uncertainty is associated with poorly known basement ages in several regions with a thick sedimentary or ice cover (e.g., Greenland, Antarctica, north-central and western Africa, central Australia, Yangtze craton in China, Rio Apa and Rio de la Plata cratons in South America), where the model constraints should be treated with caution.

The resultant map of the lithospheric thickness constrained by thermal modeling in regions with heat flow data and statistical values in other continental areas is shown in Fig. 4.44 and on the book cover.

Bimodal thickness of Archean–Paleoproterozoic lithosphere

The bimodal distribution of lithosphere thermal thickness in Archean–Paleoproterozoic terranes (Fig. 4.46) is in accord with models of mantle convection that show that depleted cratonic lithosphere should have two equilibrium thicknesses, stable at ~350 km and unstable at ~220 km (Doin *et al*., 1997). In the case of low activation energy of the upper mantle (expected for sublithospheric processes with a Newtonian rheology), $V^* < 2 \times 10^{-6}$ m^3/mol, a unique equilibrium lithospheric thickness is >450 km. However, the existence of the transition zone forbids lithosphere thickness in excess of 410 km. Lithosphere erosion from below or from the sides can occur when the heat flow supplied to the lithospheric base by sublithospheric small-scale convection exceeds the heat flow conducted through the lithosphere. In the case of thick (~350 km) lithosphere, small-scale convection at its base is sluggish and the basal part of the lithosphere is mainly destabilized by lateral erosion with a rate of ~0.4 km/Ma, so that in 2.5 Ga the width of the Archean lithospheric keel would decrease by ~1000 km (Fig. 4.50). In contrast, thinner (~220 km) lithosphere is in unstable equilibrium: it can either thicken or erode, but when the lithospheric thickness is close to the equilibrium value, its evolution should be slow. Numerical simulations demonstrate that the basal part of a ~220 km-thick depleted cratonal lithosphere is effectively eroded by strong sublithospheric small-scale convection with a rate of vertical erosion of ~0.16 km/Ma (Doin *et al*., 1997). As a result, in ~1 Ga its thickness would be reduced to a stable value typical for thin, non-cratonic lithosphere.

Several observations related to the bimodal thickness of the Archean–Paleoproterozoic lithosphere should be mentioned:

- paleo-Precambrian cratons surrounded by Proterozoic mobile belts (as in South Africa, South America, western Australia, and India) have lithospheric thickness around 200–220 km, while the cratons without surrounding Proterozoic mobile belts (as in North America, Siberia, Europe, and West Africa) are characterized by thick lithospheric roots (250–350 km) (Fig. 4.44);

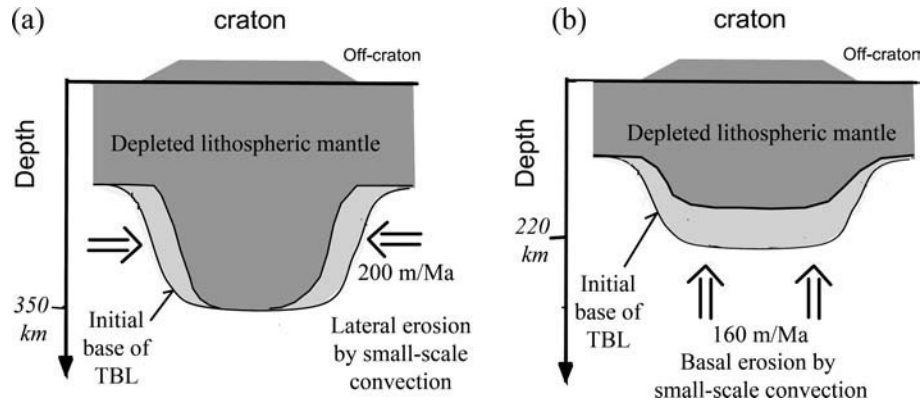

Fig. 4.50 Erosion of depleted cratonic lithosphere by small-scale sublithospheric convection (based on results of numerical modeling by Doin *et al*., 1997). Thick (~350 km) lithosphere is eroded laterally, while thinner (~220 km) lithosphere is eroded vertically.

- the cratons with thick lithospheric roots were parts of Laurasia, while cratons with thinner lithosphere roots were parts of Gondwanaland;
- the cratons with thin (200–220 km) lithosphere are, in general, older (>3.2–3.0 Ga) than the cratons with thick lithosphere (Fig. 4.49a).

These correlations cannot easily be explained with the present knowledge on how the early lithosphere was formed, a question that still remains enigmatic. The widespread occurrence of metasediments with negative Eu anomalies (e.g. in Antarctica, Anabar Shield in Siberia, Greenland) suggests that relatively large fragments of the continental lithosphere already existed by 3.4–3.55 Ga (Kröner, 1991), while seismic reflection studies across the margins of the Archean part of the Canadian Shield (e.g. Calvert *et al*., 1995; Cook *et al*, 1999) and available paleomagnetic data provide cogent evidence that some form of plate tectonics already operated in the late Archean (Hale and Dunlop, 1984; Hale, 1987). The existing models of lateral and vertical growth of the continental nuclei based on diverse geophysical, tectonic, and geochemical evidence can be reduced to two types:

(1) the "Iceland type" model which includes plume-induced mantle melting, further differentiation and magmatic underplating (e.g. Ashwal *et al*., 1982), and
(2) the "accretion model" according to which the cratons grew by collision of oceanic terranes, shallow subduction, and underplating of slabs around the perimeters of pre-existing lithospheric fragments (Abbott and Mooney, 1995; Rudnick, 1995).

Windley (1995) distinguishes four different types of Archean crust, and one may expect that due to significant differences in their formation mechanisms, several different types of Archean lithospheric mantle may exist as well:

(1) cratons with intraoceanic tectonics followed by a stage of intracontinental tectonics (Kaapvaal);
(2) cratons formed at an active continental margin (Greenland, Labrador, NW Scotland);
(3) cratons formed at a passive continental margin (India and NE China);
(4) cratons formed by collision of island arcs (the Superior Province and the Slave craton).

While cratons of the first two types have a well-documented geological and tectonic history from late to early Archean, no early-mid-Archean history is known for the last two types. The spatial correlation between thin Archean roots and Proterozoic mobile belts suggests that the initial lithospheric thickness could have been the same in all of the Archean cratons, and the lower part of the roots could have been removed during adjacent Proterozoic orogenic activity. Alternatively, thick cratonic roots with ages of 2.9–2.6 Ga could be formed by Archean–Paleoproterozoic plate tectonic processes and were not an immediate product of mantle differentiation as the "Iceland type" model implies. Such thick lithospheric roots may remain stable with respect to mantle convection, preserving their original thickness since the Archean while gradually shrinking in lateral dimensions (Fig. 4.50).

Lithosphere preservation, thermal blanketing, and heat diversion

A collision of oceanic fragments with a continental nucleus could led to tectonic stacking, lithosphere thrust-thickening, and tectonic underplating, similar to the present-day Himalayas and Tibet. These tectonic processes could result in the formation of very thick crustal (>45–50 km) and lithospheric (in excess of 300 km) roots. This hypothesis is supported by data from the Baltic Shield, where a region of thick crust, atypical for Precambrian cratons and locally reaching 60 km, and thick lithosphere is located at the tectonic boundary between the Archean Kola-Karelian and the Paleoproterozoic SvecoFennian terranes in central Finland. Long-term preservation of crustal and lithospheric roots requires that they were thermally insulated from the mantle. If not, the lowermost part of the crust may have later transformed into eclogite facies and become seismically indistinguishable from the mantle or delaminate. The presence of a thick lithospheric root is supported by mantle xenoliths from the terrane boundary, which indicate a cold cratonic geotherm and show no evidence of shearing in xenoliths (commonly interpreted as being associated with mantle zones of reduced viscosity and asthenospheric flow) down to 240 km depth (Kukkonen and Peltonen, 1999). Extremely low surface heat flow in the area (30.2 ± 7.4 mW/m^2, $n = 16$) can be explained by either an abnormally low radiogenic crust, or by a very thick lithospheric root, or by a combination of both. In agreement with observations in Fennoscandia, a 300–350 km-thick lithospheric root produces a surface heat flow anomaly over an area of *c*. 1000 km across (Fig. 4.35).

The lateral extent of thick crustal and lithospheric roots can be relatively small and in the Baltic Shield it is largely restricted to the suture between the Archean–early Proterozoic terranes. Because of their small lateral size (a hundred to a thousand kilometers across, Fig. 4.50), such cratonic roots would not necessarily be resolved in seismic tomography models. However, they will still be efficient in diverting mantle heat sideways from the area with the thickest lithosphere. The latter process will lead not only to a reduction in surface heat flow above the root, but also to a heat flow increase in the adjacent regions, the mechanism initially proposed to explain the difference in surface heat flow between the Archean terranes and the surrounding Proterozoic mobile belts in South Africa (Ballard and Pollack, 1987). In central Finland, the belt of Proterozoic anorogenic magmatic activity (rapakivi granites) encircles a region with thick lithosphere and low surface heat flow from north, west, and south. This supports the hypothesis of an effective deflection of mantle heat sideways from the region with a thick lithospheric root (>250 km) which, during Proterozoic tectonism, enhanced mantle melting which produced anorogenic granites (Artemieva, 2006).

4.5 Heat flow balance of the Earth

Data on the heat balance of the Earth and the total heat loss provide critical constraints for models of planet evolution and boundary conditions for mantle convection models. Global heat loss has been examined in several studies (Williams and von Herzen, 1974;

Davies, 1980; Sclater *et al*., 1980, 1981) and the estimated values range from 41.0 to 44.2 TW (10^{12} W). The latter value reported by Pollack *et al*. (1993) is commonly taken for the total heat loss.

Calculations of global heat loss are based on heat flow observations that are integrated over the Earth's surface. Since data are absent for significant parts of the globe, statistically averaged values calculated for well-sampled tectonic regions with certain ages and specific geological characteristics are assigned to areas with the same ages and similar tectonics. Pollack *et al*. (1993) distinguished 21 categories: 9 on continents and 12 in the oceans. Calculation of the mean heat flux of the continental lithosphere yields 65 mW/m^2. Although subdivision of oceanic lithosphere into categories is easier due to well-constrained ocean floor age, the calculation of the mean heat flux of the oceanic lithosphere is not as straightforward as for continents. The complications arise from two issues.

(1) Heat flow through oceanic lithosphere closely follows the square root dependence on ocean floor age (Parsons and Sclater, 1977). As discussed in detail in Section 4.3, thermal evolution of the oceanic plate (in particular <80 Ma) is well described by a cooling plate model (McKenzie, 1967), according to which oceanic plate is created at a mid-ocean ridge (age 0 Ma) and thickens as it cools and moves away from the ridge. This mathematical formulation does not allow integration of heat floor for all ocean floor ages because such an integration gives an infinite heat flux at the origin (the ridge). Several approaches have been proposed to overcome this difficulty. Sclater *et al*. (1980) modified the plate model following the assumption of Davis and Lister (1974): heat flow at the ridge is equal to the sum of the horizontal conductive heat loss and vertical heat loss by magmas. The error in such estimate of heat loss through the ocean floor is ~10–20% (Sclater *et al*., 1980). An alternative approach was proposed by Hofmeister and Criss (2005) who attempted to ascertain the Earth's mean oceanic heat flux directly from compiled heat flow data. Their result, which yields the global heat loss value of 31 ± 1 TW, caused heated debates and is not generally accepted (Von Herzen *et al*., 2005).

(2) The square root dependence of oceanic heat flow on ocean age may be obscured by a strong effect of hydrothermal circulation, which is particularly strong for young oceanic lithosphere (Fig. 4.22). A high scatter in heat flow values is observed near all spreading centers which leads to heat flow values significantly lower than predicted by the plate model. The reduction in measured heat flow is caused by seawater convection through oceanic crust. Most deep-sea sediments have low permeability. When the permeable crust is covered by a sufficient thickness of sediments, free water circulation in the crust still continues, but no heat is lost to the surface by advection, and heat flow measurements provide a reasonable estimate of deep heat flow (Lister, 1972).

Stein and Stein (1992) analyzed heat flow data from the oceans and concluded that, after the effect of hydrothermal circulation is excluded, heat flow in oceans older than 1 Ma can be approximated as $Q_{oc} = c / t^{1/2}$ where t is the age of ocean floor in Ma, heat flow Q_{oc} is in mW/m^2, and constant $c = 510$ for young oceans (see discussion in Section 4.3.2). These authors estimate mean heat flow in Quaternary oceans as 806.4 mW/m^2, in strong contrast to measurements that give a mean value of 139.5 mW/m^2 (Pollack *et al*., 1993) (Fig. 4.19).

Using the statistical heat flow values for the continents and oceans older than 60 Ma and the preferred values of Stein and Stein (1992) for oceans younger than 60 Ma, Pollack *et al*. (1993) estimated that the global mean heat flow is 87 mW/m^2 and the global heat loss is 44.2 TW. Of the global heat loss at the Earth's surface, only ~30% of heat is lost through continents and shelves and ~70% through the deep oceans and marginal basins (and about 50% of this loss takes place in oceanic lithosphere, which is younger than 20 My, and 75% in oceanic lithosphere, which is younger than 80 My) (Sclater *et al*., 1980).

A recent review of the heat loss of the Earth is provided by Malamud and Turcotte (1999) (Fig. 4.51). Of the heat loss from the mantle that constitutes *c*. 85% of the total heat loss, 58% is attributed to the subduction of the oceanic lithosphere and the remaining 42% are attributed to basal heating of the oceanic and continental lithosphere by mantle plumes (hotspots) and/or secondary convection. If there were no basal heating in the oceanic lithosphere, its thickness would have followed the cooling half-space model for all ocean-floor ages with a square-root relationship between the age and the ocean-floor topography (see Section 4.3 for a detailed discussion).

The mean basal heat flow through the oceanic lithosphere is estimated to be between 25 and 38 mW/m^2 (Sclater *et al*., 1980). Other estimates of basal heat flow through the oceanic lithosphere are between 40 mW/m^2 (Doin and Fleitout, 1996) and 50 mW/m^2 (Stein and

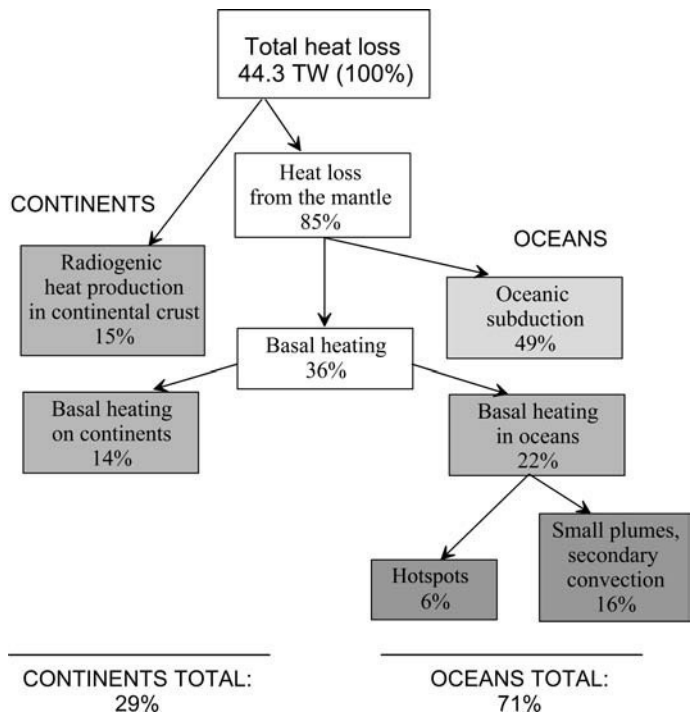

Fig. 4.51 Present heat balance of the Earth (source: Malamud and Turcotte, 1999). Total heat loss is based on the total global surface heat flow (Pollack *et al*., 1993). Numbers – rounded percentage from the total.

Table 4.14 Heat flow balance of the Earth

Source of heat	Mean surface heat flow* (mW/m^2)	Heat loss (TW)**	Total global heat loss (%)
Continents (area 2.0×10^8 km^2)	65.0 ± 1.6	13.0 ± 0.3	29.3
Radiogenic heat production in continental crust	*34 ± 8*	*6.8 ± 1.6*	*15.3*
Basal heating of continental lithosphere	*31 ± 8*	*6.2 ± 1.6*	*14.0*
Oceans and marginal basins (area 3.1×10^8 km^2)	101.0 ± 2.2	31.3 ± 0.7	70.7
Subduction of oceanic lithosphere	*70 ± 8*	*21.7 ± 2.5*	*49.0*
Basal heating of oceanic lithosphere	*31 ± 8*	*9.6 ± 2.5*	*21.7*
Total global	86.9 ± 2.0	44.3 ± 1.0	100

(after Malamud and Turcotte, 1999)
* Sources: Sclater *et al*., 1980; Pollack *et al*., 1993
** $1TW=10^{12}$ W

Stein, 1992). The mean area-averaged basal heat flow through the continental lithosphere is estimated as 25–29 mW/m^2 (Sclater *et al*., 1980; Malamud and Turcotte, 1999).

Mantle plumes are expected to contribute ~5–7% to the total heat loss, and assuming a power-law correlation between the number of plumes (hotspots) and their size (buoyancy flux), the estimate of Malamud and Turcotte (1999) requires 5200 plumes. This extreme number of plumes received unexpected support from a recent global tomography study (Montelli *et al*., 2004); however, probably not every local velocity anomaly (local upwelling?) should be considered as a plume. In contrast, calculation of plume buoyancy fluxes from swell magnitudes gives an estimate of plume heat flux of only ~1% of the global heat loss (Davies, 1988; Sleep, 1990). On the whole, ~65% of present global heat is lost by convection (which includes oceanic plate creation and continental orogenies), ~20% by conduction, and the remaining ~15% by radioactive decay of heat-producing elements in the crust. More details are provided in Table 4.14.

4.6 Thermal lithosphere: summary

Factors affecting heat flow data

Surface heat flow measurements provide the major constraint on the thermal state of the lithosphere. The measured parameters are (typically) depth variations of temperature gradient in a borehole and thermal conductivity of rocks. High quality scientific data requires that temperature equilibrium should be achieved in the borehole after drilling. This requirement is commonly not met when measurements are made in industrial boreholes.

The depth of the borehole is another critical factor for data quality. Shallow measurements are affected by temperature variations at the surface (e.g. climate change); the effect of the Pleistocene glaciation on heat flow measurements in shallow boreholes may amount to

10–20 mW/m^2. The amplitude of the paleoclimate effect on heat flow measurements decreases with borehole depth and becomes unimportant in drill holes deeper than 1.5–2 km. Groundwater circulation is another factor critical for heat flow quality; its effect is more severe in very shallow boreholes (e.g. in the coastal regions in Texas, USA), but it is difficult to assess its amplitude. Similarly, heat flow advection in shallow magmatic systems enhanced by crustal faults has a strong effect on heat flow measurements in tectonically active regions and leads to strong variability in measured values.

Even in the case when heat flow data are of high quality, several problems remain. First, data coverage by borehole measurements is very uneven. There are large areas both on continents and in oceans, where data are absent. Second, measurements in deep scientific drill holes indicate a very complex pattern of vertical variations in heat flow, inconsistent with theoretical predictions on heat flow decrease with depth. It is debatable which of the measured values is representative of surface heat flow. Importantly, heat flow measured in boreholes reflects not the present-day but the past thermal regime of the lithosphere. The reason being that conductive heat transfer is a slow process and a thermal anomaly propagates from the depth L [in km] to the surface over time $\sim L^2/31.5$ [in Ma].

Resolution problems

Surface heat flow is used to constrain lithospheric geotherms. Lateral resolution of thermal models depends critically on heat flow data coverage. The wavelength of surface heat flow variations puts an additional limit on lateral resolution of thermal models for the mantle, which is not better than 100–150 km for thermal anomalies produced below a 40 km depth (the continental Moho). Surface heat flow anomalies with lateral size <100 km originate in the upper 40 km (e.g. in the continental crust due to crustal radioactivity).

A severe problem in thermal modeling is amplitude resolution of thermal models (i.e. the range of possible temperatures at a fixed depth). On the continents, heat production plays a critical role in determining lithospheric temperatures. Several independent sets of data (such as laboratory measurements on near-surface rocks and overturned (exposed) crustal sections, geochemical constraints based on crustal/mantle chemical budgets, petrologic studies on crustal and mantle xenoliths, model constraints on heat flow–heat production relationships observed in many tectonic provinces), when used together, provide tight limits on bulk crustal heat production. However, direct data for the lower crust and lithospheric mantle is largely absent. As a result, heat production in the continental lithosphere is always a model assumption, and the true model uncertainty cannot be estimated. Temperature dependence (chiefly in the mantle and in the oceans) and compositional variability (in the continental crust) of thermal conductivity further affect thermal models, but the effect is much less important compared with heat production. Sensitivity tests for physically feasible ranges of heat production and thermal conductivity values indicate that amplitude resolution of thermal models is not better than 50–100 °C at any depth which is equivalent to *c*. 25% for lithospheric thickness. In continental regions with surface heat flow <30 mW/m^2, steady-state geotherms asymptotically approach the mantle adiabat at depths >250 km; as a result solutions are asymptotic and the true lithosphere thickness cannot be constrained; phase transition at 410 km depth limits the maximum thickness of cratonic TBL.

Major results and global trends

Surface heat flow is highly variable even at small distances. In general, higher heat flow is observed in young structures both on continents and in oceans. The mean heat flux is 65 mW/m^2 on continents and 101 mW/m^2 in oceans, with a global mean of 87 mW/m^2.

In oceans, TBL thickens by conductive cooling. Oceanic regions where bathymetry follows $1/\sqrt{\text{age}}$ are termed "normal oceans" and they are typically younger than 80 Ma. In normal oceans, heat flow depends on ocean floor age as $\sim \sqrt{\text{age}}$, and the lithosphere thickens with age as $\sim 13\sqrt{\text{age}}$. In old oceans (80–160 Ma), bathymetry is more shallow than $1/\sqrt{\text{age}}$ dependence predicts (ocean floor flattening). The plate model, with a 95 km to 125 km-thick lithospheric plate, is commonly used to explain bathymetry in old oceans. A constant temperature at the base of the plate required by the model is assumed to result from small-scale mantle convection. Two recent studies (Korenaga and Korenaga, 2008; Adam and Vidal, 2010) reanalyzed bathymetry data in old oceans; they question the existence of seafloor flattening and, as a result, the necessity to use the plate model for the evolution of oceanic lithosphere.

In continental regions, lithosphere thickens with age but does not follow any simple relationship. Two major reasons for a complex thermal structure of the continental lithosphere are heterogeneity of distribution of crustal heat production (which is not correlated either with major rock chemistry or with tectonic setting) and a 4 billion years long tectonic evolution of the continental lithosphere. Several lines of evidence indicate that old cratonic lithosphere has been formed under unique conditions and, therefore, has a significantly different composition and tectonic structure (see Chapters 6 and 9) that cannot be explained by a simple conductive cooling of TBL. Many Archean cratons (usually older than 3.0 Ga) have a 200–250 km-thick lithosphere; some Archean terranes (typically younger than 3.0 Ga, such as in the East European craton, Siberian craton, West Africa, and in the northern and northeastern parts of the Canadian Shield) may have preserved 300–350 km-thick lithospheric roots. Thickness of continental TBL decreases to younger terranes, with typical values of 200 ± 50 km in the Paleoproterozoic terranes, 140 ± 50 km in Meso-Neoproterozoic terranes and 100–120 km in the Paleozoic regions. Some Archean cratons have lost the lower parts of the lithospheric mantle and the present lithospheric thickness in the Wyoming, Tanzanian, and Sino-Korean cratons does not exceed 120–150 km. In tectonically active Cenozoic regions (except for the collisional orogens), the lithosphere thickness is typically 60–80 km.

The temperature difference between cratons, platforms, and tectonically active regions as compared to the average mantle is, correspondingly, -310 ± 200 °C, -160 ± 260 °C, and $+30 \pm 130$ °C at 100 km depth and -90 ± 70 °C, -80 ± 100 °C, and -30 ± 70 °C at 200 km depth. More details are provided in Table 4.15.

Table 4.15 Summary of thermal structure of the lithosphere for some tectonic provinces

Tectonic structure	Summary of thermal structure of the lithosphere
Normal oceans (<80 Ma)	Bathymetry ~ $1/\sqrt{\text{age}}$; heat flow ~ $\sqrt{\text{age}}$; lithosphere thickness L is approximated by cooling plate or cooling half-space models with $L \sim 13\ \sqrt{\text{age}}$
Normal oceans (80–180 Ma)	Bathymetry more shallow than predicted by $1/\sqrt{\text{age}}$ and lithosphere thinner than predicted by $\sqrt{\text{age}}$. Some recent studies question these conclusions
Back-arc basins	Mean heat flow is similar to the major ocean basins of the same age and follows the theoretical $\sqrt{\text{age}}$ predictions
Mid-ocean ridges	A high scatter in heat flow values; mean heat flow values significantly lower than predicted due to seawater convection through the crust
Archean–Paleo-proterozoic cratons	Approximately steady-state thermal regime with very low heat flow. Moho temperatures 300–500 °C, lithospheric thermal thickness typically exceeds 200 km and in some terranes can be >300 km
Meso-Neoproterozoic cratons	Approximately steady-state thermal regime with low heat flow. Moho temperatures 500–700 °C, typical lithospheric thermal thickness 120–160 km
Paleozoic basins	Approximately steady-state thermal regime with moderate heat flow. Moho temperatures 600–700 °C, typical lithospheric thermal thickness 100–140 km
Collisional orogens	Transient thermal regime. Geotherms are depressed in the subducting slab
Extended crust	Transient thermal regime. Moho temperatures 700–900 °C, lithosphere thermal thickness typically 60–80 km

5 Thermal state of the lithosphere from non-thermal data

The previous chapter discussed the thermal regime of the lithosphere constrained by borehole heat flow measurements; the present chapter focuses on other methods to assess lithospheric temperatures. These include conversion of physical parameters measured in remote geophysical sampling, such as seismic velocities, seismic attenuation, and electrical conductivity, into the temperature of the crust and the upper mantle. The chapter also discusses magnetic methods for determining depth to the Curie point and lithospheric geotherms, while other approaches that provide additional information on the thermal state of the lithosphere (such as apatite fission track analysis, data from metamorphic core complexes, and data on temporal variations in magmatism) are excluded from the discussion.

Mantle xenoliths provide invaluable constraints both on lithosphere composition and its thermal structure, in particular in Precambrian terranes. Uneven worldwide coverage by high-resolution geophysical and mantle xenolith data makes comparison of different approaches for estimating mantle temperatures (or calibrating models) difficult in many regions (Table 5.1). The major reference books on petrologic studies of mantle xenoliths are Nixon (1987) and Pearson *et al.* (2003). Chapter 6 discusses petrologic studies of mantle xenoliths related to density of the lithospheric mantle, the chemical boundary layer, and the tectosphere, which closely links thermal and compositional anomalies in the cratonic lithospheric mantle.

5.1 Xenolith data

5.1.1 Xenoliths: advantages and disadvantages

Xenoliths and xenocrysts

Xenoliths (from the Greek word meaning "foreign rock") are rock fragments entrapped by magmas (such as basalts, kimberlites, lamproites, and lamprophyres) during eruption and transported to the surface. They range in size from small fragments to more than 1 m across, have a composition different from the host volcanic rock, and represent pieces of crustal or mantle rocks that were picked up by rising magmas either from the margins of a magma chamber or from the walls of magma conduit. In contrast, xenocrysts ("foreign crystals") are individual crystal inclusions within igneous rocks, such as diamonds within kimberlite diatremes.

Xenoliths and xenocrysts (together with orogenic peridotite massifs and ophiolites – mantle fragments exposed by tectonic activity) provide a direct, although non-uniform, sampling of the lithosphere at the time of eruption. This invaluable geochemical information on chemical and physical properties of the lower crust and the upper mantle forms a

Table 5.1 Geophysical and petrological data coverage for cratons

Cratons	Data on crustal structure[1]	Seismic tomography models	Heat flow boreholes[2]	Electrical conductivity data[3]	Mantle xenolith data[4]
North America and Greenland					
Superior province	Largely well known	Regional	Mostly at the southern margin, few in the NE part	Available, high-resolution	Available at the southern margin
Slave craton	Poorly known	Global	Only two boreholes	Available, high-resolution	Available
Northern margin of the Canadian Shield	No data	Global	Few boreholes	Unavailable	Available
Greenland	Poorly known	Regional	Only three boreholes	Unavailable	Available at the western margin
South America					
South American craton	Poorly known	Regional, poor ray coverage	Poor and patchy coverage, no data for large areas, quality variable	Unavailable	Mostly from the Guyana craton
Siberia					
Siberian Platform	Patchy coverage	Regional, poor ray coverage	Uneven coverage, particularly bad in the central part, good at the kimberlite fields and in the south	Available, largely old models	Available in the eastern part
Europe					
East European Platform	Good, except for central parts of the craton	Regional in south-west, global in northeast	Dense coverage with deep boreholes	Available, largely old models	Unavailable
Baltic Shield	Well known	Regional	Good coverage	Available	Available
Australia					
Australian craton	Patchy coverage	Regional	Mostly good coverage, but poor in Central Australia	?	Available in some locations, mostly at the margins

Africa					
South African craton	Well known	Regional	Dense coverage	Available, high-resolution	Available both in the craton and in mobile belts around it
West African craton	Largely unknown	Global	Sparse coverage	Unavailable	Unavailable?
Tanzanian craton	Good	Regional	Good coverage	Unavailable	Available, but can be affected by rift-related Cenozoic magmatism
India					
Indian Shield	Good	Global, old regional	Dense coverage	Unavailable	Available
China					
Sino-Korean and Yangtze cratons	Patchy coverage, does not exist in many regions	Regional	Largely good coverage, but of unknown quality	Unavailable ?	Available, but can be affected by Meso-Cenozoic tectonic activity

(1) Data on crustal structure is critical for accurate crustal corrections (see Fig. 3.38b for data coverage).
(2) See Fig. 4.16a for data coverage.
(3) See Chapter 7 for details.
(4) See Fig. 5.1 for data coverage.
(5) See Fig. 3.83a for ray coverage.

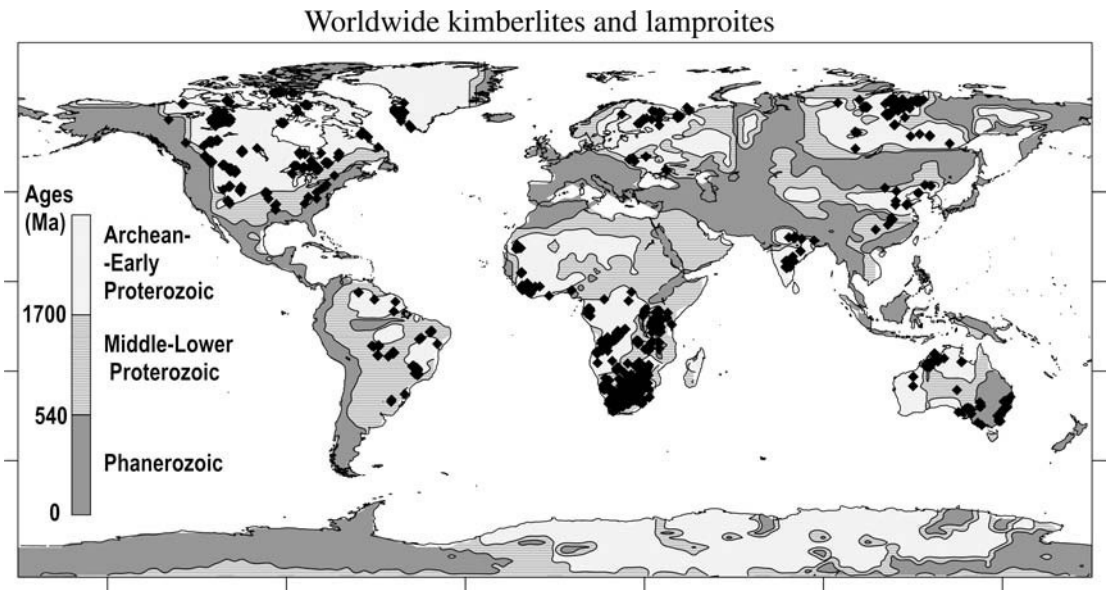

Fig. 5.1 Map showing worldwide distribution of kimberlites and lamproites (data source: www.consorem.ca) superimposed on a simplified map of crustal ages (source: Artemieva, 2006).

substantial part of present knowledge on the composition and thermal regime of the deep parts of the lithosphere (a review of lower crustal xenolith studies can be found in Rudnick and Fountain, 1995). In particular, mantle xenolith studies indicate that peridotite volumetrically dominates the composition of the upper mantle.

Mantle-derived xenoliths are abundant (at present ~3500 localities are known globally, see Canil, 2004 for references); however, their occurrences are largely restricted to certain tectonic settings, while large areas of the Earth remain un(der)sampled (Fig. 5.1). On the continents, peridotite xenoliths are available for many of the Archean–Proterozoic cratons of Africa, Canada (Fig. 5.2), Siberia (Fig. 5.3), Baltic Shield, Australia, India, China, and South America (Guyana craton). These xenolith data have significantly contributed to the knowledge of the composition and thickness of cratonic upper mantle and the mechanisms of formation, preservation, and destruction of lithospheric roots. Xenoliths from the Wyoming craton in North America and the Sino-Korean and Yangtze cratons in China provide data on the compositional and structural modification of the cratonic mantle during Proterozoic and Phanerozoic tectonism (Hearn, 2003). Spinel peridotites from xenoliths from the Phanerozoic mantle of the continents (e.g. the Vitim plateau in Siberia, Eastern Australia, the Pannonian Basin, French Massif Central, the Rhenish Massif) provide further constraints on the thermal regime of active continental regions and variations in mantle composition, related to the global evolution of the Earth. Some kimberlites contain eclogite xenoliths which are the products of high-pressure metamorphism of subducted oceanic basaltic crust.

Geochemical studies of mantle-derived xenoliths from different tectonic settings reveal a pronounced correlation between the age of the overlying continental crust and the mantle chemical composition, which is interpreted as a secular, irreversible trend from highly depleted (due to loss of iron during melt extraction) Archean continental lithospheric mantle

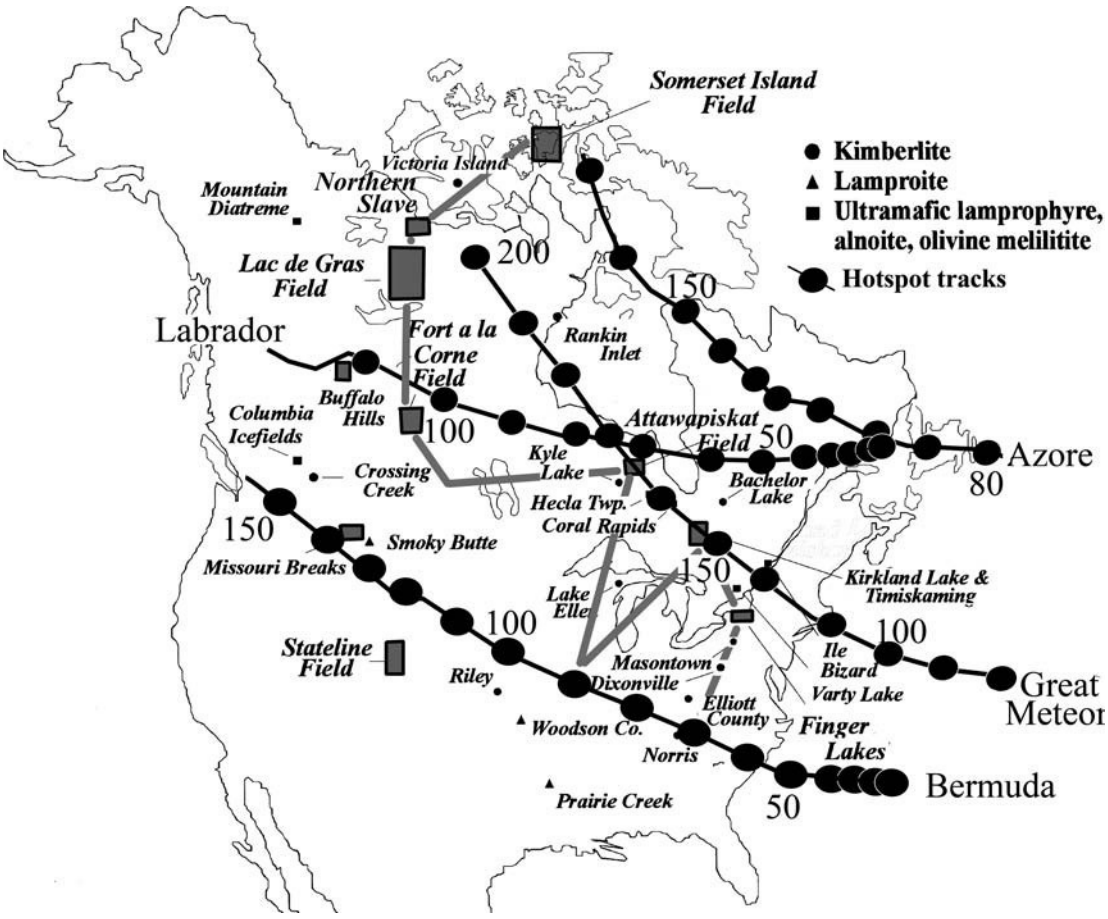

Fig. 5.2 Distribution of kimberlite clusters and fields in North America (after Heaman and Kjarsgaard, 2000) and the continental extensions of four Mesozoic and Cenozoic hotspots tracks (after Morgan, 1983). Gray line marks the profile discussed in Fig. 6.15.

to fertile Phanerozoic continental and suboceanic mantle (Griffin *et al*., 1998a). This fundamental difference in major-element composition of the oceanic and cratonic lithospheric mantle had been recognized in the 1980s (Boyd, 1989; Fig. 3.105). The number of mantle-derived xenoliths from oceanic basins is very limited, although extensive xenolith suites are available from oceanic hotspots (Hawaii, the Canary Islands, Grande Comore, and Tahiti) and from the Ontong–Java oceanic plateau. Some xenoliths with metasomatized mantle wedge or mantle lithosphere compositions have been reported for several oceanic subduction zones (Indonesia, Japan, Lesser Antilles).

Limitations of xenolith data

Certain limitations related to geochemical studies of mantle-derived xenoliths should be mentioned:

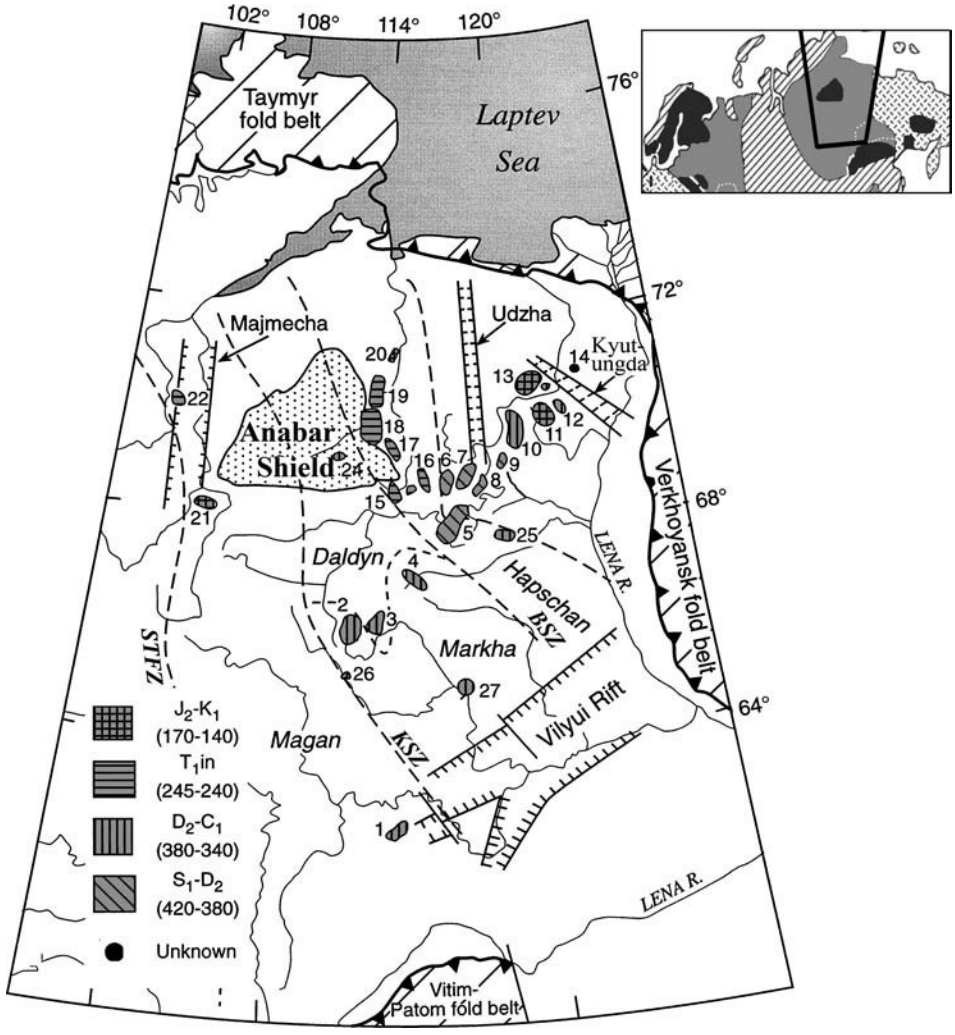

Fig. 5.3 Distribution of kimberlite clusters and fields in Siberia (Source: Griffin *et al.*, 1999a) plotted onto the tectonic map of Siberia with names of major terranes and rifts (Source: Rosen *et al.*, 1994). Abbreviations: SFTZ = Sayan-Taymyr fault zone; KSZ = Kotuykan shear zone; BSZ = Billyakh shear zone. Key to kimberlite fields: 1 – Malo-Botuobinsk (pipe Mir), 2 – Alakit, 3 – Daldyn (pipe Udachnaya), 4 – Upper Muna, 5 – Chomurdakh, 6–7 – Ukukit, 8 – Upper Motorchuna; 9 – Merchimden; 10 – Upper Molodo; 11 – Kuoika; 12 – Toluopka; 13 – Kuranakh; 14 – Lower Lena; 18 – Middle Kuonamka; 19 – Lower Kuonamka; 20 – Orto Irigakh; 21 – Kharamai; 22 – Dalbicha; 23 – Chadobez; 24 – Central Anabar; 25 – Severnei; 26 – Morkoka; 27 – Markha. The profiles along the kimberlite fields 1–13 are shown in Figs. 5.11 and 6.17.

(1) since xenolith occurrences are restricted to certain tectonic settings, it is unclear how representative "Nature's sampling" is, and if lithospheric mantle unsampled by xenoliths has the same composition as xenolith-sampled (see Section 6.3 for details);
(2) the small size of mantle xenoliths limits accuracy of estimates of their bulk composition and restricts studies of compositional heterogeneity of the mantle;

(3) chemical reactions between xenoliths and host magmas further complicate petrologic interpretations;
(4) xenoliths provide a snapshot of the thermal state of the mantle at the time of eruption; but this thermal regime (in particular, in cratonic settings) can be significantly perturbed from the steady state by active tectono-magmatic processes which caused magma eruption;
(5) compared to orogenic peridotite massifs, xenoliths lack a field relationship with surface tectonics. However, in contrast to peridotite (orogenic) massifs which tend to re-equilibrate during emplacement, xenoliths erupt fast and preserve the mineralogical and chemical signatures of their depth of origin;
(6) the maximum depth sampled by xenoliths does not exceed 250 km. This depth limitation, however, is apparently directly linked to the P–T conditions of kimberlite magma generation but not to the maximum depth extent of the lithospheric mantle. For example, some ultrahigh-pressure xenoliths from the Jagersfontein kimberlite in Kaapvaal, South Africa, and from Sierra Leone were derived from a depth of ~500 km (13–15 GPa) (Haggerty and Sautter, 1990).

5.1.2 Xenoliths and the boundary layers

Xenolith data are often used to constrain lithospheric thickness in various tectonic settings. Different lithosphere definitions (discussed further in detail) are employed for this purpose (Fig. 5.4).

Thermal boundary layer

Geothermobarometers (reviewed by Smith, 1999 and discussed in Section 5.2) provide a possibility for estimating equilibrium temperature and pressure (i.e. the depth of origin) of individual mineral grains in mantle-derived xenoliths at the time when they were entrained into the host volcanic rock. Such xenolith P–T arrays (commonly referred to as xenolith geotherms) provide an estimate of the lithospheric geotherm and of lithospheric *thermal thickness* (TBL) at the time of eruption of xenolith-carrying volcanic rocks (sometimes erroneously interpreted as reflecting the present-day, but not paleo-thermal regime of the mantle during magmatism). Similarly to thermal models, the base of the thermal boundary layer may be defined by the transition from a conductive to an adiabatic (isentropic) geotherm (Fig. 5.4).

In the petrologic community, xenolith P–T arrays are commonly compared with the family of conductive geotherms of Pollack and Chapman (1977) (Fig. 4.33), which provides a reference frame for comparison of the deep thermal regime of various tectonic settings. This family of conductive geotherms is based on a simple assumption that 60% of surface heat flow comes from the mantle. However, petrologic and thermal data indicate that average crustal heat production decreases with age and is the lowest in the Archean crust (e.g. Rudnick *et al*., 1998; Tables 4.4 and 4.5), where only 30% of surface heat flow is generated in the crust (Artemieva and Mooney, 2001). Although the trend of

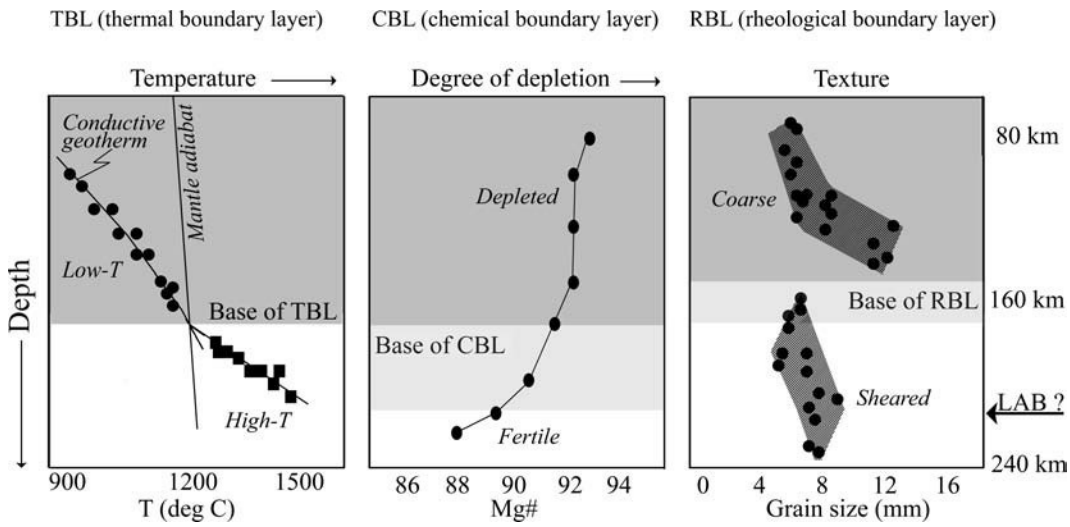

Fig. 5.4 Relations between thermal, chemical, and rheological boundary layers as constrained by mantle-derived xenoliths. The bases of the TBL, CBL, and RBL may be at approximately the same depth which corresponds to the transition from low-temperature, depleted, and coarse peridotites to high-temperature, fertile, and sheared peridotites. The examples are based on xenolith data from southern Africa, the corresponding details are shown in Fig. 5.7b for TBL, Fig. 6.15a for CBL, and Fig. 3.9a for RBL. In this cratonic region, the base of the lithosphere (LAB) is expected to be at a depth of 200–240 km as indicated independently by seismic and thermal models (e.g. Figs. 3.98, 5.5) and thus it does not correspond either to TBL or to RBL bases as inferred from xenolith data. The transitional nature of the CBL base complicates comparison of CBL thickness with other data sets.

increasing mantle heat flow from Archean to Phanerozoic crust partly compensates for an increase in the crustal contribution to surface heat flow, any extrapolation of cratonic xenolith geotherms to surface heat flow along cold reference geotherms should be interpreted with caution.

Sometimes the lower part of the mantle section sampled by xenoliths exhibits a significant deviation (inflection) of xenolith P–T arrays from a conductive geotherm with a characteristic "kink" of the P–T array. This abrupt (almost step-like) change in mantle temperature gradient is often interpreted as the transition from a pure conductive to a non-conductive (adiabatic and convective) heat transfer regime. Thus, the depth of the transition from low-temperature (i.e. located along a conductive geotherm) to high-temperature peridotites is often interpreted as the base of the thermal boundary layer (thermal lithosphere) (Fig. 5.4). Other interpretations are possible as well (see Section 5.2.2 for discussion); they show that a kink on the xenolith geotherm may not necessarily mark the base of TBL.

Chemical boundary layer

Variations of major-element mantle composition with depth as indicated by geochemical studies of mantle-derived xenoliths from different tectonic settings provide information

on the thickness of the *chemical boundary layer* (CBL). In most regions, mantle composition exhibits significant (commonly systematic) variation with depth, but no sharp compositional boundaries are observed (Fig. 5.4, see Section 6.1.4). In cratonic settings, however, the transition from low-T (with equilibrium $T < 1100–1200\,°C$) to high-T (with equilibrium $T > 1100–1200\,°C$) peridotites is often associated with a notable, although gradual, change in major-element mantle composition (from depleted in basaltic components to fertile mantle) (e.g. Fig. 6.15). Boyd and Gurney 1986) argue that high-T and low-T mantle peridotites have been formed under different physical–chemical conditions, and thus the boundary between them approximately corresponds to the petrologic lithospheric base. Alternatively, it may indicate the transition from the "intact" cratonic nucleus to the lowermost lithosphere metasomatized by melts and fluids from the convective mantle (Fig. 5.5).

As an example, the boundary at ~150 km depth between low-T and high-T xenoliths in the Williams kimberlite, Montana, USA, has been interpreted as the base of the ancient lithospheric keel, which apparently had been removed during the formation of the Rocky Mountains in the late Mesozoic (Carlson *et al*., 1999). This conclusion is based on Os isotope studies which indicate that low-T samples have Archean–Paleoproterozoic Re depletion model ages (2.5–1.7 Ga), while high-T samples have Os isotope compositions similar to modern abyssal peridotites, and thus the high-T peridotites are recent additions to the lower parts of the lithosphere. Strong chemical stratification has been noted for the Slave craton (Kopylova and Russell, 2000). An important chemical boundary (with an increase in mantle fertility) identified between 160 and 200 km depth in the northern Slave craton can be interpreted as the boundary between the depleted Archean petrologic lithosphere and the lower lithosphere chemically and texturally modified by pre-kimberlitic magmatic activity (Fig. 5.6) (see Chapter 6). Alternatively, its geometry and sharpness (imaged by seismic receiver function analysis) suggests a structural origin, such as shallow paleosubduction (Bostock, 1997).

Ryan *et al*. (1996) propose that in cratonic regions the depth to the base of the petrologic lithosphere can be determined by the change from depleted (lithospheric) to undepleted (asthenospheric) trace-element signatures in garnet (see Section 5.2.3, Fig. 3.104). In some cratons the depth of this transition corresponds to mantle temperatures of 1200–1300 °C at which the change from a conductive to an isentropic geotherm occurs, and thus the bases of the chemical (petrologic) and thermal lithospheres may coincide (Poudjom Djomani *et al*., 1999). However, this is not necessarily the global pattern (see Chapter 6).

Rheological boundary layer

Two main populations of xenoliths, distinguished by their equilibrium temperatures and pressures, low-T and high-T peridotites, also differ by their texture (Fig. 5.4). The latter reflects differential stress conditions in the upper mantle at the time the xenoliths were sampled by ascending magmas. Low-T peridotites are usually coarse grained (grain size greater than 2 mm) and show a low level of lithosphere deformation over tens or hundreds

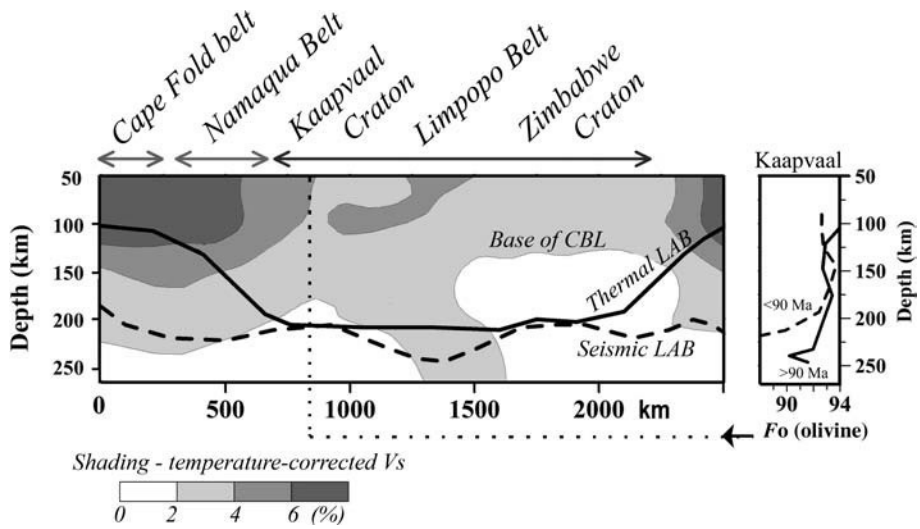

Fig. 5.5 Compositional profile through the lithosphere of southern Africa (modified from Artemieva, 2009). The cross-section shows compositional variations in the upper mantle (gray shading) constrained by absolute δVs velocity perturbations (surface-wave model of Shapiro and Ritzwoller, 2002) corrected for lateral temperature variations (thermal model of Artemieva and Mooney, 2001). Dark shading corresponds to fast (iron-depleted?) lithosphere, whereas white shading refers to fertile mantle. The transition from gray to white shading (2% temperature-corrected δVs anomaly) can be interpreted as the base of CBL. Black lines – lithospheric base as defined by a 2% δVs seismic (uncorrected for *T*-variations) anomaly with respect to *ak135* continental reference model (dashed line) or by a 1300 °C isotherm (solid line). Right insert: depth distribution of *Fo* in Kaapvaal for mantle peridotites emplaced at > 90 Ma and < 90 Ma (data of Gaul *et al*., 2000). The location of kimberlite is shown by dotted line.

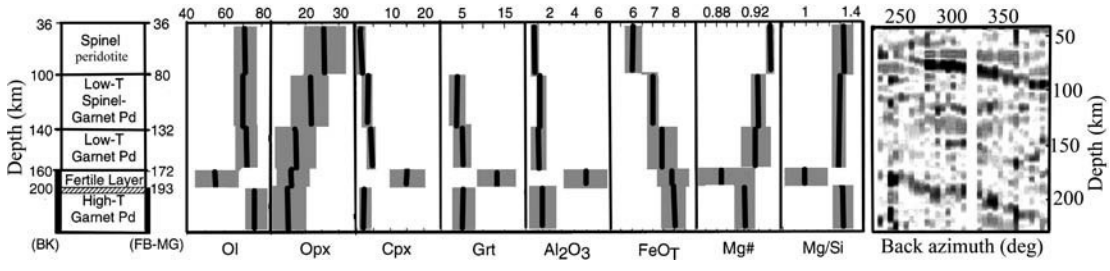

Fig. 5.6 Chemical stratification of the lithospheric mantle beneath the Slave craton (Source: Kopylova and Russell, 2000). Black lines in each panel show mean value determined for each type of peridotite (Pd), gray bars denote one standard deviation for each suite. Depth (left scales) based on Brey and Kohler (BK) and the Finnerty-Boyd and MacGregor (FB–MG) thermobarometry. Right panel: seismic P-to-S transmissivity (receiver function method) beneath the Slave craton as a function of depth and back azimuth (darker shades refer to negative values) (Source: Bostock, 1997).

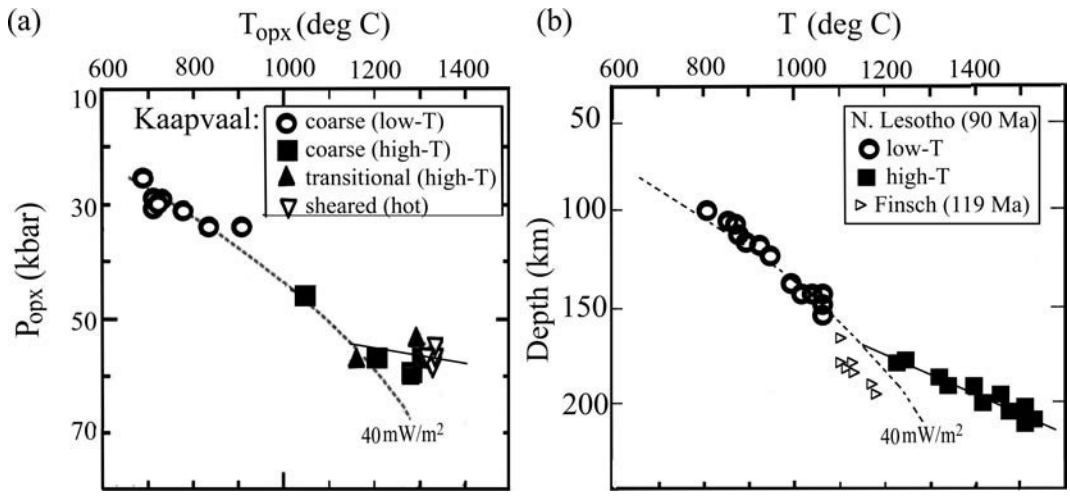

Fig. 5.7 Mantle peridotites from Kaapvaal (Sources: Hanrahan *et al*., 2003; Pearson, 1999). (a) High-temperature coarse and sheared peridotites may fall very close in the P–T field; (b) the kink in the P–T array corresponds to the transition from low-temperature to high-temperature peridotites. However, the kink may not exist if other geothermobarometers are used (compare with Fig. 5.9d).

of millions of years (Fig. 3.104,d–e). In contrast, high-*T* peridotites are generally (but not always) finer grained (porphyroclastic) and highly deformed (sheared) (Nixon and Boyd, 1973) (Fig. 5.7). Porphyroclastic textures may be formed by shear heating or deformation during diapiric upwelling (Nixon and Boyd, 1973); however, their origin is not yet fully understood. Due to a fast rate of recrystallization and coarsening of olivine grains, these textures cannot exist for a long time at high mantle temperatures and thus are transient features acquired by xenoliths for a short time before their entrainment by ascending magmas (Pearson *et al*., 2003).

Variations in texture of xenoliths brought to the surface from different depths in the mantle are often interpreted in terms of the *rheological* ("*mechanical") boundary layer* (RBL). High-temperature, sheared (and often metasomatized) peridotites are commonly interpreted as being associated with mantle zones of reduced viscosity and asthenospheric flow (compare with Fig. 3.117). Since mantle viscosity is strongly temperature dependent, the thickness of the RBL should be proportional to the thickness of the TBL, unless weak mantle rheology is due to the presence of fluids.

Os isotope results indicate that the transition from low-*T* granular xenoliths to high-*T* sheared xenoliths does not mark the base of the present lithosphere in the Kaapvaal and the Siberian cratons (Carlson *et al*., 1999). In the Baltic Shield, high-*T* sheared peridotites were not found even in xenoliths of deepest origin (from ~240 km depth) which do not show the shearing associated with flow in the rheologically active boundary layer beneath the base of the conductive thermal boundary layer (Kukkonen and Peltinen, 1999). This implies that the thickness of the rheological boundary layer beneath the central Baltic Shield is greater than 240 km.

LAB and xenolith-based TBL, CBL, and RBL

Figure 5.4 based on xenolith data from southern Africa illustrates that the base of the lithosphere (the lithosphere–asthenosphere boundary, LAB) does not necessarily correspond to any of the TBL, CBL, or RBL bases inferred from xenolith data. Seismic and thermal models available for the Kaapvaal craton independently indicate 200–240 km as the depth to the LAB (Fig. 5.5), while xenolith data suggest that the TBL (defined by the kink on the geotherm) is ~180 km thick and the RBL constrained by grain size variations is ~140–160 km thick (Fig. 5.4). The position of the CBL base is somewhat arbitrary due to a gradual change in mantle composition with depth; however (particularly for young kimberlites, < 90 Ma) it is shallower than a 200 km depth where Mg# decreases to ~90.

This conclusion is further illustrated by Fig. 5.5 which shows compositional variations in the upper mantle beneath southern Africa as constrained by joint analysis by surface-wave seismic tomography and thermal modeling. Compositional velocity anomalies (Artemieva, 2009) have been calculated by subtracting the elastic and anelastic effects of lateral temperature variations (temperature deflection from the 50 mW/m^2 continental geotherm) on Vs from observed seismic shear-velocities. The results illustrate that while there is a good agreement between the lithospheric thickness as constrained by seismic velocities (defined here by a 2% shear velocity perturbation uncorrected for T-variations) and mantle geotherms, the seismic and thermal LAB do not correspond to the base of the CBL in significant sections of the profile. The discrepancy between geophysically determined LAB and CBL is particularly strong beneath the Zimbabwe craton.

5.2 TBL and xenolith geotherms

5.2.1 Geothermobarometers

Major principles and assumptions

The idea of using mineralogical geothermobarometers to constrain ambient P–T conditions in the mantle sampled by xenoliths was first proposed by Boyd (1973) and further developed by O'Neill and Wood (1979), Finnerty and Boyd (1984), Brey and Köhler (1990) and many others (see Table 5.2 for summary). The approach is based on pressure and temperature dependence of the activity of exchange reactions (characterized by element diffusion, D) between coexisting (equilibrated) minerals. Since mantle peridotite is made of a small number of minerals (the abundant minerals include olivine, orthopyroxene, clinopyroxene, garnet, and spinel), exchange reactions are limited to a few mineral phases only.

Exchange reactions are experimentally calibrated for exchange equilibria. However, experimentally measured values of diffusion rates for cations in peridotites span over

Table 5.2 Some geothermobarometers used in xenolith studies

Method	Reference	Mineral system	Exchange reaction	P* (GPa)	T* (°C)	Accuracy**
Barometers						
BKN	Brey, Köhler and Nickel, 1990	Gt-Opx	Al	1.0–6.0[(2)]	900–1400	0.5 GPa (15 km)
KB	Kohler and Brey, 1990	Ol-Cpx	Ca	0.2–6.0 [(1)]	900–1400	0.7 GPa (20 km)
NT00	Nimis and Taylor, 2000	Cpx-Gt	Cr	0–6.0[(2)]	800–1500	0.3 GPa (10 km)
FB	Finnerty and Boyd, 1987	Ol-Cpx	Ca	[(1?)]		?
P38	Grutter *et al*., 2006	Cpx-Gt	Cr	2.0–7.0[(2)]	600–1300	?
MC74	MacGregor, 1974	Opx-Cpx	Al-in-Opx	0.5–4.0	900–1600	?
Thermometers						
WS	Witt-Eickschen and Seck, 1991	Opx-Sp	Al/Ca	1.5[(1)]	900–1400	20 °C
Ba	Ballhaus *et al*., 1991	Ol-Sp	Fe-Mg[(4)]	0.3–2.7	1040–1300	30 °C
BKN	Brey, Köhler and Nickel, 1990	Opx-Cpx	Ca-Mg[(3)]	1.0–6.0	900–1400	60 °C
BKopx	Brey and Köhler, 1990	Opx	Ca-Mg[(3)]	1.0–6.0	900–1400	62 °C
Ta	Taylor, 1998	Opx-Cpx	Ca-Mg[(3)]	2.5–6.0	900–1400	60 °C
EG	Ellis and Green, 1979	Gt-Cpx	Ca-Mg [(3,5)] Fe-Mg [(4)]	2.4–3.0	750–1300	?
Ha	Harley, 1984	Opx-Gt	Fe-Mg[(4)]	0.5–3.0	800–1200	92 °C
LG	Lee and Ganguly, 1988	Opx-Gt	Fe-Mg[(4)]	2.0–4.5	975–1400	96 °C
Kr	Krogh, 1988	Cpx-Gt	Fe-Mg[(4,5)]	< 3.0	600–1300	100 °C
OW	O'Neill and Wood, 1979	Ol-Gt	Fe-Mg[(4)]	3.0–6.0	900–1400	180 °C
NT00	Nimis and Taylor, 2000	Cr-Di	En-in-Cpx	0–6.0	800–1500	30 °C

Abbreviations: Gt = garnet; Sp = spinel; Di = diopside; Opx = orthopyroxene; Cpx = clinopyroxene; Ol = olivine; En = enstatite

* pressure and temperature used in development and calibration of the method;
** 2σ accuracy in data reproduction;
[(1)] Sp-facies only;
[(2)] Gt-facies only;
[(3)] insensitive to Fe^{3+};
[(4)] depends on Ca-content;
[(5)] no systematic dependence on Mg# (this information may be incomplete since it was found only for a few methods).
Pressure–depth conversion: 1 GPa = 10 kbar = 10^9 kg/m sec^2. Pressure at the base of a 40 km-thick crust with density $\rho_{cr} = 2900$ kg/m^3 is $P = 1.16$ GPa; in the upper mantle pressure $P = g[\rho_{cr} z_{cr} + \rho_m(z\text{-}z_{cr})]$ and for upper mantle density $\rho_m = 3300$ kg/m^3 $P = 6.0$ GPa is achieved at a depth $z \sim 187$ km.

four and more orders of magnitude at single temperatures and are not well constrained for aluminium and chromium cations in mantle minerals (Canil, 2004). Mineral rims are more likely to be representative of equilibrium pressures and temperatures (Smith, 1999).

Reliable geothermobarometers should comply with several fundamental criteria.

(1) A critical assumption behind all geothermobarometer methods of estimating ambient temperature and equilibrium pressure of individual mineral grains in xenoliths (discussed by O'Reilly and Griffin, 1996 and Smith, 1999) is the assumption that equilibration has been attained in major elements in the minerals. In cases where this assumption is not valid, geothermobarometer techniques may give misleading constraints on xenolith P–T arrays and the corresponding geotherms. For example, evidence of mineralogical disequilibria has been found for xenoliths from the Siberian craton (Griffin *et al*., 1996).
(2) Estimated P–T arrays should satisfy petrologic constraints imposed by plagioclase–spinel–garnet and graphite–diamond phase transitions. The transition of spinel peridotite to garnet peridotite in Cr-free, Al-bearing peridotites occurs at pressures of ~16–20 kbar (55–65 km depth). With increasing Cr/(Cr+Al) ratio, the phase transition depth shifts to pressures as high as 70 kbar (~220 km depth) (O'Neill, 1981). This dependence is employed, for example, in a widely used thermobarometer of Nimis and Taylor (2000). In cold cratonic lithosphere, the graphite–diamond phase transition occurs at ~130 km depth for $T = 800$ °C and deepens to ~190 km depth for $T = 1500$ °C (Kennedy and Kennedy, 1976).

A number of other geochemical criteria which depend on a particular exchange reaction may be critical for geothermobarometer reliability (see discussion in Nimis and Taylor, 2000).

Pressure constraints

The aluminium-bearing minerals of xenoliths (i.e. calcic plagioclase that is stable down to 25 km depth, spinel and garnet) are commonly used to constrain the depth of their origin. Studies based on garnet peridotite assume that all Al is within the pyroxene structure (specifically $MgAl_2SiO_6$) and rely on the Al content of orthopyroxene which is typically in the range between 0.7 and 2.0 wt% Al_2O_3 (Fig. 5.8e).

Most geobarometers are confined to garnet-facies samples; the number of geobarometers available for spinel-facies rocks is very limited (Table 5.2). Furthermore, the only quantitative geobarometer for spinel facies, that of Kohler and Brey (1990) is analytically challenging. For these reasons, geotherms in the shallow mantle within the spinel stability field are commonly poorly constrained by xenolith data. Since mineral exchange reactions used in geobarometry depend strongly on temperature as well, usually at the first stage the equilibrium T is estimated and the T value is next used to estimate the equilibrium pressure.

There is a fundamental difference between thermal arrays defined by Opx-Grt and Cpx-Grt barometry (Grutter and Moore, 2003). The temperature dependence of the Opx-Grt P–T arrays (such as MC74 and BKN) is of the order of 40–60 bar/ºC and they follow steady-state conductive geotherms (e.g. of Pollack and Chapman, 1977). In contrast, the Cpx-Grt barometer NT00 of Nimis and Taylor (2000) has a temperature gradient of ~25–50 bar/ºC. As a result, P–T arrays based on NT00 barometry transect conductive geotherms at a shallow angle (Fig. 5.8ab). In particular, at $T > 850$ ºC the Cpx-Grt barometry (NT00) data for the Somerset Island fall parallel to the graphite–diamond equilibrium (and produce the apparent kink in the

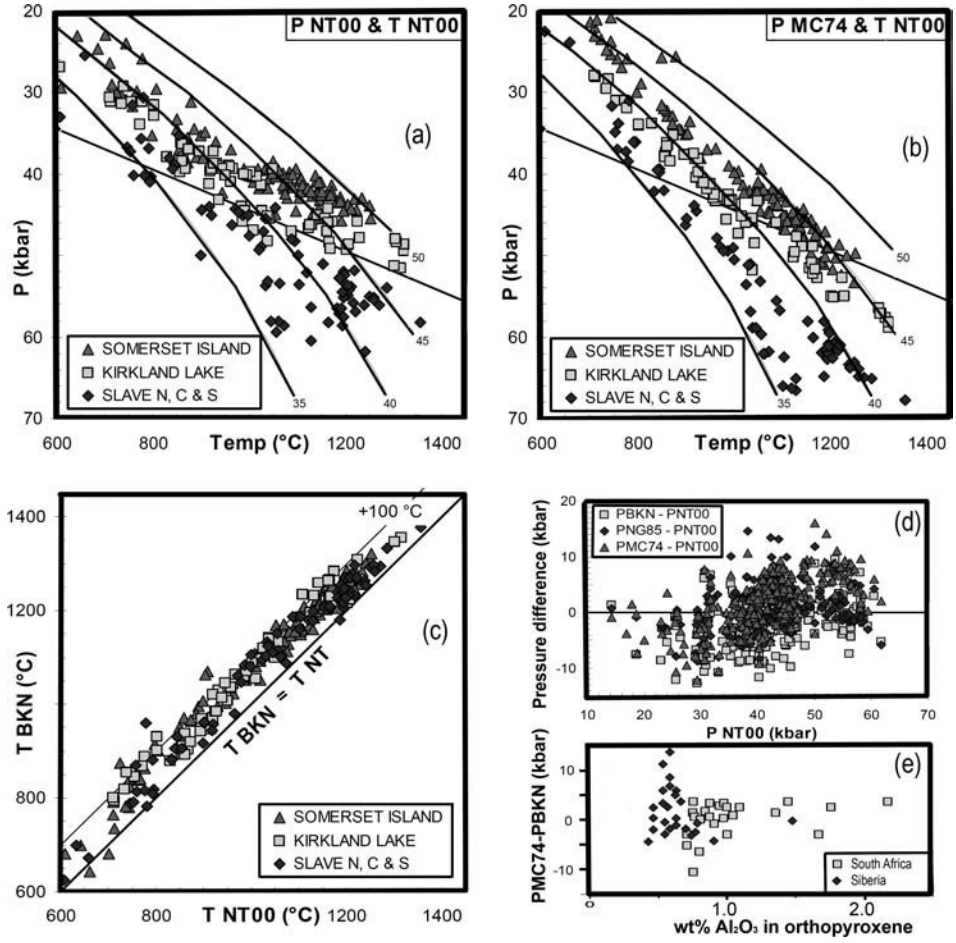

Fig. 5.8 Comparison of different geothermobarometers for garnet peridotite xenoliths (Sources: Grutter and Moore, 2003; Smith, 1999). Notations as in Table 5.2. (a–d) Thermobarometry for the same set of Canadian samples: (a–b) xenolith P–T arrays constrained by different geothermobarometers; black lines: reference conductive geotherms labeled in surface heat flow values and graphite–diamond phase transition. (c) Temperature difference between BKN and NT00 thermometry; (d) pressure difference between Opx-Grt and Cpx-Grt barometry; all pressures calculated at T(NT00); (e) pressure difference between Opx-Cpx and Opx-Grt barometry as a function of Al content of orthopyroxene for South African and Siberian xenoliths.

P–T array), while P–T arrays from the same xenoliths based on Opx-Grt barometry (MC74, PBKN and PNG85) intersect the diamond stability field at P ~ 50 kbar with no deflection of xenolith geotherm.

Temperature constraints

A detailed discussion of various thermobarometers can be found in Smith (1999). A popular thermometer OW is based on Fe–Mg exchange reactions between garnet and olivine

(O'Neill and Wood, 1979). However, temperature determinations based on the assumption that all iron in garnet is ferrous can differ by > 200 °C from the results in which the amount of ferrous iron is determined by Mossbauer spectroscopy (Canil and O'Neill, 1996). Similarly, for Fe–Mg exchange reactions between garnet and clinopyroxene the uncertainty in ferrous iron can result in > 300 °C difference in temperature determinations. Orthopyroxene-based thermometry may be less affected by bulk compositional variations and is potentially more accurate at temperatures below ~1000 °C. Two popular thermometers, BKN and NT00, produce temperature estimates with a small difference of ~50–100 °C, but BKN temperatures are systematically higher (Fig. 5.8c).

It is also important to remember that typically:

- xenoliths with temperatures between 900–1100 °C have equilibrated at ambient P–T conditions just before eruption;
- xenoliths with temperatures below 800–900 °C may not have equilibrated to ambient P–T conditions, since diffusion rate is temperature dependent;
- xenoliths with temperatures above 1100–1200 °C sample mantle affected by melt percolation, heat advection, and with transient thermal regime.

Xenolith geotherms: general remarks

A set of pressure–temperature pairs measured on xenolith samples from the same location forms a xenolith P–T array (xenolith geotherm) (e.g. Fig. 5.8a). The following remarks should be made:

- xenolith geotherms do not extrapolate to the surface temperature;
- the low-temperature subset of P–T data points probably provides the best estimate of the geotherm at the time of eruption;
- downward extension of the xenolith geotherm to its intersection with the mantle adiabat provides an estimate of the TBL even when no deep xenoliths are available;
- xenolith geothermobarometry may be inconsistent with estimates of the mantle adiabat based on studies of mid-ocean ridge basalts (MORB) (Bell *et al*., 2003);
- in some regions where multiple magmatic episodes took place, xenoliths erupted at different times make it possible to reconstruct the evolution of mantle thermal regime in time;
- for tectonically active regions with a clearly transient thermal regime and significant heat advection by ascending magmas, a comparison of xenolith P–T arrays with the family of conductive geotherms does not have physical meaning and is a matter of practical convenience.

Uncertainties in xenolith P–T arrays

Temperature and pressure estimates obtained on the same rock by different geothermobarometers may differ by hundreds of degrees Celsius and tens of kilobars (Finnerty and Boyd, 1984; Smith, 1999; Grutter *et al*., 2006) (Fig. 5.8). However, since most geothermobarometers are experimentally calibrated at temperatures between 900–1400 °C and pressures

between 2–6 GPa (Table 5.2), most of them agree in this P–T range. At pressures and temperatures outside this range, the accuracy of P–T determinations for samples with mineral chemistries different from those used in calibration experiments cannot be assessed, since many thermobarometers are sensitive to bulk composition (Smith, 1999).

Uncertainties in temperature determinations based on Fe–Mg partitioning result from uncertainties in ferric/ferrous iron (Fe^{3+}/ Fe^{2+}) in pyroxene, spinel, and garnet. In iron-poor pyroxenes, like those from the cratonic settings with Mg# = 100 Mg/[Mg+Fe] of 91–94, the values of relative abundances of ferric and ferrous iron can be almost meaningless because of uncertainties in more abundant cations (such as Si) (Canil and O'Neill, 1996). For example, Fe^{3+}/ Fe^{total} in low-temperature peridotite garnets is between 0.02 and 0.07.

Some general observations based on experimental comparisons of different thermobarometers (see Table 5.2 for notations) are the following (Smith, 1999; Grutter and Moore, 2003; Preston and Sweeney, 2003):

- BKopx and BKN thermometers provide similar temperature estimates at T~900–1000 °C, but at T~1150 °C BKopx provides temperatures 100–150 °C lower than BKN;
- FB temperatures are 50–100 °C lower than BKN temperatures in the range 900–1200 °C; at higher temperatures T(FB) approaches T(BKN) and becomes hotter at $T > 1400$ °C;
- Kr and BKN temperatures are within 80 °C for the South African peridotites for all temperatures, but for the Siberian samples T(BKN) is 50–150 °C higher than T(Kr) at $T < 1000$ °C;
- The Ha thermometer, as compared to the BKN thermometer, provides higher temperature at $T < 800$ °C but lower temperature at $T > 1000$ °C;
- NT00 temperature values correlate well with temperatures calculated using Cpx-solvus thermometers (e.g. BKN) and give temperature 50–100 °C lower than BKN (Fig. 5.8c);
- the difference in equilibration temperatures determined with FB and NT00 thermometers reaches 200 °C but decreases with temperature increase;
- The LG thermometer, as compared to the BKN thermometer, provides temperature within 100 °C at $T > 1000$ °C but significantly higher temperature at $T < 1000$ °C;
- The Cr-barometer (Ryan *et al*., 1996) agrees with P38 at $P = 55 \pm 2$ kbar, but provides 6–12% higher values at lower pressures;
- Opx-Grt barometers yield pressures less than NT00 at pressure $P < 40$ kbar and higher than NT00 at high pressure, with absolute differences as large as ±10 kbar;
- temperature gradients of Cpx-Grt barometers (NT00) and Opx-Grt barometers (MC74, PBKN and PNG85) are significantly different. As a result, at high temperatures Opx-Grt geotherms are parallel to cratonic conductive geotherms, while Cpx-Grt geotherms may orient sub-parallel to the graphite–diamond phase transition boundary and form a "kink" on the geotherm (Fig. 5.8ab).

5.2.2 Kink in xenolith geotherms

Xenolith P–T arrays from cratonic regions often display a characteristic kink at depths below 120–150 km, where mantle temperature gradient changes stepwise (Fig. 5.7). For example,

xenolith geotherms for the Kaapvaal and Slave cratons and for the mobile belts in South Africa show kinks at depths of 220, 170, and 140 km, correspondingly, where they deflect from the conductive geotherm into the region of higher temperature. Boyd (1973) postulated that a sharp steepening of the shield geotherm from a normal temperature gradient of 2–4 °C/km at shallow depths to a high temperature gradient of > 10 °C/km below 140–200 km depth marks the base of the continental lithospheric plate. This conclusion has been questioned by different authors on several grounds (e.g. Green and Gueguen, 1974; Jordan, 1975a). Up to date, however, there is still no general agreement on the physical meaning of the kinks. Three new, principally different explanations have been proposed recently.

Kink as an artifact of thermobarometry

Recent experimental studies of cratonic mantle xenoliths with different geothermobarometers suggest that the presence or the absence of the kink often depends on the choice of thermobarometer. In particular, the kink in xenolith P–T arrays commonly appears in data based on Finnerty and Boyd (1987) thermobarometers but is absent in xenolith geotherms constrained by the BKN thermobarometer. For instance, for the African xenoliths from many different locations, P–T arrays based on P(MC)-T(FB) (see Table 5.2 for abbreviations) appear to be made of two linear branches which intersect at a "kink", while the same samples analyzed by the P(BKN)–T(BKN) thermobarometer combination show no kink. Similarly, for the Canadian data a kink is not observed for all thermobarometers (compare Figs. 5.8a,b and 5.9c).

Another concern was raised as early as 1975 (Wilshire and Jackson, 1975) when it was argued that high-temperature peridotites may represent unequilibrated mixtures of rocks with different compositions and are not likely to have been subject to their apparent equilibration temperatures for very long. Furthermore, Re–Os studies show no difference in Os model ages between high-*T* and low-*T* peridotites (Pearson *et al*., 1995; Carlson *et al*., 1997). These authors argue that high-temperature deformed peridotites are not derived from asthenospheric flow but represent pieces of the ancient lithosphere overprinted by later tectono-thermal events, and their fertile nature can be a recent phenomenon. This implies that *high-temperature peridotites should be included in the constraints on xenolith geotherms and the thickness of the TBL*.

Syn- or post-eruption thermal disequilibrium

The depths of the kinks, when they are present in P–T arrays, commonly correlate with the transition from undeformed (coarse) low-*T* to sheared high-*T* peridotites and with changes in peridotite composition: high-*T* peridotites are close in composition to the primitive mantle (Boyd, 1987). Thus, it is tempting to associate the boundary temperature between low-*T* and high-*T* mantle peridotite (~1100–1200 °C) either with the base of the thermal lithosphere (Finnerty and Boyd, 1987) or with the base of the rheological boundary layer (Boyd, 1973; Sleep, 2003).

An alternative explanation of the kink in xenolith geotherms implies that the lower part of the geotherm reflects a local thermal disequilibrium related to a thermal perturbation in the

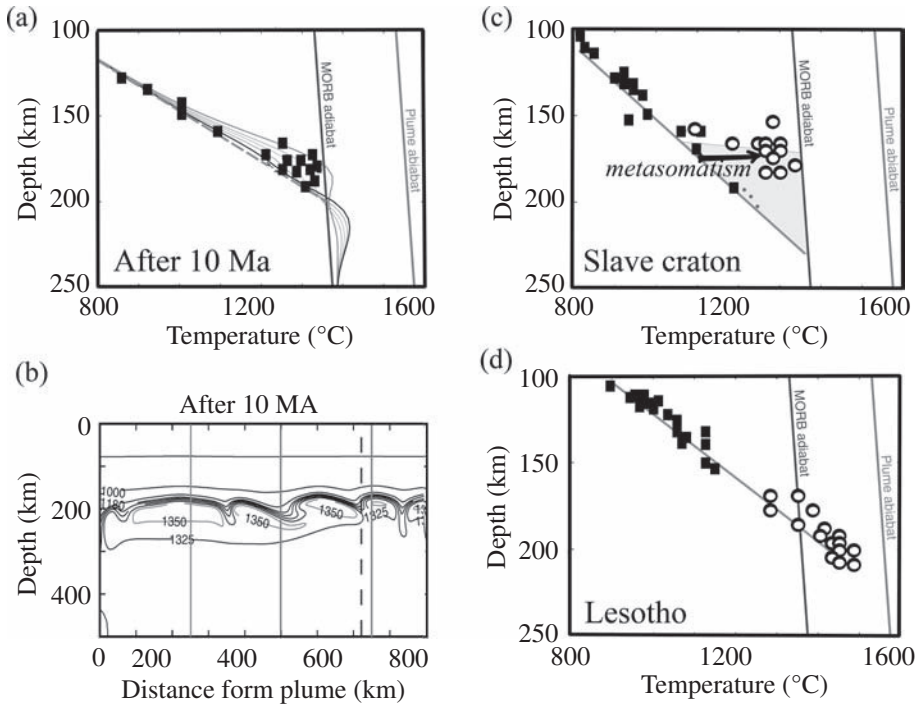

Fig. 5.9 Disequilibrium continental geotherms perturbed by plume–lithosphere interaction (after Sleep, 2003). (a) Mantle geotherms at 10 Ma after plume impact; different lines refer to different distances from the plume (shown in (b)). Symbols illustrate the scatter that might occur in a P–T array of xenoliths emplaced at slightly variable distances from the plume. (b) Potential temperature field at 10 Ma after plume impact. Different lines refer to mantle temperatures shown at steps of 250 °C. Vertical lines – positions of geotherms shown in (a); dashed vertical line – position of closely spaced geotherms in (a). (c–d) Symbols – xenolith P–T arrays (the BK method) from the Slave province (the Jericho pipe) and Lesotho. Solid symbols – coarse low-*T* xenoliths; open circles – sheared high-*T* xenoliths. Gray line – the inferred regional conductive geotherm determined by low-*T* xenoliths. In the Slave craton (c), high-*T* xenoliths lie hotter than this geotherm and require mantle heating proportional to the area of the gray triangle. In Lesotho (d), high-*T* xenoliths are at temperatures hotter than the MORB adiabat and are likely to sample the plume material.

mantle at the time of the magmatic event, while the upper part (constrained by low-*T* peridotites) refers to the unperturbed steady-state thermal regime (Green and Gueguen, 1974). Numerical models of mantle convection provide further insights into the possible physical origin of the kink on xenolith geotherms and illustrate features that may be observed in P–T studies of xenolith suites (Sleep, 2003). The results illustrate that the shape of transient geotherms depends on the distance from the plume and on the time elapsed since its interaction with the lithosphere. For example, xenolith samples erupted in a single event along-strike of a kimberlite dike may sample variable geotherms, causing scatter in the depth–temperature array (Fig. 5.9ab). As a result,

random sampling of the lithosphere by kimberlites, as well as any systematic bias in the location of kimberlites may cause similar cratons to look different and obscure real differences between cratons (Sleep, 2003).

Xenolith data from two cratons, the Jerico pipe in the Slave craton and kimberlites from Northern Lesotho illustrate the complexity of interpretations of P–T arrays. Xenolith data from the Slave craton analyzed by BK thermobarometry displays a kink at ~170 km depth, that can be explained by significant (plume-related) local heating (Fig. 5.9c). In contrast, a linear P–T array that extends to high temperatures without any noticeable kink or curvature, as observed beneath Lesotho in South Africa, can be explained by ponding of plume material beneath a craton at ~90 Ma (Fig. 5.9d).

Steady-state inflected geotherms

Recent numerical simulations of mantle convection have demonstrated that there is no theoretical reason to assume that high-*T* peridotites reflect disequilibrium thermal conditions in the upper mantle (Lenardic and Moresi, 2000). Inflected geotherms can exist in thermal equilibrium in specific continental regions, such as transitions from a thick cratonic to a thin oceanic lithosphere (Fig. 5.10a).

In such regions, steep temperature gradients can be produced at a depth below the base of the thin lithosphere where vertical conduction is replaced by high horizontal heat flow in the mantle. The flowing upper TBL of the mantle convection cell moves from the oceanic region with high heat flow to the continental region with low heat flow. The uppermost layer of the convective mantle must adjust to the heat flow beneath the continent, thus forming the inner boundary layer and creating an inflected but still steady-state geotherm in the area of the ocean–continent transition. Similarly, inflected geotherms can exist at the cratonic margins, in areas with a steep change in the lithospheric thickness from cratonic to young continental lithosphere (Fig. 5.10b).

The third option for when an inflected steady-state geotherm is produced is the flow of a convective boundary layer below a plate with a step-like temperature discontinuity (Fig. 5.10c), although such conditions exist at the upper surface only temporally. Similarly to the first two cases, the inflected geotherm is produced by thermal inertia of the convective layer, which cannot instantly adjust its temperature over the full depth of the convective cell when convective flow encounters lateral heterogeneity. As a result, equilibrium thermal profiles of a non-classic shape are produced locally.

5.2.3 Garnet geotherms: CBL or TBL?

Griffin and co-authors (Ryan *et al*., 1996; Griffin *et al*., 1996, 1999a) use garnet T_{Ni} geotherms (temperature estimates from the Ni content distribution in xenocryst garnets) to analyze the structure of the continental lithospheric mantle. Their approach (illustrated in Fig. 5.11) is significantly different from classical geothermobarometry. At the first step, the temperature at the base of petrologic lithosphere is determined. This is defined as the

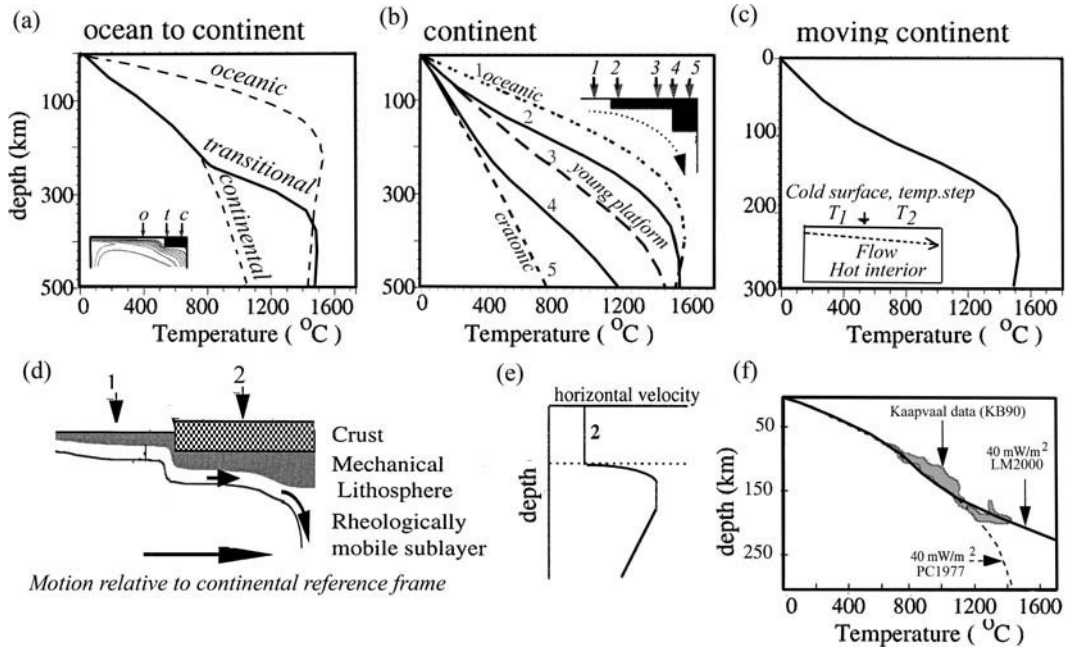

Fig. 5.10 Steady-state geotherms based on mantle convection simulations with account taken for continents (after Lenardic and Moresi, 2000). (a) Transitional equilibrium geotherms at the continent–ocean transition; (b) the same as (a) but with a step-like change in lithospheric thickness within the continent; (c) steady-state geotherm in the continental lithosphere with a temperature step at the upper cold free slip surface and with mantle flow within a hot interior. Inserts in (a–c) illustrate model configurations. (d) Cartoon illustrating subcontinental flow in the mantle and its effect on the lateral velocity profile near the edge of the continent (e). (f) Comparison of convection model predictions (LM2000) and conductive geotherm of Pollack and Chapman (1977) with Kaapvaal xenolith P–T arrays (Brey and Kohler, 1990 thermobarometry).

temperature above which garnets depleted in yttrium (a signature of the lithospheric mantle) disappear. Based on worldwide statistics, Y-depleted garnets are defined as those with less than 10 ppm Y. The base of the petrologic lithosphere defined in this manner may represent the upper limit of marked magma–wall interaction. In the next step, the thus determined T_{Ni} temperature at the base of the petrologic lithosphere is converted to depth along a conductive geotherm. This allows for the constraining of depth profiles of major (and trace-) element distribution in the lithospheric mantle and for calculating depth variations of density and seismic velocities. Griffin and co-authors have used this approach to map the olivine content and the thickness of the cratonic lithospheric mantle (e.g. Figs. 6.15 to 6.17; 6.24; 6.28).

In contrast to classical geothermobarometry, the definition of the lithospheric base by garnet geotherm combines features of both CBL and TBL definitions, since the depth at which Y-depleted garnets disappear is constrained from a conductive geotherm. Furthermore, this approach differs significantly from the way the lithospheric base is defined

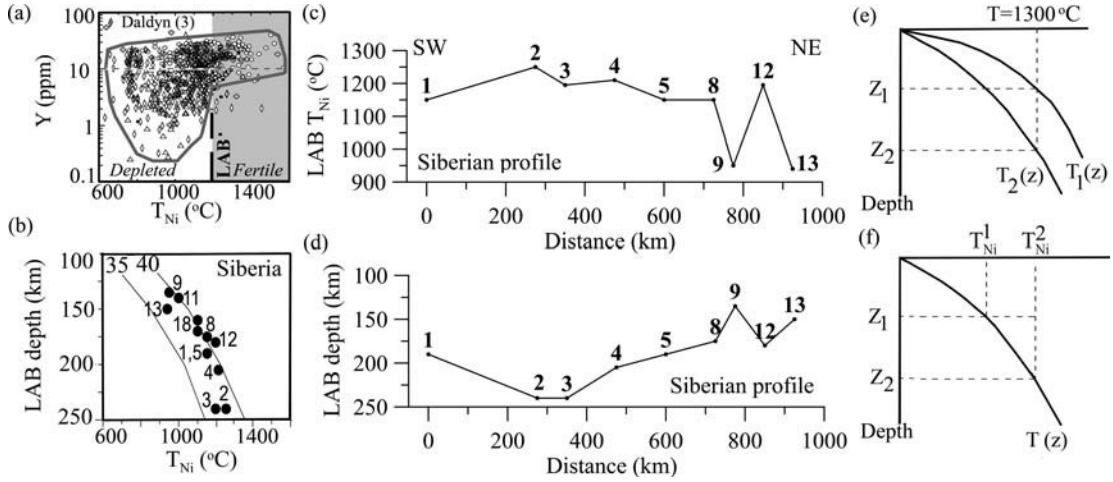

Fig. 5.11 Garnet geotherms and the Siberian lithospheric profile based on Ni-in-garnet thermometry. (a) An example of Y-T_{Ni} plot for the Daldyn kimberlite field in Siberia. The lithospheric base (LAB) is defined by the temperature above which garnets with less than 10 ppm Y disappear. The plot provides an estimate of temperature at the LAB. (b) Depth to LAB defined by Y-depleted garnets versus T_{Ni}. Temperature estimates for the LAB (a) are compared with the (assumed or independently calculated) conductive geotherm to obtain the depth of their origin. The lithospheric base defined in such a manner combines features of both CBL and TBL definitions. Solid lines – 35 and 40 mW/m^2 conductive geotherms; dots – kimberlite pipes. (c–d) SW–NE profiles across the Siberian craton showing Ni-temperatures at LAB (determined as in plot a) and the depth to LAB (determined as in plot b). Kimberlite pipes in (b–d) are numbered as in Fig. 5.3; lithological profile along the same line is shown in Fig. 6.17. (e–f) Sketches illustrating the difference between the thermal definition of the lithospheric base (e) and the definition of the lithospheric base based on Ni-in-garnet thermometry (f). (Data sources for (a–d): Griffin *et al.*, 1999a.)

in conventional thermal models (Fig. 5.11ef). According to thermal models, two regions have different lithospheric thicknesses because they have different geotherms that intersect a mantle adiabat (or a 1300 °C isotherm) at different depths. In contrast, as illustrated by garnet geotherms from the Siberian craton (Fig. 5.11b), two regions have different lithospheric thicknesses not because they have different geotherms, but because the temperature (and thus the depth) at which garnets become Y-depleted is different. All data for the Siberian craton based on Ni-in-garnet thermometry (Ryan *et al.*, 1996) fall close to the same conductive geotherm of ~40 mW/m^2, and thus according to a conventional definition of thermal lithosphere the lithospheric thickness along the Siberian kimberlite profile should be approximately the same and, in general, different from the lithosphere thickness defined by garnet-depletion. In particular, due to horizontal heat transfer short-wavelength fluctuations of the thickness of the thermal lithosphere are not possible, unless it were a non-steady-state feature immediately associated with kimberlite magmatism (Fig. 5.11cd). Note that conventional thermobarometry indicates that xenolith P–T arrays beneath all major kimberlite fields in Siberia fall close to 35–38 mW/m^2, with the coldest geotherm (~34–35 mW/m^2) beneath the Mir kimberlite pipe (e.g. Ashchepkov *et al.*, 2010) (Table 5.3).

Table 5.3 Summary of xenolith data for cratons

Location	Crustal age*	Age of emplacement	Lithospheric thickness (km) from xenoliths	Reference geotherm (mW/m^2) **	***	Reference
Africa						
Kaapvaal	ArI	< 90 Ma (Group I), 119 Ma (pipe Finsch),	200–250	40	—	RN99
			180–200	40	—	G03
			~180	39^	—	R96; ORG96
		1180 Ma (pipe Premier)	> 155–185	—	—	Gr06; Gr99
Lesotho	ArI		170–190	40	—	R96; BG86
Tanzania	ArII		~150	—	—	ORG96; LR99
West Africa	ArII	135–153 Ma, 800 Ma	> 195–205	—	—	S04 (Guinea)
			> 170	—	—	S04 (Sierra Leone)
			> 200	—	—	S04 (Liberia)
Namibia	ePt		RBL ~200	—	—	P94
			> 125	—	—	Gr99
Mobile belts of S. Africa	lPt		~ 140	—	—	BG86
			> 150	—	—	Gr99
Siberia						
Daldyn–Alakit terrane	ArII	345–360 Ma (pipe Udachnaya)	~240	~35	—	G99, B76
			> 220	34	—	R96
Magan terrane	ArII	345–360 Ma (pipe Mir)	~220	~35	—	B76; G93; G96; P91
			200–250 ?	~35	—	A10
				40^	—	RN99; G99
Markha terrane (Muna)	ArII	345–360 Ma	—	38^	—	G99
Berekla-Olenek-Anabar	ArII	380–420 Ma, 240 Ma, 140–170 Ma	—	—	—	G99
S margin of the Siberian platform (Ingashi)	ArII-ePt	1268 Ma	—	—	—	
North America						
Slave craton	ArII	170 Ma	200–250	—	40	RN99
			200–220	35–38	—	OR01
			160–190 (North)	—	37–40	K99

Table 5.3 (cont.)

Location	Crustal age*	Age of emplacement	Lithospheric thickness (km) from xenoliths	Reference geotherm (mW/m^2) **	***	Reference
			170–210 (North)	—	—	Gr99
			200 (Central)	—	—	P96
			180–200 (Central)	—	—	Gr99
			>230 (South)	—	—	K04, Gr99
Slave craton (Lac de Gras)	ArII	47–53 Ma	—	37–40	—	Me03
Superior Prov. (Wawa)	ArII	140 Ma	200–250	37–40	—	Kj96
				—	40	RN99
Superior Prov. (Kirkland Lake)	ArII	140 Ma	—	42	—	P98
Trans-Hudson Orogen	ePt		—	~40	—	Kj96
Saskatchewan	ePt	Cretaceous	—	42	—	Kj96
Wyoming craton	ArI	48–52 Ma	~140 ?	—	—	E88
			—	40^	—	R96
			>175	—	—	Gr99
SW Arkansas	mPt	106 Ma	—	—	—	
Midcontinent rift	Pt	90 Ma	—	—	—	
N Canadian Shield (Somerset Isl.)	Pt	99 Ma	—	44	—	SF99
Asia						
Sino-Korean craton	ArII	Pz	180	40^	—	ORG96
			140 ??	—	—	G98b, X00
Craton's core			>217	—	—	Gr99
Australia						
E Australia	Pz	Permian, Mz	~80–100	~90	—	ORG85
South America						
Guyana craton	ArII		160–180	—	—	G98a

Sao Francisco craton	ArI	89 Ma	—	34–40	—	R03
		85–80 Ma	—	39–50	—	RO3
Europe						
Baltic Shield (Karelia)	ArII-ePt	ePt, 589–626 Ma	220	36	—	PD99,
			200–240 (RBL > 240)	—	—	KP99
Baltic Shield (Archangelsk)	ArII-ePt	365–382 Ma	> 200	—	—	PD99, M03
Baltic Shield (Kola Province)	ArII-ePt	365–382 Ma	~ 150	—	—	PD99
Baltic Shield (SvecoFennian province)	ePt	Late Pz	~150	—	—	PD99
Baltic Shield (S Sweden)	ePt-mPt	Tertiary	< 100	—	—	PD99
Baltic Shield (SW Norway)	Pz-lPt	Tertiary	< 100	—	—	PD99
Ukrainian Shield	ArI		—	—	—	

* Crustal ages (see Table 4.13 for details): ArI – Archean I (> 3.0 Ga); ArII – Archean II (2.5–3.0 Ga); ePt – Paleoproterozoic (1.7–2.5 Ga); mPt – Mesoproterozoic (1.0–1.7 Ga); lPt – Neoproterozoic (540–1000 Ma); Pz – Paleozoic (250–540 Ma); Mz – Mesozoic (65–250 Ma); Cz – Cenozoic (< 65 Ma).
** Reference conductive geotherms of Pollack and Chapman, 1977
*** Conductive geotherms calculated in the original publications (see references)
^ Ni-in-garnet thermometry

References: A10 = Aschepkov *et al*., 2010; B76 = Boyd *et al*, 1976; B84=Boyd, 1984; BG86 = Boyd and Gurney, 1986; E88 = Eggler *et al*., 1988; G96 = Griffin *et al*., 1996; G98 = Griffin *et al*., 1998a, 1998b; G99 = Griffin *et al*., 1999a; G03 = Griffin *et al*., 2003b; Gr99 = Grutter *et al*., 1999; Gr06 = Grutter *et al*., 2006; Kj96 = Kjarsgaard, 1996; K99 = Kopylova *et al*., 1999; K04=Kopylova and Caro, 2004; KP99 = Kukkonen and Peltinen, 1999; LR99 = Lee and Rudnick, 1999; M03 = Malkovets *et al*., 2003; Me03 = Menzies *et al*., 2003; ORG95 = O'Reilly and Griffin, 1985; ORG96 = O'Reilly and Griffin, 1996; OR01 = O'Reilly *et al*., 2001; PD99 = Poudjom Djomani *et al*., 1999; P91 = Pokhilenko *et al*., 1991; P94 = Pearson *et al*., 1994; P99 = Pearson *et al*., 1999; RN99 = Rudnick and Nyblade, 1999; R03 = Read *et al*., 2003; R96 = Ryan *et al*., 1996; S04 = Skinner *et al*., 2004; SF99 = Schmidberger and Francis, 1999; X00 = Xu *et al*., 2000.

5.2.4 Xenolith geotherms and TBL thickness

Figure 5.12 summarizes xenolith constraints on temperature distribution in the continental lithosphere in various tectonic settings. Following widely accepted practice in the petrologic community, xenolith geotherms are compared with conductive continental geotherms constrained by surface heat flow. The discussion to follow (Fig. 5.13) only includes xenolith geotherms constrained by classical geothermobarometry as described in Section 5.2.1, since garnet geotherms do not constrain pressure independently, but instead project temperature estimates from the Ni content distribution in xenocryst garnets onto a conductive geotherm to estimate pressure (depth).

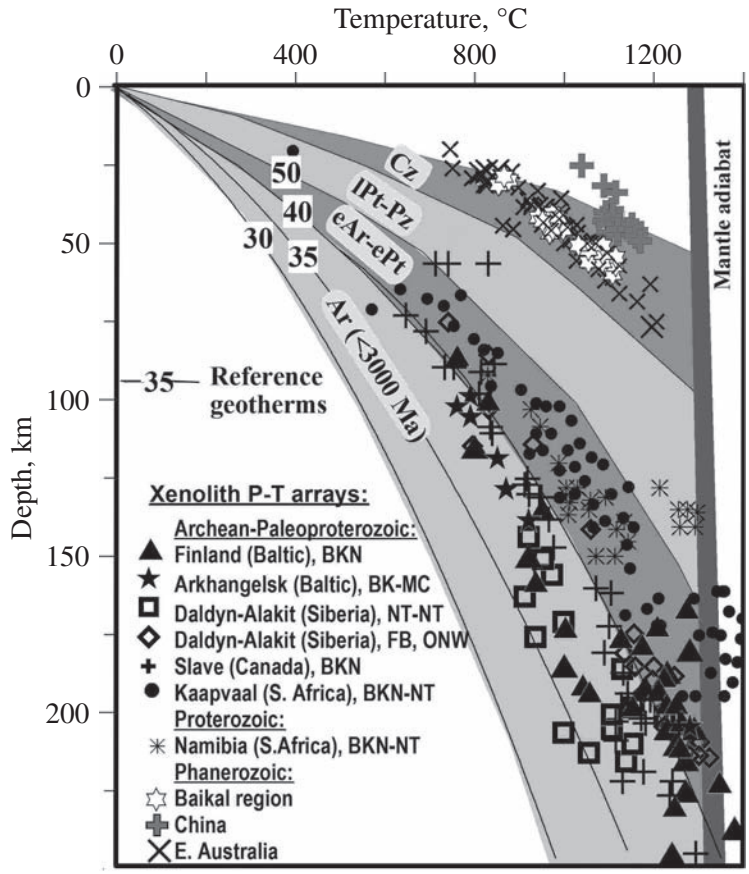

Fig. 5.12 A comparison of xenolith P–T arrays from different continental tectonic settings with reference geotherms from Pollack and Chapman (1977) and typical continental geotherms constrained by heat flow data (based on Artemieva, 2006). Abbreviations: Ar = Archean (< 3.0 Ga), eAr-ePt = Paleoarchean (> 3.0 Ga) and Paleoproterozoic (2.5–1.8 Ga); lPt = Neoproterozoic, Pz = Paleozoic, Cz = Cenozoic. For notations of thermobarometers used in xenolith studies see Table 5.2.

Xenolith constraints on mantle temperatures are of utmost importance in constraining the deep thermal regime of tectonically active regions where steady-state thermal models are invalid, while thermo-mechanical modeling requires detailed information on the crustal and upper mantle physico-chemical processes in these regions. Xenolith P–T arrays from different regions of Cenozoic extension, rifting, and volcanism from China, Australia, Siberia, Spitsbergen, and Europe are surprisingly similar and indicate high mantle temperatures, along 70–90 mW/m^2 conductive geotherms (Figs. 5.12, 5.13(i)). Assuming the MORB adiabat is representative of the convective upper mantle, xenolith thermobarometry yields a surprisingly uniform lithosphere thickness in tectonically active regions, ~60–80 km.

Cratonic geotherms constrained by xenolith geothermobarometry fall between 35 and 50 mW/m^2 conductive geotherms, with lower estimates of mantle temperatures for the Archean–Paleoproterozoic regions. Some cratonic regions (e.g. South Africa, Siberia) have been affected by several pulses of tectono-magmatic activity. Repeated eruptions that brought xenoliths to the surface during different tectonic episodes allow reconstruction of the evolution of paleolithospheric temperatures. For example, deep crustal xenoliths from South Africa suggest that the thermal regime of the lithosphere remained unchanged between 800–600 Ma and ~200 Ma (Schmitz and Bowring, 2003). It is likely, however, that a significant change in thermal regime occurred in the Mesozoic, as indicated by different xenolith P–T arrays below ~160 km depth from the Finsch pipe that erupted at 119 Ma and kimberlites from Northern Lesotho that erupted at ~90 Ma (Fig. 5.7b). Similarly, two generations of kimberlite eruptions in the SW São Francisco Craton, Brazil (at 89 Ma and at ~85 Ma) indicate significant change in the thermal regime of the lithospheric mantle (Fig. 5.13f). Kimberlites erupted at ~85 Ma clearly follow a 40–45 mW/m^2 conductive geotherm and show lithospheric temperatures ~ 250ºC higher than xenoliths from the earlier eruption (~89 Ma) which follow a 35–40 mW/m^2 conductive geotherm. This thermal anomaly can be related to the Late Cretaceous opening of the South Atlantic and the break-up of Gondwana (Read *et al*., 2003).

Xenolith geotherms from the off-craton Proterozoic mobile belts in South Africa and from the Archean cratons that have been significantly reworked in Phanerozoic (the Wyoming, Sino-Korean, and Tanzanian cratons) follow the cratonic conductive geotherm only down to ~120–150 km depth (Fig. 5.13b). At these depths, mantle temperatures reach 1000–1200 °C and increase over a small pressure (depth) interval. The deflection of xenolith P–T data from the conductive geotherm may be interpreted as the base of the upper mantle layer with a (pure) conductive heat transfer regime. Phanerozoic tectono-thermal events probably involved thermo-mechanical removal (delamination) or compositional transformation (refertilization by asthenosphere-derived fluids and basaltic melts) of the lower 80–140 km thick layer of these Archean keels (Eggler *et al*., 1988; Griffin *et al*., 1998b; Lee and Rudnick, 1999; Xu *et al*., 2000).

5.2.5 Lithosphere thickness in Archean cratons

Two types of Archean xenolith geotherms?

Lithosphere thickness in the Archean cratons is a subject of great importance for global geochemical and geodynamical models of the Earth's early evolution, crustal and mantle

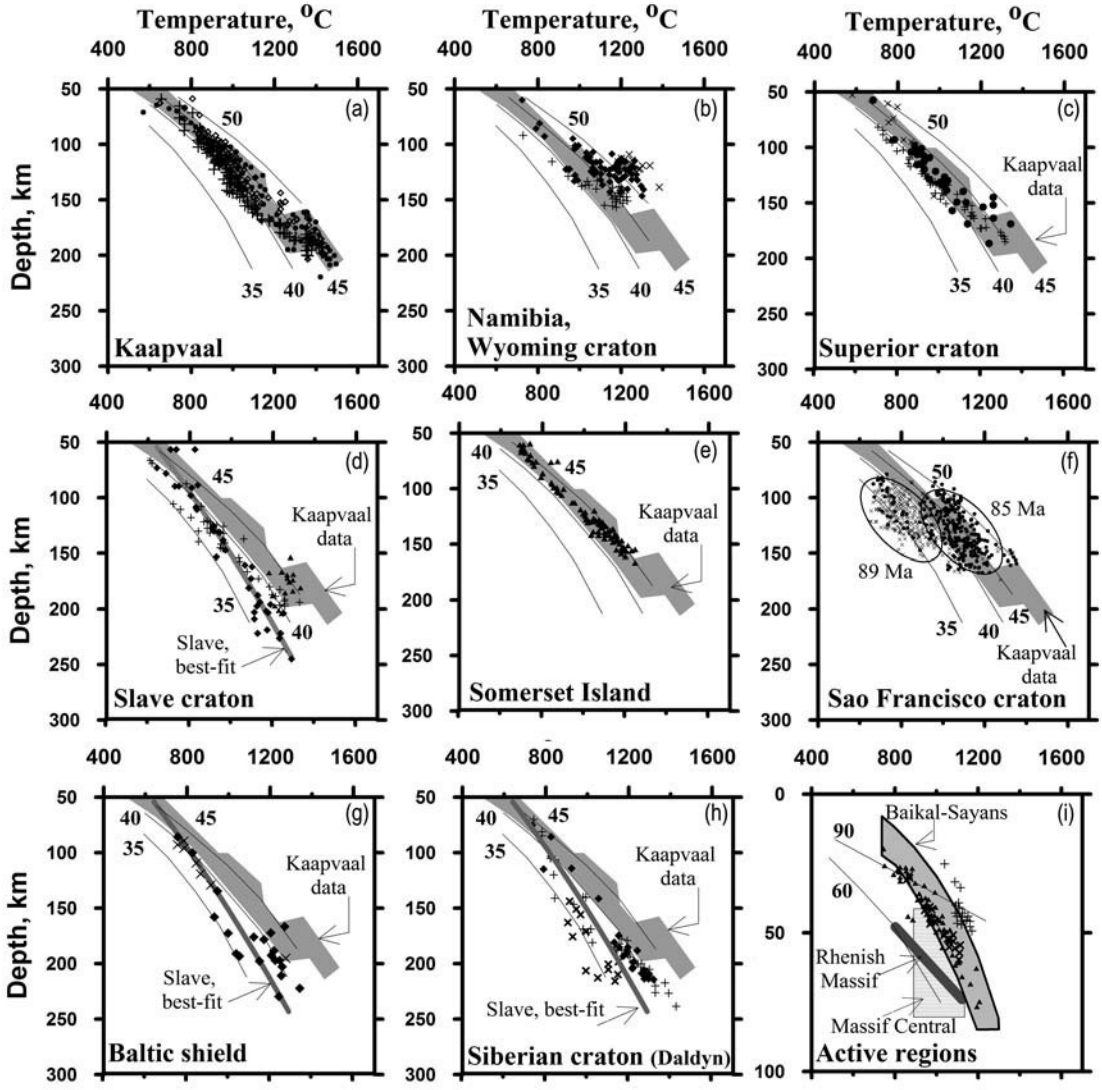

Fig. 5.13 Xenolith geotherms for continents (most of the data for the BKN method; for notations of other geothermobarometers see Table 5.2). Gray shading in (a–h): xenolith data from several locations in Kaapvaal (compilation of Rudnick and Nyblade, 1999); gray line in (d, g, h): best-fit for low-*T* peridotites from Slave craton (BKN data from Kopylova *et al*., 1999; Kopylova and McCammon, 2003). Two geotherms are typical for the cratonic lithosphere: ~45 mW/m^2 (a–c, e, f) and ~37 mW/m^2 (d, g, h). Thin lines – conductive geotherms of Pollack and Chapman (1977), values are surface heat flow in mW/m^2. Note different depth scale of plot (i). For references and details see Artemieva (2006).

differentiation, longevity of the Archean lithosphere, and mantle–lithosphere convective interaction. It is also the subject of significant controversy and heated on-going debates.

Rudnick and Nyblade (1999) have compiled xenolith P–T arrays for four Archean cratons (Kaapvaal, Siberia, Slave, and Superior) and concluded that all of them fall onto

the same mantle geotherm of ~40–42 mW/m^2. An extended analysis of xenolith P–T arrays from various Archean cratons does not support this conclusion (Artemieva, 2006). The analysis is based on a preferred choice of xenolith P–T arrays constrained (where available) by the BKN method, with the distinction of xenolith P–T data from different kimberlite clusters within a craton, and with account taken for different crustal and mantle densities (2.7 and 3.3 g/cm^3, correspondingly) when converting pressures into depth values (unaccounted for by Rudnick and Nyblade, 1999). Figure 5.13 shows xenolith geotherms for different cratonic regions, which are compared with the family of reference conductive geotherms (Pollack and Chapman, 1977). P–T arrays from the Archean cratons fall into two distinctive groups:

(1) Xenolith geotherms from South Africa (Kaapvaal), South America, and the Superior Province follow a 40–45 mW/m^2 conductive geotherm (except for a high-temperature part which can be attributed to transient thermal effects, Sleep, 2003).
(2) Xenolith P–T arrays from the Slave craton, Fennoscandia (central Finland and Arkhangelsk region), and the Siberian craton (the Daldyn terrane) indicate a significantly colder conductive geotherm, 35–38 mW/m^2 (Table 5.3). There is, however, significant scatter of xenolith P–T data for the Siberian craton and the Baltic Shield, which can probably be attributed to mineralogical disequilibria, as observed in xenolith suites from Siberia (Griffin *et al*., 1996). In this case, xenolith P–T geotherms and associated lithospheric thermal structure should be interpreted with caution.

These results suggest that, because of the difference in xenolith geotherms between the two groups, the Archean cratons are likely to have two different lithosphere thicknesses. Small differences in references geotherms lead to large differences in the TBL thickness. Ignoring the existence of a rheologically active boundary layer with perturbed geotherm between the conductive TBL and the convecting mantle, a warmer 42 mW/m^2 geotherm intersects the mantle adiabat at ~220 km depth, while a colder 37 mW/m^2 geotherm – at ~300 km depth (the exact depth is difficult to constrain because at depths > 300 km the geotherm asymptotically approaches the mantle adiabat). This conclusion is in general agreement with the results of thermal modeling (Fig. 4.46) and mantle convection models (Fig. 4.50) which indicate bimodal distribution of lithospheric thickness in depleted Archean cratons, 200–220 km and ~300 km (Doin *et al*., 1997; Artemieva and Mooney, 2001; Levy *et al*., 2010).

Do xenolith data ban a 300 km-thick lithosphere?

In accordance with the conclusion of Rudnick and Nyblade (1999), xenolith P–T arrays published for various cratonic settings (Table 5.3) are conventionally interpreted as indicating a globally uniform thickness of *c*. 200–220 km of cratonic lithosphere that has not undergone significant thermo-tectonic events since the Precambrian. This interpretation is constrained by the depth at which a 40–42 mW/m^2 xenolith geotherm intersects the MORB adiabat. As noted earlier, estimates of the mantle adiabat constrained by mid-ocean ridge basalts (MORB) may be inconsistent with xenolith thermobarometry (Bell *et al*., 2003).

A surprising similarity of thermal regime of the cratons as apparently indicated by xenolith P–T arrays, despite significant differences in the composition of the lithospheric mantle, tectonic evolution of the cratons, their size, and kimberlite emplacement ages can be easily understood if xenolith geotherms reflect a disequilibrium thermal regime of the cratonic lithosphere *during kimberlite magmatism*. In this case, xenolith geotherms carry information only on the P–T conditions of the eruption, but not on the ambient thermal structure of the lithosphere, making almost meaningless their comparison with *the snapshots of the present state of the mantle* provided by seismic and electromagnetic studies. The very fact that kimberlite magmatism is so restricted both in time and in space (Table 9.5) suggests that it reflects not the equilibrium P–T conditions within the cratonic lithosphere, but rather some unusual localized thermal events in its tectonic history, such as plume–lithosphere interaction (see e.g. Fig. 5.9 and discussion in Section 6.3). The Re–Os studies of Carlson *et al*. (1997) show no difference in Os model ages between high-*T* and low-*T* peridotites. The authors conclude that the fertile nature of high-*T* peridotites is likely to be a recent phenomenon, and thus *the lithospheric base must lie below the depth range sampled by xenoliths in kimberlites*. The absence of shearing associated with flow in the rheologically active boundary layer in the deepest xenoliths from the Baltic Shield suggests that, at least locally, lithospheric thicknesses can be significantly greater than 240 km (Kukkonen and Peltinen, 1999; Poudjom Djomani *et al*., 1999).

Another line of argument against a 300 km-thick cratonic lithosphere is based on the evidence (as seen in Fig. 5.13) that the deepest known mantle xenoliths usually come from a ~200–220 km depth with few samples from a ~240 km depth found in the Baltic Shield and in the Slave craton. *The absence of 'evidence for' is commonly interpreted as 'evidence against'*. However, the absence of known xenoliths derived from depths greater than 250 km within the lithospheric mantle does not prove that the cratonic lithosphere cannot be thicker than 220–250 km. The deeper layers of the upper mantle may not be sampled by xenoliths because kimberlite magmas from deeper mantle may not reach the surface or they are not generated deeper than 240–250 km. This view is supported by the petrologic studies of Brey *et al*. (1991) who suggest that xenoliths may not be representative of the entire cratonic lithosphere as a depth of *c*. 150 km is critical for generation of kimberlite magmas; at this depth they become highly fluid-charged which enhances their ability to capture and transport xenoliths to the surface.

Xenolith versus geophysical data

While numerous interpretations of xenolith P–T arrays from different cratons apparently favor a globally uniform thickness of 200–220 km of the Archean–Paleoproterozoic lithosphere, geophysical interpretations are less consistent and indicate significant variations in thickness of the cratonal lithospheric roots. A globally uniform thickness of *c*. 200–220 km of cratonic lithosphere is supported by electromagnetic studies from various cratonic regions (Fig. 7.38), but contradicts global and regional seismic tomography models, some of which show significant variations in cratonic lithosphere thickness from ~150–200 km to 300–400 km (e.g. Figs. 3.87, 3.90, 3.98, 3.101, 3.120, 3.122). However, the interpretations of seismic tomography models in terms of lithospheric thickness are non-unique and, among

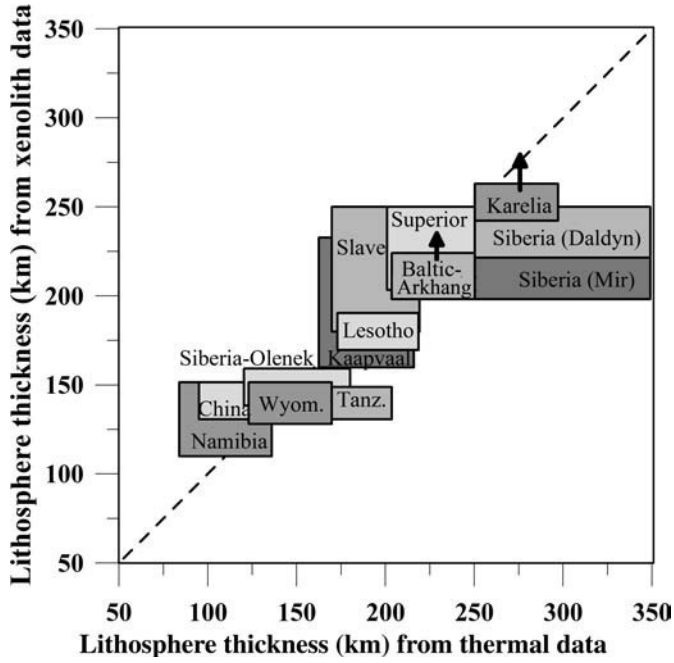

Fig. 5.14 A comparison of lithosphere thickness in the continental regions constrained by xenolith P–T arrays (Table 5.3) and surface heat flow (Artemieva and Mooney, 2001). Peridotites from the deepest known xenoliths from the Archean–Paleoproterozoic parts of the Baltic shield (Karelia and the Arkhangelsk region) do not show shearing, suggesting that the lithospheric mantle extends deeper than sampled by xenoliths (marked by arrows).

other factors, depend on the choice of reference models and the amount of velocity anomaly chosen to mark the lithospheric base (Sections 3.6.2–3.6.3). In agreement with high-resolution seismic tomography models, thermal modeling for the stable continental regions also indicates large differences in lithospheric thickness beneath different Archean cratons, with variations from ~200–220 km in South Africa, Western Australia, and the south-central parts of the Canadian Shield to ~300–350 km in West Africa, Baltic Shield, Siberia, and the northern parts of the Superior Province (Fig. 5.14) (Artemieva and Mooney, 2001; Levy *et al*., 2010).

A direct comparison of lithospheric thickness estimates from xenolith, seismic, electromagnetic, and thermal data should, however, be made with caution. The South African craton is probably the only region where all four sets of data exist and where all of the methods agree in estimating the lithosphere to be ~200–220 km thick (Fig. 5.5). Yet, in some cratons either high-resolution regional seismic models, or good quality electromagnetic models, or reliable thermal constraints diverge from xenolith P–T constraints on the lithospheric thickness. The Archean–early Proterozoic part of the Baltic Shield is of special interest as seismic, thermal, electrical, and xenolith data are available there. In this region,

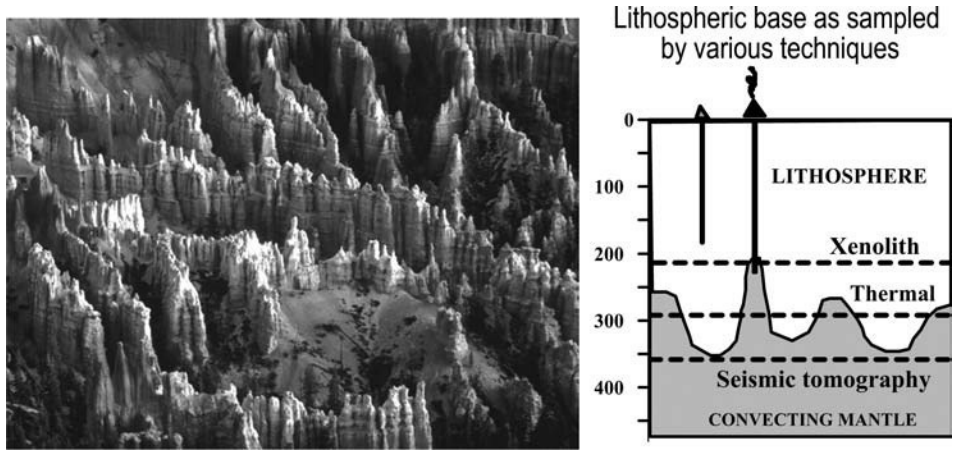

Fig. 5.15 The erosional pattern of the Bryce Canyon (Utah, USA) may be equivalent to the topography of the lithospheric base with short-wavelength significant variations in lithospheric thickness created by convective erosion. Different geophysical methods and petrologic xenolith-based data sample different depths in the upper mantle, leading to significant discrepancies in lithospheric thickness estimated by different methods.

(i) the electrical asthenosphere has not been found down to 220 km depth in high-resolution surveys (Jones, 1999),
(ii) seismic tomography and thermal models both indicate ~300 km-thick lithosphere (Figs. 3.120 and 4.44), regional high-resolution body-wave tomography suggests the lithosphere can be ~400 km thick (e.g. Sandoval *et al*., 2004), and
(iii) even the deepest xenoliths from 240 km depth have depleted composition and coarse texture (Poudjom Djomani *et al*., 1999; Kukkonen and Peltonen, 1999). In contrast to these diverse data sets, reinterpreted xenolith P–T arrays for the central Fennoscandian Shield in eastern Finland suggest only ~230–250 km thick TBL (Kukkonen *et al*., 2003), whereas earlier interpretations of the same data by the same group yielded values > 240 km for lithosphere thickness in the region (Kukkonen and Peltonen, 1999).

The apparent contradiction between lithosphere thickness estimates from geophysical and petrologic data reported for some cratons can be reconciled if the base of the lithosphere is highly heterogeneous at small scales (Artemieva and Mooney, 2002). The inverted topography created in the Bryce Canyon (Utah, USA) by surface erosion is an easy analog to think of (Fig. 5.15). In the case of an undulating lithospheric base with short-wavelength significant variations in lithospheric thickness, various techniques sample different depths in the upper mantle as the lithospheric base. The diffuse character of the seismic lithospheric base, especially pronounced in surface wave studies which would fail to resolve short-wavelength velocity variations, supports the model. Xenoliths sample the most shallow parts of the lower lithosphere where the pressure–temperature regime is favorable for producing kimberlite-type magmas. Thus, xenolith-based estimates of the lithosphere thickness are not representative of large-scale lithospheric thickness, but

rather refer to a localized thinning of the lithosphere, much as a deeply eroded river gorge does not portray the average topography of a region. Seismic tomography and mantle convection models "average" the top of the convective mantle, i.e. the lowermost parts ("dips") of the lithospheric base (Fig. 5.15), whereas thermal data (due to laterally smoothing heat transfer) provides an averaged picture of lithospheric structure with values of lithospheric thickness intermediate between xenolith and seismic estimates.

5.3 Geotherms constrained by seismic data

5.3.1 Correlations between seismic velocity, attenuation, and temperature

Velocity–temperature correlations

The strong dependence of seismic velocity and elastic moduli on temperature is well known from laboratory studies (Fig. 3.3). Most measurements, however, were made at relatively low temperatures (< 600–$700\,^{\circ}C$) where the temperature dependence of seismic velocities is approximately linear (eq. 3.7). Limited experimental data for $T > 1000\,^{\circ}C$ indicate that at near-solidus temperatures seismic velocities decrease rapidly even before any melting starts and both Vp and Vs show a pronounced drop with increasing percentage of melt (Murase and Kushiro, 1979; Murase and Fukuyama, 1980; Sato *et al*., 1989; Jackson, 1993).

The high sensitivity of seismic velocities to temperature variations provides important constraints on the thermal regime of the upper mantle. A large number of high-resolution global and regional seismic tomography models which have become available recently have been used to convert seismic velocities to temperatures. Such studies have been performed globally (Yan *et al*., 1989; Rohm *et al*., 2000), for the continents (Priestley and McKenzie, 2006), and on continent-scale for Europe (Furlong *et al*., 1995; Sobolev *et al*., 1996; Goes *et al*., 2000), North America (Goes and van der Lee, 2002; Godey *et al*., 2004), Australia (Goes *et al*., 2005); regional studies are available for South Africa (Kuskov *et al*., 2006), while beneath subduction zones mantle temperatures were estimated from seismic attenuation data (Sato *et al*., 1989; Roth *et al*., 2000; Nakajama and Hasegawa, 2003).

A pronounced geographical correlation observed in seismic tomographic models between velocity anomalies and surface heat flow further supports the idea that a significant proportion of seismic velocity variations may have a thermal origin. Shapiro and Ritzwoller (2004) propose to use thermodynamic constraints based on surface heat flow data and the thermal state of the upper mantle to improve seismic models by reducing their uncertainty (Fig. 5.16).

Knowledge of seismic velocity structure alone, however, does not allow for its unique interpretation in terms of mantle temperatures without using additional independent data. Starting from Jordan (1975a, 1979), Anderson and Bass (1984), Bass and Anderson (1984) it has been recognized that large-scale compositional variations in the upper mantle (such as in peridotite composition and Fe content), also play an important role in producing seismic velocity variations. This conclusion is supported by calculation of the density-to-velocity scaling factor which indicates significant compositional heterogeneity of the mantle

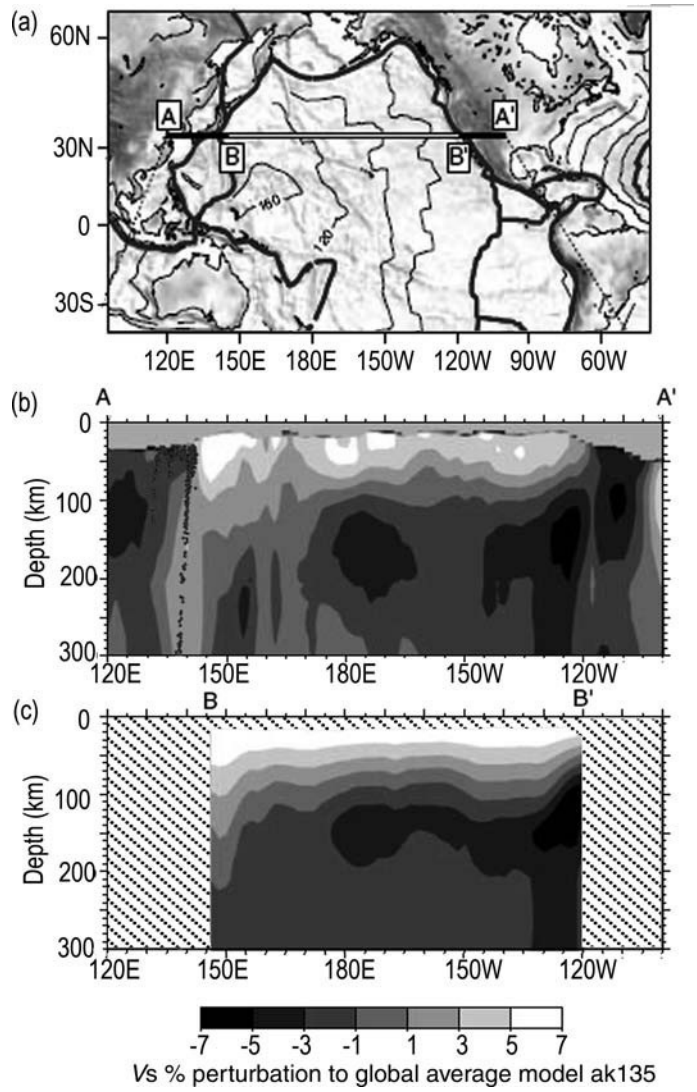

Fig. 5.16 Vertical cross-sections across the Pacific Ocean along the line AA′/BB′. (a) Location map; (b–c) seismic shear-wave velocity models: (b) with ad-hoc seismic parameterization; (c) with thermodynamic parameterization by the use of independent temperature profiles in the upper mantle (modified from Shapiro and Ritzwoller, 2004).

(Fig. 3.110; Godey *et al*., 2004; van Gerven *et al*., 2004; Artemieva, 2009; Simmons *et al*., 2009). Theoretical constraints demonstrate that a +1% *V*s velocity anomaly can be produced either by a 100–150 °C temperature decrease or by a +4% δFe anomaly (Fig. 5.17). Other factors, such as the presence of partial melt or water and anisotropy also have a strong influence on seismic velocities and can significantly affect the results of velocity–temperature inversion (e.g. Sobolev *et al*., 1996). In particular, the presence of water enhances anelastic relaxation and, by affecting *Q*, may reduce the seismic wave velocities by a few percent (Karato, 1995).

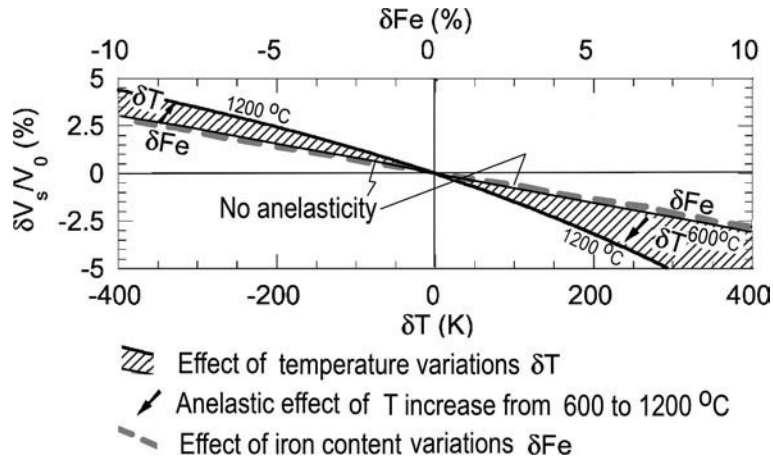

Fig. 5.17 The effect of temperature and iron-content variations in the mantle on shear velocities. The reference values are PREM for *Vs* and Fo89 for iron-content. Anelasticity significantly affects the temperature dependence of relative d*Vs* anomalies (Fig. 3.6, eqs. 3.8–3.11). If its effect is ignored (thin black line), the temperature effect on *Vs* perturbations is underestimated for cold regions and overestimated for hot regions. The effect of Fe-depletion on d*Vs* is of the same magnitude as the anelastic effect due to a 600 °C increase in temperature. The effects of temperature- and iron-content variations on density are shown in Fig. 6.14.

Attenuation–temperature correlations

Laboratory experiments demonstrate that at subsolidus temperatures, seismic attenuation ($1/Q$) in olivine-rich mantle rocks increases exponentially with temperature T (eq. 3.8; Figs. 3.6, 3.8). The high sensitivity of $1/Q$ to temperatures was used to correlate seismic attenuation anomalies in the oceanic and continental mantle with temperature variations (Romanowicz, 1995, 1998; Roth *et al*., 2000; Artemieva *et al*., 2004; Yang *et al*., 2007; Dalton *et al*., 2008) and to calculate mantle geotherms from seismic attenuation (Figs. 3.124 to 3.129). Sato *et al*. (1988, 1989) were among the first to apply the correlation between temperature and seismic attenuation to constrain oceanic geotherms from seismic attenuation and laboratory data, and to argue that attenuation anomalies do not necessarily require the existence of partial melting. Other attempts to calculate temperatures from seismic attenuation data included studies on the crust of south-central Eurasia (Sarker and Abers, 1999) and the mantle wedge beneath northeastern Japan (Nakajima and Hasegawa, 2003).

The validity of conversion of seismic attenuation anomalies into mantle temperature performed by Sato and co-authors was questioned by Karato (1995). He argued that in Sato's experiments, anelastic relaxation was likely to be enhanced by water supplied by the dehydration of hydrous minerals (Karato and Spetzler, 1990). Since the enhancement of anelastic relaxation causes seismic velocity reduction, the low seismic wave velocities and high attenuation observed in back-arc basins and subduction zones are caused not only by high temperatures, but also presumably by high water fugacities. Thus, an

analysis of seismic data (seismic velocities and attenuation) in terms of temperature profile should take into account the effect of water separately from that of temperature. In practice, this is not done in any of the published studies. A part of the problem arises from the fact that presently available laboratory studies of seismic attenuation do not examine the effects of water in detail (Sato *et al*., 1989; Jackson *et al*., 1992, 2000; Faul and Jackson, 2005). As a result, seismic attenuation (or velocity)–temperature conversions constrained by laboratory data need to be treated with caution. This is particularly important when a large amount of water may be present in the upper mantle, such as in (paleo)subduction settings (Fig. 7.19).

The opposite approach is to calculate theoretical models of upper mantle attenuation from the Arrhenius law (eq. 3.8) on the attenuation–temperature correlation, using independently constrained mantle temperatures (Artemieva *et al*., 2004). A comparison between a theoretical attenuation model and seismic attenuation provides information on non-thermal effects on seismic Q, primarily caused by the presence of hydrogen and partial melt (uncertainties in seismic and theoretical models also contribute to the difference between the two models). The correlation between attenuation and temperature globally at any depth in the upper 200 km beneath the continents is less than 0.47 (Fig. 3.128), supporting the conclusion that effects other than temperature play an important role in producing attenuation anomalies in the upper mantle. Therefore, the attenuation–temperature correlation in the upper mantle is subject to significant uncertainty.

The attenuation values determined in laboratory experiments include only intrinsic (anelastic) attenuation, while global and regional seismological studies measure the sum of anelastic and scattering effects (eq. 3.6). A regional study of the Japan islands has demonstrated that scattering can account for 10–30% of the measured attenuation (Hoshiba, 1993) and thus can reduce the attenuation–temperature correlation. However, in the case of small *variations* of scattering in the upper mantle, the correlation between intrinsic (and total) attenuation and temperature will still hold.

The following discussion focuses only on velocity–temperature conversions.

5.3.2 Seismic constraints on temperatures: methodology and uncertainties

Velocity–temperature conversions are based on theoretical and experimental constraints on the elastic and non-elastic behavior of mantle rocks at high P–T conditions (e.g. Duffy and Anderson, 1989; Jackson *et al*., 1990; Karato and Spetzler, 1990; Karato, 1993). However, seismic velocities can vary not only with temperature, but with mineral composition, phase changes, anisotropy, grain size, the presence of water, and with the onset of melting (see Chapter 3.1 and Figs. 3.2 to 3.8). Therefore, a significant proportion of velocity anomalies can be due to physical mechanisms other than thermal, as reflected in a low (< 0.60) correlation coefficient between shear seismic velocities and temperatures in the upper 200 km of the subcontinental mantle (Fig. 3.128). As a result, the conversion of seismic velocities into temperatures is subject to considerable uncertainty since non-thermal effects on seismic velocity variations are difficult to quantify. Furthermore, limitations associated with seismic models (see Section 3.2.3) propagate into additional uncertainties in velocity–temperature conversions.

Tomographic models

Major limitations and uncertainties "inherited" from seismic velocity models include:

- *Vertical and lateral resolution of seismic models*. In particular, seismic models based on fundamental-mode surface waves typically cannot resolve mantle structure deeper than 200–250 km and have a relatively low lateral resolution. In contrast, body-wave tomographic models smear the depth distribution of velocity perturbations (Figs. 3.79, 3.80).
- *Ray path coverage*. In teleseismic tomography it is globally very uneven (Fig. 3.77) and poor in some regions due to the fact that the majority of seismic events are restricted to the subduction zones and the areal distribution of seismic stations is highly non-uniform. On the continents, the worst ray path coverage in teleseismic tomography exists for Siberia, north-central-western Africa, large parts of South America, as well as Arctic and Antarctic regions (including northern Canada and Greenland). The problem is usually less important in regional tomographic models.
- *The regularization method and damping used in seismic inversion*. As a result, the amplitude of velocity perturbations can vary significantly between different seismic tomography models and their quantitative correlations are weak (Section 3.2.3).
- *Uncertainty specific to velocity–temperature conversions* (Fig. 5.18). Adjacent lithospheric blocks may have a strong contrast in seismic velocities (due to contrasts in composition, anisotropy, or grain size), whereas lateral heat transfer will prevent these blocks having a sharply localized contrast in temperatures (unless the thermal anomaly is young or associated with a very sharp contrast in thermal properties). As a result, strong horizontal temperature gradients produced by velocity–temperature conversions based on high-resolution regional seismic models are likely to be artifacts (such as a 800 °C temperature variation over a lateral distance of ~300–400 km at 100 km depth beneath south-eastern Europe in the interpretation of Goes *et al*., 2000).

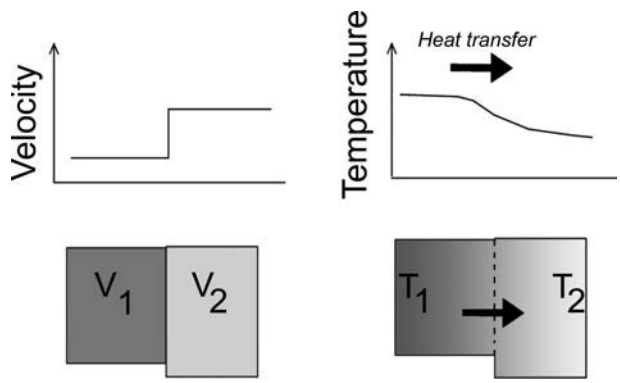

Fig. 5.18 Sketch illustrating an example of velocity-to-temperature conversion. Two adjacent blocks may have a sharp contrast in seismic properties, while lateral heat transfer smears the temperature contrast between them.

Relative and absolute velocities

A calculation of mantle temperatures from seismic velocities consists, in general, of the following steps. First, relative seismic velocity anomalies are converted to absolute velocities (unless the seismic model is in absolute velocities), since the velocity–temperature relation is strongly non-linear at near-solidus temperatures (Fig. 3.3). One of the largest problems arises, apparently, when the PREM model is used as the reference model in seismic inversion for the continents. The isotropic PREM has a 5% step in *V*s velocity at 220 km depth, not necessarily required by continental data (see discussion in Chapter 3), and therefore a 220 km velocity discontinuity requires special consideration in velocity–temperature conversions for the continental regions, such as in the inversion by Röhm *et al*. (2000) (see below).

Effect of iron content

Weak, even at a regional scale, quantitative correlation of seismic velocity anomalies with surface heat flow suggests that factors other than temperature are important in producing velocity perturbations (Fig. 5.19). In the next step of velocity–temperature conversions, some assumptions on compositional anomalies in the upper mantle are made. In the simplest case, all observed seismic anomalies are assumed to result from variation in temperature and iron content. Using this first-order assumption, Röhm *et al*. (2000) estimated the contribution of iron-content variations to velocity anomalies beneath the continents. However, their results may be significantly biased since the values of iron depletion in the Archean cratons were derived from the data set of Jordan (1979) which includes both low-*T* and high-*T* Kaapvaal peridotites. Yan *et al*. (1989) interpret a global surface-wave tomographic model of Woodhouse and Dziewonski (1984) in terms of temperature anomalies (with respect to 1300 °C) or iron-depletion anomalies (with respect to Fo_{10}) (Fig. 5.20) (see Table 5.4 for summary of major model assumptions). Clearly, the approach does not allow for separation of thermal and compositional (iron-content) contributions to shear-wave velocity

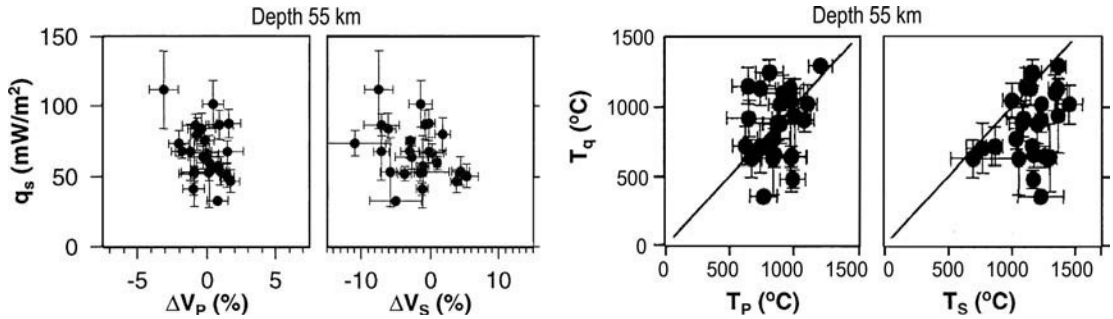

Fig. 5.19 Left: correlations between surface heat flow and seismic velocity anomalies (all data averaged on a $1^o \times 1^o$ grid). Right: correlations between mantle temperatures extrapolated from surface heat flow using conductive geotherms (Pollack and Chapman, 1977) and temperatures derived from P- and S-seismic velocities. All data refer to the European upper mantle at 55 km depth (source: Goes *et al*., 2000).

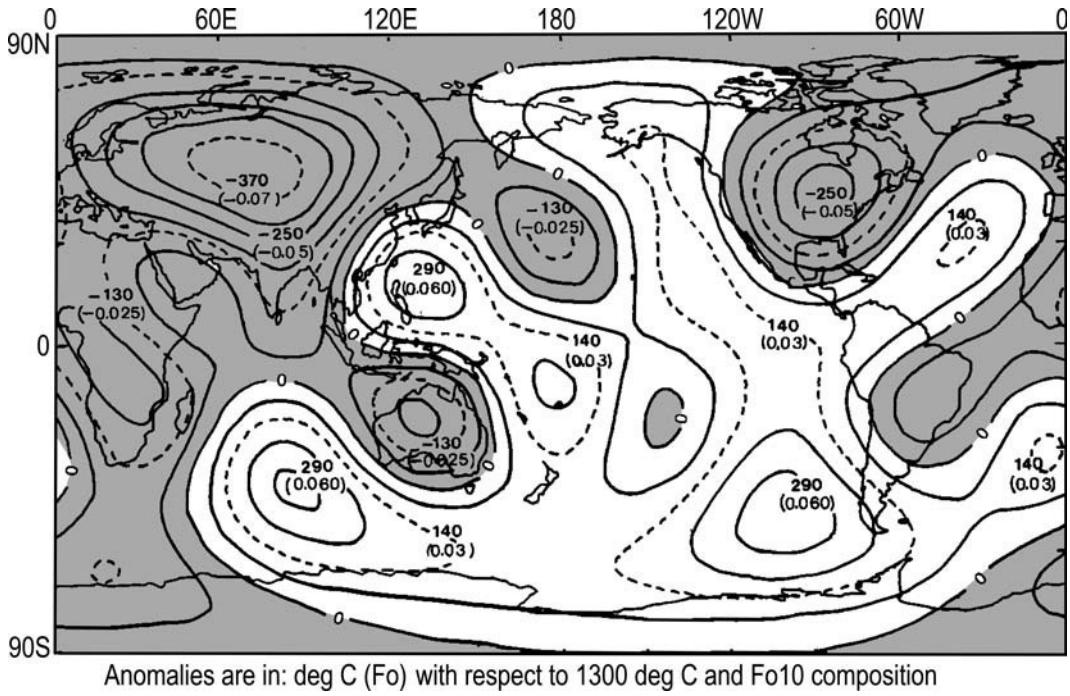

Fig. 5.20 Anomalies of temperature *or* iron content at 150 km depth constrained by a global surface wave tomographic model of Woodhouse and Dziewonski (1984). Positive velocity anomalies (with respect to PREM) in the upper mantle beneath the continents are attributed either to cold temperatures (given in deg C with respect to 1300 deg C) or to iron-depletion anomalies (given in brackets with respect to $Fo_{10} = (Mg_{90},Fe_{10})SiO_4$), or to a combination of both, and the interpretation does not allow for their separation. No anelastic correction is introduced in the calculation. Anelasticity may reduce the amplitude of the inferred anomalies by up to ~50%. Redrawn from Yan *et al.* (1989).

perturbations which can have very close amplitudes (Fig. 5.17). The greatest negative temperature anomalies are associated with cratons and thus are well correlated with surface heat flow. In the case where all velocity anomalies have thermal origin, mantle temperatures at 150 km depth are expected to be ~900–950 °C beneath cratonic Eurasia, ~1050 °C beneath the Canadian Shield, and ~1150–1200 °C beneath cratonic Africa and Australia, with ~1440 °C along the mid-ocean ridges and up to +300 °C temperature anomalies in some parts of the Pacific Ocean. In contrast, if all velocity anomalies originate from iron anomalies, the composition of the cratonic mantle should be extremely depleted in Eurasia and North America. Note that this study did not account for anelastic effects on seismic velocity which, in regions of high attenuation, can reduce temperature anomalies derived from velocity perturbations by a factor of 2 (Sato *et al*., 1989; Karato, 1993).

Effect of composition and anharmonicity

Different effects of pressure and temperature variations on elastic moduli and thermal expansion of single crystals produce anharmonic effects (due to the deviations of mineral

Table 5.4 Some velocity–temperature models

Region and reference	Tomographic model	Assumptions in V–T conversion
Global (Yan *et al*., 1989)	• Fundamental mode Rayleigh and Love waves with their first few overtones (periods > 135 s) and long-period body-wave data (periods > 45 s) (Woodhouse and Dziewonski, 1984); • Lateral resolution ~5000 km (up to degree l = 8 of spherical harmonics) • Velocity perturbations with respect to PREM	• Consider only 150 km depth slice • Composition: isotropic olivine, the only variable parameter: iron content • No anharmonicity • No anelasticity • No melting
Massif Central, France (Sobolev *et al*., 1996)	• Teleseismic P-wave delay-time regional tomography model (in relative velocity anomalies) (Granet *et al*., 1995)	• Compositional variations neglected • Vp, Vs, and density constrained by regional peridotite xenoliths • Account for anharmonicity • Anelactic correction[1] • Melting assumed
Europe (Goes *et al*., 2000)	• Teleseismic body-wave Vp model (Bijwaard *et al*., 1998); Relative velocities with respect to *ak135*; Lateral resolution ~60 km • Teleseismic body-wave Vs model (Marquering and Snieder, 1996)	• The approach of Furlong *et al*. (1995) • Independent inversion for Vp and Vs • Anharmonicity accounted for • Anelactic correction[1,2] for wave period of 20 s • Melting assumed
Global (Röhm *et al*., 2000)	• Fundamental mode Love and Rayleigh surface-wave dispersion (period 40–150 s) plus a waveform data set (Trampert and Woodhouse, 1995); • Vertical resolution: 50–70 km in the upper 400 km • Lateral resolution ~2500 km (up to degree l = 16 of spherical harmonics) • Velocity perturbations with respect to PREM	• Archean cratons assigned a 42 mW/m^2 conductive geotherm, and Vs(z) velocity profiles for other regions are scaled by perturbation from Archean δVs(z) profiles converted to $\delta T(z)$ from a 42 mW/m^2 geotherm • Two model compositions: primitive mantle (Mg# = 0.89) and cratonic mantle based on data of Jordan (1979) from both low-T and high-T peridotites (Mg# = 0.91) • No anharmonicity • Anelactic correction[1,2] for wave period of 20 s • No melting
North America (Godey *et al*., 2004)	• Phase velocities of fundamental-mode Rayleigh waves (periods 40–150 s) • Average lateral resolution ~800 km, the best resolution (~400 km) in the western USA • Vertical resolution down to 260 km depth	• Iron anomalies are constrained by density-to-velocity scaling factor, calculated from a joint inversion of seismic model and geoid • Also considered variations in olivine and garnet • Anelactic correction[1,2] included

Table 5.4 (cont.)

Region and reference	Tomographic model	Assumptions in *V*–*T* conversion
	• Velocity perturbations with respect to PREM	• Partial melting ignored
North America (mostly USA) (Goes and van der Lee, 2002)	• Regional Rayleigh waves fundamental and higher mode model NA00 (van der Lee, 2002); Vertical resolution ~50 km; loses resolution below ~250 km depth • Global teleseismic body-wave *V*p model (Bijwaard *et al*., 1998; Bijwaard and Spakman, 2000); the best vertical resolution ~50–100 km, minimum horizontal resolution ~100 km; relative velocities with respect to *ak135*; • Regional teleseismic body-wave *V*p model (Dueker *et al*., 2001); the best vertical resolution ~50–100 km, minimum horizontal resolution ~50 km	• The approach of Furlong *et al*. (1995) • Independent inversion for *V*p and *V*s • Anharmonicity accounted for • Anelactic correction[1,2] • Assumed three compositions: primitive mantle (Mg = 89), average garnet lherzolite (Mg = 90), depleted mantle (Mg = 93) • Partial melting ignored
Australia (Goes *et al*., 2005)	• Regional fundamental Rayleigh waves (40–200 s) and higher modes (20–125 s) (Simons *et al*., 2002); best resolution ~250 km laterally and ~50 km vertically; poor resolution for Western Australia (see Fig. 3.83); • Regional multimode Rayleigh wave phase velocities (40–150 s) (Yoshizawa and Kennett, 2004); best resolution ~400 km laterally and ~50 km vertically	• The approach of Furlong *et al*. (1995) • Anharmonicity accounted for • Anelactic correction[1] included • Assumed pyrolite composition • Partial melting ignored
Cratons and oceans (Priestley and McKenzie, 2006)	• Fundamental and first four higher modes Rayleigh wave SV-velocities (period of 50–160 s); • Velocity perturbations with respect to PREM (bad for continents); • Great circle approximation (invalid in case of strong lateral velocity gradients); • Poor resolution for some regions (e.g. Western Australia and Siberia, Fig. 3.83)	• Archean cratons assigned a ~40 mW/m2 conductive geotherm based on xenolith P–T arrays; • Oceanic geotherms calculated for the plate model; • Archean and oceanic geotherms used to calibrate velocity–depth profiles worldwide • Two compositions: primitive mantle (Mg# = 90) and melt-depleted cratonic mantle (Mg# = 92.5) • Anelactic correction[3] included • Partial melting ignored

Table 5.4 (cont.)

Region and reference	Tomographic model	Assumptions in V–T conversion
Kaapvaal (Kuskov *et al*., 2006)	• Several regional Vp and Vs models	• Compositional variations constrained by regional peridotite xenoliths, also included are average garnet peridotite and primitive mantle compositions • Account for anharmonicity • Anelactic correction[1] included • Partial melting ignored

[1] Q model based on average experimental data and calibrated for wave period of 1 s to fit seismic observations with the old oceans geotherm (assumed to be a global average) and for mantle potential temperature of 1100 °C (Sobolev *et al*., 1996).
[2] Q model based on experimental data for forsterite (Berckhemer *et al*., 1982).
[3] Q model calibrated to fit seismic observations with the cratonic xenolith P–T arrays and with oceanic geotherms, taking into account the effect of grain size variations on Vs (experimental data of Faul and Jackson, 2005).

lattice vibrations from harmonic oscillations) (Duffy and Anderson, 1989; Chopelas and Boehler, 1989; Anderson *et al*., 1992). Most velocity–temperature models that are constrained by petrologic data on crustal and upper mantle composition take these effects into account. For example, Sobolev *et al*. (1996) use regional mantle-derived peridotites from the Massif Central to calculate equilibrium mineralogical composition, density, and Vp and Vs seismic velocities which account for anharmonicity. In particular, with temperature increase (at constant pressure), the solubility of Al in pyroxenes increases leading to a decrease in volume fraction of spinel and garnet in ultramafic rocks. As a result, the overall density and seismic velocities of mantle rocks decrease (Fig. 6.12). To separate temperature and compositional effects of velocity variations, Furlong *et al*. (1995) propose the use of Vp and Vs velocities simultaneously in velocity–temperature conversions.

Mineral reactions, in particular at $P < 3$ GPa, may have a further effect on the temperature dependence of density and seismic velocities. In the deeper mantle, the effects of phase transitions should be included in velocity–temperature inversions. A self-consistent thermodynamic approach to calculate mantle temperatures from absolute P- and S-wave velocities and geochemical constraints has been used for the Kaapvaal craton (Kuskov *et al*., 2006). The results (see below) show that calculated mantle temperatures depend strongly on bulk composition and on the proportion of stable phases at various depths, so that relatively small compositional differences lead to substantial variations in the inferred upper mantle temperature.

Effect of anelasticity

As a first-order approximation, mantle temperatures can be calculated from seismic velocities assuming linear dependence of velocity on temperature (eq. 3.17). If anelasticity is

Table 5.5 Temperature derivatives of elastic wave velocities for upper mantle olivine

Q	$\partial \ln Vp/\partial T$ ($\times 10^{-4}$ 1/K)	$\partial \ln Vs/\partial T$ ($\times 10^{-4}$ 1/K)
50	− 2.18	− 2.32
100	− 1.40	− 1.54
200	− 1.01	− 1.15
300	− 0.88	− 1.02
400	− 0.82	− 0.96
∞	− 0.62	− 0.76

(From Karato, 1993).
For finite Q, temperature derivatives are the sum of anharmonic and anelastic effects. Anelastic effects for various Q values are calculated assuming $T = 1600$ K and $H^* = 500$ kJ/mol. For $Q = \infty$, temperature derivatives are caused by anharmonic effects (values from Isaak, 1992).

ignored, the temperature effect on seismic velocities perturbations is underestimated for cold regions and overestimated for hot regions (Fig. 5.17). At seismic frequencies, a −5% anomaly of Vs at 100 km depth can be explained by a ~650 °C temperature anomaly if (eq. 3.17) is used, or by a ~325 °C temperature anomaly if the correction for anelastic effects is introduced (Karato, 1993). The anelasticity correction to the elastic part of seismic velocities can be introduced through seismic attenuation (eq. 3.11) which depends strongly on temperature (eq. 3.8) and the oscillation period (eqs. 3.9–3.10). Laboratory results on seismic attenuation in dry peridotite allows us to estimate Q_p from known geotherms in the vicinity of solidus temperatures. The relationship (3.17) allows introduction of anelastic corrections to Vs as well as Vp velocities. Taking the derivatives of eqs. (3.11, 3.8), one gets temperature derivatives of elastic wave velocities $\partial \ln Vp/\partial T$ and $\partial \ln Vs/\partial T$, which are the sum of anharmonic and anelastic effects. Table 5.5 lists their values for upper mantle olivine. Since for a given temperature, $Q_{s<}Q_p$, at any given depth $\partial \ln Vs/\partial T$ is significantly larger than $\partial \ln Vp/\partial T$.

Partial melts, fluids, grain size, and anisotropy

After assumptions on composition are made and the corrections due to anelasticity and anharmonicity can be introduced into velocity–temperature inversions, other non-thermal factors should be accounted for. These include the effects of melts, hydrogen, grain size, and LPO anisotropy on seismic velocities. An overview of these effects on elastic moduli is presented in Section 3.1 (see Figs. 3.8; 3.13; 3.14). Without repeating much of the text, the major aspects relating to velocity–temperature conversions are the following.

The amount of melt present in the upper mantle in different tectonic settings is not well constrained and the geometry of melt inclusions (which has a dramatic effect on seismic velocities) is hardly known. Thus, if the melt phase is present in the mantle, its effect is difficult to account for in velocity–temperature inversions. Typical assumptions used in inversions tend to underestimate the melt effect. For example, Sobolev *et al*. (1996) assumed

the spherical geometry of melt inclusions, while Godey *et al*. (2004) assume that partial melting occurs locally and has negligible effect on the regional mean values of temperature and compositional variations.

Similarly, water (e.g. supplied by the dehydration of hydrous minerals) has a strong effect on seismic velocities and on attenuation, and an inversion of seismic data to mantle temperatures should take into account separately the effects of water and temperature. Most important are the indirect effects of water on seismic velocities due to enhanced anelastic relaxation and the possible change in preferred orientation of olivine with corresponding changes in seismic anisotropy (see Section 3.6.3). The effect of water is difficult to quantify due to the absence of systematic laboratory results on the effect of hydrogen on seismic attenuation.

Both seismic anisotropy and grain size variations may play an important role in seismic velocity variations, but at present their effects cannot be reliably quantified. For this reason, both effects are commonly ignored in velocity–temperature inversions.

5.3.3 Seismic constraints on temperatures: major results

Mapping temperature variations only

Velocity–temperature inversions have been applied globally and regionally to the calculation of lithospheric temperatures. These results provide useful constraints on lithospheric geotherms, especially for tectonically active regions, where any modeling of thermal structure of the mantle is highly uncertain (e.g. van Wijk *et al*., 2001). A number of thermal models based on the conversion of seismic velocities to upper mantle temperatures are available for most of the continents. Such studies are limited to few research groups, and a summary of major assumptions and limitations associated with each of the approaches is provided in Table 5.4. As discussed earlier, the uncertainties of inversions include the uncertainties inherited from the seismic models used in the calculations and the assumptions of the velocity–temperature inversion itself.

Comparison of the results of velocity–temperature inversions with continental geotherms inferred from surface heat flow and xenolith data indicate a good agreement between the different approaches (Figs. 5.21, 5.22, 4.33). Röhm *et al*. (2000) calculated temperature variations in the upper mantle using the S-wave tomographic model S16RLBM (Woodhouse and Trampert, 1995). Since the S16RLBM model is constrained with respect to the PREM reference model, the velocity discontinuity at 220 km depth requires special handling. In the absence of a clear thermodynamic understanding of its origin (or its very existence under continents), its parameterization through a discontinuous variation of composition or rheology is not possible. To overcome this problem, the authors assume that all Archean cratons are characterized by a 42 mW/m^2 reference conductive geotherm. Under this assumption and assuming a cold mantle adiabat of 1200 °C, it is possible to eliminate a 220 km discontinuity for the velocity profile calculated from a 42 mW/m^2 conductive geotherm. Velocity–depth profiles for other tectonic regions are scaled by perturbation from the Archean velocity profiles and are converted to temperature perturbations from a 42 mW/m^2 geotherm. In the absence of independent data other than the

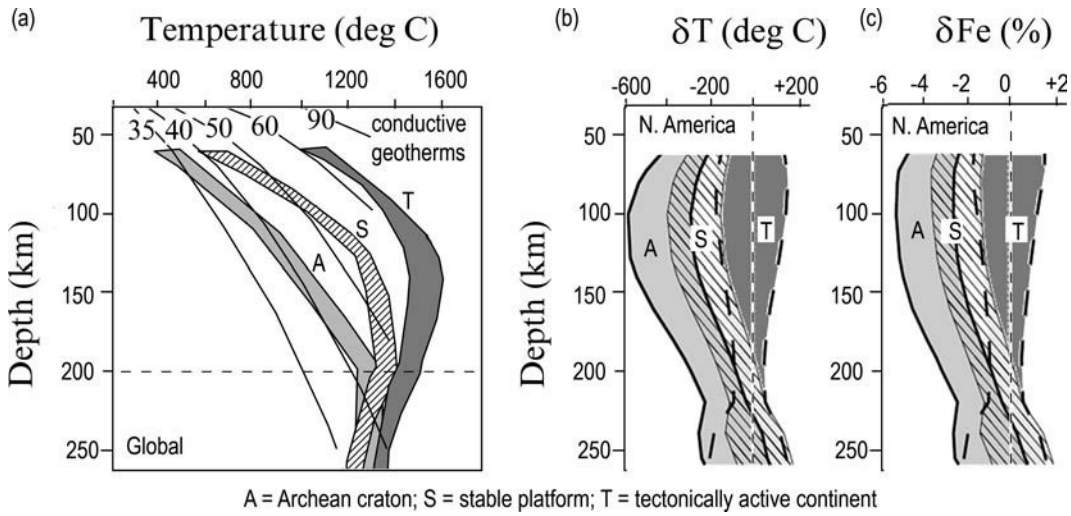

Fig. 5.21 Vertical profiles for three different tectonic provinces of: (a) temperature variations assuming mg# = 0.89 and 0.91 (see details in Table 5.4), (b) temperature anomalies, and (c) iron anomalies with respect to XFe = 11% (Mg# = 0.89). All profiles are calculated from seismic velocities assuming that velocity anomalies are caused only by temperature and iron-content variations. (Sources: (a) Röhm *et al*., 2000; (b–c) Godey *et al*., 2004.)

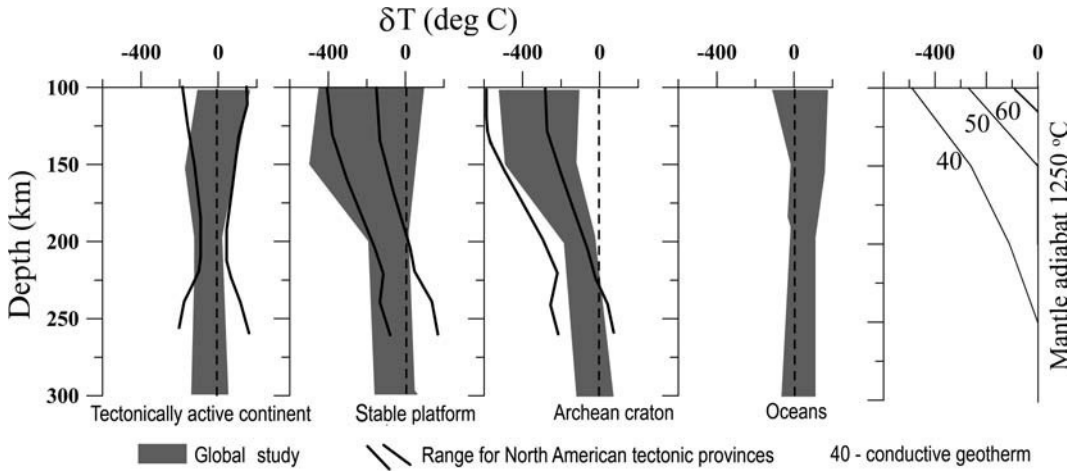

Fig. 5.22 Vertical profiles of temperature variations for different tectonic provinces based on a joint inversion of the S-wave tomographic model S16RLBM (Woodhouse and Trampert, 1995) and the geoid model EGM96 (Lemoine *et al*., 1998) (gray shading). Reference temperature is 1250 °C (the results of Deschamps *et al*., 2002). The results of Godey *et al*. (2004) for North America are shown by black lines (see Fig. 5.21). For a comparison, the right plot shows the difference between reference conductive geotherms and a 1250 °C mantle adiabat.

tomographic model, the study does not allow for separation of compositional and thermal effects, but allows for calculation of typical geotherms for three continental tectonic provinces (defined using the 3SMAC regionalization of Nataf and Richard, 1996). The effect of iron-content variations on inferred mantle temperatures is calculated for two compositions, with Mg# = 89 and 91, which provides the bounds on estimated mantle temperatures (Fig. 5.21a).

Priestly and McKenzie (2006) use oceanic geotherms derived from the plate model and cratonic geotherms constrained by xenolith P–T arrays from the Siberia, Slave, and Kola-Karelian cratons to calibrate shear-velocity perturbations (with respect to PREM) and convert them to mantle temperatures. Because of problems with the crustal correction, the tomographic model for Siberia may not be well constrained (the difference in the Moho depth in regional seismic data and in global crustal models is 5–10 km). Similarly to the study by Röhm *et al*. (2000), the approach relies heavily on the notion that xenolith geotherms are representative of the steady-state thermal regime of ancient continental nuclei. However, in contrast to the calculations of Röhm *et al*. (2000), no attempts are made to compensate for the 220 km velocity discontinuity when inverting relative velocity anomalies to mantle temperatures in the cratonic regions (see Figs. 3.85 and 3.86 and discussion in Section 3.6). The model also does not account for possible lateral variations in composition within the continental lithospheric mantle, which is assumed to be depleted cratonic and produced by a 20–25% melt removal with the residue composition characterized by Mg# ~92–92.5. For the oceans, temperature variations at 150 km depth beneath the entire Pacific region are within 20 °C of 1400 °C when anelasticity is accounted for. Analysis of seismic velocities for the East Pacific Rise indicates that the observed shear-velocity structure does not require the presence of melt and a 2.3% variation in shear velocity at 60 km depth at the eastern and western flanks of the Rise can be attributed to a 23 °C temperature difference at near-solidus temperatures when velocity–temperature dependence becomes strongly non-linear and anelastic effects are accounted for. By comparison, the elastic estimates of Dunn and Forsyth (2003) require a temperature difference of 350 °C to explain differences in velocity beneath the two flanks of the East Pacific Rise.

A velocity–temperature inversion for North America was performed by Goes and van der Lee (2002), following the approach used by Furlong *et al*. (1995) and Goes *et al*. (2000) for Europe. It includes independent inversion for Vp and Vs velocities with account taken of anelastic effects and it assumes three basic compositions of the upper mantle. As such, the approach does not allow for vertical mapping of compositional variations in the upper mantle. The results suggest a strong temperature anomaly in the upper 150 km of the mantle beneath the stable eastern USA with mantle temperature at 100 km depth of ~700–800 °C ($\delta T \sim 600$ °C) as constrained by the surface-wave velocity model. Beneath the active western USA, mantle temperatures at 100 km depth are close to the mantle adiabat. Using a similar approach and independently inverting two shear-wave velocity models for mantle temperatures, Goes *et al*. (2005) estimated geotherms for Australia. Again, in the absence of independent data or xenolith constraints on compositional heterogeneity of the mantle, seismic velocity perturbations are interpreted in terms of purely thermal anomalies. Importantly, seismic tomography models used in the velocity–temperature inversion have

reduced resolution for the Archean cratons in Western Australia (Fig. 3.83). The results indicate that mantle temperatures beneath the cratonic part of Australia (both Archean and Proterozoic) follow a 40–45 mW/m^2 conductive geotherm with mantle temperatures along a 50–60 mW/m^2 conductive geotherm beneath the Phanerozoic regions.

Mapping thermal and compositional variations

Several studies aim to separate the effects of thermal and compositional variations in the cratonic upper mantle on velocity perturbations. These studies, in addition to seismic models, utilize independent data sets such as gravity data or regional petrologic data on the composition of the lithospheric mantle.

Deschamps *et al*. (2002) perform a joint inversion of the S-wave tomographic model S16RLBM (Woodhouse and Trampert, 1995) and the geoid model EGM96 (Lemoine *et al*., 1998). Use of two independent data sets allows for separation of thermal and compositional anomalies in the upper 300 km; the latter are ascribed solely to iron-content variations (Figs. 3.19 and Fig. 5.22). The tectonic provinces are also defined using the 3SMAC regionalization. The results indicate that strong temperature anomalies (with respect to convective mantle) in stable continental regions are restricted to the upper 150 km with a fast decrease in amplitude between 150 km and 200 km depth. According to this study, below a 200 km depth, the temperature structure of the upper mantle beneath the continents and the oceans becomes indistinguishable. This specific depth is "inherited" from the velocity discontinuity at 220 km in the PREM model: a significant deviation of a 40 mW/m^2 reference conductive geotherm (expected for many cratonic regions) from the mantle adiabat extends deeper than 200 km depth (Fig. 5.22).

A similar analysis for the North American continent has been performed by Godey *et al*. (2004). They performed a joint inversion of a regional surface-wave tomographic model and geoid to separate thermal and compositional effects from shear velocities and density-to-velocity scaling factor. Compositional anomalies are interpreted in terms of iron-content variations, but the effects of other compositional parameters (garnet and olivine content) are examined as well. Since garnet contains iron, the global volume fraction of iron is kept constant, so that variations in garnet content effectively reflect variations in the aluminium content. The results indicate that a 2% increase in shear velocity can be caused either by a 120 °C temperature decrease, or a 7.5% iron depletion, or a 15% aluminium depletion. Variations in the fraction of olivine have a much weaker effect on shear velocities: a 50% depletion in olivine produces a 1% velocity perturbation (Fig. 6.14b). Depth profiles of temperature and iron-depletion variations in the upper mantle of North America are in overall agreement with the global results of Deschamps *et al*. (2002). The principal difference is that in the cratonic part of North America both temperature and iron-depletion anomalies persist down to at least 250 km depth (Fig. 5.21bc). Below this depth the model lacks resolution. Iron-content variations in the lithospheric mantle of the North American craton are in striking agreement with global xenolith data, which indicate a ~4% iron-depletion anomaly above 150–200 km depth reduced to ~2% at 200–240 km depth (Fig. 3.19). It is likely

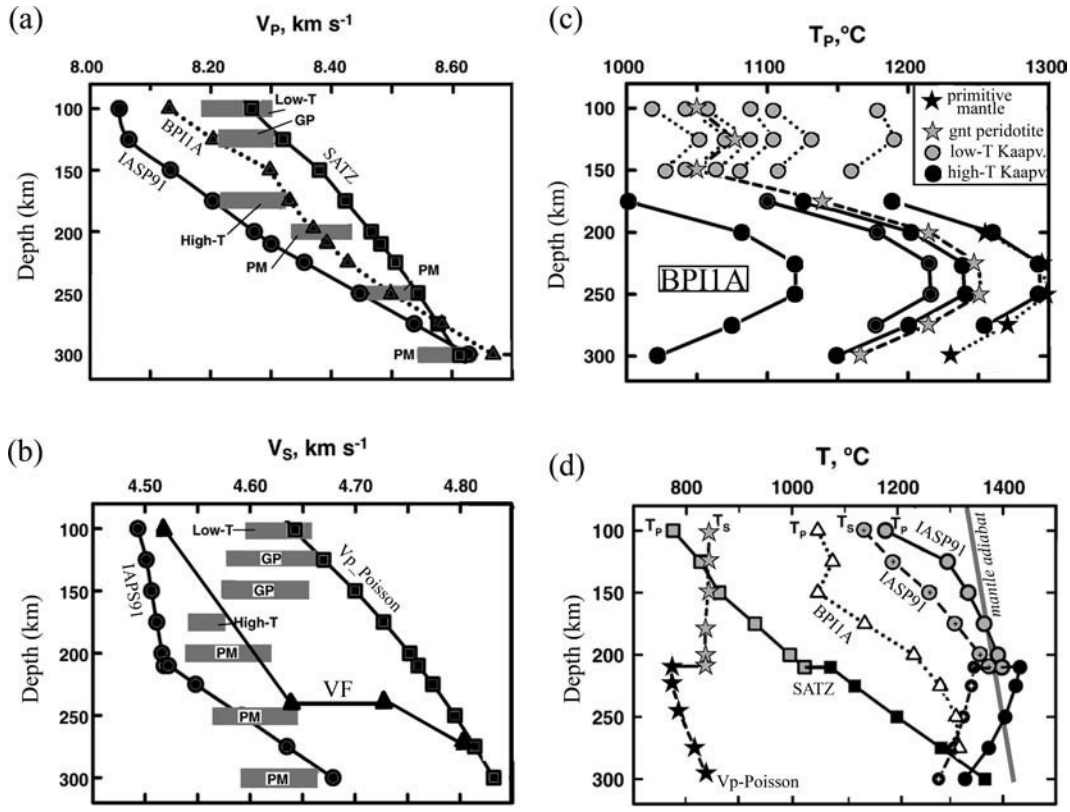

Fig. 5.23 (a–b) P- and S-velocities calculated from the anharmonic part of seismic velocities for reference model *iasp91* and regional seismic models for southern Africa: VF (Vinnik and Farra, 2002), BPI1A (Simon *et al*., 2002), SATZ and *V*p_Poisson (Zhao *et al*., 1999). Gray boxes – *V*p and *V*s for low-*T* and high-*T* peridotites from the Kaapvaal craton (at 900 °C and 100 km depth, and at 1300 °C and 175 km depth, respectively) and *V*p and *V*s for compositions of average garnet peridotite (GP, depth 100–175 km) and primitive mantle (PM, depth > 175 km). (c) Effect of specific composition of garnet peridotite xenoliths from the Kaapvaal craton on the *T*p temperatures evaluated from the BPI1A model. For both low-*T* and high-*T* xenoliths, inferred temperatures vary by ~200 °C. Symbols refer to different kimberlite pipes. (d) T_P and T_S inferred from different P- and S-velocity models (BPI1A, IASP91, SATZ and *V*p_Poisson) for three compositions: depleted garnet peridotite at depths of 100–210 km (GP, gray symbols), primitive mantle composition at depths of 210–300 km (PM, black symbols), and variable bulk composition with a gradual increase in fertility at depths between 200 and 275 km (BPI1A model, open triangles). Gray line – 1300 °C mantle adiabat. (Source: Kuskov *et al*., 2006).

that the amplitude of iron depletion in the platform areas is overestimated compared with xenolith data.

Petrologic data from numerous kimberlite pipes in the Kaapvaal craton, South Africa, together with regional high-resolution seismic models were used to calculate mantle temperatures and to estimate the effect of the specific composition of garnet peridotite xenoliths on the temperatures evaluated from velocity models (Kuskov *et al*., 2006).

Mantle composition was constrained by xenolith data and included petrologic data on garnet-bearing lherzolite xenoliths, average composition of garnet peridotites, and composition of primitive mantle. Phase equilibrium relations were computed by minimization of the total Gibbs free energy combined with a Mie–Grüneisen equation of state. Modeling included forward calculation of phase equilibria, seismic velocities and density, and inverse calculation of temperature with account for anharmonicity, anelasticity, and the effects of mineral reactions, which included calculations of phase proportions and chemical compositions of coexisting phases. The results indicate that the inferred temperatures can vary by ~200 °C for both low-T and high-T peridotites (Fig. 5.23c). Furthermore, for models with a uniform bulk composition (irrespective of the composition model), mantle temperatures inferred from regional seismic models display a non-physical behavior with a negative temperature gradient at depths below ~200–220 km. Neither inflexions of geotherms nor an anticorrelated behavior for T_P and T_S (mantle temperatures inferred from Vp and Vs, respectively) can be explained by a sharp change in composition from depleted garnet peridotite to fertile pyrolitic mantle. Temperature inflexions can be evaded if the mantle beneath the Kaapvaal craton is chemically stratified: the upper layer at 100–175 km depth consists of depleted garnet peridotite, while in the lower layer (at 200–275 km) mantle fertility increases continuously with a substantial gradual increase in FeO, Al_2O_3, and CaO content, and the lower layer does not differ from normal fertile mantle below 275 km depth.

5.4 Magnetic methods to determine lithospheric geotherms

5.4.1 Major principles

Magnetization of crustal and upper mantle rocks plays a critical role in paleomagnetic reconstructions, analysis of ocean floor ages, and ocean spreading rates. It is worth remembering that the ocean floor is dated by the magnetic method, which played a critical role towards widespread acceptance of plate tectonics (Heirtzler *et al*., 1968). Additionally, Curie temperature (a characteristic property of a ferromagnetic or piezoelectric material which is the reversible temperature above which the material becomes paramagnetic) may provide independent constraints on lithospheric temperatures. Only the latter aspect is discussed here.

The magnetic field of the Earth consists of contributions from the core and from the lithosphere (for review of terrestrial magnetism see Langel and Hinze, 1998; Purucker and Whaler, 2007). The magnetic field of the crust makes < 10% of the core magnetic field, but dominates at short (< 2600 km) wavelengths. At longer wavelengths, crustal signal may be distorted by overlap with the long-wavelength magnetic field from the core (Meyer *et al*., 1985).

Crustal magnetization consists of two components: remanent and induced magnetism. The Königsberger ratio Q is the ratio of remanent to induced magnetization in a rock; it ranges between 1 and 160 in oceanic basalts. Induced magnetism is caused by the present

Earth's core magnetic field and depends on the field strength (additionally affected by the interaction between the core field and the solar wind), the magnetic susceptibility of rocks, and the thickness of the magnetic layer ("magnetic crust"). A global model of induced and remanent lithosphere magnetization based on satellite data shows (i) long-wavelength magnetizations dominated by the continent–ocean contrast and (ii) short-wavelength enhanced magnetizations dominated by seafloor spreading. The remnant magnetization spectrum of the oceans has been modeled based on both non-satellite and satellite magnetic data (Cohen and Achache, 1994; Dyment and Arkani-Hamed, 1998). However, for the continents neither global nor regional remanent magnetization models exist because of incomplete knowledge on continental remanent magnetization. In practical modeling of continental magnetism, either the oceanic remanent model is used or it is assumed that induced magnetism dominates the continental magnetic field (Fox Maule *et al*., 2005).

Practical applications of magnetic methods are based on spectrum analysis of the magnetic field using forward and inverse methods. Forward methods are based on calculations of magnetic anomalies for bodies modeled as collections of simple geometric bodies (e.g. Bhattacharyya, 1966; Dyment and Arkani-Hamed, 1998). Inverse methods aim to estimate the depth to the magnetic bodies, their dimensions, and magnetization contrast. The depth to the magnetic source is often calculated in the spectral domain (e.g. Spector and Grant, 1970). The problem is extremely difficult since contributions from the bottom of the magnetic sources are, at all wavelengths, dominated by contributions from the top, and the top of the source is, in general, also unknown.

Until recently, studies of the lithospheric magnetic signal were based on regional aeromagnetic or global magnetic data such as provided by the Magsat satellite mission (launched in 1979). The launch of the Danish Ørsted high-precision geomagnetic field satellite in 1999 and the German CHAMP satellite in 2000 marked a breakthrough in studies of the magnetic field of the lithosphere (Olsen *et al*., 2000; Neubert *et al*., 2001; Mandea and Purucker, 2005). In satellite-based magnetic studies, with satellites typically orbiting at altitudes of a few hundred kilometers, the lithospheric anomaly field at (or above) the Earth's surface, depends on the magnetization of only a small lithospheric sector located directly beneath the observation point. Model resolution is, however, smoothed to at least a few hundred kilometers. In contrast, regional models based on aeromagnetic data provide high-resolution images of small-size lithospheric bodies (such as kimberlite pipes, impact structures (e.g. the Chicxulub), plutons, and ophiolites) which have a magnetic contrast with ambient rocks.

5.4.2 Calculation of lithospheric geotherms from magnetic data

The procedure for calculating lithospheric geotherms from satellite magnetic data typically includes the following steps and assumptions (e.g. Fox Maule *et al*., 2005):

- the magnetic field is represented in spherical harmonics (up to degree and order 90); the strong time-variable magnetic field in polar regions is controlled by combining data with spherical harmonic representations of the magnetic field with data from magnetically quiet times (as a result, satellite models of crustal magnetic fields are constrained);

- the core magnetic field is removed by high-pass (above degree 14) data filtering;
- the induced part of the magnetic signal is separated; in the oceans this is done by removing the remanent part (e.g. following Dyment and Arkani-Hamed, 1998); on the continents it is assumed that induced magnetization dominates (the assumption fails over the Bangui and Kursk magnetic anomalies);
- crustal magnetization is modeled by dipoles evenly distributed at the surface and the direction of the dipole is assumed to be given by the present core field;
- average crustal magnetization is proportional to the average magnetic susceptibility and the thickness of the magnetic layer;
- lateral crustal thickness variations dominate over magnetic susceptibility variations (which are assumed to be 0.035 and 0.0040 for the continental and oceanic crust, respectively);
- a crustal thickness model is used to account for the long-wavelength field component.

This approach allows modeling of the depth to the bottom of the magnetic layer, since magnetic methods for determination of the depth to the Curie isotherm build on the idea that average magnetization tends to zero below the Curie depth point. It is further assumed that:

- this depth corresponds to ~550–580 °C (the Curie temperature of magnetite);
- under certain assumptions (such as a steady-state thermal regime and thermal properties of the lithosphere) the depth to the Curie isotherm can be recalculated to surface heat flow values and lithospheric temperatures.

5.4.3 Curie temperature of mantle minerals

Curie temperature (Tc) is an intrinsic property of minerals which depends on their chemical composition and crystal structure; it determines the temperature (upon heating) at which (remanent or induced) magnetization of minerals disappears (ferromagnetic or ferrimagnetic minerals become paramagnetic). Lithospheric rocks consist of several mineral phases, and frequently their magnetization is characterized by a range of Curie temperatures (Fig. 5.24). The situation is similar to the melting of a multicomponent system, where solidus and liquidus temperatures provide the bounds on rock melting temperatures.

Magnetization of crustal and upper mantle rocks is controlled by ferromagnetic minerals of the iron–titanium oxide group and, to a much smaller extent, of the iron sulfide group, while iron hydroxides are also important in sedimentary rocks. Magnetite (Fe_3O_4) is the main ferromagnetic mineral in the lithosphere with Curie temperature Tc ~ 575–585 °C (see overview by Hurt *et al*., 1995) (Table 5.6; Fig. 5.25). The only iron oxide with ferromagnetic properties, maghemite (γ-Fe_2O_3) which is formed by the low-temperature oxidation of magnetite, is thermodynamically metastable and at $T > 250$ °C it converts to paramagnetic hematite (De Boer and Dekkers, 1996).

In general, the composition of the primary iron–titanium oxides varies with SiO_2 content of the rock. For this reason, the Curie temperature in titanomagnetites, which are the main magnetic minerals of igneous rocks, varies from less than 244 °C in basic rocks (gabbro,

Table 5.6 Curie temperature of some minerals

Mineral	Composition	*Tc* (°C)
Iron	Fe	770
Magnetite	Fe_3O_4	575–585
Titanomagnetites	$Fe_{3-x}Ti_xO_4$	100–550
Magnesioferrite	$MgFe_2O_4$	440

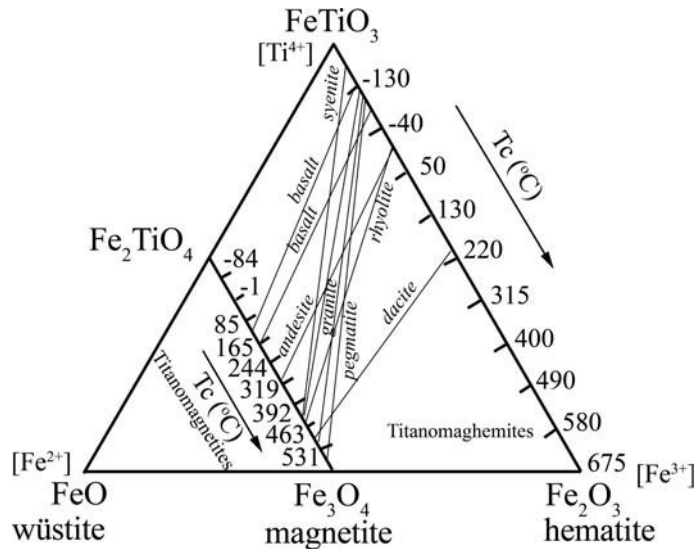

Fig. 5.24 Composition and Curie temperatures of primary Fe–Ti oxides from different igneous rocks, shown in the ternary system FeO (wüstite) – Fe_2O_3 (hematite) – TiO_2. Thin lines connect coexisting members of the (Fe_{2-y} Ti_yO_3) and (Fe_{3-x} Ti_xO_4) series (modified after Buddington and Lindsley, 1964).

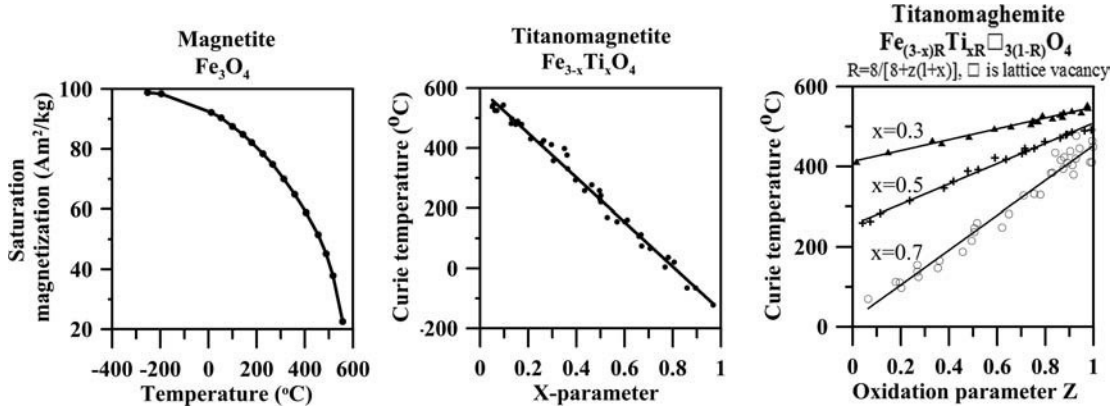

Fig. 5.25 Magnetic properties of mantle minerals. Left: Dependence of magnetite saturation magnetization on temperature. Middle and right: variations of Curie temperature in titanomagnetite and titanomaghemite as a function of composition (*x*-parameter) and oxidation (*z*-parameter) which is defined as the fraction of the initial Fe^{2+} ions in titanomagnetite converted to Fe^{3+} ions. (Data source: Hunt *et al*., 1995.)

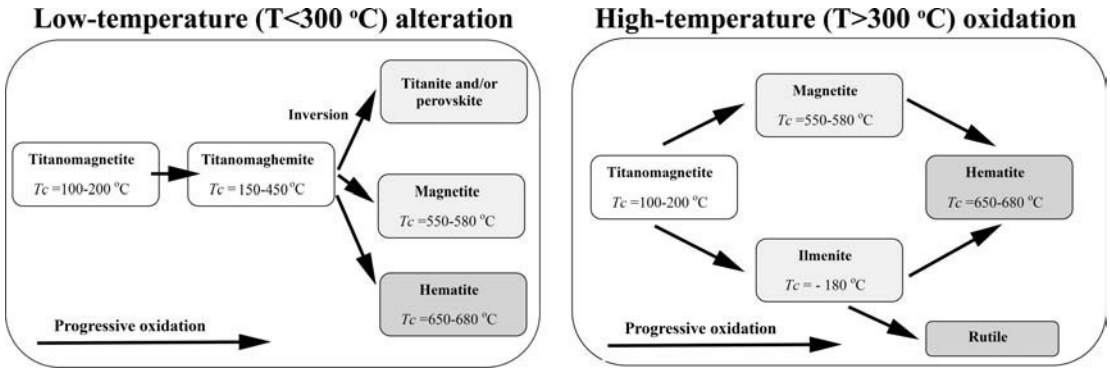

Fig. 5.26 The effect of low-temperature alteration and high-temperature oxidation on the primary Fe–Ti oxides in basalt.

basalt) to 165–463 °C in intermediate rocks (dacite) and to 463–580 °C in acid rocks (e.g. granite). The Curie point of titanomagnetitesis is strongly dependent on the amount and type of titanium and iron oxides, and *Tc* varies from 100 to 550 °C (Nishitani and Kono, 1983) (Fig. 5.25). The ferric–ferrous iron transition is also important for preservation of magnetic properties within the lithosphere. It is characterized by oxidation parameter defined as the fraction of the initial Fe^{2+} ions in titanomagnetite converted to Fe^{3+} ions. The temperature range for the ferric–ferrous iron transition is 200–400 °C. This is sometimes used to explain the discrepancy between the depth to the Curie point determined by geothermal and magnetic methods in stable continental regions.

The effect of oxidation on the primary Fe–Ti oxides in basalt is illustrated by Fig. 5.26. In particular, low-temperature oxidation is typical for alteration in oceanic basalts (Fig. 5.27). Magnetic properties of rocks are strongly affected by hydrothermal circulation and metamorphism. The former replaces magnetite by paramagnetic rocks (except for serpentinization of olivine-rich ultramafic rocks); the latter may have different effects depending on the P–T–t path of metamorphism and the composition of the protolith. Within the mantle, a significant magnetization can be associated with subducting slabs at temperatures below the Curie point (due to subsequent phase transitions metabasalt->eclogite->serpentine). Metallic alloys found in upper mantle xenoliths can produce significant magnetic anomalies down to depths of ~100 km (Purucker and Whaler, 2007). Because of the strong effect of chemical alteration on rock magnetization, primary and secondary Curie temperatures are distinguished. The primary Curie temperature characterizes the original composition of the primary magnetic minerals, while the secondary Curie temperature characterizes alteration of the original magnetic components of a rock which was subject to oxidation, reduction, or phase inversion. Comparison of the measured Curie temperature in a rock with its theoretical primary Curie temperature (e.g. Fig. 5.24) provides a measure of the degree of rock alteration.

5.4.4 Depth to the Curie point

Strictly speaking, it is unclear which Curie temperature, for magnetite or for titanomagnetite, should be used in interpretations of magnetic data since the concentration of Ti-oxides at

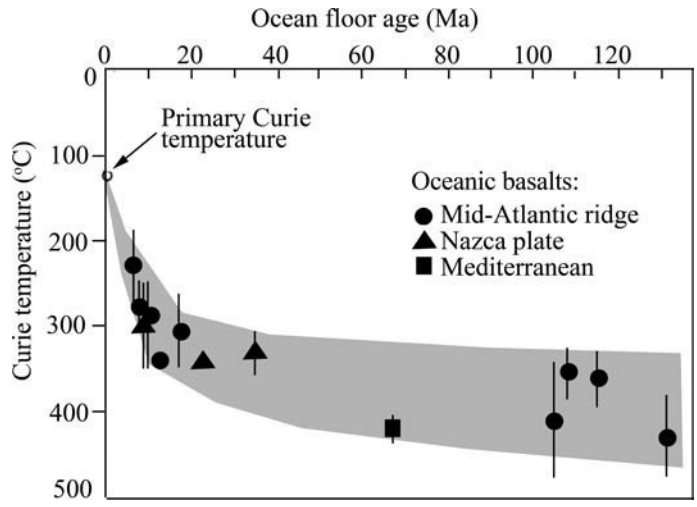

Fig. 5.27 The age dependence of Curie temperature in oceanic basalts based on data from DSDP drill holes in different locations. Error bars – range of measured Curie temperatures (modified after Petersen and Bleil, 1982). The observed pattern is unrelated to ocean plate cooling, but reflects the effect of low-temperature oxidation on Curie temperature of titanomagnetites which were separated from oceanic basalts.

different lithospheric depths is unknown. Commonly, the *T*c of magnetite is used to determine the depth to Curie point, for the reasons that:

(i) magnetite is the most abundant magnetic mineral in the crust,
(ii) magnetite and its compounds have the highest magnetization;
(iii) the Curie point of magnetite is the highest among the abundant magnetic minerals. This implies that the thus defined depth of the Curie point is the maximal possible depth for minerals to preserve their magnetization.

One should keep in mind that, due to compositional heterogeneity of the lithosphere, lateral and vertical variations in mineral concentrations should be expected. Chemical alterations, such as oxidation, further affect Curie temperature. As a result, the Curie depth determined for different regions may relate to different Curie temperatures and hamper their comparison.

Satellite magnetic data combined with the 3SMAC crustal model (Nataf and Ricard, 1996) were used to constrain the thermal regime of the lithosphere of Antarctica, where heat flow measurements are absent (Fox Maule *et al*., 2005). The first-order features of the model indicate: (i) the magnetic layer is thicker in East Antarctica than in West Antarctica; (ii) the highest lithospheric temperatures are calculated for regions of current volcanism where basal melting may occur; (iii) surface heat flow displays large lateral variations, 40–185 mW/m^2 (the model error is 20–25 mW/m^2).

A map of the depth to the 550 °C isotherm for the continents provides a geothermal estimate of the depth to the Curie point of magnetite (Fig. 4.44b). In Europe, magnetic data, in accordance with thermal data, show that craton-to-non-craton transition (the

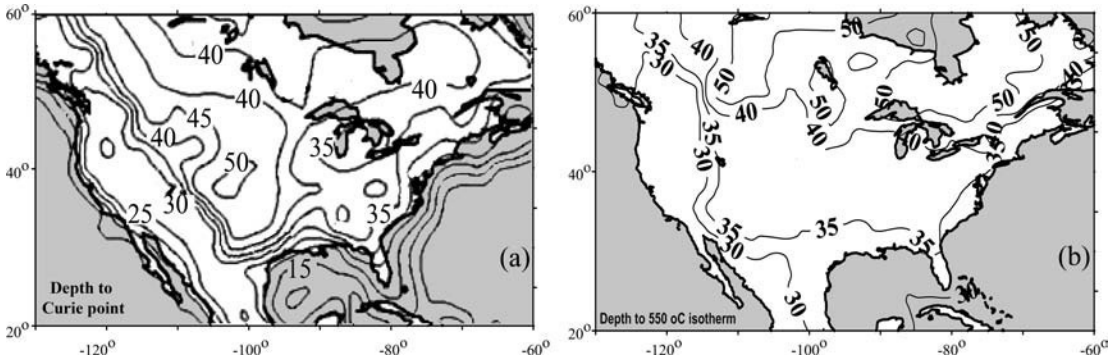

Fig. 5.28 (a) Map of the magnetic crustal thickness from the initial induced magnetization model over the North American region (modified from Purucker *et al.*, 2002); (b) depth to 550 °C isotherm constrained by geothermal data (Artemieva, 2006; www.lithosphere.info). The depth uncertainties of both maps are about 5 km.

Trans-European Suture Zone, TESZ, in central Europe) is a first-order feature in the lithospheric structure. In the Variscan Europe to the west of the TESZ the depth to the bottom of the magnetic layer is 29–33 km (Chiozzi *et al.*, 2005) and corresponds approximately to the seismic Moho. Similarly, in North America the thickness of the magnetic layer and the depth to 550 °C isotherm are > 40 km in the Canadian Shield, become less than 30–35 km across the southern edge of the North American craton, and have values of 10–20 km in tectonically active regions of western USA (Fig. 5.28). The results for North America (Hinze and Zietz, 1985; Purucker *et al.*, 2002) illustrate that although thermal and magnetic estimates of the depth to 550–580 °C isotherm generally agree, there are significant short-wavelength differences that result from assumptions behind thermal and magnetic modeling.

5.5 Summary of non-thermal studies of lithosphere thermal state

Xenolith data

The advantage of xenolith data is that it provides the only available direct sampling of the deep sections of the lithosphere. The disadvantage is that the areal coverage by xenoliths is strongly non-uniform, and it is unclear how representative xenolith-based constraints are on the *in situ* unperturbed thermal state of the lithosphere.

There is a significant difference in xenolith geotherms constrained by different geothermobarometers (Fig. 5.8). Since most of them are calibrated at temperatures 900–1400 °C and pressures 2–6 GPa, the best consistency of xenolith P–T arrays is achieved at this P–T range. When different geothermobarometers are used on samples derived from the lithospheric mantle in the same location, pressure estimates may differ by 1.0–1.5 GPa and temperature estimates by > 200 °C. The accuracy of P–T

determinations on xenolith samples cannot be assessed since many thermobarometers are sensitive to bulk composition. There are no reliable geobarometers for pressures within the spinel stability field. Because of significant differences in temperature gradient, some geothermobarometers may produce a kink on the geotherm, while others (for the same data), do not. Geothermobarometry is based on the critical assumption of mineralogical equilibria in the system. This condition is not satisfied, for example, in xenoliths from some parts of Siberia. Garnet geotherms, widely used by Griffin and co-authors in their studies, have a conceptually different meaning than xenolith geotherms based on conventional approaches and their depth constraints should not necessarily agree (Fig. 5.11).

Xenoliths provide information on the thickness of TBL, CBL, and RBL (Fig. 5.4). The base of RBL can be constrained by variations in xenolith texture (the transition from coarse to sheared), CBL – by variations in major element composition (the transition from depleted to fertile), and TBL – by P–T arrays. Commonly the bases of all three boundary layers as constrained by xenolith data are at about the same depth. However, this depth may differ significantly from the lithospheric base determined by various geophysical methods. The kink commonly observed on xenolith geotherms should not necessarily correspond to the base of TBL; it can be an artifact of geothermobarometry, reflect thermal disequilibrium related to magmatism, or be a true steady-state feature produced by a sharp contrast in lithospheric thickness at the edge of a craton (Figs. 5.9, 5.10).

Xenolith P–T arrays from the Archean cratons apparently indicate that while some cratons have a 200–220 km thick TBL, others may extend down to at least ~300 km. Since the absence of evidence for cannot be interpreted as evidence against, the absence of known xenoliths derived from depths greater than 250 km within the lithospheric mantle does not prove that the cratonic lithosphere cannot be thicker than 220–250 km. Their absence may be related to the conditions of kimberlite magma generation and ascent.

Lithosphere temperatures derived from seismic data

Velocity–temperature conversions provide important constraints on lithospheric temperatures in regions with no (or low quality) borehole heat flow data, or regions where thermal modeling is subject to large uncertainty.

Velocity–temperature conversions are subject to a set of assumptions on the physical origin of seismic velocity perturbations. While temperature variations are assumed to be the major factor producing seismic velocity perturbations, non-thermal effects on seismic velocity variations such as anisotropy, the presence of melt and water, compositional and grain size variations may be equally important. However, most non-thermal effects are difficult to quantify and, except for the presence of melt, most of these factors are ignored in velocity–temperature conversions.

The effect of water on seismic velocity reduction can be dramatic, both direct and indirect through the enhancement of anelastic relaxation. This means that an analysis of seismic velocities and seismic attenuation in terms of mantle temperatures should take into account the effect of water, separately from the effect of temperature. However, currently, systematic

laboratory results on the effect of hydrogen on seismic attenuation are unavailable, and there is no proper experimental basis for such corrections.

Compositional effects may be significant in producing seismic velocity anomalies, but velocity–temperature conversions cannot separate temperature and compositional effects unless an independent set of data (such as gravity) is used. Alternatively, assumptions on variations in the lithosphere composition are used to invert seismic data to temperatures.

Limitations associated with seismic models (such as model resolution in terms of vertical, lateral, and amplitude resolution) propagate into additional uncertainties in velocity–temperature conversions.

As a result, the uncertainty of temperature constraints from seismic data cannot be quantified and is not known. Additionally, horizontal heat transfer prevents the existence of sharp temperature contrasts in the lithosphere, and strong (several hundred degrees Celsius) short-wavelength lateral temperature contrasts are artifacts of inversion, unless they are caused by recent geodynamic processes.

Geotherms constrained by Curie temperature

Similarly to velocity–temperature conversions, magnetic data allow constraining of lithospheric geotherms in regions with no heat flow data (e.g. Antarctica). The depth where lithosphere magnetization tends to zero is interpreted as the depth where the Curie point of magnetite (550–580 °C) is reached. This depth–temperature pair constrains the lithospheric geotherm.

Lithospheric rocks have several Curie points associated with different minerals, and it is unclear which Curie point should be used in interpretations. Mineral alterations, in particularly oxidation, have a strong effect on Curie temperature. Therefore, the Curie depth determined for different regions may relate to different Curie temperatures. As a consequence, lithospheric geotherms may also be significantly different.

For these reasons, it is difficult to put uncertainty limits on lithosphere geotherms constrained by magnetic data. Additionally, separation of the induced part of the magnetic signal from the remnant part is subject to a significant uncertainty on the continents. Despite these limitations, a comparison with thermal models shows general agreement between the depth to Curie point and the depth to a 550 °C isotherm, but the details are different.